UNIVERSITY OF BIRMINGHAM

Development of On-Demand Low Temperature Electrolysers and Their Systems

by

Daniel Robert Symes

Thesis submitted in accordance with the requirements of

The University of Birmingham for the degree of

DOCTOR OF PHILOSOPHY

School of Chemical Engineering

College of Engineering and Physical Sciences

The University of Birmingham

1st May 2015

Abstract

Water electrolysis represents a technology for converting surplus renewable energy generation into hydrogen energy. With an increasing market penetration of intermittent renewable energy generation, the need for energy storage is more apparent. Options for hydrogen via water electrolysis include injection into the natural gas grid, refuelling of fuel cell vehicles and conversion back into the electricity grid via fuel cell when a deficit in supply/demand chain exists.

Industrial on-demand hydrogen generating alkaline electrolysers were electrochemically characterised and analysed on an internal combustion engine. These electrolysers exhibited low efficiencies, low gas flowrates and subsequently zero change in engine emissions due to the poor design and build. An improved alkaline electrolyser was designed, built and tested, and exhibited improved efficiency and gas output compared to the industrial electrolysers and an improved reduction in engine emissions.

The increased power consumption of the electrolyser results in a rise in electrode degradation which is responsible for the decrease in electrode lifetime. A method for prolonging the electrode lifetime is proposed through a metallic “oxygen-getter”. This implementation of an oxygen-getter has shown to prevent corrosion of the electrode material and thus reduces oxide content on the surface. The electrode lifetime in an alkaline electrolyser was proven to increase, but the commercial trend is shifting towards the more attractive PEM technology for electrolysis due to higher current densities, ability to handle variable input loads and non-caustic liquid requirement.

PEM electrolysis is a rapidly evolving newly commercial electrolyser technology which uses a solid polymer membrane to split pure water into hydrogen and oxygen. The

disadvantages of the technology are high cost due to the expensive PGM electrocatalyst and the ultrapure water requirement, with the latter the source of minimal research. The impact of water quality on two different membranes (Nafion® and Fumea®) performance was compared and tolerance to domestic tap water was highlighted.

The cations present in varying grades of water were measured and systematically added to ultrapure water. This cation targeting demonstrated the limitations of specific cations in ultrapure water and the subsequent effect they had on MEA lifetime. The efficiency and degradation characteristics were analysed between alkaline and PEM technology and PEM technology was proven to show better performance and robustness over prolonged operation, along with the other advantages highlighted previously.

A commercial on-demand PEM electrolyser was then tested and system designed for integration with an existing hydrogen refuelling station at the University of Birmingham. This mimicked the case for a distributed hydrogen system where the hydrogen is produced onsite for fuel cell vehicles resulting in a carbon neutral fuel.

I dedicate this thesis to my family for their love, support and encouragement

Acknowledgements

I would like to dedicate this thesis to my first supervisor Waldemar Bujalski without who I would not be in this position on the doctorate programme. I would like to thank my supervisors Dr Bushra Al-Duri for her support, patience and diligence when assessing my work, and Dr Aman Dhir for his knowledge in the research area, I.T. DIY, and his keen eye for a bargain. I would like to thank staff, students and friends at the Centre for Hydrogen and Fuel Cell Research and School of Chemical Engineering for their assistance, entertainment and tolerance over the 4 years. I also thank the EPSRC for funding this PhD as part of the DTC in Hydrogen, Fuel Cells and their Applications.

I would like to give thanks to the numerous undergraduate students who have assisted towards this research, specifically Connie Taylor-Cox, Leighton Holyfield, James Girling, Dhiren Mistry & Ailsa Crawford. Without your extra pairs of hands in the lab I would not be in this position to submit this thesis at this time. I also thank Jose Martin Herreros for his knowledge, assistance and support with the engine testing.

Simon also wishes to express his gratitude to Bob Sharpster and Bill "Burns" Harris for their assistance in the manufacture of the electrolysers built herein, fire awareness, endless coffees, life lessons, Sara's Specials and Friday Breakfasts enjoyed.

There have been some great memories during the PhD: The Oil Spill, JENNY the Fuel Cell, Tony Bang, Dr Oxbig, Lickey Hills, FCV Snow Testing, Amy Winehands, The QHC Army, Coq au Vin, The Easter Flood, Bingo Backseat Journeys, General Election Debate FCV Debacle, Mandelsongate, Ben Millington. I give thanks for all the laughs.

Finally I would like to thank my family for their love and support. It is done.

"Yes, my friends, I believe that water will one day be employed as fuel, that hydrogen and oxygen which constitute it, used singly or together, will furnish an inexhaustible source of heat and light, of an intensity of which coal is not capable….water will be the coal of the future". **Jules Verne – Mysterious Island 1874**

Contents

List of Figures

List of Tables

Glossary of Terms & Abbreviations

°bTDC	Degrees Before Top Dead Centre
α	Electron Transfer Coefficients
γ	Interfacial Tension
η_o	Ohmic Overpotential
θ	Contact Angle (^{o})
ρ_o	Electrical Resistivity (Ω m)
Λ	Molar Conductivity ($m^2\ \Omega^{-1}\ mol^{-1}$)
κ	Electrical Conductivity ($\Omega^{-1}\ m^{-1}$)
χ	Electronegativity
ψ	Membrane Thickness (cm)
ω	Conductivity of the Cell (Siemens cm^{-1})
Atomic%	Atomic Percentage of an Element present in a Sample
BPR	Back Pressure Regulator
BSE	Back Scattered Electrons
CCM	Catalyst Coated Membrane
CLD	Chemiluminescence detection
CMP	Compressor

E_B	Binding Energy of the Electron at a certain Energy Level
EDX	Energy Disruptive X-Ray Spectroscopy
EI	Electron Ionisation
E_K	Kinetic Energy of Released Photon
ESCA	Electron Spectroscopy for Chemical Analysis
E_{volH2}	Energy supplied per unit volume of hydrogen
FCVs	Fuel Cell Vehicles
FID	Flame ionisation detection
FTIR	Fourier transform infrared spectroscopy
HER	Hydrogen Evolution Reaction
HHO	Combination of Hydrogen and Oxygen Gas (Oxyhydrogen)
HHV	Higher Heating Value of Hydrogen (MJ kg^{-1})
hv	Incident ray/electron energy
IC	Inorganic Carbon
ICE	Internal Combustion Engine
ICP-MS	Infrared Coupled Plasma Mass Spectroscopy
Imep	Indicated Mean Effective Pressure
LCV	Lower Calorific Value (MJ kg^{-1})

lpm	Litres per minute - Flowrate
LSV	Linear Sweep Voltammetry
MEA	Membrane Electrode Assembly
NDIR	Non-Dispersive Infrared
NPOC	Non-Purgeable Organic Carbon
OER	Oxygen Evolution Reaction
P&ID	Piping & Instrumentation Diagram
PEM	Polymer Electrolyte Membrane or Proton Exchange Membrane
PFSA	Perfluorosulfonic acid
PGM	Platinum Group Metal
RPM	Revolutions per Minute of an Internal Combustion Engine
SEI	Secondary Electron Imaging
SEM	Scanning Electron Microscopy
SPE	Solid Polymer Electrolyte
THC	Total Unburnt Hydrocarbon
TOC	Total Organic Carbon
XPS	X-Ray Photoelectron Spectroscopy

Chapter 1

Introduction

1.1. Project Motivation

There is growing global emphasis on the increase of greenhouse gases (GHGs), including carbon dioxide (CO_2), in the Earth's atmosphere (Figure 1.1). Many believe it is responsible for global warming and is leading to climate change [1]. This change in the Earth's atmosphere is thought to be due to man-made processes.

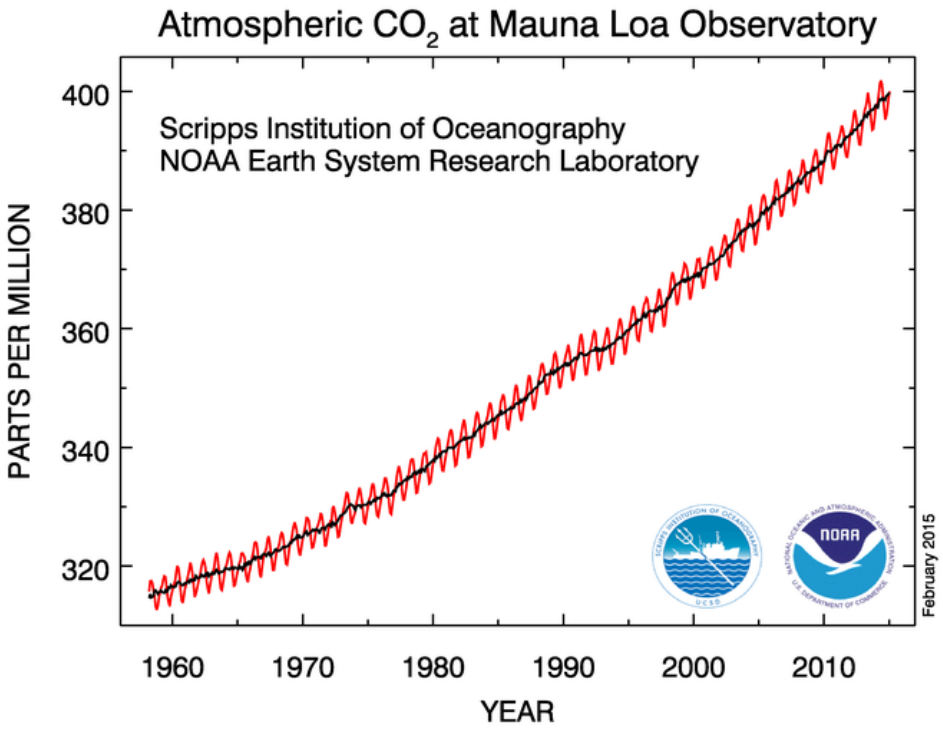

Figure 1.1: Atmospheric CO_2 Concentration Levels [2]

A large proportion of GHG emissions are from the extraction, processing and utilisation of fossil fuels for global energy requirement. Endeavours to reduce GHG emissions are in progress through methods such as carbon capture and storage (CCS) and amine scrubbing [3]. These processes however are not a sustainable solution and are seen as a temporary step to reducing GHG emissions.

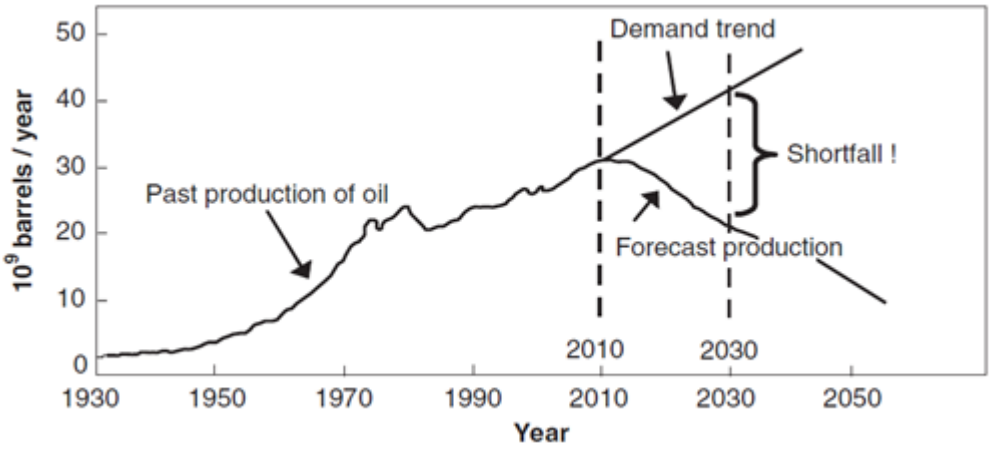

Figure 1.2: The 'Peak Oil' Concept [4]

Fossil fuels are not a sustainable source for energy supply. Crude oil reserves are expected to be exhausted within the next 30-50 years, which will shortly lead to 'peak oil' (Figure 1.2), here demand is greater than supply [4]. This will lead to a large rise in the price of oil. The search for a renewable and sustainable energy source is currently a major focus area in research institutions. Ideally the energy source would be carbon neutral. This means there would be zero GHG emissions from the energy production lifecycle resulting in no adverse effects on the planet us humans inhabit.

Hydrogen is being proclaimed as a future energy source, ideally for transportation applications, where the energy contained in hydrogen is utilised in hydrogen fuel cells (HFCs) (Figure 1.3). Compared to gasoline (transportation fuel), hydrogen has a higher gravimetric energy density (gasoline = 48.6 MJ/kg; hydrogen = 140.4 MJ/kg) [5].

HFCs produce water and electricity, with no GHG emissions, hence if the hydrogen supplied to the fuel cells is made from carbon neutral sources, then the entire process of energy extraction to utilisation is GHG free [6]. This is the hydrogen cycle (Figure 1.4).

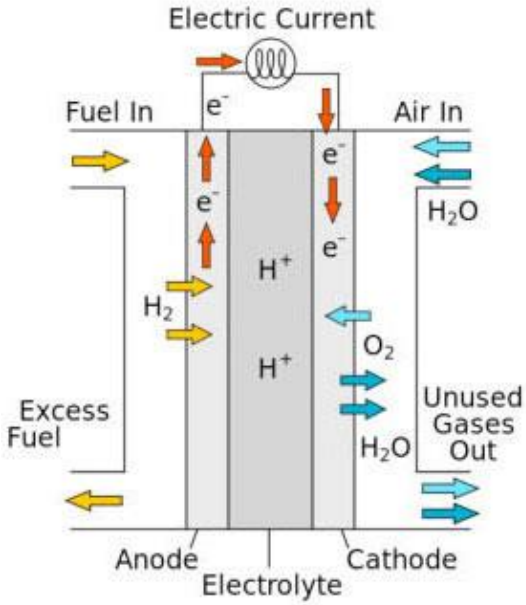

Figure 1.3: Diagram of a Hydrogen Fuel Cell [7]

Hydrogen required for a HFC does not occur naturally on our planet, even though it is abundant in the universe. It is naturally found joined in compounds to other atoms e.g. water (H_2O) and methane (CH_4). Hydrogen is consequently known as a secondary energy source or energy 'vector' [8].

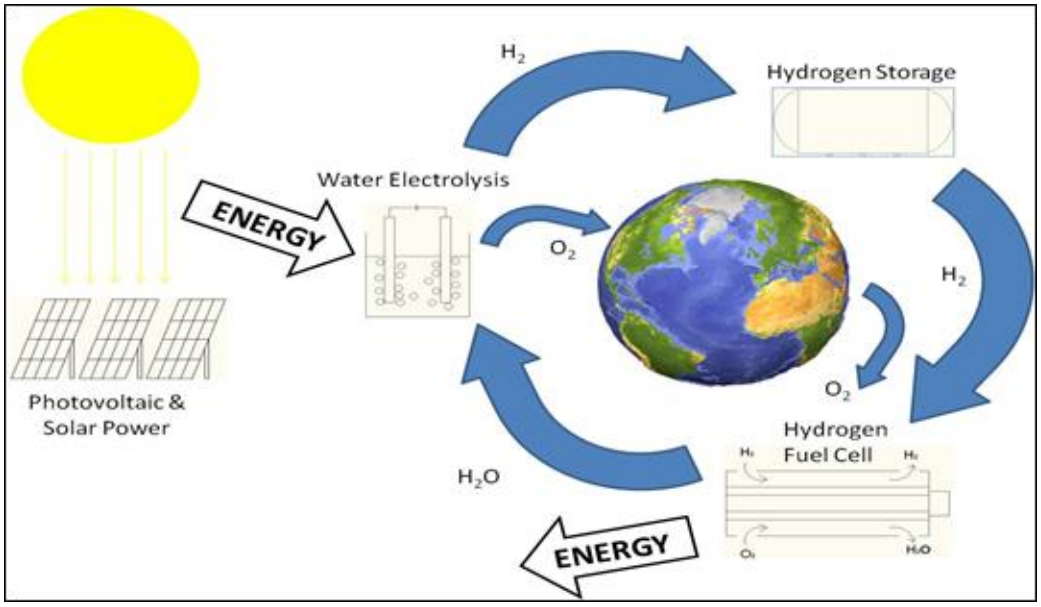

Figure 1.4: The Hydrogen Cycle

This introduction examines the various production pathways for producing hydrogen with an emphasis on water electrolysis as the future for large scale zero-carbon hydrogen production.

1.2. Hydrogen Production Overview

There are currently 50 million tonnes of hydrogen produced annually [9]. This figure is expected to rise over the coming decades with the growth of a hydrogen economy. This hydrogen is currently used in industry to produce ammonia, hydrogenation of fats and pharmaceutical manufacture (Figure 1.5) [4, 10].

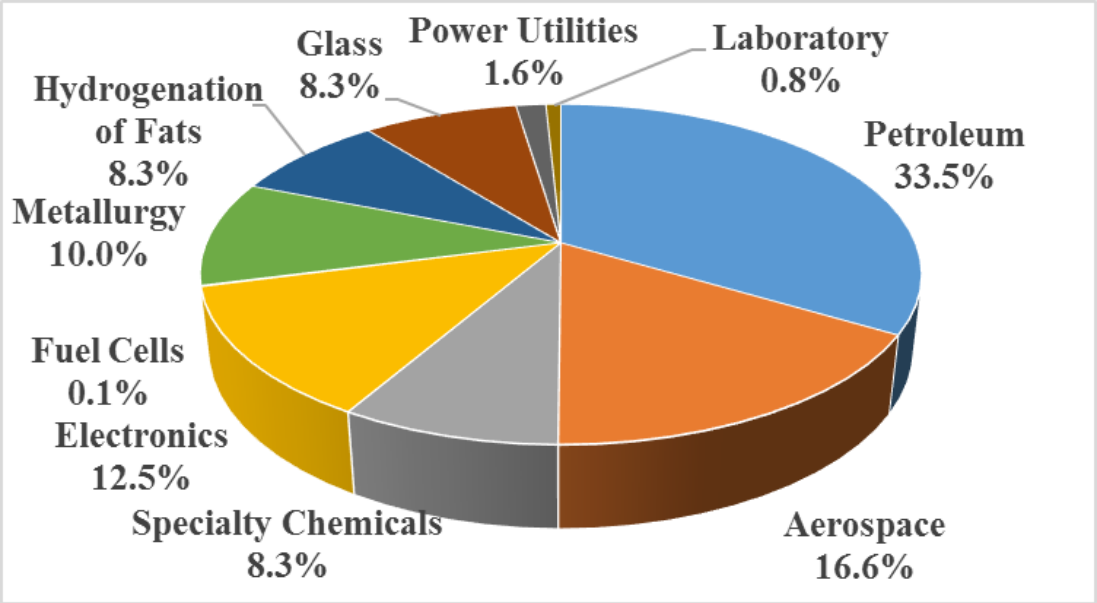

Figure 1.5: Representation of Uses of Hydrogen [4, 10]

These industries will continue to use this feedstock of hydrogen gas, so a huge increase in the volume of hydrogen produced each year will be required for a growing hydrogen economy.

If a future hydrogen economy is to succeed, hydrogen would need to be sourced from more than one single production pathway. Each production pathway has unique benefits and disadvantages, such as cost of production and the purity of hydrogen produced. As a result for new sustainable methods of producing hydrogen more research is required in the optimisation and commercialisation.

Of current hydrogen production, 96% comes from fossil fuel sources (Figure 1.6) [10]. The feedstocks to these processes are finite and produce GHGs which is unsustainable and undesirable for the vision of a long term hydrogen economy.

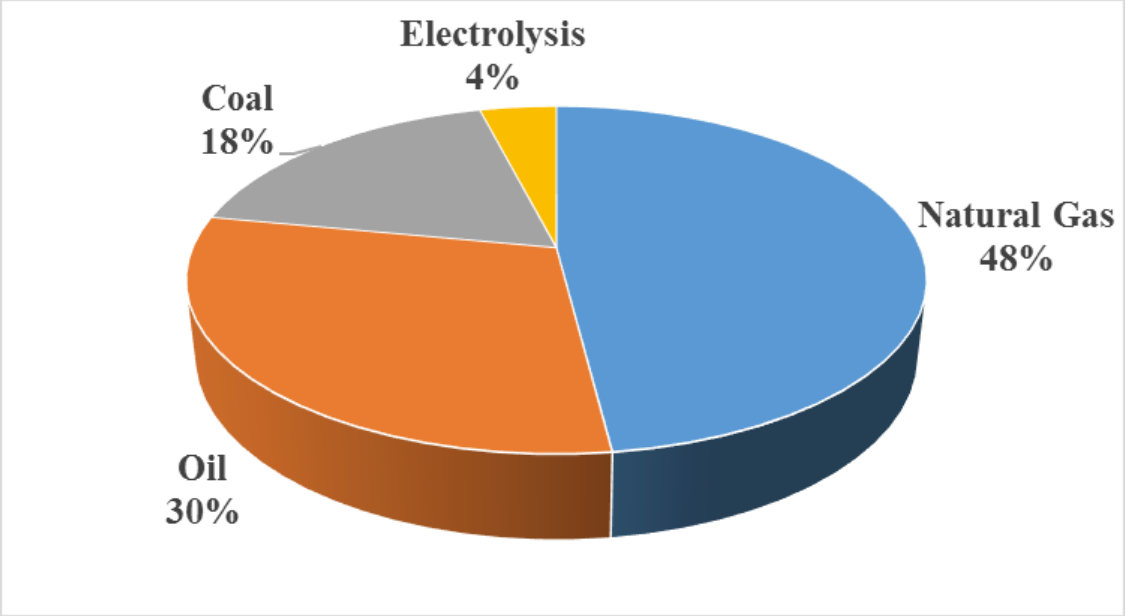

Figure 1.6: Current Processes for Producing Hydrogen [10].

Currently water electrolysis contributes only 4% of global hydrogen production [10]. This is due to the high economic cost compared to fossil fuel derived hydrogen. Hydrogen produced from water electrolysis currently supplies niche applications, which require a higher purity hydrogen than that produced by fossil fuel derived hydrogen [11].

An example of this type of applications is for Proton Exchange Membrane Fuel Cells (PEMFCs). PEMFCs require an ultra-high purity of hydrogen i.e. no impurities. This reduces the chance of poisoning the highly expensive platinum based catalyst, which would decrease the performance of the PEMFC irreversibly.

1.3. Hydrogen Production Methods

1.3.1. Fossil Fuel Derived

1.3.1.1. Steam Methane Reforming

Hydrogen production from methane is a well-established technology which produces almost half of all hydrogen produced today. When compared to other fossil fuels, methane (natural gas) is the most desirable, since it's widely available, relatively cheap and easy to handle [12]. Methane also has a high hydrogen-carbon ratio (4:1) of all fossil fuels (oil = 2:1; coal = 0.5:1).

The reaction mechanism for producing hydrogen from SMR is to pass methane and steam over a nickel based catalyst at approximately 900^{o}C, and high pressure (3-4 MPa) (see Eq. 1.1) [5].

$$CH_4 + H_2O \leftrightarrow CO + 3H_2 \qquad \text{Eq. 1.1}$$

The hydrogen and carbon monoxide produced is commonly known as synthetic gas or 'syngas', because it is used to prepare various organic chemicals such as methanol and formaldehyde [9]. The reaction is endothermic and requires 252 kJ per mole of methane (under standard temperature and pressure (25^{o}C; 1atm).

Hydrogen yield can be enhanced further, through the water-gas shift reaction which oxidises carbon monoxide to carbon dioxide (see Eq. 1.2) [5].

$$CO + H_2O \leftrightarrow CO_2 + H_2 \qquad \text{Eq. 1.2}$$

This reaction takes place in two stages at a much lower temperature than the initial reaction mechanism. First, the high temperature water-gas shift reaction takes place at 400^{o}C where the CO content is reduced to < 2 volume%, and secondly the low temperature water-gas shift reaction takes place at 200^{o}C where the CO content is reduced to < 0.2 volume% [5].

Simplifying the two reactions above, the complete reaction mechanism is:

$$CH_4 + 2H_2O \leftrightarrow CO_2 + 4H_2 \qquad \text{Eq. 1.3}$$

A diagram illustrating the basic process for hydrogen production from steam methane reforming is illustrated in Figure 1.7.

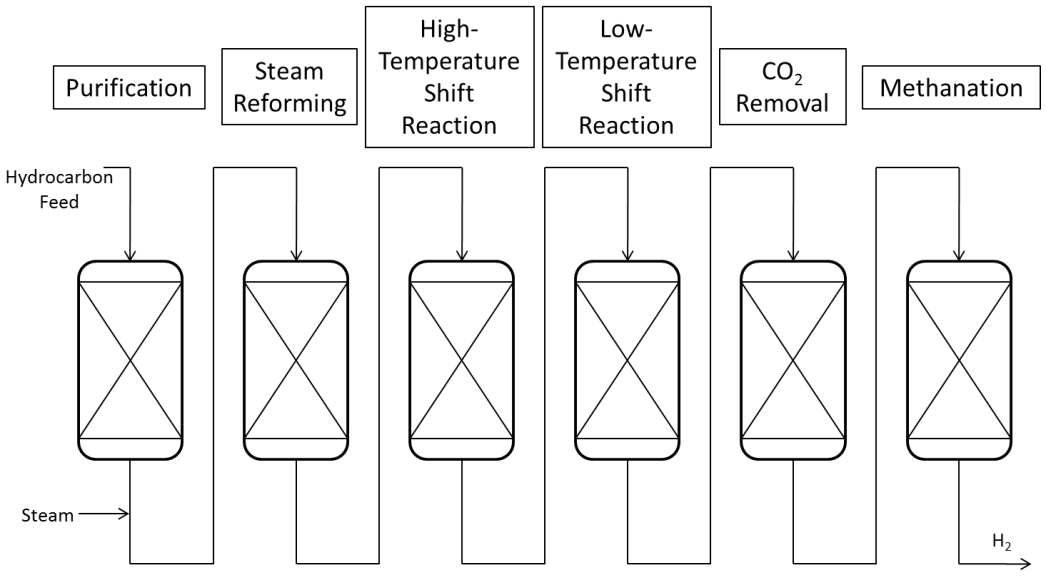

Figure 1.7: Process Flow Diagram for SMR

1.3.1.2. Partial Oxidation

Partial Oxidation (POX) is a process that is used to convert heavy liquid hydrocarbons e.g. oils and residues, to hydrogen. This process is similar to that of SMR, but involves the use of oxygen gas instead of steam to react the hydrocarbons with [13]. The reaction mechanism is outlined below (see Eq. 1.4) [4].

$$2C_aH_b + aO_2 \rightarrow 2aCO + bH_2 \qquad \text{Eq. 1.4}$$

The minimum amount of oxygen required to oxidise the carbon to carbon monoxide is used, whilst leaving behind elemental hydrogen, which gives rise to the name 'partial oxidation' [13]. The reaction is exothermic and produces syngas which undergoes water-gas shift reaction and then the CO_2 and H_2 are separated. The reaction is carried out at 1250 ^oC -1500^oC and 3-13 MPa [5]. This high temperature and pressure removes the requirement for a catalyst. The typical thermal efficiency is 60-75% for methane fuel based on the higher heating values [8]. This process is illustrated in Figure 1.8.

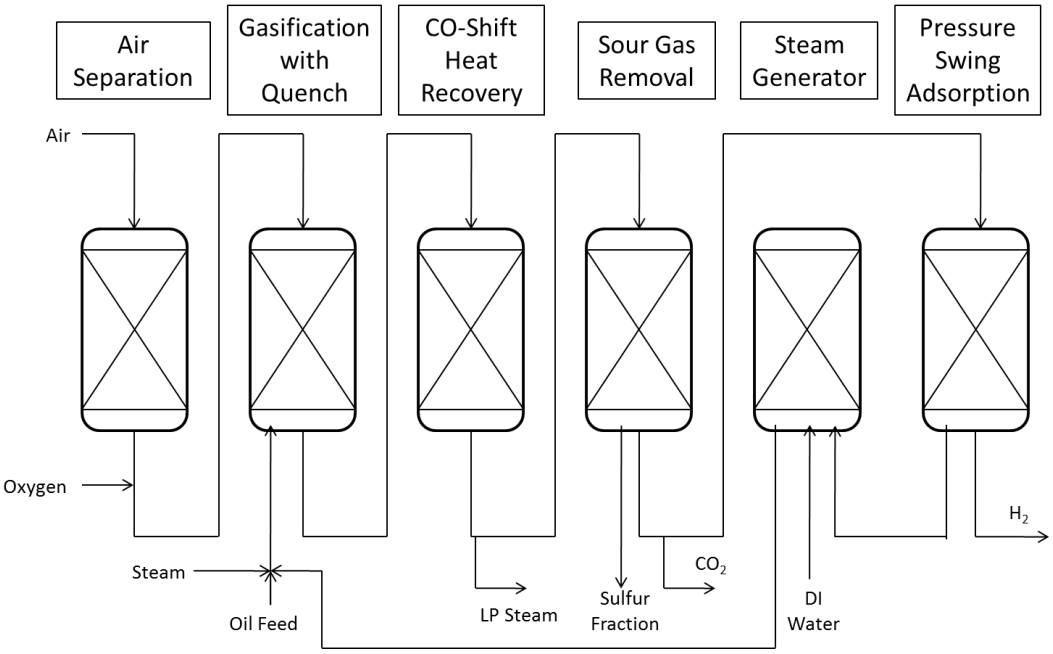

Figure 1.8: Process Flow Diagram for POX

A disadvantage of POX when compared to SMR, is the hydrogen-carbon ratio. When comparing the SMR and POX for pre-water-gas shift reactions we find the ratios are 3:1 and 2:1-1:1 respectively (depending on the feedstock used). An advantage of POX is that the reaction is highly exothermic, so no external heat source is required, whereas for SMR the reaction is endothermic and requires additional heat [9].

1.3.1.3. Coal Gasification

With supplies of natural gas being depleted, coal is expected to be the preferred technology to meet our electrical energy needs for the future (there are estimated 150 years of coal reserves compared to estimated 50 years of natural gas) [8].

By definition, gasification is a process which converts solids into combustible gases in the presence of oxygen/air at high temperatures > 700^{o}C [3]. This reaction, where coal is the solid feedstock, produces, as with SMR and POX, syngas. The reaction mechanisms are detailed below (see Eq. 1.5 to Eq. 1.10) [5].

Gasification	$C + 0.5O_2 \rightarrow CO$	Eq. 1.5
	$C + H_2O \rightarrow CO + H_2$	Eq. 1.6
	$CO + H_2O \leftrightarrow CO_2 + H_2$	Eq. 1.7
Water-Gas Shift	$CO + H_2O \leftrightarrow CO_2 + H_2$	Eq. 1.8
Purification	$CaO + CO_2 \rightarrow CaCO_3$	Eq. 1.9
	$CaO + H_2S \rightarrow CaS + H_2O$	Eq. 1.10

The syngas is then placed under water-gas shift reactions to produce a suitable yield of hydrogen. Purification involves the use of lime (CaO), to separate carbon from the hydrogen [14].

There are three types of gasification reactor, entrained flow reactors, fixed bed reactors and fluidised bed reactors. Entrained flow reactors are the most aggressive form of gasification where concurrent flows of preheated coal and oxygen are reacted together. The operating temperature of reaction is 1500^{o}C and operating pressure of 2-3 MPa. The feed consists of dried, milled coal and this reacts with oxygen and steam to produce syngas [4].

Fixed bed reactors are the oldest form of gasification technology. The reactor resembles a blast furnace, where coal is lowered into the furnace on a grate into the furnace. Steam and oxygen enter at the bottom of the furnace where the temperature is approximately 2000^{o}C [15]. The syngas produced is removed from the reactor near the top of the furnace where the temperature is lower at 450^{o}C. The solid waste (slag) at the bottom of the reactor is removed and the pressure in the reactor is approximately 2-3 MPa. The residence time of coal gasification in this reactor is between 30 minutes and one hour. These long residence times result in a slow throughout of coal and are therefore limited in industrial applications [8].

A fluidised bed reactor is currently the most commonly used gasification reactor and involves the suspension of fine particles in the reactor through the flow of steam/oxygen upwards until the mixture behaves like a fluid [3]. This reaction is carried out at 900-1100^{o}C and 2-3MPa. This type of reactor gives rise to high mass and heat transfer rates between the coal and the gas. The syngas produced is removed from the reactor where it undergoes water-gas shift reaction to increase the hydrogen produced [15].

A diagram illustrating the basic process for hydrogen production from coal gasification is illustrated in Figure 1.9.

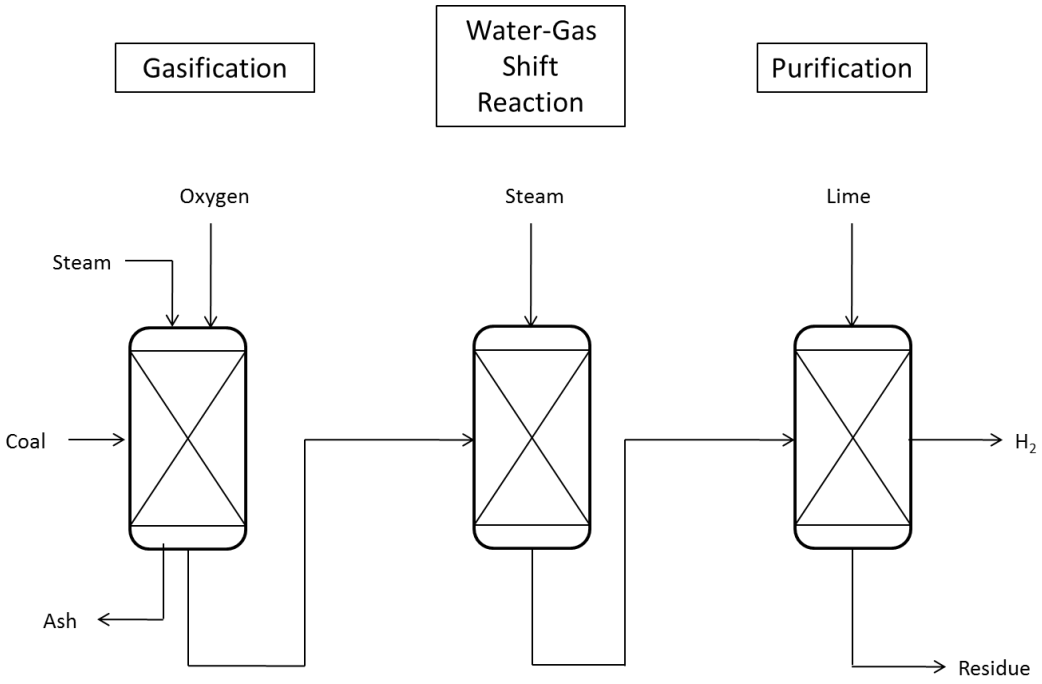

Figure 1.9: Process Flow Diagram of Coal Gasification

Coal gasification produces hydrogen at a faster rate than SMR and POX, but the capital costs are greater due to the pre-treatment required on the coal (milling, desulphurising) and the increased number of particulates in the syngas produced [5]. These cleaning processes are a vital component of the gasification process, since the restriction of catalyst poisoning in the reactor, and the purity of syngas produced are of vital importance to meet the preset requirements.

1.4.2. Biologically Derived

Hydrogen is primarily produced from fossil fuel sources, and research is growing into hydrogen derived from biological sources, because of its attractive sustainability value. These methods are discussed here.

1.3.2.1. Anaerobic Digestion

Anaerobic Digestion is the breakdown of microorganisms in the absence of oxygen to produce a biogas consisting of methane and carbon dioxide [16]. This methane then undergoes reformation in the presence of steam to produce hydrogen and carbon monoxide (syngas) [13]. The high temperature and low temperature water-gas shift reaction converts the remaining CO to CO_2 and is then removed, through a process such as pressure swing adsorption [5].

1.3.2.2. Pyrolysis

Pyrolysis is a process similar to thermolysis for organic materials, from which biomass undergoes thermal decomposition to produce bio-oils in the absence of oxygen [17]. This bio oil is then partially oxidised in a reformer with the addition of steam to produce syngas. This syngas then goes through the similar water-gas shift reactions and purifications processes to produce hydrogen [5]. The partial oxidation of the bio-oil results in a lower hydrogen-carbon ratio than biogas produced from anaerobic digestion of biomass [17].

1.3.2.3. Fermentation

Fermentative Hydrogen production consists of biomass producing ethanol through distillation from organic substrates. This reaction involves the use of a group of bacteria using various enzyme systems to produce ethanol [18]. The ethanol produced is then reformed with steam to produce hydrogen, carbon monoxide & carbon dioxide [19]. The water-gas shift reactions convert the CO to CO_2, and this is then separated from the hydrogen. The reaction is similar to that of anaerobic digestion and pyrolysis, since hydrogen is produced in the absence of oxygen (air). There are two main types of fermentation, dark fermentation which does not require light to produce H_2, and photofermentation which does require light [5].

1.3.2.4. Photolysis

Photolysis is a process for producing hydrogen from solar energy through photosynthesis. The process utilises energy from the Sun to split water and produce hydrogen [20]. The reaction occurs in the thylakoid membrane in the chloroplast [20]. This is where the energy in the light is converted to chemical energy. Water molecules oxidise to produce hydrogen and oxygen gases, and the electrons are transferred through a membrane to Adenosine Triphosphate (ATP). This passes chemical energy in the cells for metabolism. This ATP then undergoes hydrolysis to produce orthophosphate (PI) which is an inorganic phosphate [5]. The reaction mechanism is illustrated in the diagram (Figure 1.10).

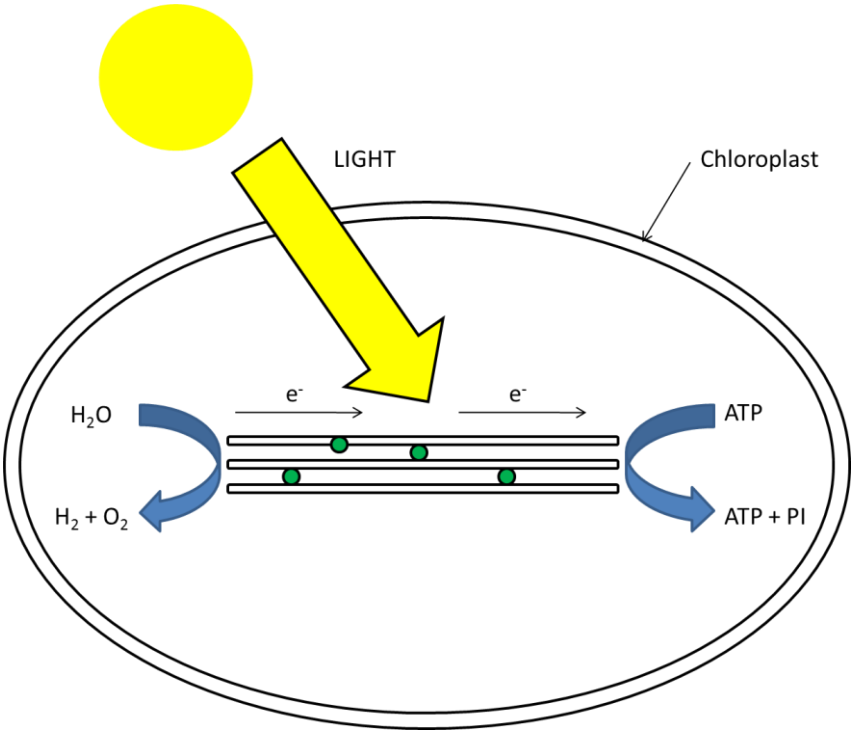

Figure 1.10: Reaction Mechanism for Photolysis

1.3.2.5. Photocatalysis

Similarly to photolysis, photocatalysts for splitting water directly to produce hydrogen have been considered. The photocatalysts absorb light from the Sun and generate free electrons and free holes, which are capable of performing reduction and oxidation (redox) reactions [8]. The electrons are transferred from the water to oxygen gas reaction to the hydrogen evolution reaction. Many catalysts have been researched which include TiO_2, RuO_2, CdS_2 and cobalt. These catalysts continue to be an active area of research and as of yet are not commercially viable to produce hydrogen on a large-scale [5]. The reaction mechanism is illustrated in Figure 1.11.

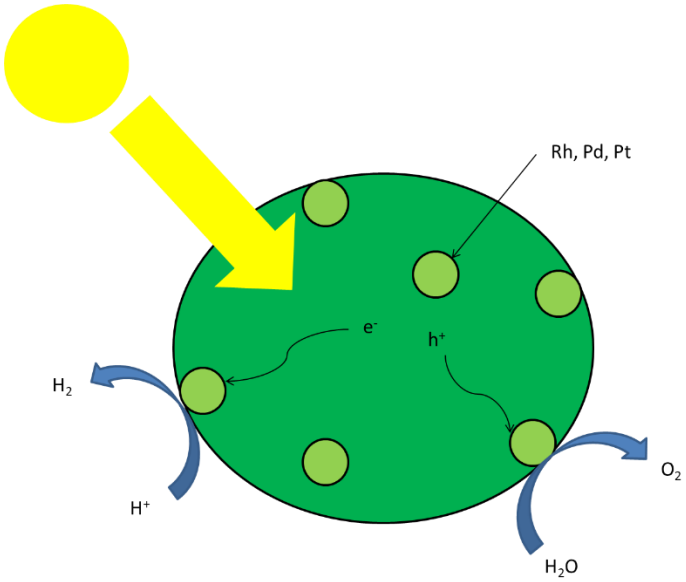

Figure 1.11: Reaction Mechanism of Photocatalysts

These bio-derived sources of hydrogen provide a sustainable feedstock of 'fuel' to produce hydrogen and are seen by many as a likely method for producing hydrogen once the fossil fuel feedstocks for hydrogen production have been depleted.

1.3.3. Thermally Derived

This section describes processes for producing hydrogen which require high temperatures and have potential to be coupled with nuclear power generation.

1.3.3.1. Thermolysis

Water is a very stable molecule, which gives rise to a high temperature requirement to split it into its constituent atoms. Steam enters the reactor and temperatures of between 2000-3000^{o}C are required to thermally split the water molecules [7]. These high temperatures are very limited in industry, so the coupling of this technology with nuclear

power generation (which produces heat in this temperature range), could be a beneficial use of this waste heat [10].

1.3.3.2. Chemical Looping

Commonly researched in the nuclear industry, the sulphur-iodine cycle has been studied extensively since the 1970s [10]. It promotes the oxidation of $S^{(IV)}$ to $S^{(VI)}$ through I_2. The reaction mechanism is below (see Eq. 1.11 to Eq. 1.13).

$$I_2 + SO_2 + 2H_2O \rightarrow 2HI + H_2SO_4 \qquad \text{Eq. 1.11}$$

$$H_2SO_4 \rightarrow SO_2 + H_2O + 0.5O_2 \qquad \text{Eq. 1.12}$$

$$2HI \rightarrow I_2 + H_2 \qquad \text{Eq. 1.13}$$

The first reaction (Eq. 1.11) is exothermic, whilst the other two reactions (Eq. 1.12 & Eq. 1.13) which see the decomposition of the sulphuric acid and hydrogen iodide are endothermic and require heat for the reaction to proceed. The sulphur and iodine are continuously looped through the reactors, with hydrogen and oxygen being removed from the endothermic reactors and water inserted in the Bunsen reactor. The Bunsen reaction occurs at 120^{o}C, the sulphuric acid decomposition occurs at 850-900^{o}C, and the hydrogen iodide decomposition occurs at 300-450^{o}C [4]. The process is illustrated in Figure 1.12.

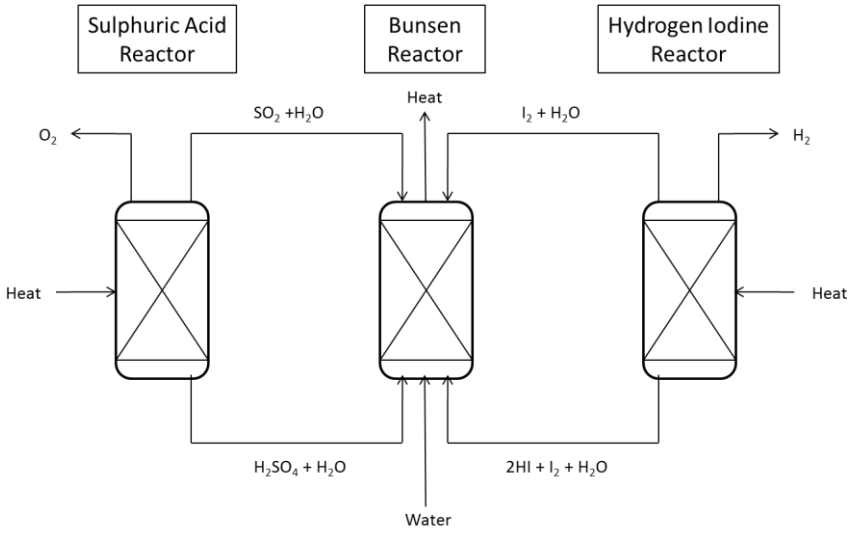

Figure 1.12: Process Flow Diagram for Chemical Looping

1.3.4. Electrically Derived

Electrolysis is defined as applying an electrical current to split compounds [21]. Water splitting occurs when a direct current is passed between an anode and a cathode submerged in water separated by a solid electrolyte or a aqueous electrolyte to transport ions and complete the electrical circuit [22].

If the electrical energy is supplied from renewable resources, 'Green' hydrogen i.e. greenhouse gas emission free, is produced. Water is also in limitless supply, there are approximately 1.26×10^{21} litres of water on Earth [23]. It is not geographically limited either, which could lead to the fall of energy poverty globally.

Water is a very stable molecule with a heat of formation of -285.83 kJ/mol under standard conditions [24]. To enhance the conductivity of the water based solution, electrolytes, which consist of ions with high mobility, are added. This increases the electrical conductivity of the solution.

The purity of hydrogen produced from electrolysis is very high (> 99.999%), this requires less gas-cleaning processes than fossil fuel derived hydrogen needs. For applications that require ultra-pure hydrogen, such as polymer electrolyte membrane fuel cells (PEMFCs), electrolysis is currently the only method of hydrogen production that can meet this requirement. Fuel cells are predicted to play a vital role in the future automotive industry, portable and stationary power sectors, therefore a supply chain of high purity hydrogen is required to fuel these electrochemical devices.

It is important to remember that hydrogen is a form of energy storage, not a primary energy source. An application for electrolysis is in energy storage. During electricity generation at power stations, nuclear power plants, renewable energy sources (wind turbines, photovoltaic power station) there may be an excess in electrical energy than is required by the grid. In this case, instead of wasting the electricity, it could be converted to hydrogen through electrolysis and stored. This hydrogen can then be put back into the grid via fuel cells to produce electricity when the consumer demand is higher, or sold off by the energy company. This is discussed in more detail later.

There are three main types of electrolysers; alkaline, polymer electrolyte membrane (PEM), and solid oxide (SO).

1.3.4.1. Alkaline Electrolysis

Alkaline Electrolysis is an established technology, with the first concepts of electrolysis carried out using acid/alkaline electrolytes. Alkaline solutions are the preferred electrolyte in modern systems due to less corrosion caused to the electrodes, which acidic solutions cause [25]. A schematic of alkaline electrolysis is illustrated in Figure 1.13.

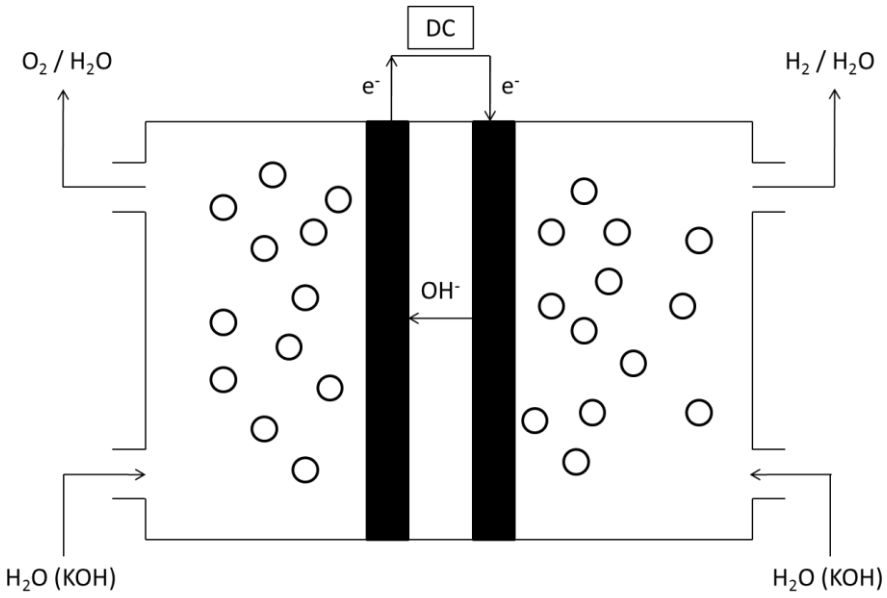

Figure 1.13: Schematic of Alkaline Electrolysis

The main electrolytes used are potassium hydroxide (KOH) and sodium hydroxide (NaOH), and usually consist of 25-30 weight% in industrial electrolysis units [23]. The liquid electrolyte enables the conduction of ions between the electrodes in the solution

and is not consumed in the reaction. Concentrations of up to 50 weight% can be used, but this results in faster rates of electrode degradation [5].

The most commonly used materials of electrodes for alkaline electrolysis are nickel and stainless steel; due to their high conductivity and low cost [24, 26]. The operating temperature during electrolysis is approximately 80ºC and can go up to 150ºC. Temperatures higher than this can result in rapid degradation of electrodes from the caustic solution. Alkaline electrolysers can operate and produce hydrogen at 5-30 bar pressure [27].

Alkaline electrolysers typically operate with current densities (current per surface area) between 100-4000 mA/cm^2 [24]. Efficiencies of these electrolysers are typically 64-70%, and production ranges from 10-100 m^3/hour [24].

The reaction mechanisms are

Cathode	$4H_2O + 4e^- \rightarrow 2H_2 + 4OH^-$	Eq. 1.14
Anode	$4OH^- \rightarrow O_2 + 2H_2O + 4e^-$	Eq. 1.15
Overall	$2H_2O \rightarrow 2H_2 + O_2$	Eq. 1.16

1.3.4.2. Polymer Electrolyte Membrane (PEM) Electrolysis

PEM electrolysis technology uses a solid polymer electrolyte (SPE) membrane to split water into its constituent elements [28]. As a consequence no liquid electrolyte is required which enables safer handling of the electrolyte for the end user [29].

The membrane is non-electrically conductive and proton conducting. The standard membrane material used in PEM electrolysis is Nafion® 117 which is produced by DuPont [30]. Nafion® (chemical structure in Figure 1.14) is a co-polymer of perfluorinated vinyl-ethersulfonyfluoride and tetrafluorethylene. Perfluorinated sulfonic acid (PFSA) membranes have proved to be highly resistant to the oxidative nature of oxygen [30].

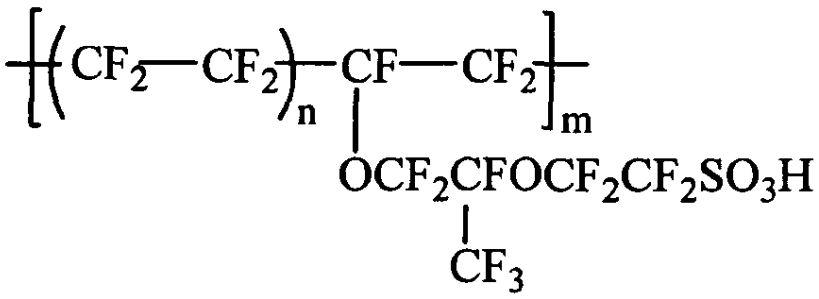

Figure 1.14: Chemical Structure of Nafion®

The PEM is part of the membrane electrode assembly (MEA) which consists of highly expensive platinum catalyst layers on either side of the PEM [31]. Platinum is highly susceptible to poisoning from cation impurities commonly found in natural water [32]. As a result ultrapure water, (minimum 10 MΩ) is a vital requirement for long term PEM electrolysis [23]. Poisoning of the catalyst layer results in an irreversible drop in electrochemical performance and the high cost of platinum makes degradation undesirable [21]. A schematic of PEM electrolysis is illustrated in Figure 1.15.

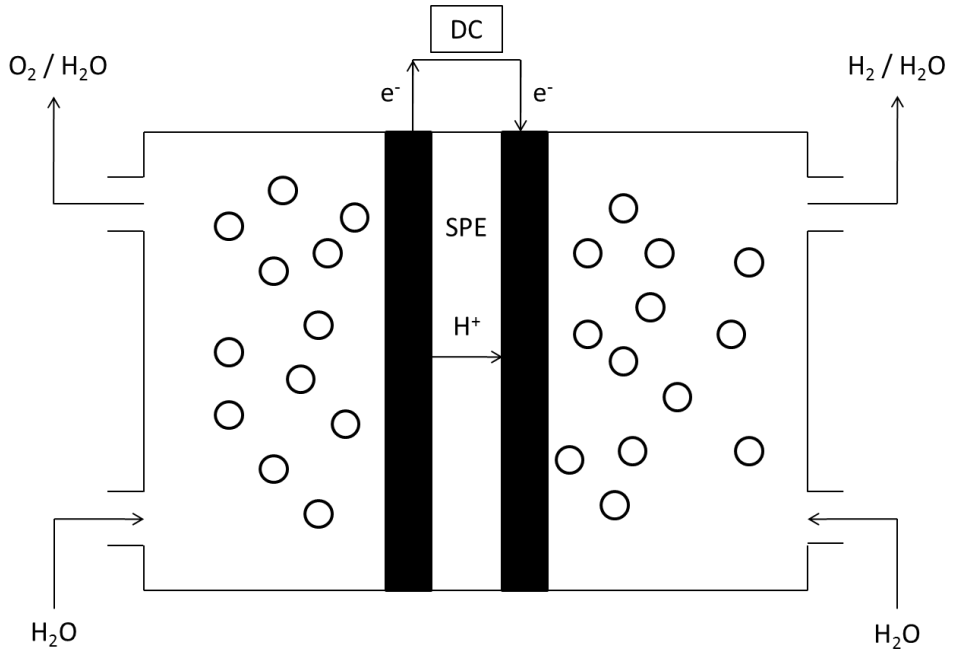

Figure 1.15: Schematic of PEM Electrolysis

At the anode catalyst layer, water is split into oxygen, electrons and protons by applying a direct current (DC) [33]. The oxygen gas evolved leaves to the atmosphere above the anode. The electrons pass through the external circuit to the cathode and the protons pass through the PEM [22]. On the cathode electrocatalysts the electrons from the external circuit and protons passed through the membrane recombine to produce hydrogen gas [34].

PEM electrolysers operate with current densities of > 1600mA/cm^2 and efficiencies of 55-85% [35]. Nafion® membranes suffer from degradation at high temperatures, therefore the operating temperature of PEM electrolysis has to be kept <100^{o}C [36].

The reaction mechanisms are

Cathode	$4H^+ + 4e^- \rightarrow 2H_2$	Eq. 1.17
Anode	$2H_2O \rightarrow O_2 + 4H^+ + 4e^-$	Eq. 1.18
Overall	$2H_2O \rightarrow 2H_2 + O_2$	Eq. 1.19

1.3.4.3. Solid Oxide (SO) Electrolysis

Solid oxide electrolysis, also known as steam electrolysis, introduces the concept of electrolysis at higher temperatures (700-1000^{o}C) than alkaline and PEM electrolysis. This enables a more efficient electrolysis system, since heat supplies a proportion of the energy required to split water [5]. In addition to this, overpotential is also reduced as a direct result of the higher temperature [37]. One of the main disadvantages of electrolysis, as a production pathway for large scale hydrogen production, is the high electrical energy consumption. The decrease in electrical energy requirement provides a more economically realistic process. This makes steam electrolysis thermodynamically and kinetically more favourable than its low temperature counterparts [23].

Steam electrolysis uses an oxide conducting electrolyte to split steam into hydrogen and oxygen. Steam enters the electrolyser on the cathode side of the cell and reacts with electrons from the external circuit to produce hydrogen and oxide ions. The oxide ions transport through the electrolyte to the anode where the oxide ions are oxidised to oxygen gas and electrons, which are transported through the external circuit to the cathode. A schematic of SO electrolysis is illustrated in Figure 1.16.

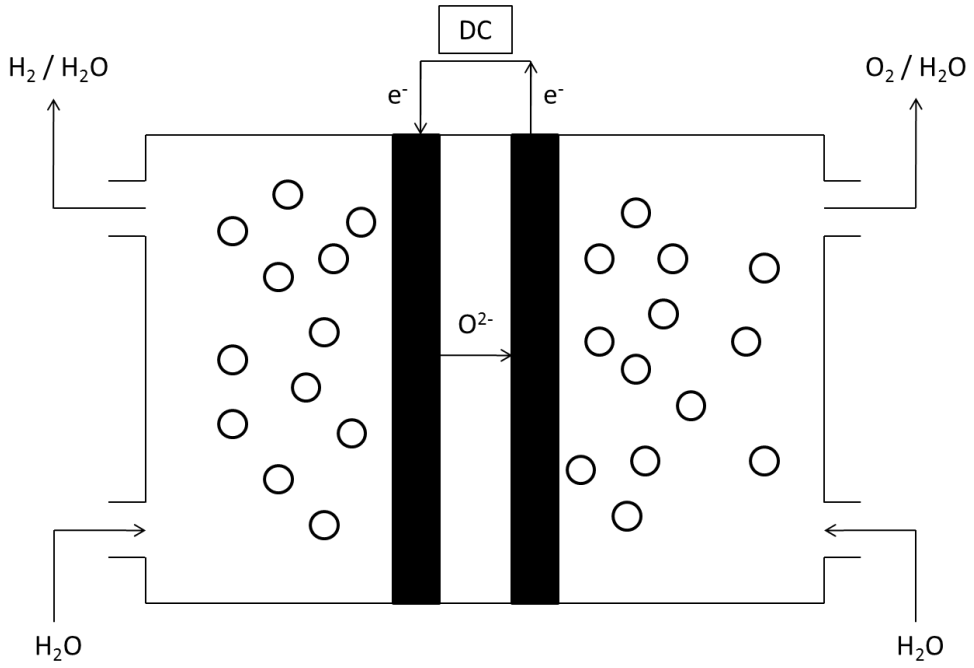

Figure 1.16: Schematic of Solid Oxide Electrolysis

Oxide conducting electrolytes are usually zirconia (ZrO_2) stabilised by Y_2O_3, CaO or MgO [38]. The electrode materials for the cathode are usually nickel (Ni) based yttria stabilised zirconia (YSZ), and the anode material is lanthanum strontium manganate (LSM) [5].

Small scale SO electrolysis cells have been produced, which have demonstrated hydrogen production efficiencies of 70-90% [5]. This is much higher than its low temperature (alkaline and PEM) electrolyser equivalents.

A method of decreasing the electrical energy requirement for steam electrolysis even further is through the use of methane. In this process, the air on the anode side is replaced by methane, which reduces the open-circuit voltage and therefore the electrical energy consumption [39].

The reaction mechanism is

Cathode	$2H_2O + 4e^- \rightarrow 2H_2 + 2O^{2-}$	Eq. 1.20
Anode	$2O^{2-} \rightarrow O_2 + 4e^-$	Eq. 1.21
Overall	$2H_2O \rightarrow 2H_2 + O_2$	Eq. 1.22

1.3.5. Summary of Technologies

A summary of the various hydrogen technologies including their feedstocks, efficiencies and maturities is shown in Table 1.1.

Table 1.1: Summary of Hydrogen Production Technologies (Reproduced from [8])

Technology	Feedstock	Efficiency	Maturity
Steam Methane Reforming	Hydrocarbons	70-85% [a]	Commercial
Partial Oxidation	Hydrocarbons	60-75% [a]	Commercial
Biomass Gasification	Biomass	35-50% [a]	Commercial
Photolysis	Sunlight + Water	0.5% [b]	Long Term
Dark Fermentation	Biomass	60-80% [c]	Long Term
Photo Fermentation	Biomass + Sunlight	0.1% [d]	Long Term
Thermochemical Water Splitting	Water + Heat	N/A	Long Term
Photoelectrochemical Water Splitting	Water + Sunlight	12.4% [e]	Long Term
Alkaline Electrolysis	Water + Electricity	50-60% [f]	Commercial
PEM Electrolysis	Water + Electricity	55-70% [f]	Near Term
Solid Oxide Electrolysis	Water + Electricity + Heat	40-60% [g]	Medium Term

[a] Thermal efficiency, based on the higher heating values.

[b] Solar to hydrogen via water splitting and does not include hydrogen purification.

[c] Percent of 4 mole H_2 per mole glucose theoretical maximum.

[d] Solar to hydrogen via organic materials and does not include hydrogen purification

[e] Solar to hydrogen via water splitting and does not include hydrogen purification

[f] Lower heating value of hydrogen produced divided by the electrical energy to the electrolysis cell.

[g] High temperature electrolysis efficiency is dependent on the temperature the electrolyser operates at and the efficiency of the thermal energy source. For example, SOEC operating from advanced high temperature nuclear reactors may be able to achieve up to 60% efficiency. If thermal energy input is ignored, efficiencies up to 90% have been reported [40].

1.4. Project Rationale

The increasing growth of a hydrogen economy requires an increased capacity of hydrogen generation. This coincides with the increasing rollout of hydrogen refuelling stations to supply fuel cell vehicles. The objective of the research completed herein is to investigate and produce solutions to common problems associated with alkaline and PEM electrolysis.

On demand hydrogen production is highly desirable as it eliminates the need for storage which has safety implications (codes and regulations) and is costly. Hydrogen cannot be produced on demand from SOECs due to the high heat energy requirement, which cannot be instantaneously provided.

There are currently numerous on-demand hydrogen generators available on the market, which promote unfeasibly high efficiencies and gaseous production rates using the mature alkaline technology. A sample of these generators will be analysed and then one will be redesigned using electrochemical, thermodynamic and kinetic principles to improve productivity, efficiency and lifetime for their predetermined applications.

The plan of the thesis is given in Figure 1.17. Chapter 1 gives an introduction to motivation and rationale of the research completed. Chapter 2 explains the scientific principles of water electrolysis and the theory which will be utilised throughout the thesis. Chapter 3 explains the scientific measurement techniques undertaken in this work and the materials used.

Chapter 4 investigates the performance of commercial on-demand oxyhydrogen alkaline electrolysers on the bench and through integration in an internal combustion engine (ICE) to reduce exhaust emissions and increase engine efficiency through a more complete combustion. The integration of hydrogen in ICEs could be considered a stepping stone to a fully-fledged hydrogen economy.

Chapter 5 then redesigns one of these commercial alkaline electrolysers and characterises a prototype of this new design electrochemically and through integration with an ICE. Chapter 6 investigates the degradation mechanisms of the electrodes in an alkaline environment and a process for the reduction of this is analysed.

The newly commercial PEM technology will also be analysed and developed to reduce cost and convenience to the consumer, through the adaptability to impure water supplies. The integration of an on-demand hydrogen generator with a hydrogen refuelling station has no standard at this time and a system will be designed for said application.

Chapter 7 analyses the modern PEM electrolysis technology as an alternative for on demand hydrogen generation and quantifies the impact of water quality on the performance characteristics. Finally in Chapter 8, the integration of a commercial PEM electrolyser with an existing hydrogen refuelling station for fuel cell vehicles is designed and analysed for a 'zero carbon' supply of compressed hydrogen gas.

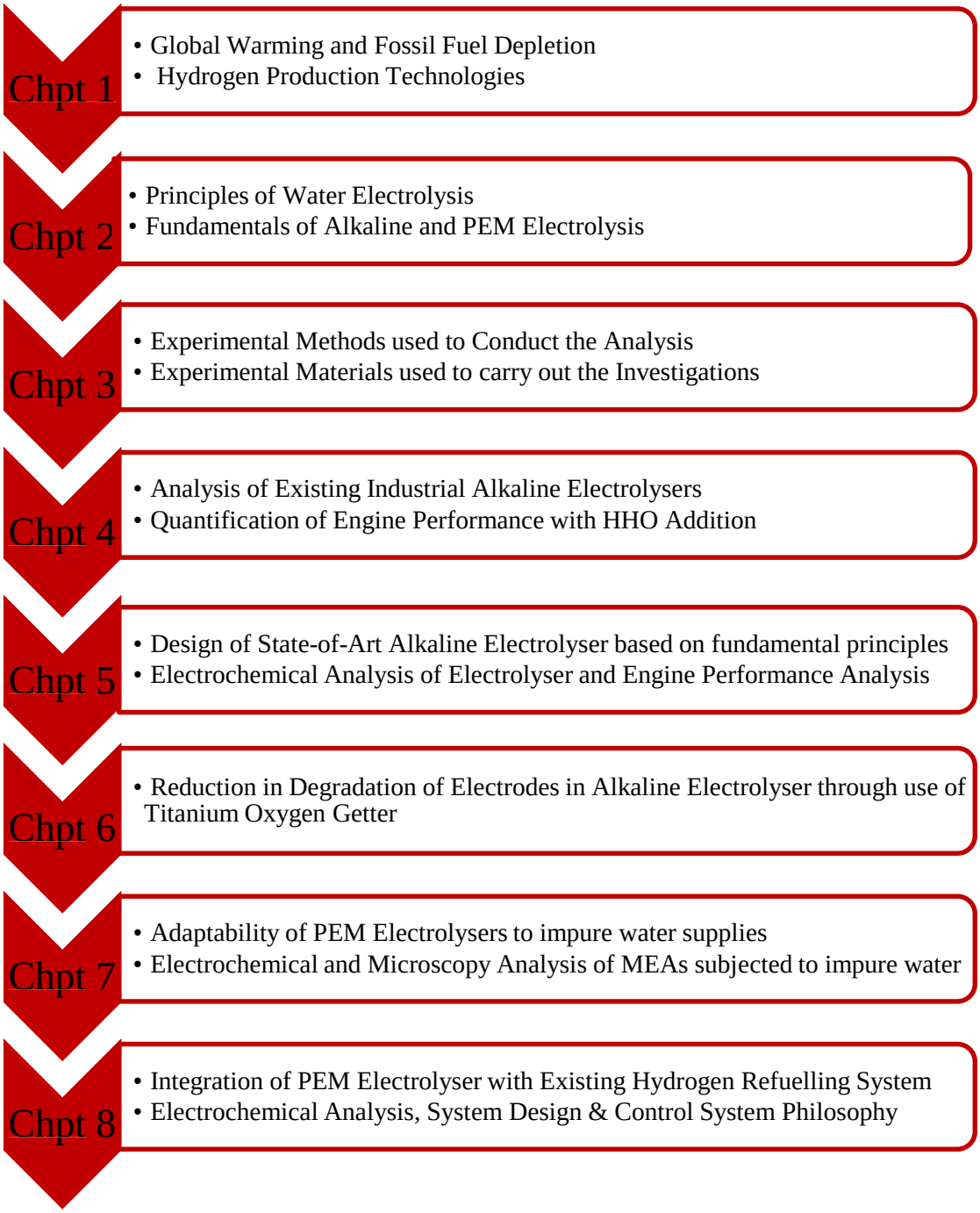

Figure 1.17: Thesis plan

Chapter 2

Low Temperature Electrolysis for Hydrogen Production

2.1. Principles of Water Electrolysis

2.1.1. Thermodynamic Principles

The overall reaction of the water electrolysis is shown in Eq. 2.1. This is in the format of Eq. 2.2 using the heat capacities of the reactants and products. The equation shows positive signs for products (hydrogen and oxygen) and negative for reactants (water) with definitions for ΔB, ΔC & ΔD. Table 2.1 shows the thermodynamic properties for constants A,B, C & D [41].

Table 2.1: Constants for heat capacities of gases in ideal state and liquid water [41]

	A	*B*	*C*	*D*
H_2	3.249	0.422×10^{-3}	0	0.083×10^{5}
O_2	3.639	0.506×10^{-3}	0	-0.227×10^{5}
H_2O	8.712	1.25×10^{-3}	-0.18×10^{-6}	0

$$H_2O \rightarrow H_2 + \tfrac{1}{2}O_2 \qquad \text{Eq. 2.1}$$

$$\Delta A \rightarrow AH_2 + \tfrac{1}{2}AO_2 - AH_2O \qquad \text{Eq. 2.2}$$

The model (Eq. 2.3) determines the Gibbs free energy of reaction (ΔG^o) from the specific heat capacity and gases in the ideal state [41].

$$\Delta G^o = RT\left[\frac{\Delta G_0^o - \Delta H_0^o}{RT_0} + \frac{\Delta H_0^o}{RT} + \frac{1}{T}\int_{T_0}^{T}\frac{\Delta C_p^o}{R}dT - \int_{T_0}^{T}\frac{\Delta C_p^o}{R}\frac{dT}{T}\right] \qquad \text{Eq. 2.3}$$

where ΔG^o and ΔH^o are the Gibbs energy and standard enthalpy of formation respectively, of liquid water at reference temperature T_0. When Eq. 2.3 is integrated, it takes into account the temperature dependency of the heat capacities of the reactants and products. These are shown in Eq. 2.4 & Eq. 2.5.

$$\int_{T_0}^{T} \Delta C_p^o dT = (\Delta A)T_0(\tau\text{-}1) + \frac{\Delta B}{2}T_0^2(\tau^2\text{-}1) + \frac{\Delta C}{3}T_0^3(\tau^3\text{-}1) + \frac{\Delta D}{T_0}\left(\frac{\tau\text{-}1}{\tau}\right) \qquad \text{Eq. 2.4}$$

$$\int_{T_0}^{T} \frac{\Delta C_p^o}{R}\frac{dT}{T} = \Delta A \ln\tau + \left[\Delta B T_0 + \left(\Delta C T_0^2 + \frac{\Delta D}{\tau^2 T_0^2}\right)\left(\frac{\tau+1}{2}\right)\right](\tau\text{-}1) \qquad \text{Eq. 2.5}$$

where T is reaction temperature (K), T_0 is the reference temperature (298K), tau (τ) is defined as $\tau = T/T_0$, and R is the universal gas constant (8.314 J mol^{-1} K^{-1}).

Gibbs free energy (ΔG) is defined as the net internal energy available to work, therefore less work is done by changes in temperature and pressure. Enthalpy (ΔH) is an intrinsic property of a material that is a function of temperature and pressure [42].

In electrolysis, the energy is supplied to the cell by heat (Q) and electrical energy (W_{elec}). The relationship between enthalpy, energy input and Gibbs free energy is shown in Eq. 2.6 [43].

$$\Delta H = W_{elec} + Q = \Delta G + T\Delta S \qquad \text{Eq. 2.6}$$

where T is temperature and ΔS is change in entropy. By considering the change in the functions above, the overall change in Gibbs free energy and the operating potential can be calculated.

At standard temperature and pressure (S.T.P., 298K, 1atm), Gibbs free energy of formation represents the thermo-neutral voltage and is where hydrogen and oxygen are produced with 100% thermal efficiency. To enable electrolysis mode the voltage must

be greater than the voltage corresponding to zero current (open circuit voltage (OCV)). It is determined by the variation in Gibbs free energy of formation between reactants and products. As previously mentioned, Gibbs free energy varies with temperature and state (gas or liquid) [24]. Eq. 2.7 shows this relationship.

$$E_o = -\frac{\Delta G^o}{zF} \qquad \text{Eq. 2.7}$$

where E_o is the theoretical minimum reversible potential of an electrolysis cell, z is the number of electrons transferred in the reaction and F is the Faraday constant (96,485 Coulomb mol^{-1}).

At S.T.P., the Gibbs free energy of formation of water is +237.2 kJ mol^{-1}; therefore E_o = 1.23 V. The minimum voltage required to split water. Ignoring heat transfer in the system, the total enthalpy required must be provided by the inputted electrical energy [44]. In reality however, heat transfer does exist and the thermo-neutral potential (1.48 V) is required to enable the electrochemical reaction.

The real potential (E_{cell}) needed to split water at a reasonable rate will require E_{cell} to be greater than E_o. The difference between the two is known as overpotential, losses or polarisation [23]. The Nernst potential (V_n) accounts for the changes in the activity of the reaction and is shown in Eq. 2.8 [42].

$$V_n = E_o + \frac{RT}{2F} \ln\left(\frac{P_{H_2} P_{O_2}^{\frac{1}{2}}}{P_{H_2O}}\right) \qquad \text{Eq. 2.8}$$

where P_{H2}, P_{O2} & P_{H2O}, are the partial pressures of hydrogen, oxygen and water respectively.

The partial pressure of water is determined from [42] and shown in the Eq. 2.9. This equation enables the calculation from experimental data, since the temperature of water entering the electrolyser varies [23].

$$P_{H_2O} = 610.78 \exp\left[\frac{T_c}{T_c + 238.3}(17.2694)\right] \qquad \text{Eq. 2.9}$$

where T_c is the temperature (^oC) of water entering the electrolysis cell.

The partial pressures of hydrogen and oxygen are calculated using measurements from the electrolysis cathode and anode (Eq. 2.10 & Eq. 2.11) [23].

$$P_{H_2} = P_c - P_{H_2O} \qquad \text{Eq. 2.10}$$

$$P_{O_2} = P_a - P_{H_2O} \qquad \text{Eq. 2.11}$$

where P_c and P_a are the partial pressures (atm) measured at the cathode and anode of the electrolysis cell respectively.

In practice however, as previously mentioned, hydrogen evolution does not occur at the reversible potential (1.23V). This is the result of resistances (overpotential) in the electrolysis system. These resistances in the process mean a higher potential is required to split water in order to overcome these barriers.

An electrical circuit analogy can be used to illustrate the various resistances encountered during the electrolysis process (Figure 2.1) [45].

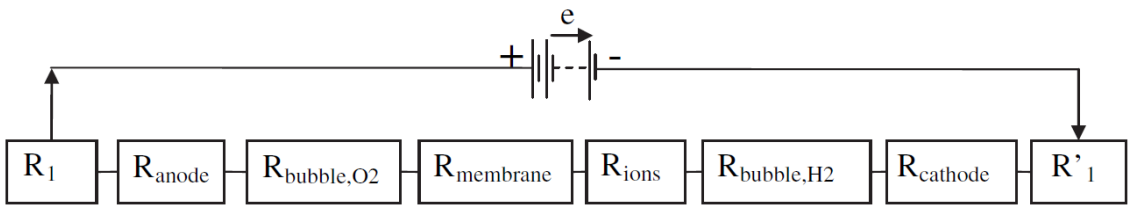

Figure 2.1: Electrical Circuit Analogy of Water Electrolysis

$$R_{cell} = R_1 + R_1' + R_{bubble,O2} + R_{bubble,H2} + R_{ions} + R_{membrane} + R_{anode} + R_{cathode} \quad \text{Eq. 2.12}$$

The three main types of resistance in the electrolysis cell are electrical, transport and electrochemical reaction resistances.

Electrical resistances (R_1 & R_1') directly result in heat generation which points to waste electrical energy in the form of heat according to Ohm's law. In water electrolysis the resistances in electrical circuits. The resistances of the electrodes and connecting circuits are determined by the material types and dimensions, preparation methods, and the conductivities of each component. It can be expressed as follows (Eq. 2.13) [5, 45]:

$$R=\sum \frac{1}{A\kappa_g} \qquad \text{Eq. 2.13}$$

where κ is the electrical conductivity (Ω^{-1} m^{-1}), subscript g represents each component of the circuit, which includes wires, connectors and electrodes. These items can be improved by decreasing the length of wire, using a higher surface area of electrode and using a material with higher electrical conductivity.

The ion transfer in the electrolyte is dependent on the electrolyte concentration (if liquid), membrane (if solid), and distance separating the cathode and anode [46]. The molar conductivity, which is different from the conductance rate in the metallic conductor, is used instead of conductivity. It is illustrated in Eq. 2.14.

$$\Lambda=\frac{\kappa}{C} \qquad \text{Eq. 2.14}$$

where Λ is the molar conductivity (m^2 Ω^{-1} mol^{-1}) and C is the electrolyte concentration. Molar conductivity is also a function of the mass transfer of ions and concentration.

The presence of bubbles on the electrode surfaces creates resistances to the ionic transfer and thus the electrochemical reaction. The study of the bubble effect in electrolytes is a wide area of research and Eq. 2.15 is most commonly accepted [45].

$$\kappa_g=\kappa(1-1.5f) \qquad \text{Eq. 2.15}$$

where κ is the specific conductivity of the electrolyte (gas-free) and f is the volume fraction of gas in the electrolyte solution [47]. If bubble coverage (θ) is taken into

consideration, the electrical resistance caused by bubble evolution can be calculated using Eq. 2.16 [48].

$$\rho=\rho_0(1-\theta)^{-\frac{3}{2}} \qquad \text{Eq. 2.16}$$

where ρ_0 is the specific resistivity of the electrolyte (gas-free).

Electrical resistances can also be calculated by Ohm's Law → R = V/I, in which, when potential V is applied only at R_1 or R_1', current I is measured [45]. Alternatively, resistance can be calculated using R = L/(kA), where L is the length, k is the specific conductivity, and A the cross-sectional area of the conductor [5].

Transport resistances ($R_{bubble,O2}$, $R_{bubble,H2}$, R_{ions} & $R_{membrane}$) are physical resistances such as gas bubbles covering the electrode surface, resistances to ionic transfer of species in the electrolyte, and due to resistance of ion flow in the membrane [23]. These losses are known as ohmic loss.

Mass transfer, temperature distribution and bubble sizes, are determined by the viscosity and the flow field of the electrolyte. Other parameters affected include: bubble detachment and rising velocity, of which all functions are transport related resistances. It is important to note, that during electrolysis the concentration of electrolyte increases (since water is being consumed), and therefore the solution will become increasingly viscous; therefore resulting in a rise in transport related resistances [49].

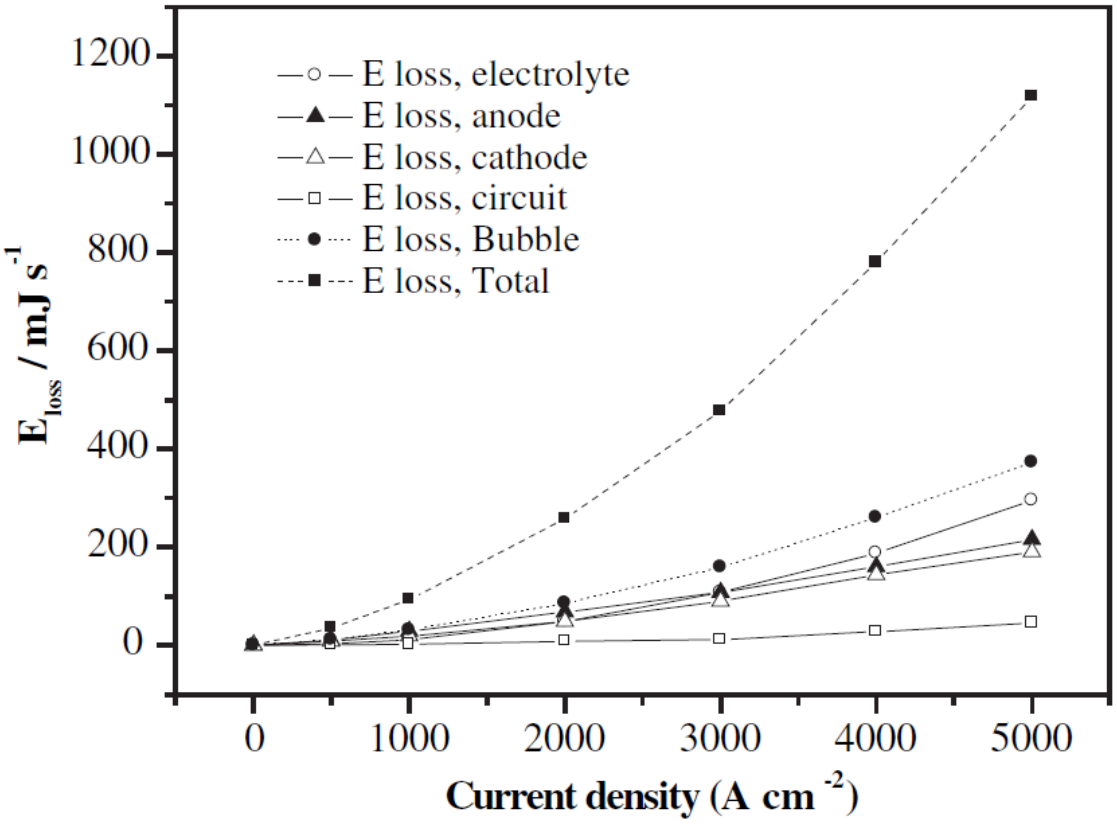

Figure 2.2: Potential Losses Contributions from Water Electrolysis [45]

Current research trends in water electrolysis are to increase mass transfer on the electrode surfaces, but this could disadvantage the production rate of hydrogen. Aiding mass transfer on the electrode surfaces will enable higher bubble formation, which would reduce the contact surface area between the electrode and the electrolyte, and consequently limit the availability of sites for nucleation. Circulating the electrolyte through the electrolyser via pumps can mechanically remove gas bubbles from the surface quicker, and subsequently reduce bubble overpotential in the electrolyser [50].

Electrochemical reaction resistances (R_{anode} and $R_{cathode}$), also known as activation losses, are overpotentials required to overcome the activation energies on the cathode and anode surface for the formation of hydrogen and oxygen respectively. These are inherent energy barriers of the reactions and determine the reaction kinetics of the electrochemical reaction (Figure 2.2) [45].

2.1.2. Overpotentials

When equilibrium occurs at OCV, there are dynamic currents at both electrodes and are symbolic of electrode behaviour. These dynamic currents at the cathode and anode is known as the exchange current density. The exchange current density is defined as the rate of reduction at the cathode and oxidation at the anode.

The exchange current density is defined as an electrode's ability to transfer electrons and happens equally in both directions, culminating in zero change in electrode composition. A small exchange current density shows slow reaction kinetics and slow rate of electron transfer. A large exchange current density exhibits the opposite behaviour [51].

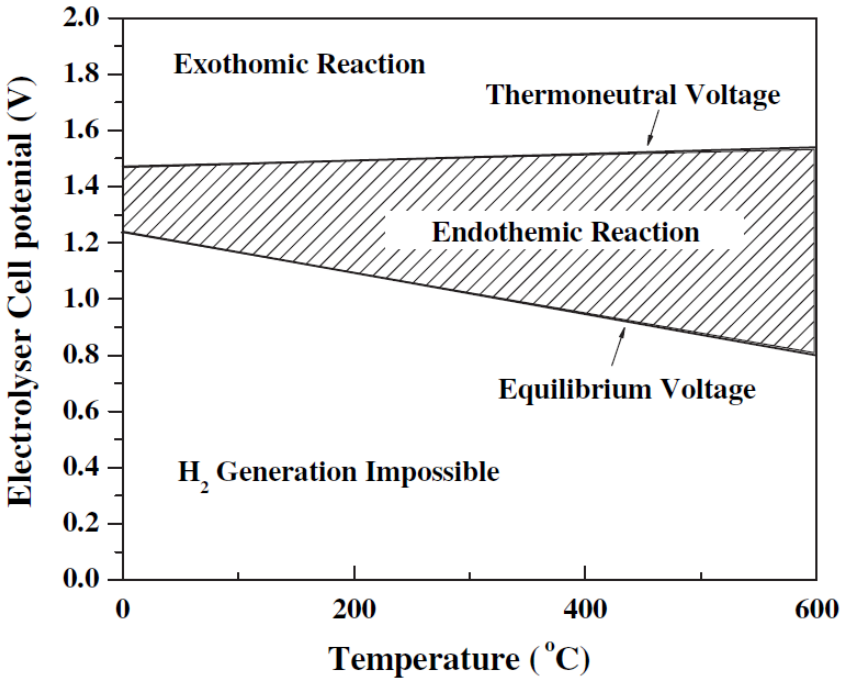

Figure 2.3: Temperature Effect on Cell Potential [45]

It can be shown in Figure 2.3 that an increasing the cell temperature results in a drop in overpotential at the constant current density. Overpotential is also a function of current density not only temperature.

Figure 2.4 shows with increasing current density, the different types and overall cell overpotential increase [23]. It also illustrates that the overpotentials from the HER and OER are the main resistances to the electrochemical reaction. Ohmic losses are the other main contributor to overpotential, and this includes bubble, membrane and ion resistance.

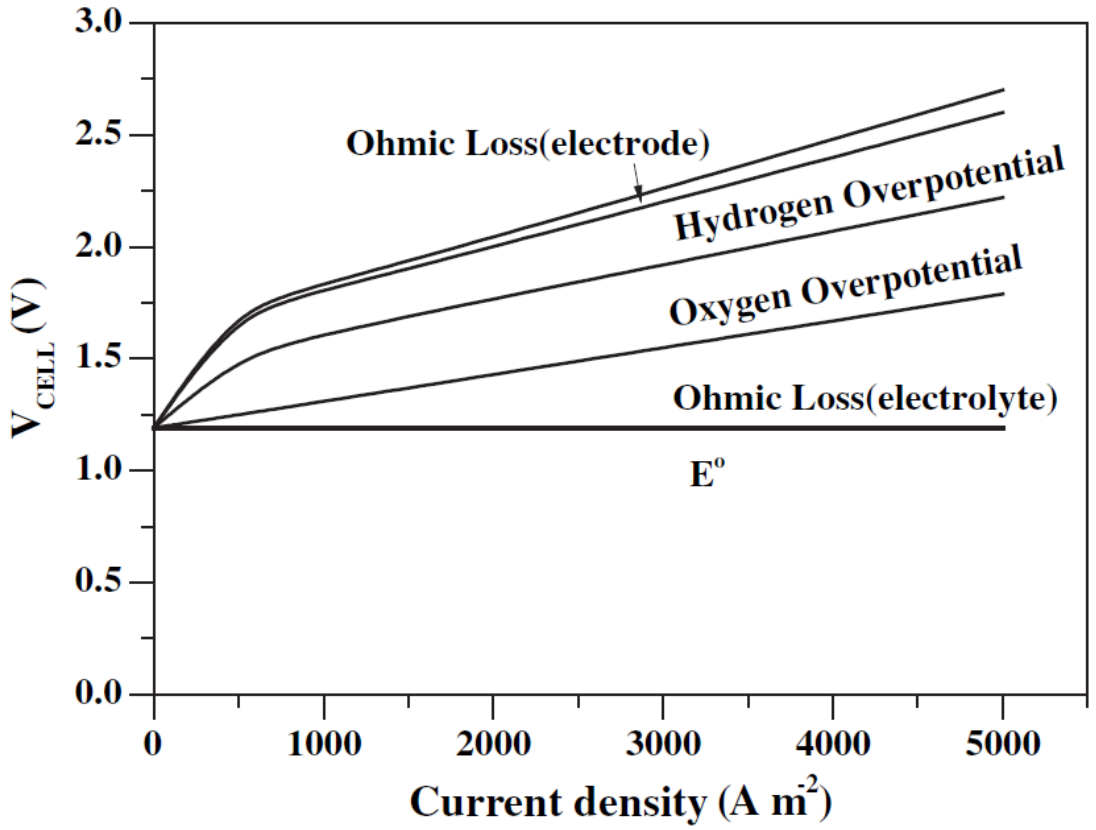

Figure 2.4: Overpotential Variation with Current Density [52]

Activation Overpotential

The initiation of an electrochemical reaction on an electrodes surface requires the overcoming of an energy barrier. This energy barrier is more commonly known as activation energy and is the extra energy required to overcome energy barrier of the rate determining step of the electrochemical reaction to a value at which the reaction will proceed at a suitable rate [51]. It is known as an activation overpotential in the electrochemical reaction. Eq. 2.17 shows the Butler-Volmer equation, used for calculating activation overpotential.

$$I = A \times j_o \left\{ exp\left[\frac{\alpha_c nF}{RT}(E - E_{eq})\right] - exp\left[-\frac{\alpha_a nF}{RT}(E - E_{eq})\right]\right\} \quad \text{Eq. 2.17}$$

Where I is the electrode current, A is the electrode active surface area, j_o is the exchange current density, E is the electrode potential, E_{eq} is the equilibrium potential, T is the absolute temperature, n is the number of electrons in reaction, F is the Faraday constant, R is the universal gas constant, α_c is the cathodic charge transfer coefficient, α_a is the anodic charge transfer coefficient.

These activation losses can also be calculated for the anode, η_a, and cathode, η_c and are presented in the Tafel Equations (Eq. 2.18 & Eq. 2.19) [23].

$$\eta_a = \frac{RT}{\alpha_a zF} \ln\left(\frac{i}{i_{a,o}}\right) \qquad \text{Eq. 2.18}$$

$$\eta_c = \frac{RT}{\alpha_c zF} \ln\left(\frac{i}{i_{c,o}}\right) \qquad \text{Eq. 2.19}$$

where α_a and α_c, are the electron transfer coefficients of the anode and cathode respectively, $i_{a,o}$ and $i_{c,o}$ are the exchange current densities (A cm^{-2}) for the anode and cathode respectively, and I is the current density (A cm^{-2}) of the electrolysis cell.

Ohmic Overpotential

Resistances in the electrolysis reaction that are ohmic losses, are the resistance to the flow of ions in the solution and membrane and the resistance to flow of electrons in the electrode materials [51]. As previously mentioned, these resistances can be calculated by Ohm's law. The ohmic overpotential, η_o, can be calculated using the electrolysis cell's current density, i, membrane thickness (cm), φ, and the conductivity (Siemen cm^{-1}) of the cell, ω. This is shown in Eq. 2.20 [23].

$$\eta_o = \frac{\varphi}{\omega} i \qquad \text{Eq. 2.20}$$

where ω takes into account the sum of membrane resistance, ion transfer resistance and electrical resistances of electrodes and interconnects if the cell is part of a stack.

Other Overpotentials

Other forms of overpotential include bubble overpotential, which arises from resistance caused by bubble evolution on the electrode surface, and thus limits the contact area of the electrode available for electrochemical reactions to occur [49]. This decreases the current density on the electrode. The extra potential required to overcome this resistance is usually considered negligible.

Another form of resistance in the electrolysis reaction is concentration overpotential. This occurs due to the depletion of charge carriers at the electrode surface. It is linked to bubble overpotential, in that bubble evolution at the electrode surface, prevents charge carriers making contact with the electrode surface for the triple phase boundary reaction to occur [49].

2.1.3. Electrolysis Efficiencies

In electrolysis, there are many forms of efficiency measurements. This section presents descriptions and formulae for calculating these efficiencies.

The efficiency of an electrolysis cell is inversely proportional to the cell voltage, which is dictated by the current density. The current density is also directly correlates to the hydrogen productivity per unit electrode surface area [23].

It is commonly seen that higher potentials result in higher rates of hydrogen production, however, this results in low efficiencies. As a result of this, commercial electrolysers usually operate around 2 V, which maximises the electrolyser efficiency, where hydrogen output is not as important as the overall electrolysis efficiency [23].

The system efficiency (Eq. 2.21) can be calculated from the electrolysis cell energy and the ancillary losses. The system efficiency uses the higher heating value (HHV) of hydrogen (39 kWh/kg), the energy used by the cell (kWh), the DC power supply efficiency, and the ancillary loads e.g. pumps, values etc. (kWh) [23].

$$\text{System Efficiency} = \frac{\text{HHV}}{\left(\frac{\frac{\text{Cell Input Energy}}{\text{Power Supply Efficiency}} + \text{Ancillary Losses}}{\text{Hydrogen Produced}} \right)} \qquad \text{Eq. 2.21}$$

where HHV is measured in kWh/kg, cell input energy and ancillary losses are in kWh, and hydrogen produced is measured in kg. To calculate the cell efficiency, the Nernst equation as shown in Eq. 2.8 can be used to calculate the theoretical cell potential and then the cell efficiency can be calculated from Eq. 2.22 [23].

$$\text{Cell Efficiency} = \frac{\text{Theoretical Cell Potential}}{\text{Actual Cell Potential}} \qquad \text{Eq. 2.22}$$

Voltage efficiency allows the measurement of effective voltage to split water in the total voltage applied to the whole electrolysis cell [23]. This is shown in Eq. 2.23.

$$\text{Voltage Efficiency} = \frac{(E_a - E_c)}{E_{cell}} \qquad \text{Eq. 2.23}$$

where E_a and E_c are the potential of the anode and cathode respectively.

Two other types of efficiency measurement of electrolysis reactions, which are based on energy changes in the system, are the Faraday Efficiency and the Thermal Efficiency. They used Gibbs free energy and enthalpy of the water splitting reaction respectively [45]. Both use the theoretical open-circuit energy requirement plus ancillary losses as the energy input.

$$\text{Faraday Efficiency} = \frac{\Delta G}{\Delta G + \text{Losses}} = \frac{E_{\Delta G}}{E_{cell}} \qquad \text{Eq. 2.24}$$

$$\text{Thermal Efficiency} = \frac{\Delta H}{\Delta G + \text{Losses}} = \frac{E_{\Delta H}}{E_{cell}} \qquad \text{Eq. 2.25}$$

At S.T.P. (25^oC, 1 atm), these equations can be simplified further

$$\text{Faraday Efficiency } (25^oC) = \frac{1.23\ V}{E_{cell}} \qquad \text{Eq. 2.26}$$

$$\text{Thermal Efficiency } (25^oC) = \frac{1.48\ V}{E_{cell}} \qquad \text{Eq. 2.27}$$

where $E_{\Delta H}$ and $E_{\Delta G}$ are the thermo-neutral and open-circuit potentials respectively, and E_{cell} is the cell potential.

The Faraday efficiency is the percentage of theoretical energy needed for water to decompose in the actual cell potential [49]. In contrast, the thermal efficiency defines that additional cell potential is required, above the open-circuit voltage, to maintain the thermal balance throughout the reaction. Theoretically, this means that if the reaction is occurring endothermically, then the thermal efficiency may exceed 100% (heat being consumed from the environment) [45].

The Faraday efficiency will always be less than 1, because there are always resistances (losses) in an electrochemical system. Thermal efficiency can be higher than 1, if the cell potential is between the open-circuit voltage and the thermo-neutral voltage.

Another type of efficiency calculation is the measurement of hydrogen gas output from the electrolysis cell in terms of the total electrical energy applied to the system (Eq. 2.28). These are with respect to the HHV of hydrogen and the hydrogen production rate [49].

$$\text{Efficiency of } H_2 \text{ Production Rate} = \frac{\text{Productivity per unit Volume}}{\Delta E} = \frac{V}{Uit} \qquad \text{Eq. 2.28}$$

where ΔE is the cell energy input (kJ), V is the hydrogen productivity per unit volume (m^3/m^3h), U is the cell potential (V), i is the current (A), and t is the time (s).

Alternatively, the yield of hydrogen produced can be measured in terms of electrical energy input.

$$\text{Hydrogen Yield} = \frac{\text{Useable Energy}}{\Delta E} = \frac{283.8}{Uit} \qquad \text{Eq. 2.29}$$

where 283.8 kJ is the HHV of one mole of hydrogen and time t, corresponds to the time required to produce one gram of hydrogen.

Lastly, energy efficiency can also be calculated by subtracting the energy losses (sum of resistances as mentioned in Eq. 2.12) from the energy input [45]. This is shown in Eq. 2.30.

$$\text{Net Efficiency} = 1 - \frac{E_{losses}}{E_{input}} \qquad \text{Eq. 2.30}$$

Applying Eq. 2.30 allows the identification of high resistance locations in the electrolysis cell, which need to be improved. A method for increasing efficiency is to lower these resistances which contribute a significant amount to the overall resistance of the electrolysis cell. This can include electrode materials with a lower activation overpotential, and the movement of electrodes together to reduce ohmic resistance [45].

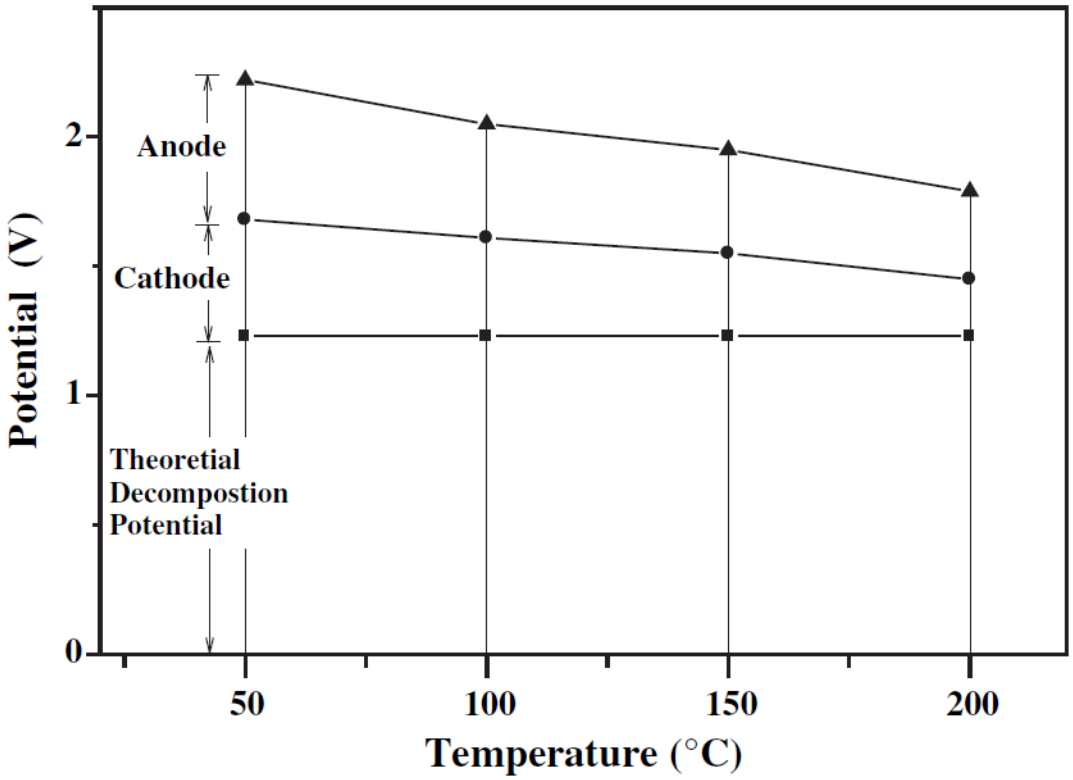

Figure 2.5: Effect of Temperature on the Overpotential of the Cathode and Anode

Another way is to thermodynamically reduce the energy needed for water splitting, whilst maintaining a high hydrogen yield. This can be achieved by increasing the temperature and/or pressure. The temperature of reaction, electrolyte type and properties, as well as electrode materials, has huge implications on the performance of the electrolysis reaction (Figure 2.5) [45].

2.1.4. Electrolysis Kinetics

The reactions within electrolysis occur at the electrodes. The electron flow through the contact between the electrode and the electrolyte enables the formation of hydrogen and oxygen gas to occur. The rate of the electrode reaction is determined by the current density, and this depends on various parameters [52].

Firstly, the material and any pre-treatment of the electrode surface affect the rate of reaction. Secondly, the electrode potential impacts the flow of electrons through the electrolysis cell i.e. higher potential results in a faster rates of reaction on the electrode surface and hence a higher current density [45].

Finally, the rate of reaction on the surface of the electrode is dependent on the composition of the electrolyte solution next to the electrodes. When under operation, these ions adjacent to the electrode undergo migration in the solution to form layers near the electrode surface. This is known as the electrical double layer (Figure 2.6) [52].

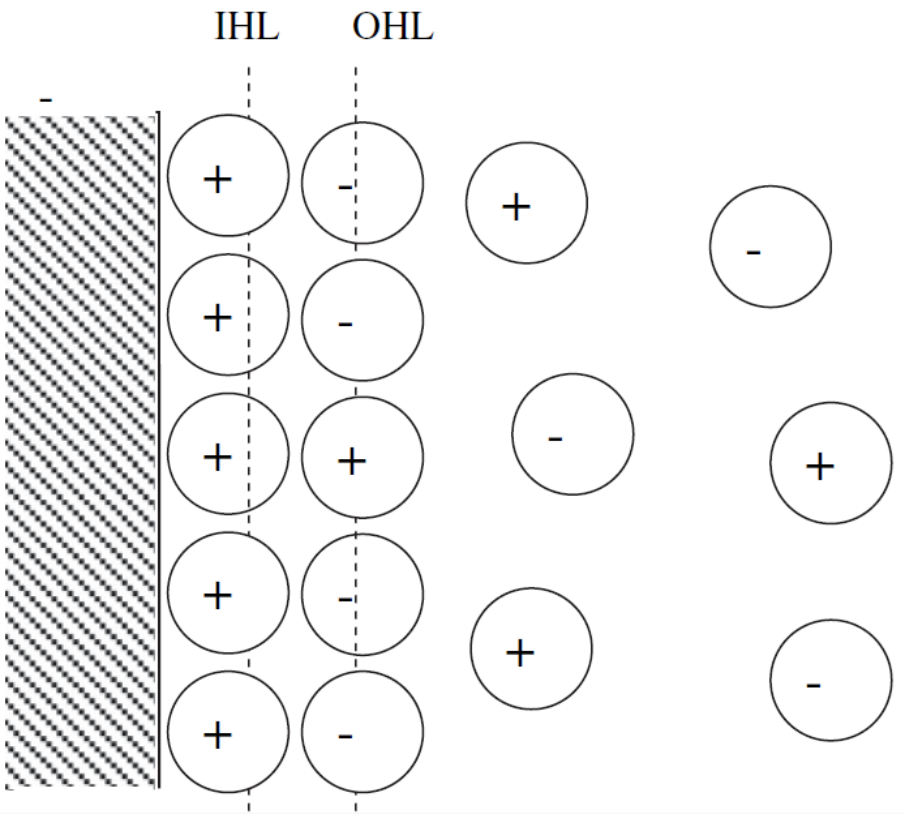

Figure 2.6: Schematic of Electrical Double Layer [45]

When a current is forced to flow between two electrodes through an electrolyte, charge separation is created at each solid/liquid interface and two electrochemical capacitors are formed. In these capacitors at the electrode/electrolyte interface, dissolved ions in the bulk electrolyte are attracted to the electrode surface by an equal and opposite charge.

It is considered that the behaviour at the interface is described in terms of a capacitor. It is a consequence of the "free charge" approach that when a continuous current flow is applied through the interface a strict distinction should be made between Faraday and non-Faraday currents. Faraday currents are responsible for charging of the double-layer

capacitor, while non-Faraday currents are the charge flow connected with the charge transfer processes occurring at the interface. An interface at constant pressure and temperature can be changed by varying the concentration of the components in the bulk phases.

The accumulation of ions near the electrode forms two mobile layers. The layer closest to the electrode is called the inner Helmholtz layer (IHL), where the ions are well ordered and aligned with one another. The other layer is termed the outer Helmholtz layer (OHL), which consists of non-uniform ions adjacent to the IHL [52]. The ionic charges of the ions adjacent to the electrode surface are balanced by oppositely charged ions in the electrode itself. The potential between the electrode and ions can be plotted against the distance from the electrode surface. This is shown in Figure 2.7 [52].

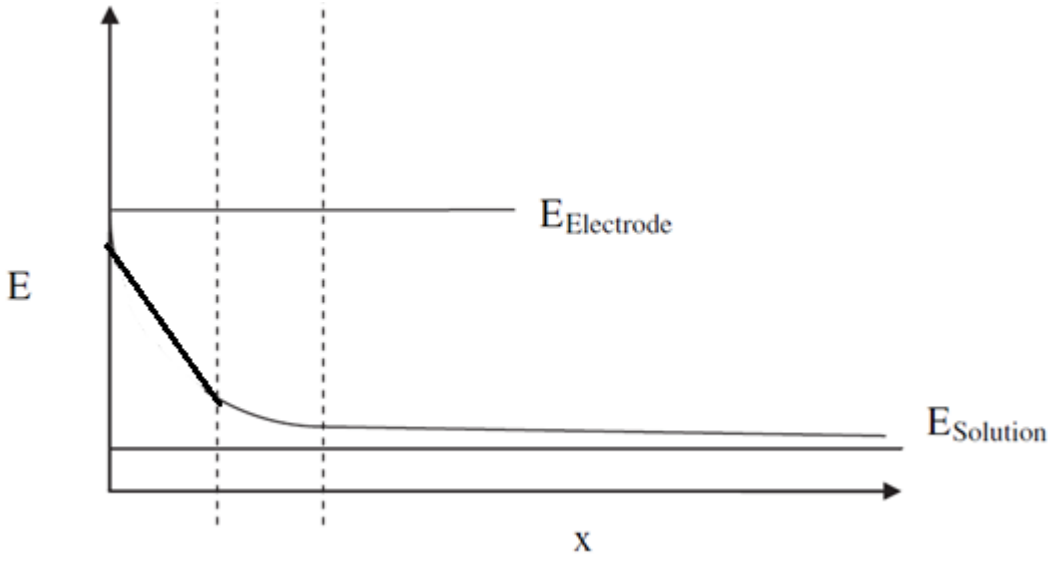

Figure 2.7: Effect of Distance on the Potential Between the Electrode and Ions [45]

Figure 2.7 shows that voltage exists between the electrode and electrolyte solution. This is a direct result of the double layer. The addition of inert electrolyte to the electrolysis process compresses (reduces the thickness of) the double layer and consequently the distance that the potential decays to zero is much shorter.

The electrical double layer phenomenon leads to capacitive behaviour of the electrode reaction. This principle of the electrical double layer acting as capacitor needs to be taken into account when considering electrode kinetics.

Faraday's laws are based quantitative relationships of electrode reactions during the process of electrolysis. Faraday's law states

$$m=\left(\frac{Q}{F}\right)\left(\frac{M}{z}\right) \qquad \text{Eq. 2.31}$$

where m is the mass (grams) of a substance liberated at the electrode, Q is the total electrical charge (coulombs) passed through the substance, F is the Faraday constant (96,485 Coulomb/mol), M is the molar mass of the substance, and z is the valency number of electrons transferred per ion. This equation can be rearranged to form

$$N=\frac{Q}{zF} \qquad \text{Eq. 2.32}$$

where N is the number of moles of electrolysed species. From this the rate of electrolysis can be defined as

$$\text{Rate}=\frac{dN}{dt} \qquad \text{Eq. 2.33}$$

and dQ/dt can be expressed as electrical current (since Q=It). When considering electrode kinetics, the surface area is vital parameter for the electrochemical reaction kinetics, and therefore should not be excluded from thought [53]. The rate of electrolysis can be rewritten as

$$\text{Rate}=\frac{I}{nFA}=\frac{j}{nF} \qquad \text{Eq. 2.34}$$

where j is the current density (A/cm^2). To calculate the reaction rate constant, the Arrhenius equation is used

$$k=Ae^{\frac{E_a}{RT}} \qquad \text{Eq. 2.35}$$

where E_a is the activation energy (kJ/mol), A is the pre-exponential factor, R is the gas constant (8.314 J/K mol), and T is the reaction temperature [53].

The Butler-Volmer equation determines the link between the reaction rate and current flow, the corresponding reliance of current density on the electrode surface potential, and the composition of the electrolyte solution adjacent to the electrode surface [54]. The equation is adapted from the transition-state theory and presented in Eq. 2.36 & Eq. 2.37.

$$I=I_{cathode}-I_{anode} \qquad \text{Eq. 2.36}$$

$$=FAk^0\left(C_0(0,t)e^{-\alpha f(E-E_o)}-C_R(0,t)e^{f(1-\alpha)(E-E_o)}\right) \qquad \text{Eq. 2.37}$$

where A is the electrode surface area in contact with the electrolyte solution, k^0 is the standard rate constant, $C_0(0,t)$ is the concentration of reaction species at the cathode/anode

in the oxidised state i.e. for the cathode; the hydrogen ions (H^+). The (0,t) represents the distance from the electrode, and the specific time at which the current occurs, α is the transfer coefficient (value $0<\alpha<1$), f is the F/RT ratio, which is a constant. $C_R(0,t)$ is the concentration of reaction product at the cathode/anode in the reduced state i.e. for the cathode; the hydrogen gas ($0.5H_2$).

The transition-state theory, illustrated in Figure 2.8, shows the reaction path for the electrochemical reactions in terms of the Gibbs free energy of the reactions, and the position of coordinates in the reaction path [42].

When the potential is increased by ΔE, as shown in Figure 2.8 (a), the decrease in Gibbs free energy is $F(E-E^o)$. As a result there is a reduction in Gibbs free energy of hydrogen ions in the HER by $(1-\alpha)(E-E^o)$, and the increase in Gibbs free energy of hydrogen gas by $\alpha(E-E^o)$.

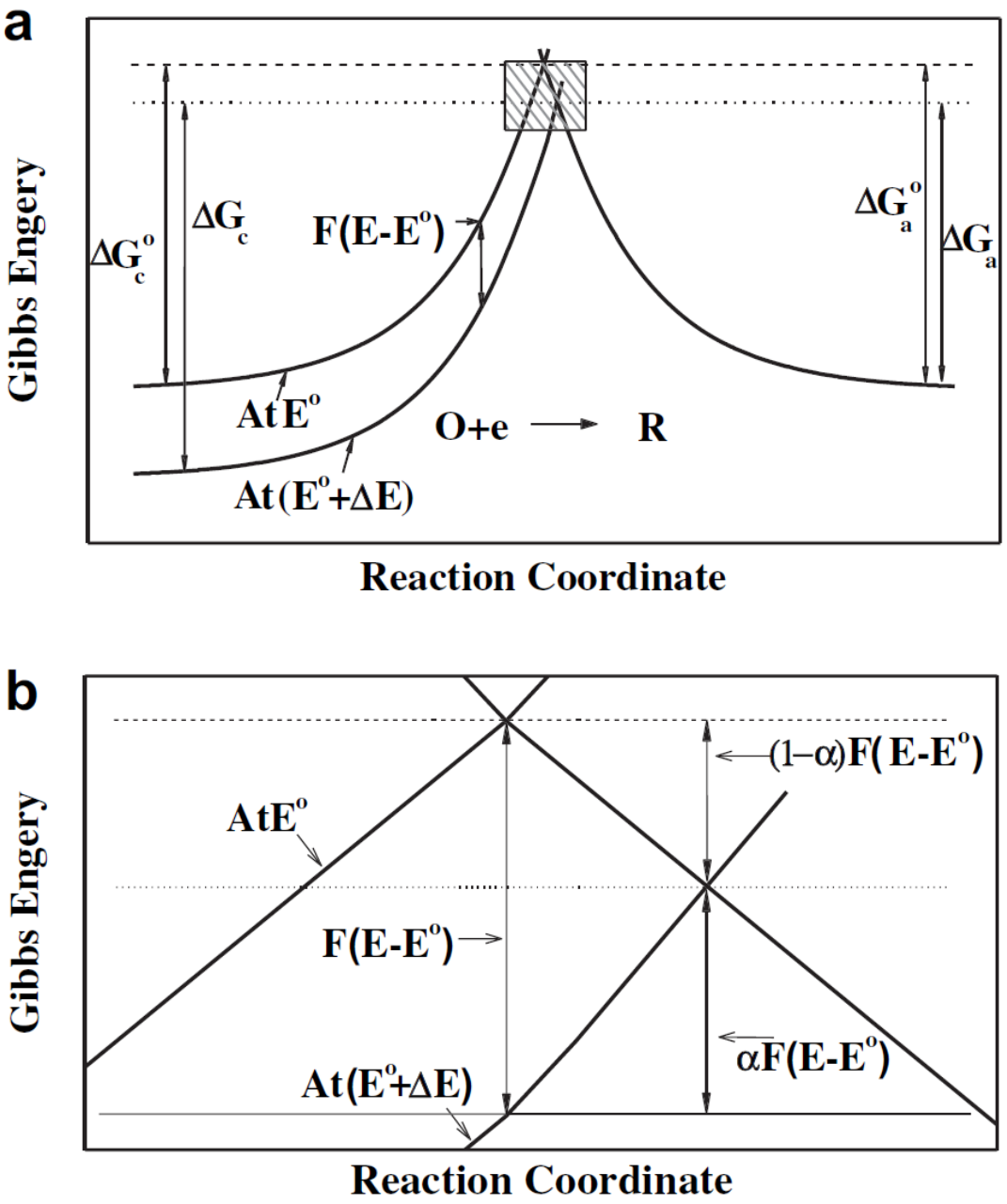

Figure 2.8: Effect of potential change on Gibbs energy for (a) the relationship between energy change and state of reaction and (b) magnified picture of shaded area (a) [45]

This proves that Butler-Volmer equation can be derived from the rate equations previously mentioned (Eq. 2.36), as long as there is no limitation to mass transfer during

the electrochemical reactions at the electrodes [42]. Using Figure 2.8 (b) the Butler-Volmer Equation can be simplified to

$$i=i_0\left(e^{-\alpha f\eta}-e^{(1-\alpha)f\eta}\right) \qquad \text{Eq. 2.38}$$

where as previously mentioned, i_o is the exchange current density. From this equation we can derive overpotential for both electrodes [55]. This is the Tafel equation

$$\eta=a+b\log i \qquad \text{Eq. 2.39}$$

where $a = (2.3RT)/(\alpha F)\log i_o$ and $b = (-2.3RT)/(\alpha F)$

The proportional relationship between the overpotential and the logarithm of current density is determined by exchange current density, i_o, and the slope b; known as the Tafel slope. Both parameters are used to measure the reaction kinetics of electrodes for electrochemistry [56].

This analysis (Figure 2.9) shows that the rate of electrolysis can be expressed by the current density. The current density can be mirrored by the exchange current density, which represents the current associated with the open-circuit potential, on the surface of the electrodes. It is also dependant on the overpotential [57].

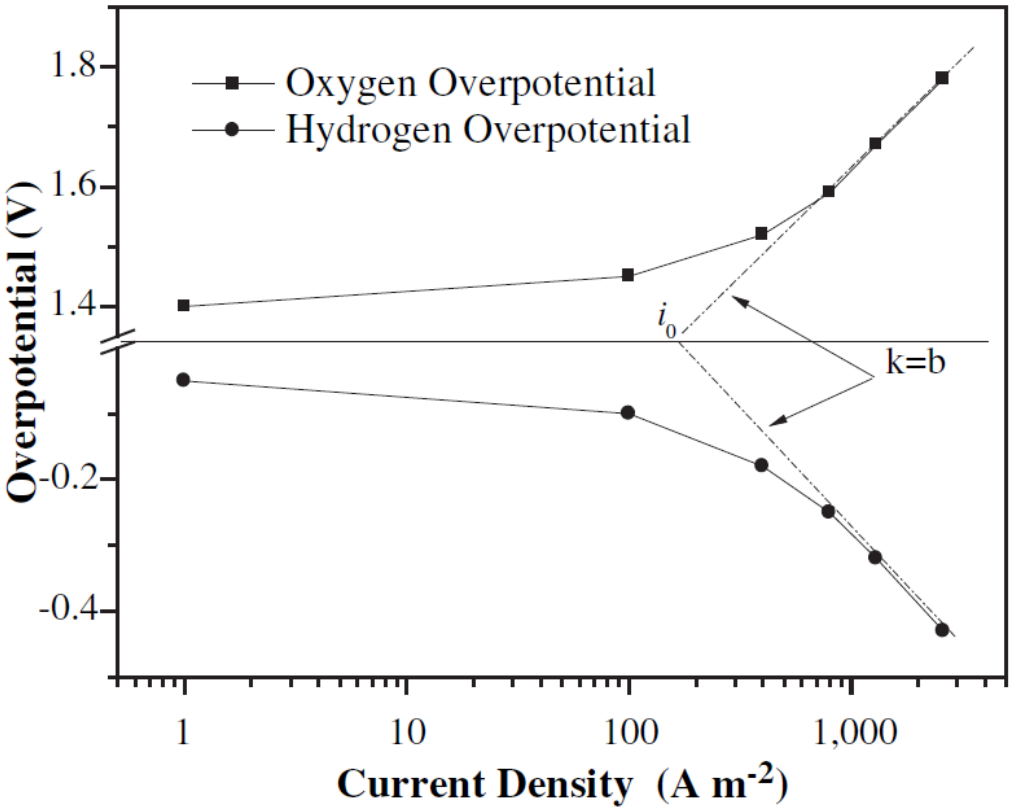

Figure 2.9: Expression of Exchange Current Density for Hydrogen and Oxygen Overpotential [45]

2.1.5. Electrolyser Layout

Traditionally, electrolysis cells do not produce a sufficient output of hydrogen for most applications. Therefore, a number of electrolysis cells are electrically connected in series to produce a higher yield of hydrogen. This is called stacking. Most electrolysers produced consist of more than one cell, and are called the electrolysis, or electrolyser stack [4].

There are two basic designs of these electrolyser stacks, unipolar and bipolar. In the unipolar design, shown in Figure 2.10, the electrodes (cathode and anode) are held apart

by microporous separators which are alternatively suspended in a tank filled with the water-based solution. The positive electrodes are all coupled together in parallel, as are the negatives [31].

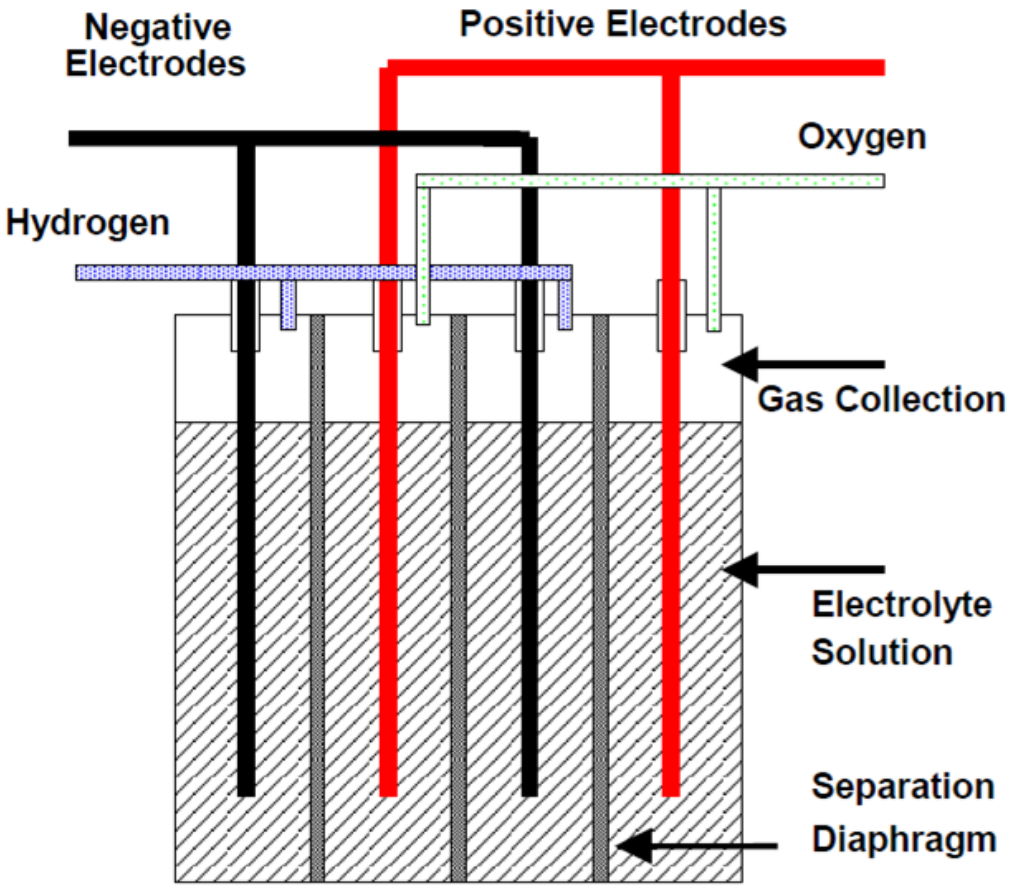

Figure 2.10: Unipolar Electrolyser Layout [45]

It is the oldest design of electrolysis stacks, due to its simplicity and it requires relatively few parts. Any damage to individual electrolysis cells can be easily located, removed and repaired, before being inserted back into the stack. The remaining cells can continue operation while the maintenance is occurring, since the electrical energy supply and gas remove is separate for each individual cell [31].

The unipolar stack, due to its design, does limit the electrochemical performance of the stack. This design suffers from low current densities however it can operate at lower temperatures [58].

The bipolar (filter-press) design, shown in Figure 2.11, consists of alternative layers of electrodes (cathode and anode), and separation membranes that are clamped together. This configuration uses metal sheets (bipoles) to join adjacent cells. These bipoles make one face of the metal sheet act as the negative electrode, and the other face, the positive electrode. The electrolysis cells are connected in series to produce higher stack potentials. Therefore, only the end plates of the stack are connected to the positive and negative DC power supply [58].

These cells are relatively thin, so have a smaller footprint that the unipolar design [23]. The bipolar design also operates at higher current densities, and has the capability to produce higher pressure gas. When a problem with the stack arises however, the whole stack is under shutdown i.e. the individual cell(s) cannot be repaired without servicing the whole stack [58].

The main differences between the two designs are that, in the unipolar design, each half reaction takes place on both sides of the electrode [31]. Whilst with the bipolar design, the HER takes place on one side of the electrode, and the OER takes on the other side

simultaneously. This happens on all electrodes which are not connected to the DC power supply.

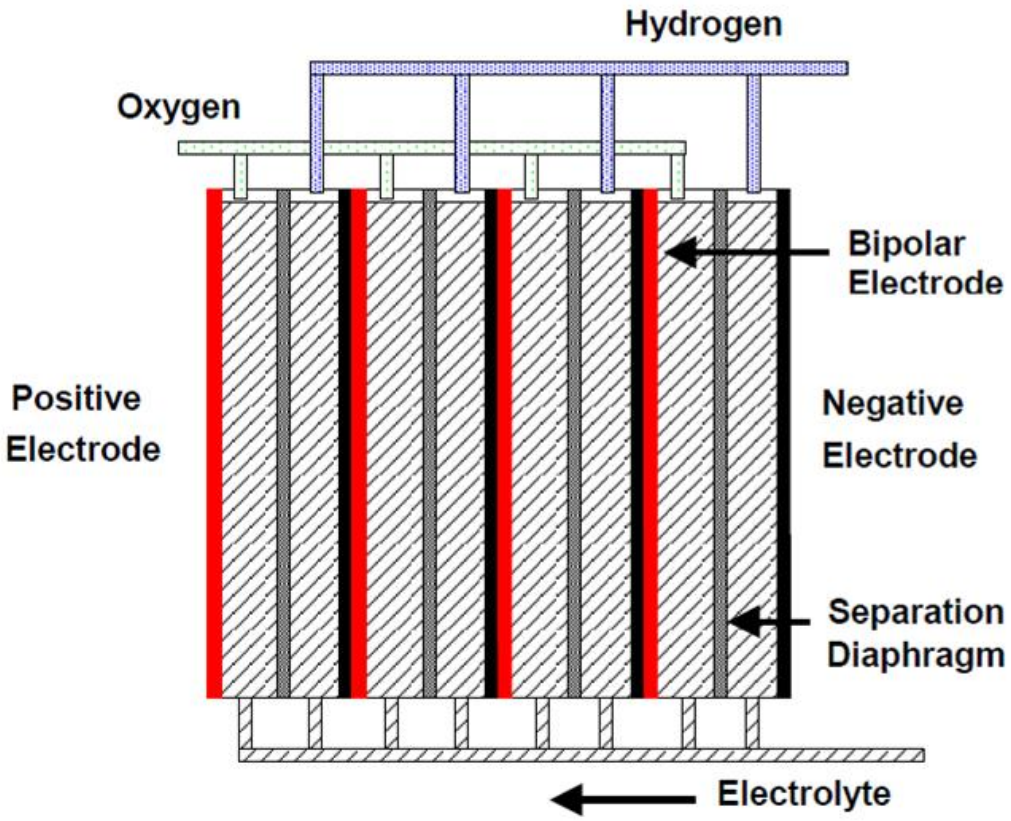

Figure 2.11: Bipolar Electrolyser Layout [45]

The cell operation potential for the designs differs also. For the unipolar design the stack usually operates at 2.0 V, whereas for the bipolar design the stack operates, for the same input potential as the unipolar design, 2.0 x (n-1) Volts, where n is the number of electrodes [23].

The design, build and testing of prototype alkaline electrolysers herein has been carried out in a unipolar configuration due to its simplicity and cost of manufacture, ease of identifying damaged cells whilst the remaining cells continue to function, and the non-requirement of product gas separation.

2.1.6. Bubble Dynamics

The key purpose of water electrolysis is to produce hydrogen and oxygen gases. These gases evolve in the form of bubbles on the surfaces of the cathode and anode respectively. The bubbles maintain contact on the electrode surface until the bubble grows large enough to produce a buoyancy force, greater than the interfacial tension holding the bubble to the electrode. When this occurs, the bubble discharges from the surface of the electrode, rises to the surface the water-based solution, and the bubble collapses to release the hydrogen or oxygen gas.

The attachment of bubbles to the electrode surface adds resistance to the electrolysis process (the bubble overpotential). The bubble formation reduces the contact area between the electrodes and electrolyte. This is turn limits the number of active sites on the surface of the electrodes available for electron transfer, and hence can be characterised as a transportation issue and thus is an ohmic loss [54].

Attempts to reduce these resistances include the addition of surfactants to the water-based solution that decrease the surface tension between the bubbles and the electrode surface.

Other methods include, as previously mentioned, the mechanical removal of bubbles from the electrode surface through continuous circulation of the water-based solution through the electrolysis cell, and modifications to the surface of the electrode which make it less favourable for bubble formation to occur [47]. This could however, reduce the productivity of hydrogen and oxygen gas evolution reactions.

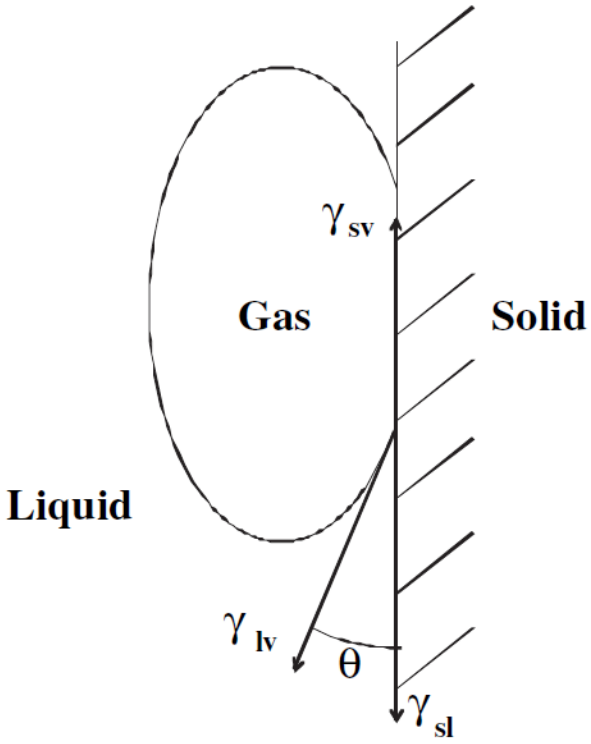

Figure 2.12: Schematic of Three Phase Boundary [53]

The theory behind the dynamics of bubble behaviour is vital to gain an understanding of the specific reaction conditions required for a bubble to leave the electrode surface. Figure 2.12 shows the three phase boundary and interfacial tensions between the electrode and bubble, γ_{sv}, the electrode and liquid solution, γ_{sl}, and the bubble and liquid solution, γ_{lv}. The contact angle between γ_{sl} and γ_{lv}, θ, is finite and an important characteristic for

measuring the thermodynamic properties of bubbles. Young's equation (Eq. 2.40) expresses the contact angle in terms of the three different interfacial tensions [53].

$$\cos\theta = \frac{\gamma_{sv} + \gamma_{sl}}{\gamma_{lv}} \qquad \text{Eq. 2.40}$$

The change in Gibbs free energy, ΔG, associated with the displacement of the solid/interface, with the electrode/bubble interface [59].

$$\Delta G = \gamma_{lv}(\cos\theta - 1) \qquad \text{Eq. 2.41}$$

The rate of bubble removal on the electrode surface is determined by the displacement of the water-based solution at the electrode/solution interface [54]. This is known as wettability.

Wetting is the ability of a liquid solution to maintain contact with a solid surface. It is a measure of adhesion and cohesive forces. Table 2.2 shows what degree of wetting the contact angle produces, and how strong the corresponding force between the adhesive and cohesive forces are [52].

Table 2.2: Different Types of Wetting & Properties

Contact Angle	Degree of Wetting	Strength of Solid/Liquid Interface
$\theta = 0$	Perfect Wetting	Strongest
$0 < \theta < 90^o$	High Wettability	Strong
$90^o < \theta < 180^o$	Low Wettability	Weak
$\Theta = 180^o$	Non-Wetting	Weakest

Treatment of electrode surfaces can make them more or less attractive to water. These are called hydrophilic and hydrophobic. An electrode surface that has a tendency to mix with water is hydrophilic, whilst hydrophobic surfaces repel water [54]. Since

hydrophilic surfaces are more likely to accept water, therefore they are more likely to reduce bubble coverage on the electrode.

Reducing the resistance caused by bubble evolution is an active area of research, and many more detailed studies are required to investigate and quantify bubble phenomena in water electrolysis.

2.2. Alkaline Electrolysis

2.2.1. Electrodes

The choice of material for the electrode is governed by numerous factors. The desired requirements are good electrical conductance, high corrosion resistance and minimum overvoltage [60, 61]. The cathode and anode materials in alkaline systems are usually made of nickel or nickel plated metal on which a catalyst can be applied. The catalyst can be noble metals like platinum, rhodium or iridium, but a large selection of non-noble catalysts is also available [27, 49, 51].

The application of precious-metal catalysts, such as platinum, enhances the electrode processes considerably and allows it to proceed more rapidly than on just nickel, but the extra cost of the precious metal is usually not considered justified [45, 62]. When platinum is used, a large surface area can be obtained by the use of platinum black, a finely divided powder of platinum metal particles which can be coated on the electrode surface [45, 63].

2.2.2. Electrolytes

2.2.2.1. Solid Electrolyte

A new design of an alkaline electrolyser is the implementation of a zero-gap electrode system with an OH^- conducting membrane. In this the electrodes are joined to either side of membrane surface which acts to reduce the potential drop between the cathode and anode [64]. Zero-gap cells with a porous separator can be constructed but they are predicted to have a larger voltage drop leading to lower current density operation and subsequently larger electrolysis systems [65].

2.2.2.2. Liquid Electrolyte

Most commercial electrolysers use alkaline solutions (potassium or sodium hydroxide) as the electrolyte. Energy consumption during water electrolysis can be significantly reduced by adding acidic/basic compounds which consist of ionic activators which reduce the resistivity of water [27]. Ionic liquids which are organic compounds are liquids solely made up of cations and anions and as a result possess excellent ionic conductivities and stability [45].

In industrial electrolyser applications, these parameters can be met by the use of a strong acid (e.g. sulphuric acid) or a strong alkali (e.g. potassium hydroxide). The majority of salts decomposed under electrolysis at voltages typical in an electrolyser cell. Acid electrolytes present the problems of severe corrosion and are not often selected for electrolysers [66]. As a result most industrial electrolysers operate with an alkaline electrolyte solution. High conductivity occurs in KOH solutions at approximately 30% concentration and this is the industrial standard concentration used [45].

2.2.3. Separators

A separator is positioned between the cathode and anode and prevents the electrodes from contacting each other and causing an electrical short. It also keeps the product hydrogen and oxygen gases separate inside their separate half-cell chambers. The separator must consist of a porous diaphragm or matrix through which the electrolyte solution can pass allowing an ionic conducting path from the anode to the cathode. These pores must remain full of liquid at all times so the product gases cannot penetrate them. Additionally, the separator material must be corrosion resistant to the electrolyte in the presence of hydrogen or oxygen gas and it must be structurally stable for the operational lifetime of the cell so that the pores do not collapse [45, 67].

In order to keep the ionic resistance of the cell low, the separator is usually in the form of a thin sheet, in which the thickness is determined by mechanical strength and gas crossover limitations. Asbestos has commonly been used for the separator material in alkaline electrolysers. Woven asbestos cloth and matted asbestos fibres are both utilised in commercial cells [67].

2.3. PEM Electrolysis

An MEA consists of the solid polymer electrolyte coated on either side with electrocatalyst to form a catalyst coated membrane (CCM) pressed between two porous current collectors. As well as acting as an electrolyte the MEA acts as a barrier between the half-cell reactions as only protons are conducted through it. This ensures that hydrogen and oxygen do not recombine to form water [68].

2.3.1. Electrocatalysts

It is important that the electrodes are resistant to corrosion as well as resist attack from the gases produced and water. Since the gases need to be expelled from the electrodes they must be built with a large surface area. They need to have a porous matrix with a low pressure drop and must have a high electrical conductivity to prevent undesired heat being produced and to avoid an imbalanced current flow. The cost and durability of the electrode must be considered to compromise between the capital cost and suitable longevity of the electrolyser cell [31, 69-71].

2.3.1.1. Hydrogen Evolution Reaction

At the cathode hydrogen evolution reactions take place (HER). Platinum black was the catalyst first used but future development found this catalyst to provide too small a surface area which led to the requirement of finding greater platinum concentration [31, 72, 73]. The most commonly used catalyst for HER is platinum particles on a carbon black support [21, 74, 75]. Platinum a good electrocatalyst for PEM electrolysis as it is resistant to acidic corrosion and is capable of withstanding high temperatures and voltages which are used [31, 33, 60, 69, 76].

The carbon black support is powder based which provides a large surface area to volume ratio and subsequent large number of active sites for adsorption. Chemisorbed functional groups of quinones, carboxyls, hydroxyls and phenols are present as a result and leads to an increased platinum adsorption. The platinum nanoparticles are distributed over the active sites of the carbon black (Pt/C) and surface areas of up to 1500 m^2/g can be achieved [44, 77, 78]. Pt/C exhibits high mass transfer and also sustains good osmotic

balance to reduce flooding in the cell. The catalytic performance of the metals: platinum, palladium, rhenium, iridium, osmium, ruthenium and nickel; have been studied and discovered that platinum showed the best electrochemical catalyst behaviour irrespective of it being highly expensive and in short supply [79].

Since OER is rate determining it is most effective to reduce the amount of platinum in the cathode rather than the electrocatalyst on the anode. This is due to the higher ratio of H^+/H_2 at the cathode compared to the ratio of H_2O/O_2 at the anode [21, 77, 78]. Combining platinum with cheaper PGMs such as palladium to make a Pt/Pd alloy, gives rise to significant reductions in the cost of the catalyst without reducing the efficiency.

2.3.1.2. Oxygen Evolution Reaction

At the anode oxygen evolution reactions (OER) takes place. The reaction is divided into adsorption, charge transfer and desorption stages. It has been reported that the adsorption and desorption rates are determined by the bond strength between metal and oxide [80]. A strong metal-oxide bond gives rise to fast adsorption and slow desorption, whilst a weak metal-oxide bond strength gives rise to the opposite. A middle ground is required to gain a transitional bond strength that favours each of the reaction steps. A high charge transfer rate is reliant on a high density of electron states at the Fermi level (top electron energy levels at absolute zero temperature) on the overlapping of active sites and the adsorbed species.

On first conception platinum was used as the electrocatalyst for the anode also, but as shown in more recent research that iridium exhibited a higher rate of oxygen evolution

[81]. Platinum obstructed the OER as it formed an oxide film that would decrease catalytic performance [66]. Iridium exhibited desirable characteristics as an anode catalyst compared to that of palladium, ruthenium, platinum, gold, rhenium and niobium. Better catalysts could be manufactured using mixtures of iridium and other noble metals as well as oxides derivatives of each [71].

Iridium oxide and ruthenium oxide are sometimes used as the catalyst but both metal oxides suffered from corrosion. This led to the use of an iridium-ruthenium alloy that would be used as a catalyst on a carbon black support [82, 83].

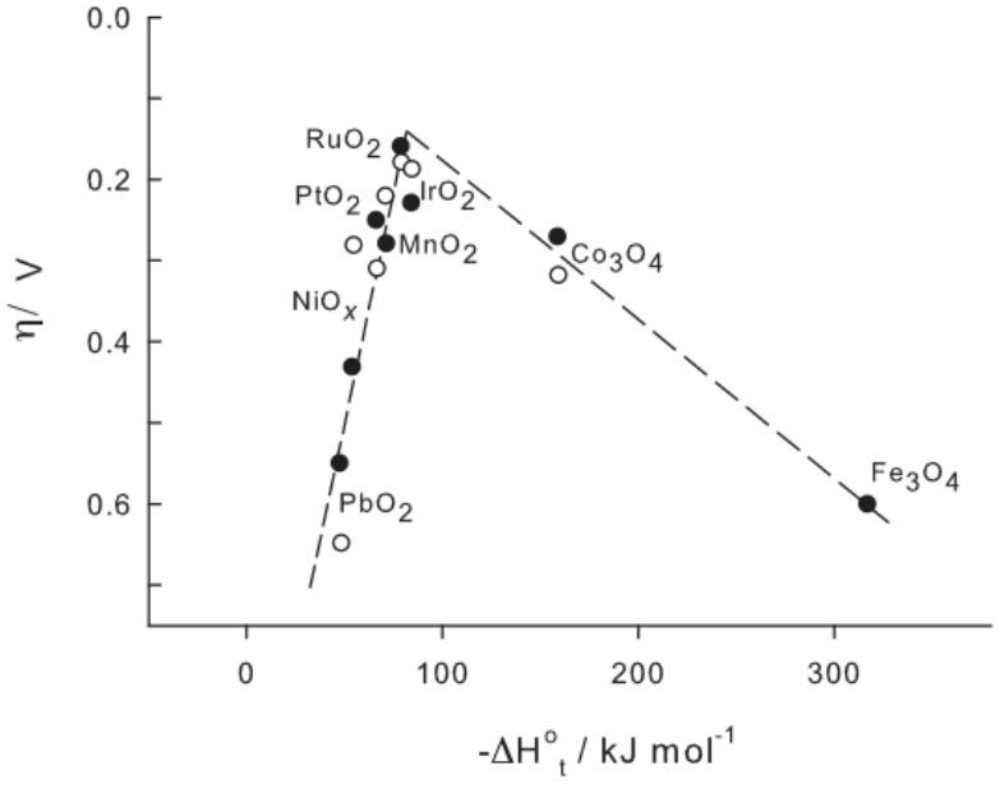

Figure 2.13: Volcano-plot of electrocatalytic activity of different oxides is acidic (white spheres) and alkaline (black spheres) electrolyte solutions [84]

The rate of reaction of the anode surface is the resultant on the material properties of the surface species at the electrode surface. Figure 2.13 compares the different electrocatalytic activities of the metal oxides used at the anode.

It shows that IrO_2 and RuO_2 display the best catalytic properties, with a lower anodic overpotential when compared to the other metal oxides studied [80, 85-88]. The electrocatalytic activity is measured by overpotential on the anode and is related to the enthalpy for the oxides to form a higher oxidation state from a lower one, which is directly related to metal-oxide bond strength.

2.3.2. Ionomer & Proton Exchange Membrane

In recent years PEM electrolysis cells are manufactured through the CCM process and they have a layer of ionomer present with ionic transport properties (e.g. Nafion® solution) applied to the electrocatalytic layers [29, 58, 89, 90]. The ionomer layer has three main functions [91]:

1. It acts as a conductor to promote proton transport from the bulk of the catalyst layer to the membrane. This results in decreased Ohmic losses and so enhance the overall efficiency of the electrolyser.
2. It acts as a binder to provide a mechanically stable 3D structure for the catalyst layer with gas channels which enhances durability.
3. It acts as a hydrophilic agent to retain moisture within the catalyst layer and reduce mass transport out of the catalytic layer.

A layer (50-250μm thick) of proton conducting membrane is used as a solid polymer electrolyte (SPE). Nafion®, which is manufactured by Du Pont®, is the commercial standard membrane and it has been widely researched [64, 92-94]. Its chemical structure is based on perfluorinated phosphonic acid copolymer (see Figure 1.14). Protons are conducted between adjacent acidic groups ($-SO_3-$) attached to the perfluorinated polymer backbone with a proton solvent as a carrier (H_2O-H_3O^+) [95, 96].

Nafion® is a popular structure for a membrane due to its high conductivity, good mechanical strength and high chemical and thermal stability which prevents corrosion by evolved oxygen [97-99]. The main drawback of Nafion® membranes is that they are expensive to purchase and its disposal can be expensive due to the fluorine content [94]. Also they are restricted to operating temperatures below the boiling point of water [100, 101]. They are dependent on water to act as a bridge between acidic groups for proton transfer so ionic conductivity is lost at temperatures above 100°C.

The proton conductivity in Nafion® is highly linked to its nanostructure and water content. Low water content results in not all acid sites being dissociated and the interaction among water molecules through hydrogen bonding is low. This results in low rate of proton transfer and a low dielectric constant, which is limited to the surface region, providing very low conductivity [102]. High water content means the properties of water in Nafion® approach those of bulk water. Consequently, the two different water environments in Nafion® have usually been easily distinguishable. The water in the middle region of the pore is referred to as bulk water through which the mobility of

protons is fast, and the water near the pore surface along the array of SO_3^- groups is referred to as surface water and the proton mobility through the surface is considerably smaller than that in the bulk, due to the strong electrostatic attraction of SO_3^- groups [102].

It has been proved that the transport of protons in Nafion® is carried out through a surface diffusion mechanism occurring close to the pore wall or under low water activity, for example in a layer 1nm from the pore wall and a bulk diffusion mechanism. In the bulk, proton diffusion is dominated by the Grotthuss mechanism, but the H_3O^+ ion also undergoes traditional mass diffusion [102].

The Grotthuss mechanism is the process by which excess protons diffuse through a hydrogen bond network of water molecules, hence the why it is important in PEM electrolysers and fuel cells to keep the membrane hydrated and enables proton transport to occur. Also known as proton-hopping, this mechanism exists in Nafion® where protons hop from one sulfonic acid group to another thus allowing protons to pass through pores from the anode to the cathode [102].

If electrolysis could be operated at higher temperatures electrode kinetics would be enhanced and the process would require less energy due to a reduction in the activation energy barriers [103, 104]. Research groups have been focusing on producing better, less expensive membranes. These include hydrocarbon membranes [105], polybenzimidazoles (PBI), poly(ether ether ketones), (PEEK), poly(ether sulfones) (PES)

and sulfonated polyphenyl quinoxaline (SPPQ) [34, 106], as well as further development of Nafion®.

2.3.3. Current Collectors

Porous current collectors (PCC) are metallic plates which transfer electrical current from the separation plates to the electrochemical interfaces the electrolysis cell. They must be highly conductive and highly corrosion resistant to the acidic electrolyte, production of oxygen and high overpotentials. PCCs must have high mechanical strength to give structure to the cell. Mass transfer also takes place across the current collectors [68]; gases must be easily expelled from the current collector and they must allow water to be transported to the catalytic sites through the membrane [71]. Current collectors are generally fabricated from sintered spherically shaped titanium powder [94]. Carbon based materials are not suitable as they cannot withstand the corrosive conditions.

These mass transfer considerations are particularly important at high current densities when mass transfer is the limiting factor. Large porosity enables easy removal of gases, but electron transfer is limited (increasing Ohmic resistance) and less water will be transported to the catalytic layer [68]. At low porosity gas removal is obstructed and channels within the current collector will be blocked, limiting mass transfer [94]. Research previously conducted into the optimisation of porosity showed plate thickness and pore size of sintered titanium current collectors. The authors empirically proved that for current densities from 0-1 A/cm^2 an optimum pore size of 20 microns is required [68].

2.3.4. Separator Plates

Separator plates provide the electrolysis cell with structure, which help maintain its stability in varying operating conditions. They also create a pathway for thermal and electron conduction and provide separation between the half-cell reactions. They are highly expensive and are responsible for 48% of the overall electrolysis stack cost as they are manufactured from expensive materials (titanium or graphite) and aren't produced on a large scale [71]. At high current densities they are responsible for a large contribution to the Ohmic losses, resulting in higher required cell voltages [71].

Titanium is one of the most commonly used materials for plates due to its low initial resistivity, high initial thermal conductivity and low permeability. However over time the titanium corrodes which causes the performance of the cell to decay [107-109]. Graphite is also frequently used due to its high conductivity. However, it is expensive, has high corrosion rates and has low strength [109]. To overcome the high costs of titanium and graphite stainless steel has been developed for use as a base material. It has low corrosion resistance so must be coated to resist the acid environment [110].

2.4. PEM Electrolyser Impurities

Proton transportation in aqueous media is much faster than that of other cations. This is because protons are transported by structural diffusion, also known as the Grotthuss mechanism, whereas other ions are transported by mass diffusion. Structural diffusion of protons is based on electrolytic joining of adjacent water molecules, resulting in only an

electron has to move. Mass diffusion is the actual movement of a charged particle, thus including both charge and mass transport. Ensing has shown experimentally that proton transport in Nafion® membranes is equally slowed down by the Nafion® environment as the transport of sodium ions, even at low water contents [111]. The results of the research suggest that structural diffusion is equally dependent on the porous Nafion® as mass diffusion, and that the Grotthuss mechanism holds in the Nafion® environment, even at low water contents.

Over prolonged operation time, degradation in the performance of PEM electrolysers occurs. The main cause is the irreversible degradation of the MEA. Degradation is proportional to temperature and duration of operation. At high currents, hot spots and uneven swelling occurs within the polymer membrane. Platinum nanoparticles on the cathode coalesce or are released into the circuitry, causing electrical efficiency losses. Electrochemical surface area is slowly and irreversibly reduced [31]. Another cause is the purity of the water supplied to the electrolyser. Metallic cations within the water feed can poison the membrane and/or catalysts.

Ion exchange processes take place as metal cations in water have a higher affinity for the sulfonic acid group sites contained within the membrane than the protons. Cations displace protons and enter the SPE, resulting in reduced proton conductivity and an increased ohmic drop in the membrane [112-114]. Under potential deposition of cation monolayers on electro-catalysts occurs at potentials much higher than the Nernst potential, meaning that poisoning is possible at working potentials [115]. Deposition on

electrode surfaces and the membrane prevent ion transfer and electrochemical reactions [116]. Cation poisoning leads to a gradual decrease in current density at a constant stack voltage [31, 115] and increased electrode overpotentials [116].

Research has been carried out on water purity in PEM fuel cells, which use similar membranes and electrocatalysts to PEM electrolysis. Research has confirmed that Nafion® exhibits a high affinity for cations (Ca^{2+}, Na^{+}, Fe^{2+} and Fe^{3+}) added to the water feed, resulting in a decrease in conductivity [117-121].

Very few publications exist related to water purity in PEM electrolysis. Millet et al. introduced $NiSO_4$ to the water feed of a PEM electrolyser and a monolayer of nickel was deposited on the surface of the cathode. This resulted in a higher cathodic overpotential than on bare platinum and a steady decrease in current density [122]. Andolfatto et al. introduced a thin layer of Cu^{2+} ions to a platinum cathode which caused an overpotential increase [115]. Millet et al. found that even small concentrations of cations in the feed (Fe^{x+},Ni^{x+} & Cr^{x+}) will poison the SPE as the ions are trapped and concentrated within the membrane [116].

Zhang et al. researched the effect of Na^{+} poisoning on water electrolysis by adding sodium sulphate to the water feed. Na^{+} ions were found to have a worse effect when supplied to the anode of the cell compared the cathode [114]. Millet et al. suggested that using an online de-ioniser would give a more stable cell voltage but the use of high

operating pressures and temperatures would be limited [122]. Current PEM electrolysers are designed for use with ultrapure water which has been de-ionised to remove ions present and subsequently prevent membrane poisoning.

Napadensky studied the proton conductivity of novel cation exchanged sulfonated polymer membranes. The investigation found that levels of solvent absorbed into the membranes varied depending on the cation exchanged, with a valence difference resulting in the most dramatic changes [123]. The amount of water absorbed by cation-containing membranes decreased by 50%–95% (as compared to acid form). Whilst swapping H^+ ions in sulfonated polymer membranes with cations did make the membranes stronger due to crosslinking effects, swollen membranes still exhibited detrimental electrochemical performance [123].

Izquierdo-Gil et al. investigated water uptake and salt transport through Nafion® cation-exchange membranes with different thicknesses [124]. The importance of membrane thickness and the effect the electrolyte has on the permeability of the membrane were researched. Membrane characteristics are influenced by the type of electrolyte in the solutions which allowed for salt diffusion [124]. Cation transport numbers were measured for the various different membranes and electrolytes, and from those values the membrane apparent permselectivity was determined. Thicker membranes exhibit increased permselectivity with increasing size of cation. Results have shown that the integral permeability coefficient decreases with membrane thickness [124].

Stenina et al. looked into the various characteristics of ion transportation in PFSA (specifically Nafion-117) membranes [125]. Ion mobility and transport numbers in Nafion® membranes are highly dependent on counter-ion and co-ion mobility in the membrane, which in turn is highly dependent on the electrolytes present. The study found the transport of anions in the salt forms of the PFSA membrane increases with the increasing size of corresponding cations and increasing electrolyte concentration [125].

Young et al. saw the determination of ion-exchange in various counter-ion Nafion® membranes using prompt gamma neutron activation analysis (PGAA) [126]. This technique was used to quantify trace ion content and water content via the detection of hydrogen in the membranes. The research purpose was to identify contamination, effectiveness of treatments to remove contamination, and extent of ion-exchange in membranes. Received membranes contained trace quantities of residual potassium contamination which was removed [126]. Ion-exchange levels for membranes in excess ion solutions varied from 94-100% which subsequently increased with valency. Partial exchange levels were achieved using monovalent, divalent, and trivalent cations introduced in ion-starved solutions. The study also indicated that ion-exchange can be used to decrease residual potassium contamination in new membranes [126].

Kienitz researched the effects of cation contamination on polymer electrolyte membrane fuel cells (PEMFCs) [127]. This can significantly reduce the performance and durability of PEMFCs. Cationic impurities such as Na^+, Ca^{2+}, Cs^+ and other metal cations compete with protons for the sulfonic acid sites in the polymer electrolyte membrane. These

impurities can be present in the hydrogen feed stream e.g. ammonia is often a byproduct of steam methane reforming most commonly used to produce hydrogen.

Contaminating cations can also access the system from the air feed: sodium in coastal environments or calcium in deicing agents. The cations can also be present in the system from the corrosion of bipolar plates and other stack/piping equipment. The cations produced by the corrosion of metal bipolar plates have been studied and have shown many different cations present [128, 129].

The problem of cationic contamination is the low amount of contaminant needed to affect an MEA e.g. a 50μm Nafion® 1100 membrane has approximately 9 μmol of sulfonic acid sites per cm^2. To displace all these protons requires approximately 206 μg of sodium ions, 155 μg of ammonia, or 62 μg of lithium ions per cm^2 [129]. Whilst there are typically >25cm^2 of active area in any fuel cell, these small quantities of cations show how low levels of corrosion or contamination have a major impact on fuel cell performance [128].

When cations replace protons in the fuel cell ionomer it is highly undesirable since cationic contaminants have a higher affinity for the sulfonate sites than protons do. Cations which have accessed the membrane affect water management and decrease ionic conductivity [130]. They also hinder the ORR on the fuel cell cathode through reducing the number of actives sites on the platinum catalyst [130].

Minimal research has been carried out on cationic contamination. This may be because in earlier fuel cells have often caused device failure before cation contamination could noticeably degrade performance. Fuel cells tested in a research environment use higher quality hydrogen feedstocks and newer components less prone to corrosion since cost is not a limiting factor. Studying cationic contamination becomes increasingly important as the durability and marketability of PEM fuel cells and electrolysers increases. Understanding exactly how and to what extent cationic contamination effects MEA performance will allow for the development of methods to recover fuel cell and electrolyser performance.

The two ends of Nafion® structure are finished with a sulfonic acid site. Both of these end sulfonic acid sites are required to be paired with a cation counter-ion to enable electro-neutrality [131]. As shown in other studies any cation can be replaced in these sites through an cation exchange process. Nafion® and other PFSA membranes show a preference to some cations over others. The change in electrostatic field strength of the anionic exchange site is directly influenced by the hydration energy of the cation counter-ion and is seen to be the main factor in determining cation selectivity. Cations with smaller hydration energies are preferred to cations with larger hydration energies [132].

The exchange of the cations within a Nafion® membrane does not occur instantaneously. An equilibrium is steadily achieved but this process takes time since cations have to diffuse to interact with the sulfonate sites [133].

Once cationic contaminants displace protons in the ionomer they are difficult to remove. The research shows that higher molecular weight cations have a higher affinity for occupying sulfonate sites in the membrane [127]. Also, multivalent cations have a higher affinity than monovalent cations. Higher affinity is a result of larger cations having, in general, greater amounts of electrostatic interaction with the sulfonate sites [127].

The conductivity of protons in MEAs is much higher than any other cation. Other cations have at least four times less mobility than protons. The mobility of multivalent cations is lower than monovalent cations, but this is due to the fact that multivalent ions have at least one more charge per molecule [127].

Efficient water management in a fuel cell or electrolyser system is vital for performance. Water is a fundamental requirement for conduction of ions in the membrane but too much water causes flooding in fuel cells [127]. Flooding decreases the amount of gases that can reach the nucleation sites resulting in extra mass transport losses. Larger cations reduce the amount of water in the membrane and carry more water per molecule due to electro-osmotic drag. Membranes contaminated with cations could result in an over 50% decrease in water content [127].

Degradation effects similar were seen when 1.0M NaCl was injected in the air stream of a PEMFC at 1 ml/min [134]. The fuel cell cathode was exposed to a solution of NaCl with sufficient sodium to displace all protons in the membrane every 15 seconds. Minimal

degradation was observed for the first 24 hours of operation. After 100 hours of operation the cell experienced a 33% loss in current density at 0.6 V. This loss was not restored when the contaminated cathode feed was replaced with clean air for 3 days. The performance continued to decrease for 10 hours after exposure to contaminant was ceased.

The slow loss in performance and sustained drop in performance after NaCl was no longer supplied to the system implying long residence times of sodium in the cathode. Once a cation is in the membrane it will move across the membrane quickly, but it may be more difficult for foreign cations to enter at the cathode side due to the half-cell potential or as a result of water generation on the cathode.

Wakizoe et al. researched the impact of calcium ion contamination on single membrane cells. The study saw membranes be contaminated with between zero and eleven percent of protons replaced [135]. This researched showed that even replacing only 0.5% of protons in the membrane resulted in a high level of cell performance degradation especially at high current densities. Membranes with 11% of the protons replaced exhibited a 67% decrease in current density at 0.6 V compared to an uncontaminated baseline sample. Resistance of the cells increased as a function of contamination level.

Calcium contamination has also been studied with calcium hydroxide solutions, consisting of 10, 50 and 500 ppm, supplied to the anode side of a fuel cell [136]. During

operation, the performance decreased as exposure time increased. Impedance data was analysed that suggested that the exchange current density had increased. The location of the calcium in the cell was analysed using electroprobe microanalysis. The analysis found that no calcium was located in the GDL, only within the membrane and electrodes. This analysis validated the theory that cations (more specifically calcium ions in this case) replace protons in the ionomer.

2.5. Effect of Hydrogen Addition to Diesel Engines

The application of these HHO generators is for use with internal combustion engines (ICEs) as a fuel additive. Traditionally, hydrogen and oxygen are generated, on demand, from water, using an electrolyser stack attached to an alternator. The hydrogen and oxygen gas can be inserted into the ICE through the air inlet pipe, resulting in higher rates of ignition and corresponding propagation of flames across the combustion range.

The enhancement of flame initiation and subsequent flame propagation decreases the ignition delay and combustion time in both petrol and diesel engines. The resultant reaction aided by the presence of hydrogen and oxygen causes a simultaneous ignition of all the petrol/diesel fuel present. As all the fuel ignites at the same time, no ignition front can exist and without it there is zero pressure wave to create knock in the ICE.

Unburned hydrocarbons, CO and NO, in the exhaust are either removed or decreased and at the same RPM the engine produces more torque from less fuel in theory. The lack of

carbon monoxide and un-burnt hydrocarbons confirms a complete and much quicker burn of fuel. Colder exhaust temperatures prove that more work is completed throughout the power stroke. Higher torque from reduced fuel at identical engine speeds concludes that higher pressure from a quicker burn, combusting through a longer power stroke, produces higher torque and consequently more power from less fuel.

The enhanced mixture of fuel, air and HHO combusts up to 10 times faster but this rapid combustion is so fast that the resultant power stroke and exhaust stroke is much cooler, resulting in much less nitrous oxides (NOx) [137]. Decreasing hydrocarbons and CO emissions causes a rise in the percentage of CO_2. As less fuel is used, the actual quantity of CO_2 produced decreases by the same ratio as the reductions in fuel usage [138]. NOx gas is nearly eliminated and GHG emissions are decreased in proportion to the reduction in fuel usage.

Previous studies on hydrogen injection into ICEs have shown varying effects on engine performance. Throughout history, many studies regarding hydrogen as a fuel in ICEs have been undertaken. Reverend Cecil in England planned to use hydrogen as fuel in 1820. Rudolf Erren conducted studies with the hydrogen engine in Germany in 1920 and research carried out by Ricardo in 1924 achieved high efficiency when working with hydrogen in an engine [139].

Saravanan et al. investigated the hydrogen mixed with air induction in a diesel engine. The findings showed a 27.9% efficiency was achieved without knocking over the entire load range with 30% hydrogen enrichment [140]. Saravanan also found that fuel consumption decreased with increasing hydrogen percentage over the operational range [140]. Saravanan also carried out research on hydrogen as a dual fuel for diesel engine system using the exhaust gas recirculation (EGR) technique [141]. The investigation demonstrated that the specific fuel consumption decreased without EGR with a hydrogen flowrate of 20 LPM and it was concluded that the reason for reduction in fuel consumption is the result of the operation of a hydrogen fuelled engine in lean burn conditions [141].

Adnan et al. investigated a hydrogen injection rate of 20 LPM into the air induction pipe at standard temperature and pressure doubled NOx emission at 1500 RPM in a 7.4kW diesel engine, with a compression ratio of 19.3:1 [142]. The cylinder peak pressure increased by 11% and indicated a power increase of 33% at 1500 RPM. This results in a fuel consumption reduction at fixed load conditions. Consequently however, If the hydrogen was produced on-demand by an electrolyser at 4.4 Wh/L then the added load would be 5.3kW, leaving around 29% of the engines power for useful work, and most likely dramatically increasing diesel consumption [142].

Saravanan et al. investigated optimising manifold injection in a direct injection diesel engine with varying hydrogen flowrates. Conclusion showed that from manifold injection, the optimised engine condition included the injection of hydrogen at top dead

centre (TDC) with injection with a hydrogen flow rate of 7.5 LPM. The brake thermal efficiency increased by 9% compared to normal fuel conditions. CO emissions varied from 0.03 to 0.12 vol% compared to 0.08-0.14 vol% in a diesel fuel investigation [143].

Bose et al. researched varying load conditions on a diesel engine injected with 27.8 LPM of hydrogen and EGR gas into a 5.2 kW, 17.5:1 compression diesel engine. Brake thermal efficiency increased 28%, and NO_2 emissions increased by 70% at 20% load and 90% at 40% load due to hydrogen injection [144]. The efficiency of the engine increased due to the increased flame speed from the presence of hydrogen in the combustion process. 27.8 LPM of hydrogen is a high production rate of gas if provided from an electrolyser and the power needs to be supplied from the engine itself. It was found that the electrolyser would require 4.4Wh/L of hydrogen produced. As a result the added load of the electrolyser is 7.34kW which is 41% greater than the engines rated power in this study [144].

Miyamoto et al. injected hydrogen at varying flowrates into a single cylinder diesel engine with a 16.7:1 compression ratio operating at 1500 RPM. The engine had varying diesel injection timing, and the coolant and air temperature were maintained at a constant level. Diesel injection timing was from 12° to 0° before top dead centre (BTDC). Hydrogen injection in this experimentation caused NOx exhaust emissions to drop 24% at 12° BTDC to make identical NOx emissions with no hydrogen injection [145].

Bari et al. operated a 4 litre diesel engine generator at three loads at 1500 LPM, supplying up to 32 LPM of HHO supplied by an externally powered electrolyser. The purpose was to determine whether an on-board electrolyser can reduce fuel consumption in a diesel engine. It was reported 14-15% reduction in fuel energy consumption (diesel and hydrogen energy both included) across a range of loading conditions and HHO injection rates [146]. It was also found HHO is best utilised in small ratios, up to 4% concentration since up to this injection rate HHO acts as an additive rather than a full diesel replacement fuel. NOx emissions increased up to 27% with an increasing rate of HHO engine injection, the same as found for tank hydrogen injection [146].

From the literature reviewed above it has been proven that NOx emissions increase with load and hydrogen and/or HHO injection rate. The small increases in engine fuel economy from hydrogen/HHO injection is not sufficient to offset the energy required to make the required flowrate of hydrogen/HHO by electrolysis of water utilising the power supplied from the engine alternator or 12V battery. The research has shown on-board HHO generation increases diesel consumption, and subsequently decreases the engine power available to primary function.

To this end, the research conducted herein will be investigating reducing exhaust emissions in engine idle conditions to meet emission requirements for EURO 5 & 6 zones, irrespective of an anticipated increase in diesel fuel consumption, as requested by the project sponsor.

2.6. Summary

The principles and theory of water electrolysis discussed are used through this research to quantify and analyse the results produced from the electrolysers characterised. The fundamental scientific principles are a vital part of the design and build of a new state of the art alkaline electrolyser, which reduces overpotentials, increases the reaction kinetics and operating efficiency when compared to the electrolyser's predecessor.

The developments in alkaline electrolysis materials has been analysed and this enabled the development of an alkaline electrolyser using cost effective materials for the electrodes, electrolytes and additives.

Analyse of current research trends in PEM electrolysis highlighted a huge focus on the reduction in PGM electrocatalyst loading and utilisation, with very little on the impacts of water feed quality, which is limiting factor on the lifetime of PEM electrolysers.

This chapter has introduced the scientific background and theory of electrolysers which serves as the backbone to the basis of the research in the following chapters. The methodology behind the research and materials used to complete this is discussed.

Chapter 3

Methods and Materials

3.1. Methods

The analytical techniques used to quantify the electrochemical performance, gas productivity and composition, microscopic surface analysis, water composition and engine integration testing are described in this section.

3.1.1. Electrolyser Polarisation

The performance of an electrolyser is governed by its polarisation curve. This type of performance curve shows the current per unit area (current density) of the electrode flowing from the anode to the cathode as function of the voltage being applied by the external power supply. This is shown in Figure 3.1.

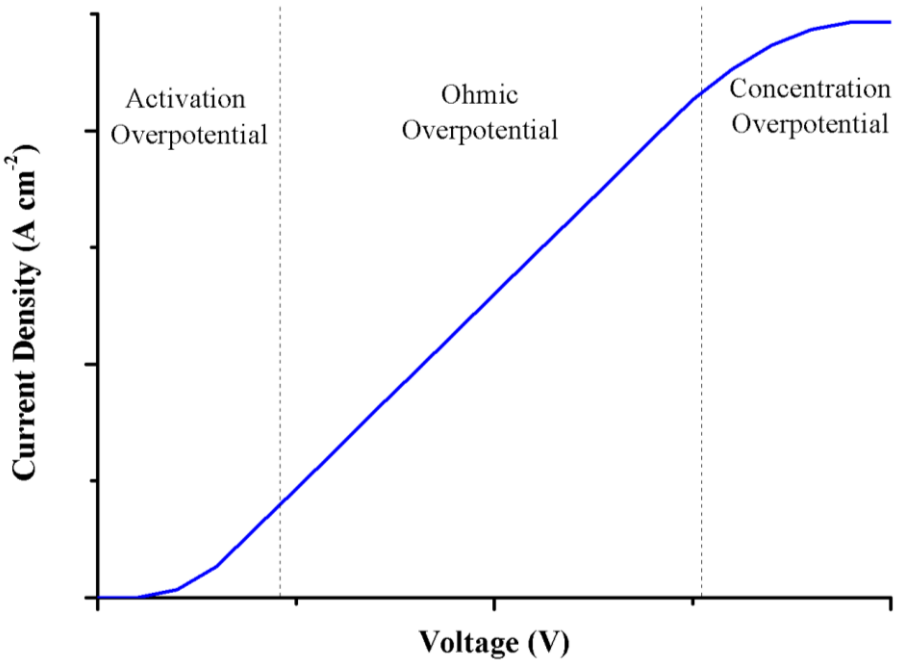

Figure 3.1: Conceptual Electrolyser Polarisation Curve

The curve and losses associated as previously described in the literature survey show the electrochemical efficiency of the electrolyser at any operating potential. The voltage (potential) across the electrolyser was varied and the subsequent current flow was plotted for each potential. Electrons will not flow with an applied potential below 1.48V (thermo-neutral voltage).

3.1.2. Gas Measurement

The gas evolution rate from the electrolyser is a vital parameter when determining the efficiency of the electrolyser. This was completed throughout using a 100ml glass measuring cylinder and a stopwatch. The gas evolution rate from an electrolyser is expected to increase with the potential across the cell (Figure 3.2).

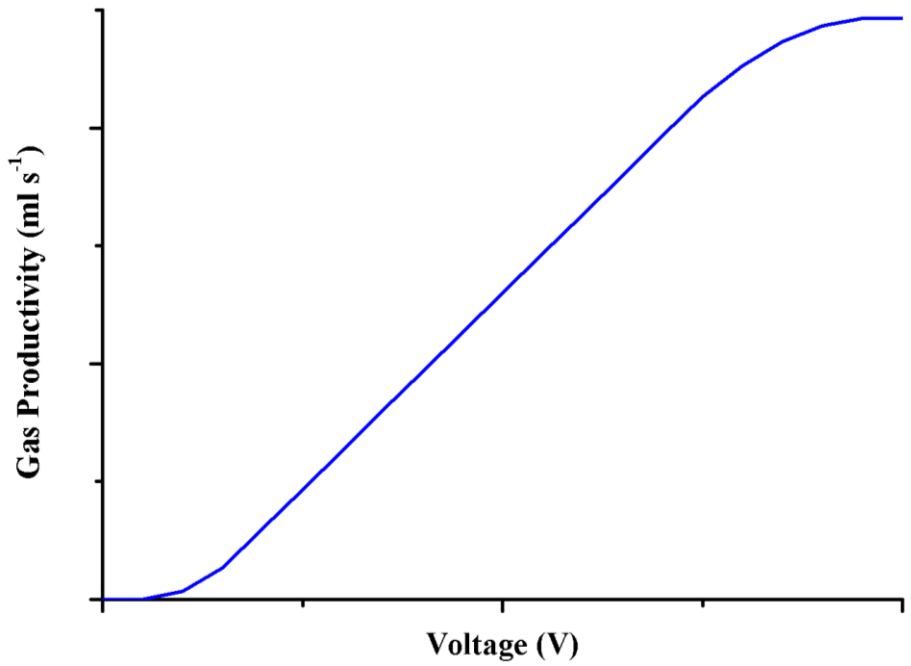

Figure 3.2: Conceptual Electrolyser Gas Evolution Curve

An identical trend is shown in Figure 3.1 and Figure 3.2 This is the validation of Faraday's First Law of Electrolysis. It states that the mass of a substance altered (evolved) at an electrode during electrolysis is directly proportional to quantity of electricity transferred at that electrode. An example plot of an electrolysis cell obeying this law is shown in Figure 3.3.

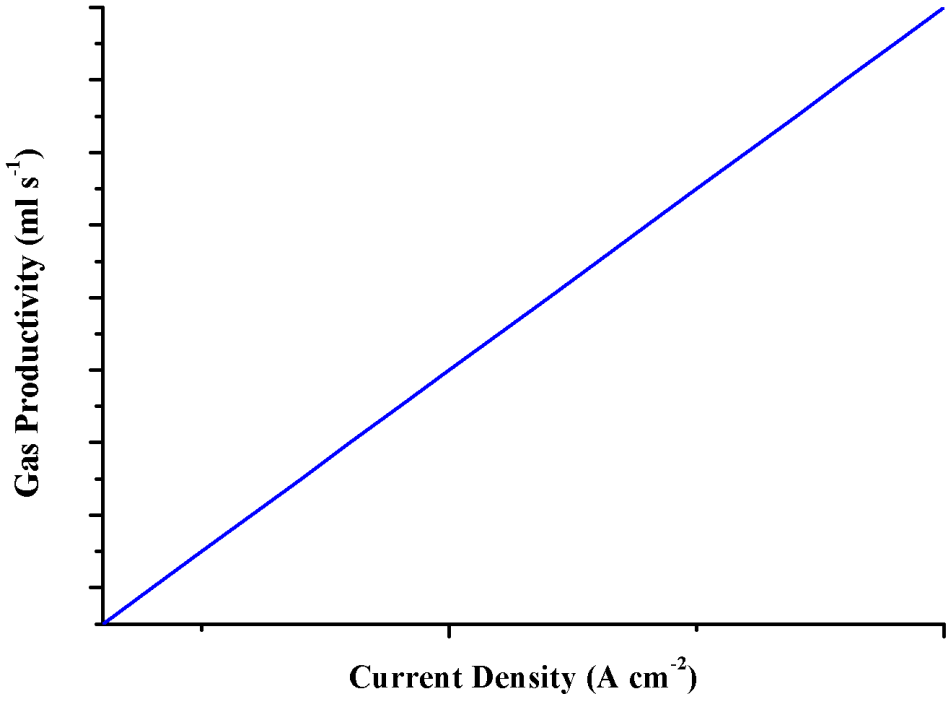

Figure 3.3: Conceptual Faraday 1st Law of Electrolysis Graph

Figure 3.3 illustrates that the quantity of gas evolved at the electrode is directly proportional to the current flow per unit electrode surface area. This demonstrates the electrolyser is operating in electrolysis mode, and the steeper the gradient, the more efficient the electrolyser is.

3.1.3. Electrical Efficiency

The efficiency of an electrolyser is an important factor when characterising an electrolyser and ultimately quantifies the energy content of the hydrogen produced as a function of the electrical energy supplied the electrolysis process.

The equation used to calculate the efficiency is:

$$\text{Efficiency } (\%) = \frac{\rho.HHV.100}{E_{volH2}} \qquad \text{Eq. 3.1}$$

where ρ is the density of hydrogen (0.08988 kg/m^3), HHV is the higher heating value of hydrogen (142 MJ/kg) and E_{volH2} (MJ/m^3) is the energy supplied per unit volume of hydrogen. A typical electrical efficiency plot for an electrolyser is shown in Figure 3.4.

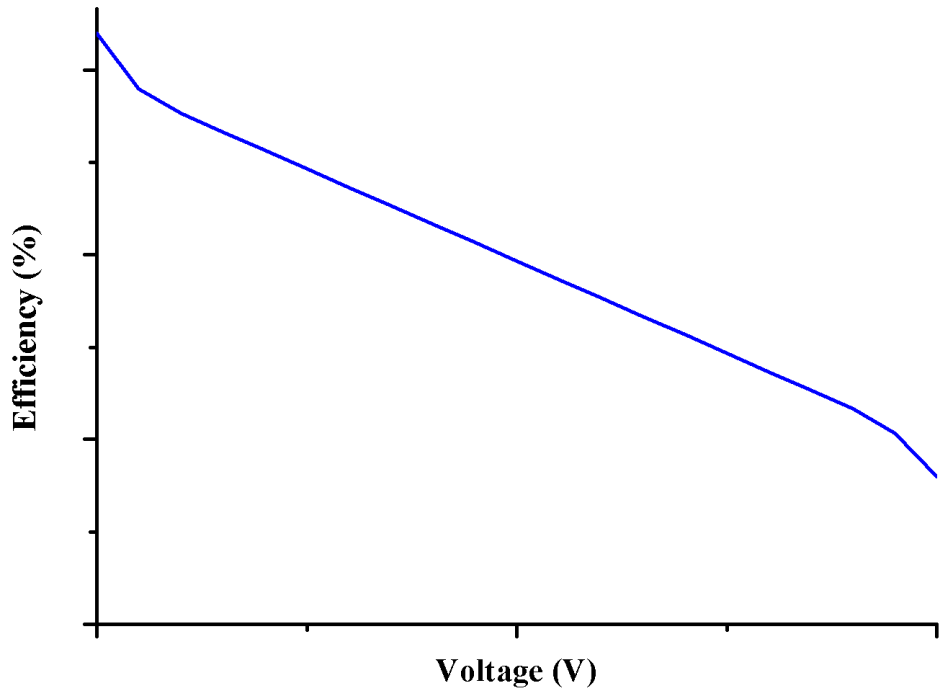

Figure 3.4: Conceptual Electrolyser Electrical Efficiency Curve

The efficiency is at its highest at low potentials when there is minimal resistance in the electrolyser, and then drops as the ohmic overpotential increases in the cell and then drops off when the high bubble overpotential is limiting gas evolution in the electrolyser whilst the energy input is still increasing. The most desirable efficiencies for electrolysis cells are found at low potentials and these cells are then connected in series to form an electrolysis stack with high hydrogen gas production rates and reduced electrical energy input.

3.1.4. Electrochemical Degradation

In real world scenarios the voltage is fixed across the electrolyser. As a result the current flow between the electrodes remains constant theoretically, however, in reality the current decreases (degrades) over time.

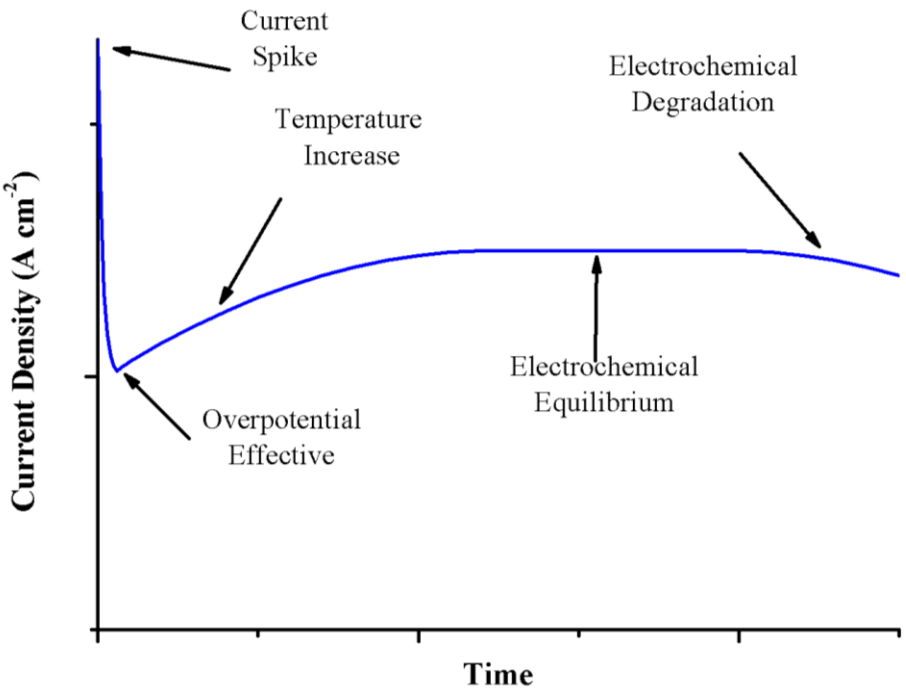

Figure 3.5: Schematic of Standard Electrochemical Degradation of an Electrolyser

Figure 3.5 shows a typical measurement of current vs. time for electrolysis systems. This is also known as chronoamperometry. The current is related to the slope of the concentration-distance profile at the electrode surface.

The current spike that follows the potential step is due to electrolysis of the molecules adjacent to the electrode surface (capacitive charging effect). Once these molecules have been electrolysed the rate of current flow is determined by the rate at which molecules arrive at the electrode surface, which is decided by the diffusion rate. The decay in the current that follows the spike emphasises the decrease in the rate of arrival of molecules at the electrode surface as the region near the electrode becomes depleted. The molecules have to travel further to reach the electrode as the experiment proceeds.

The change in current over time can be determined by the Cottrell equation in chronoamperometry. When a potential step change is applied the equation calculated the current flow as a function the diffusion of electrolyte to the electrode.

3.1.5. Scanning Electron Microscopy

The operating principle involve imaging the surface of samples by scanning it with a high-energy beam of electrons. The electrons interact with the atoms in the sample emitting signals about the samples surface composition, topography and electrical conductivity [147]. The process is shown in Figure 3.6.

An SEM produces a range of signals including secondary electrons, back-scattered electrons (BSE), characteristic X-rays, specimen current and transmitted electrons. The signals result from interactions of the electron beam with atoms at or near the surface of the sample [147].

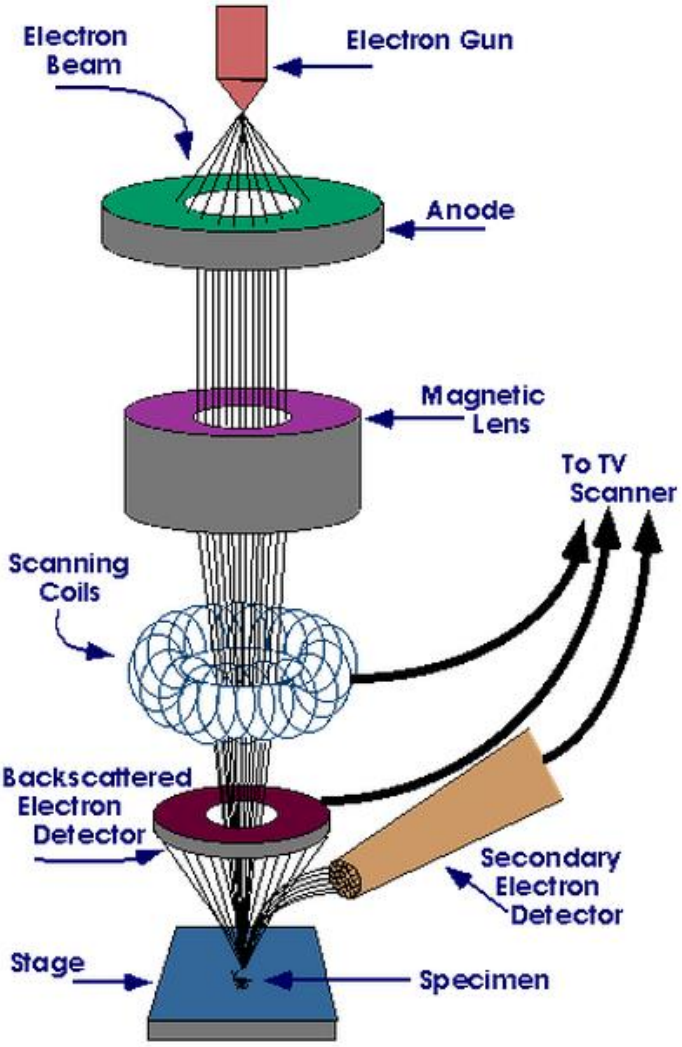

Figure 3.6: SEM Process & Schematic Reproduced from [147]

Secondary electron imaging (SEI) is the most common detection mode and it produces very high-resolution images of a sample surface. The narrow nature of the electron beam

results in a large depth of field from SEM micrographs subsequently producing a three-dimensional image which is useful for understanding the surface structure of a sample. An SEM allows a range of magnifications from about 10 times to more than 500,000 times. This is approximately 250 times the magnification ability of the best light microscopes [147].

BSE are electrons that are reflected from the sample by elastic scattering. These are usually seen in analytical SEM along with X-rays. The intensity signal of the BSE is a function of the atomic number (Z) of the sample, which results in BSE plots that can supply information about the distribution of differing elements on the sample surface. X-rays are emitted when the electron beam clears an inner shell electron from the sample, causing a higher energy electron to fill the shell and subsequently release energy. The produced X-rays allow identification of the surface composition and measure the abundance of elements in the sample [147].

3.1.6. Energy-Dispersive X-Ray Spectroscopy (EDX)

EDX is carried out simultaneously with SEM analysis and is available due to the SEMs ability to generate and analyse X-rays in order to study the surface chemical composition more thoroughly. The sample surface is hit with electrons causing the surface atoms to eject an electron. This vacancy is filled by another electron coming from a higher state and the energy difference is balanced through the release of an X-ray (shown in Figure 3.7).

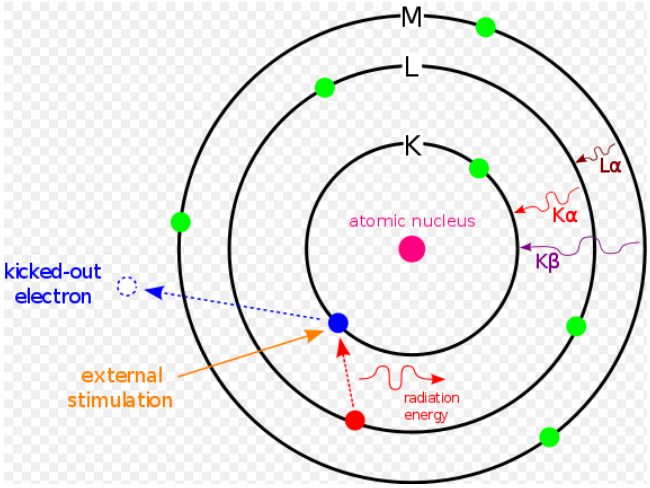

Figure 3.7: The Principles of EDX Reproduced from [148]

These various X-rays are separated into the corresponding signals of different elements enabling spectra to be produced.

3.1.7. X-Ray Photoelectron Spectroscopy (XPS)

XPS (also called Electron Spectroscopy for Chemical Analysis, ESCA) is a method of analysis to characterise surface composition of a sample. The sample is situated in a high vacuum chamber and then irradiated with photons enabling electrons to be emitted from an atom or molecule as shown in Figure 3.8.

The kinetic energy in this electron is quantified by the spectrometer and is dependent on the binding energy and the energy of the photon used and Eq. 3.2 shows this relationship.

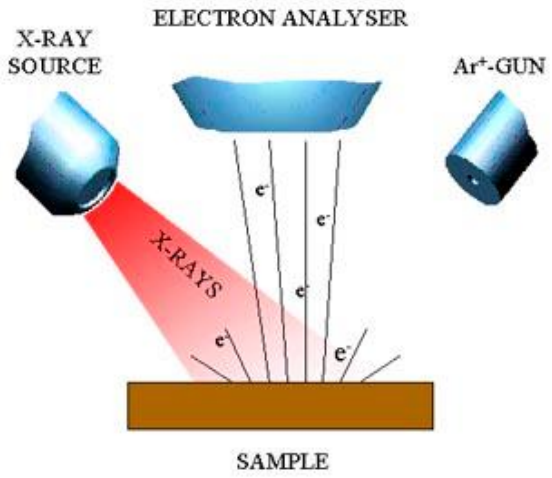

Figure 3.8: The Principles of XPS Reproduced from [149]

$$hv = E_B + E_K \qquad \text{Eq. 3.2}$$

where $hv =$ Incident x-ray/electron energy, $E_B =$ Binding energy of the electron at a certain energy level, $E_K =$ Kinetic energy of released photon.

The binding energy can be determined once the kinetic energy has been established, as the incident x-ray/electron energy is known, and then the elemental composition can be identified on the sample surface.

3.1.8. Inductively Coupled Plasma Mass Spectroscopy (ICP-MS)

ICP is inductively heated ionised plasma completed with an electrical coil and contains a concentration of ions and electrons to make the gas electrically conductive [150].

Integrating with mass spectrometry enables the ions from the plasma to be extracted through a series of cones into a mass spectrometer, usually a quadrupole. The ions are then separated on the basis of their mass-to-charge ratio and a detector receives an ion signal proportional to the concentration [150].

The equipment used for this analysis is an Agilent Technologies ICP-MS 7500ce Series and its operating principle is shown in Figure 3.9.

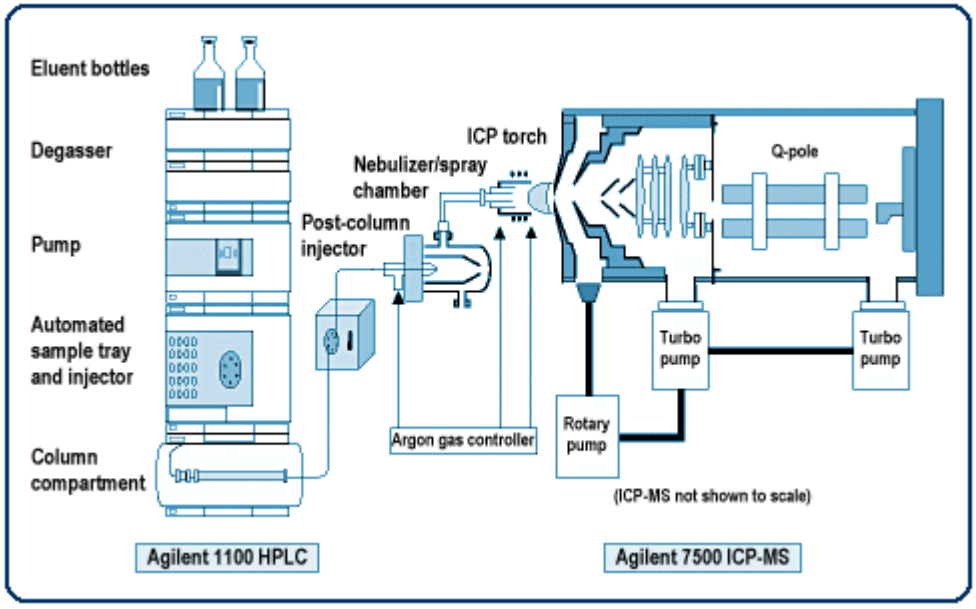

Figure 3.9: Operating Principle of ICP-MS Reproduced from [151]

Inductively couple plasma mass spectroscopy can detect elements with a mass lower than fluorine, which enables the detection of the major cations ions found in water, including sodium, potassium, calcium and magnesium. These are of interest because cations have higher affinity than protons for the sulfonic acid group sites and replace protons in accord with normal ion exchange processes in the ionomer phase. Subsequently, these reduce

the conductivity of the membrane and reduce water content in the fully hydrated membranes by replacement of protons in the Nafion® membranes.

3.1.9. Total Organic Carbon (TOC) Analysis

Total organic carbon (TOC) is defined as the amount of carbon within an organic compound and is a common indicator of water quality. Specific analysis for TOC measures the total carbon (TC) present, representing the content of dissolved carbon dioxide and carbonic acid salts, and the inorganic carbon (IC) present [152].

A Shimadzu ASI-V TOC Analyser was used to conduct this analysis and the standard operating principle is shown in Figure 3.10.

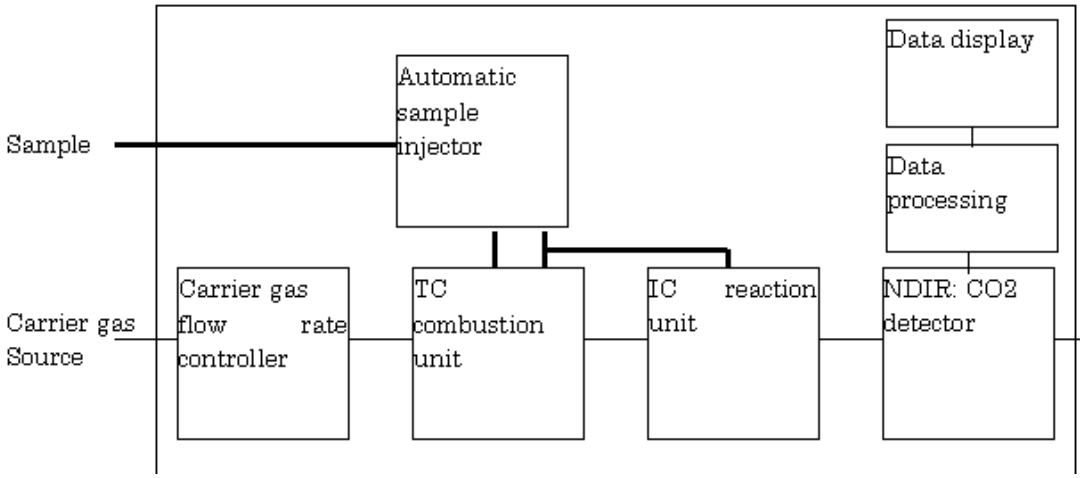

Figure 3.10: Operating Principle of TOC Analysis Reproduced from [153]

Subtracting the IC from the total carbon calculates the TOC. Removing the IC portion and then measuring the remaining carbon is common variant of TOC analysis. This

involves purging an acidified sample with air or nitrogen before measurement, and so is more commonly known as non-purgeable organic carbon (NPOC) [152].

Total organic carbon is another indicator of water quality, and can be measured by subtracting the total carbon content by the total inorganic carbon content in the sample. Organic carbon in the feed water for a PEM electrolyser represents impurities which will deactivate the PGM catalysts and subsequently accelerate the reduction in electrochemical performance of the electrolyser over time.

3.1.10. Internal Combustion Engine (ICE) Testing

The objective of these tests was to measure the initial emission benefits of the unit when the output gases are introduced in the engine intake. First, baseline tests without the use of the electrolyser were carried out and values for fuel consumption, brake thermal efficiency, carbon dioxide (CO_2), water vapour (H_2O), nitrogen oxides (NO_X), total unburnt hydrocarbons (THC) and carbon monoxide (CO) were been recorded.

Oxyhydrogen (HHO) gas from the electrolyser was added to the engine intake, and engine tests were carried out at the same engine operating conditions as the baseline tests. A single cylinder experimental diesel engine without any aftertreatment device was used to evaluate the effects of the hydroxy gas produced from the electrolyser on engine performance and emissions. A schematic for the engine testing procedure is shown in Figure 3.11 and the main engine specifications are given in Table 3.1.

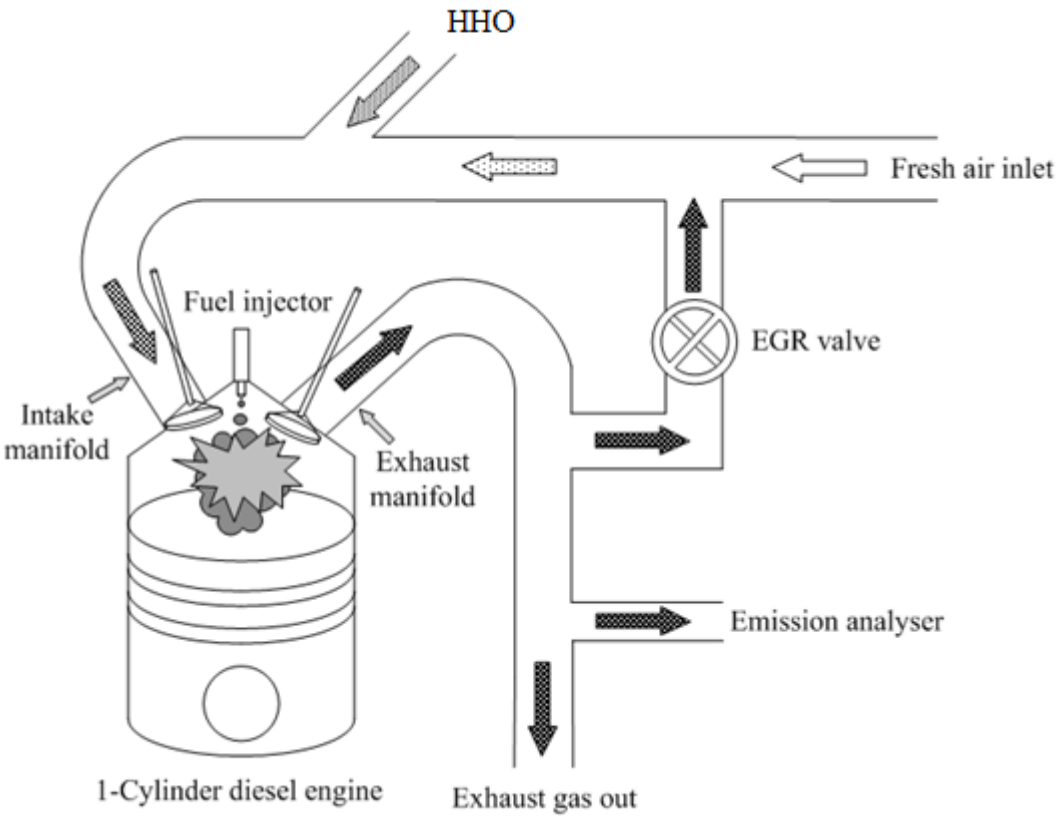

Figure 3.11: Schematic of Engine Testing Experimental Setup (Image Courtesy of Jose Herreros [154])

The load for the engine was supplied from an electric dynamometer with motor and a load cell. In-cylinder pressure traces were recorded by a Kistler 6125B pressure transducer mounted at the cylinder head and connected via a Kistler 5011 charge amplifier to a data acquisition board (National Instruments PCI-MIO-16E-4).

The crankshaft position was characterised using a digital shaft encoder. Other standard engine test rig instrumentation used to monitor intake air, temperatures (oil, air, inlet manifold and exhaust) and pressures were included in the test rig. A Horiba MEXA

7100DEGR gas analyser was used to take measurements of CO_2 and CO by Non-Dispersive Infrared (NDIR), O_2 by a magnetopneumatic method, NO_x by chemiluminescence detection (CLD) and HC by flame ionisation detection (FID). A MultiGas 2030, FTIR spectrometry based analyser was also used for the measurement of water vapour and gaseous emissions already measured with the Horiba MEXA 7100DEGR.

Table 3.1: Engine Specification for HHO Testing

Engine Specification	Data
Number of Cylinders	1
Bore/Stroke	98.4 mm/101.6 mm
Connecting Rod Length	165 mm
Displacement Volume	733 cm^3
Compression Ratio	15.5:1
Rated Power (kW)	8.6@2500 rpm
Peak Torque (Nm)	39.2@1800 rpm
Injection System	Three holes pump-line-nozzle
Injection Timing (°bTDC)	22
Engine Piston	Bowl-in-piston

The basic properties of diesel fuel used are given in Table 3.2. The electrolyser product was introduced and mixed with the air before the intake manifold valve. In the first part of the study four different engine operating conditions were studied (see Table 3.3).

Table 3.2: Fuel Analysis for HHO Engine Testing

Fuel Analysis		Method
Cetane number	53.9	ASTM D613
Density at 15°C (kg m^{-3})	827.1	ASTM D4052
Viscosity at 40°C (m^2 s^{-1})	2.467 E-06	ASTM D445
50% distillation (°C)	264	ASTM D86
90% distillation (°C)	329	ASTM D86
LCV (MJ kg^{-1})	42.6	N/A
Sulphur (mg kg^{-1})	46	ASTM D2622

The electrolysers had a 12 V potential applied across it (consistent with an alternator in a standard passenger vehicle) and a concentration of 1.0M KOH solution used as the

electrolyte in the electrolyser. The engine settings for both electrolysers is shown in Table 3.3.

Table 3.3: Engine Operating Conditions for HHO Testing

Engine Operating Conditions	Mid Load	High Load
Engine speed (rpm)	1200	1500
Indicated mean effective pressure (bar)	3 & 5	3 & 5

3.2. Materials

3.2.1. Electrolysers

An overview, description and schematic for each electrolyser analysed is presented in this section. All electrolysers are named accordingly to protect commercial impact. The materials, components and design of the commercial electrolysers supplied are the intellectual property of the suppliers and modification of these products is strictly prohibited. As a result redesign of a electrolysers has been completed.

3.2.1.1. Electrolyser A

Electrolyser A is a 6 plate (80 mm x 80 mm) stainles steel 316 (SS316) alkaline electrolyser. The total electrode surface area in the electrolyser is 384 cm^2.

The equipment was set up in a unipolar configuation as illustrated in Figure 3.12, and experiments were carried out to test the effect of varying the cell voltage across the electrolyser. Different concentrations of potassium hydroxide (KOH) solution were investigated to characterise the polarisation of the electrolyser and the equivalent HHO

production rates. A constant volume of 300 cm^3 of electrolyte solution was used for each experiment.

Two plastic tubes were connected from the fluid inlets/outlets of the electrolyser, to the underside of the larger plastic container. The plastic container was placed at a greater height than the electrolyser during operation, thus enabling the KOH solution to flow into the electrolyser under gravity.

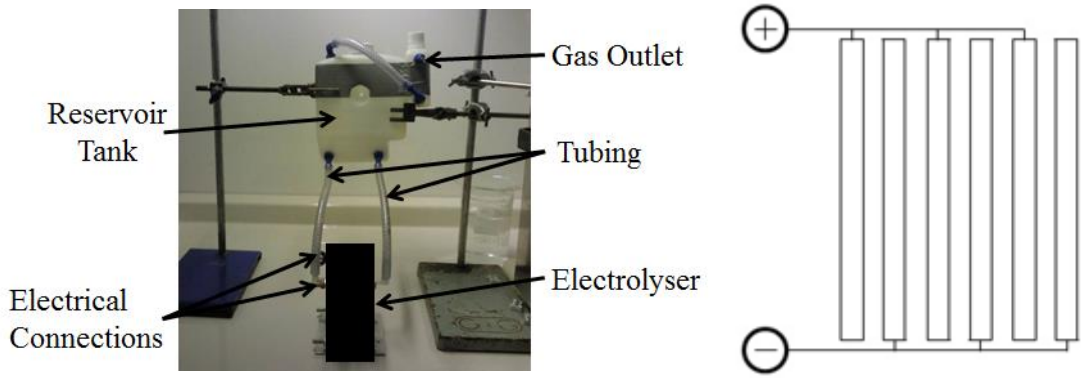

Figure 3.12: Experimental Setup & Circuit Diagram of Electrolyser A

During operation, the KOH solution flows into the electrolyser from the reservoir tank through down into the electrolyser. Simultaneously, HHO gas is produced and exits the top of the electrolyser through the tubes connecting the reservoir tank to the electrolyser as shown in Figure 3.12. The product gases exit the electrolyser against the flow of the KOH solution when the buoyancy force of the HHO gas in the electrolyser is greater than the force of gravity pushing the solution down into the electrolyser.

The purpose of the side tank is defined for HHO gas cooling. However, it can be more suitably described as a pressure relief vessel. If there was a surge of pressure in the system, it would be favourable that the smaller vessel, containing distilled water, ruptured than the larger vessel containing the alkaline solution. The connection of the main reservoir with the side vessel enables this safety feature to function.

3.2.1.2. Electrolysers B & C

Two unipolar electrolysers were supplied from the same company. They were identical except in two differences. The first variation Electrolyser C had an outlet on the underside of the electrolyser (which allowed the flow of pumped electrolyte solution through the electrolyser), whereas Electrolyser B does not. The second difference was the use of two outlets on Electrolyser C (for the purpose of separating the product gases), whereas Electrolyser B has only one.

Testing on Electrolyser B took place in a batch operation, which had the inlet on the underside of the electrolyser sealed to prevent any electrolyte leaving the cell. The cell was then filled with a fixed volume (500 cm^3) of KOH solution. Electrolyser C was tested in a continuous operation mode, with a pump constantly pumping electrolyte from reservoirs through the electrolyser cell. The pressure of the pumped electrolyte through the electroylser should help the membrane contract and reduce the crossover of hydrogen and oxygen gas.

The electrochemical behaviour of both cells was characterised at various KOH concentrations by measuring the current flow at set voltage intervals. The gas flowrate and gas produced out of each outlet on the top of the cell was also measured.

Electrolyser B

This electrolyser (Figure 3.13) has one gas outlet; no separation of hydrogen and oxygen gas. It is a 6 plate SS316 electrolyser with a total electrode surface are of 4645 cm^2. Electrolyser B will be operated in with no flowthrough of electrolyte i.e. a fixed volume.

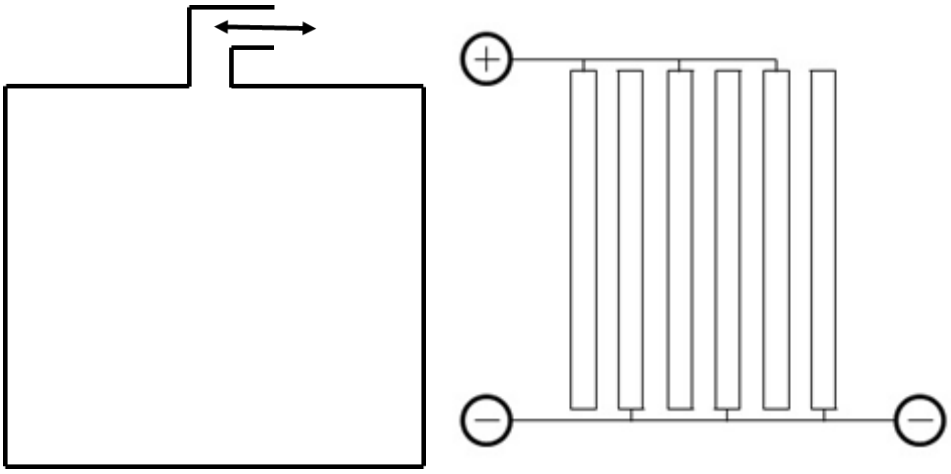

Figure 3.13: Schematic of Electrolyser B

The electrolyser is filled to capacity with KOH solution and when an electrical current is applied the bouyancy of gases evolved bring them to the surface and then dissipate through the single outlet on the roof on the electrolyser.

Electrolyser C

Electrolyser C (Figure 3.14) has two gas outlets. The addition of the two gas outlets on the electrolyser is for the separation of the hydrogen and oxygen gases which is completed by a membrane. It also is a 6 plate SS316 electrolyser with a total electrode surface are of 4645 cm^2.

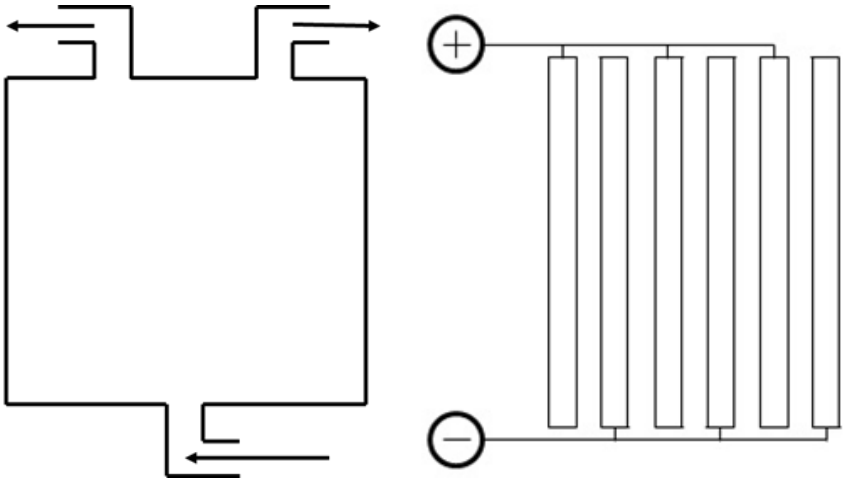

Figure 3.14: Schematic of Electrolyser C

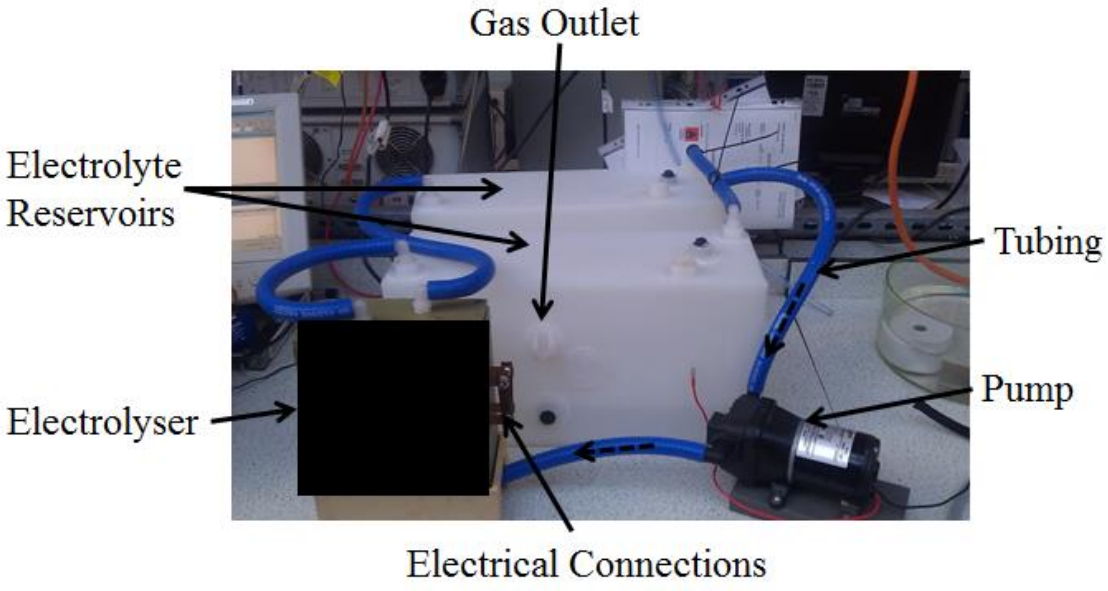

Figure 3.15: Electrolyser C Experimental Setup

Whereas the Electrolyser B was operated in a batch mode, Electrolyser C was operated in a 'continuous mode' with electrolyte continuously pumped through the electrolyser as shown in the experimental setup in Figure 3.15. The voltage of the pump was set to 4 V and two 10 L reservoirs were used to hold the electrolyte and product gases.

3.2.1.3. Electrolyser D

It was proposed to use ultrasound combined with electrochemistry (Sonoelectrochemistry) for the production of hydrogen. Sonoelectrochemistry is defined as a branch of electrochemistry which studies any electrochemical processes that are affected, assisted or promoted by power ultrasound [155]. Reports (in the form of papers, patents, etc.) on the subject have been examined from over the last 100 years to the present day to understand how this area of research has evolved.

During operation, the collection of bubbles on electrode increases electrical resistance of the cell. Ultrasonic irradiation causes "cavitation" of bubbles on electrode surfaces; these bubbles then coalesce to form larger gas bubbles that then implode and collapse, thus releasing dissolved gases (degassing effect). This results in an increase in active sites on the electrode and hence increases the electrical efficiency and yield of the cell [156].

Ultrasound is a sound wave with a high pitch that cannot be heard by the human ear (>16 kHz) [157]. Above that frequency, the use of ultrasound in chemistry (Sonochemistry) is divided into two categories: high frequency or diagnostic ultrasound,

and low frequency or power ultrasound. High frequency or diagnostic ultrasound operates at frequencies of 2 -10 MHz and is mainly used for medical applications. Low frequency or power ultrasound operates at frequencies of 20 kHz – 2 MHz and this is where the cavitation phenomenon occurs [158, 159].

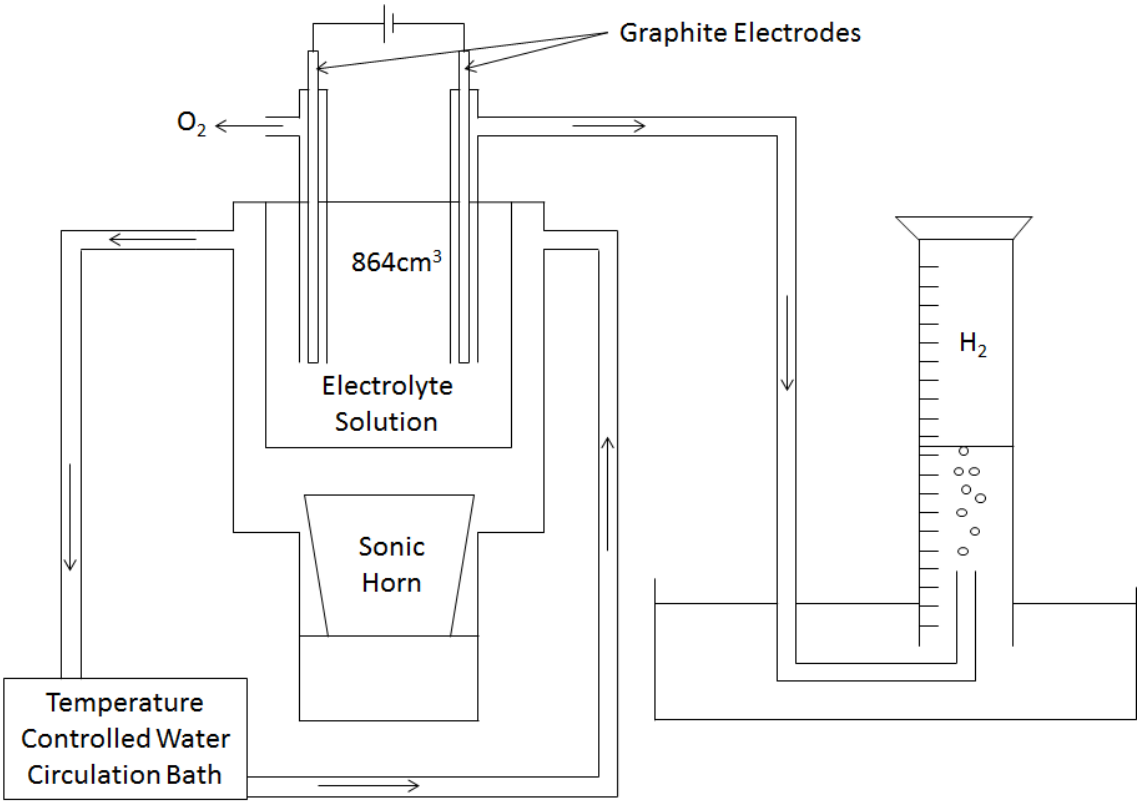

Figure 3.16: Electrolyser D Schematic & Experimental Setup (Image not to Scale)

Electrolyser D (Figure 3.16) was designed and built inhouse for the purpose of improved hydrogen gas generation from alkaline electrolysis. The cell consisted of a reaction vessel (diameter 10 cm, height 11 cm, volume 864 cm^3) surrounded by an outer vessel, providing a continuous flow of water at 298 K (Tecam Water Bath & Techne Tempette TE-8A Heating Bath Circulator) to regulate a constant temperature in the inner vessel. Two carbon electrodes (active area 7.61 cm^2) were inserted into the inner vessel and an

electrical current was passed through these electrodes to the aqueous solution. Gases produced were collected and measured by water displacement using a glass cylinder.

Ultrasonic irradiation was provided by an ultrasonic horn (Sonics Ti Alloy, 47 mm in diameter connected to a Sonics VCX750 VibraCell operating at 20 kHz and maximum power of 750 W). For the experimentation at 20 kHz, the ultrasonic power was 20.7 W/cm^2 unless otherwise stated. The carbon electrodes used were manufactured by Morganite which had a diameter of 5 mm and a length of 300 mm.

The custom glassware used was manufactured by Soham Scientific (reference 0210-109e). For all experiments the power was supplied by a Thurlby AC/DC PL320 32V-2A.

3.2.1.4. Electrolyser E

Electrolyser E (Figure 3.17) is also a 6 plate (10 mm x 100 mm) SS316 electrolyser with a 600 cm^2 electrode surface area in a unipolar configuation. Five hand built electrolysers (E.1-E.5) were provided by the supplier. Experimentation was completed on units E.2, E.4 & E.5 and then the data of the best performing electrolyser is presented.

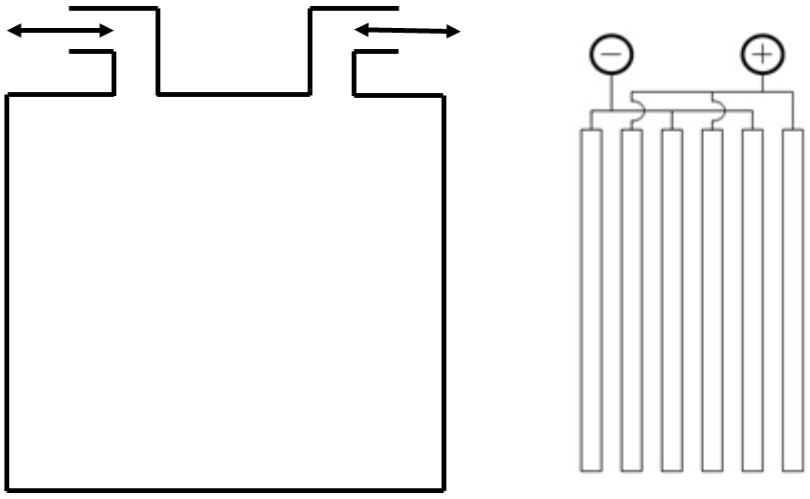

Figure 3.17: Schematic of Electrolyser E

The equipment was set up as illustrated in Figure 3.18, and several experiments were carried out to test the effect of varying the cell voltage across the electrolyser.

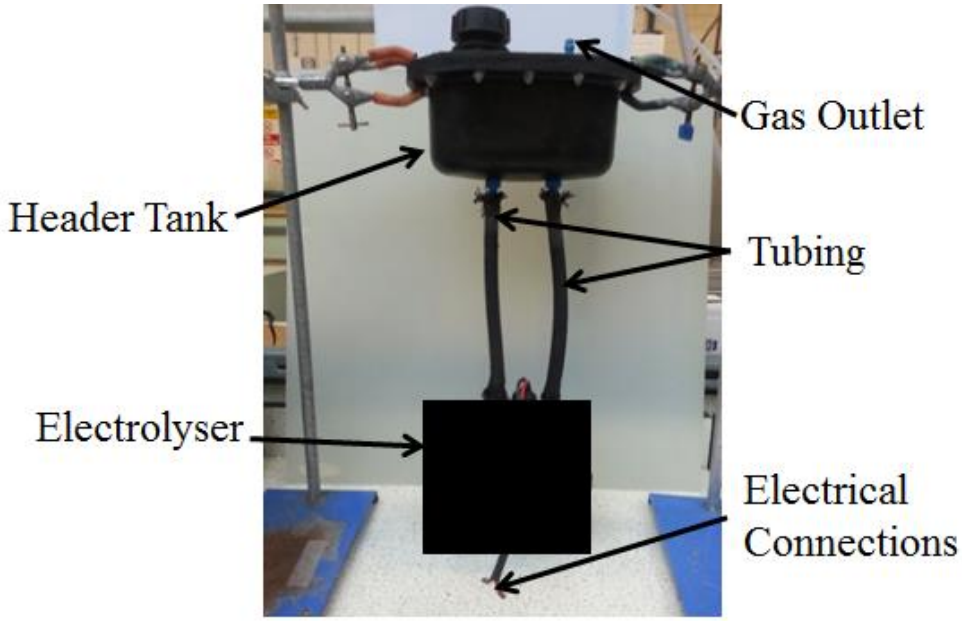

Figure 3.18: Electrolyser E Experimental Setup

Different concentrations of KOH solution were investigated to characterise the polarisation of the solution and the equivalent HHO production. A constant volume of 800 cm^3 of aqueous solution was used for each experiment.

Electrolyser E was setup identically to that of Electrolyser A, which consisted of connecting the electrolyser to a reservoir tank (with plastic tubing) which holds the KOH electrolyte solution.

3.2.1.5. Electrolysers F & G

Electrolyser F

The first electrolyser design took into account the need for no increase in electrolyser size and managed to build in the ability to hold up to 24 electrode plates (100 mm x 100 mm x 1 mm), with a 6 mm spacing between each plate. These 24 plates represent up to 12 electrolysis cells in the electrolyser stack in a unipolar configuation. A CAD design of Electrolyser F is shown in Figure 3.19.

The casing was built out of Perspex (10 mm thickness), which enabled visual insight (poor electrode connections, bubble evolution restrictions) at the reaction occurring in the electrolyser. Precision slots were made, which allowed for ease of removal and modification of each electrode. The plates were connected in parallel using two stainless steel (SS316) bars (150mm x 20mm x 1mm), which were connected to the electrodes using SS316 screws. A circuit diagram on Electrolyser F is shown in Figure 3.20.

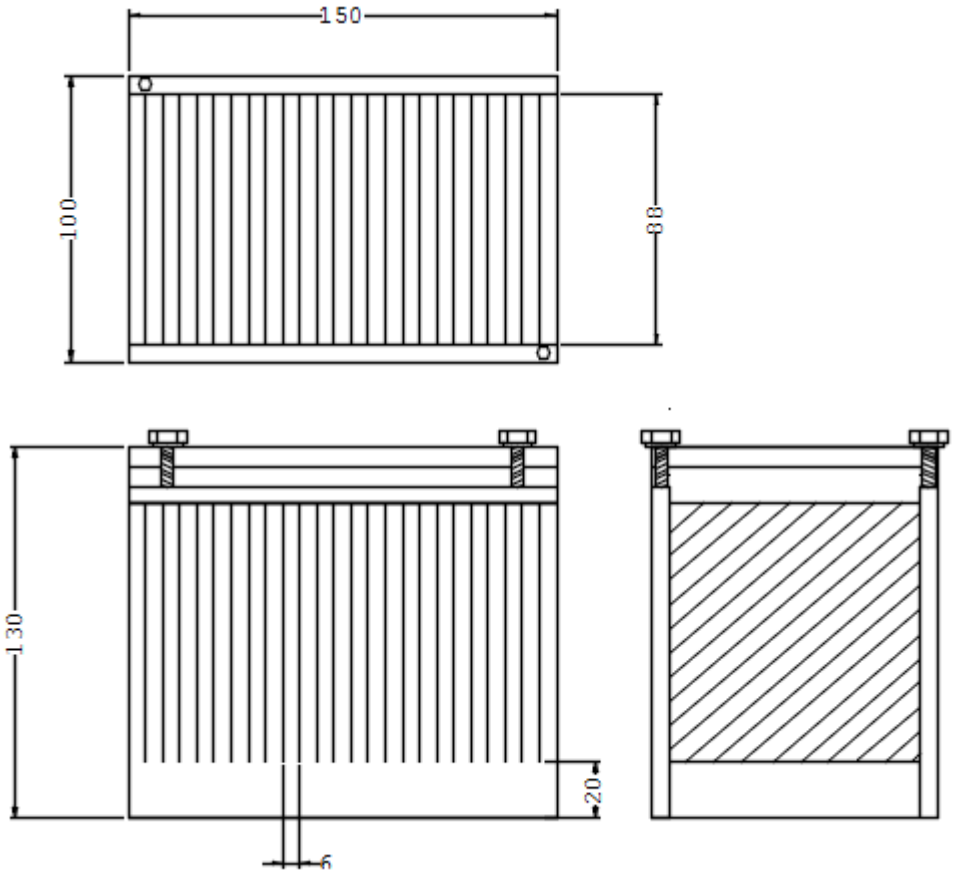

Figure 3.19: Electrolyser F CAD Design of 24 100mm x 100mm x1mm electrodes with 6mm spacing between electrodes

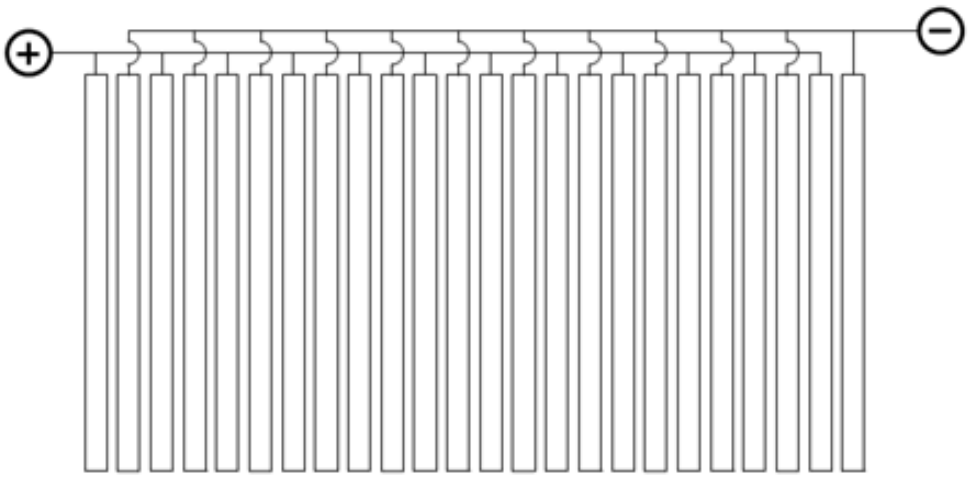

Figure 3.20: Electrolyser F Circuit Diagram

At one end of each interconnect was a SS316 (4 mm diameter) screw soldered onto it for the electrical energy input to the electrolyser stack. These were accompanied with two 3/8'' ID nylon nozzles which were placed symmetrically central in the electrolyser lid for the connection of the stack to the electrolyte reservoir. Images of the constructed Electrolyser F are shown in Figure 3.21.

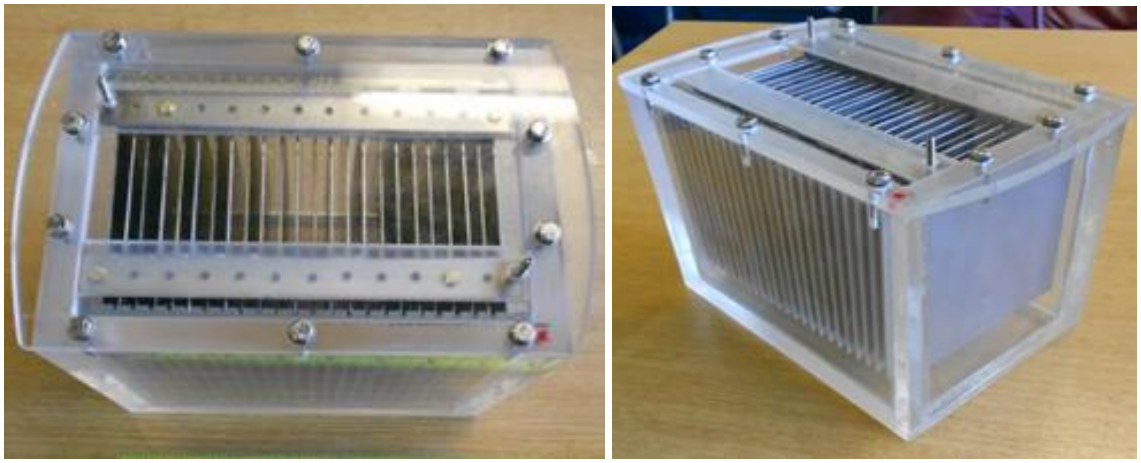

Figure 3.21: Image of the Constructed Electrolyser F

5.2.1.6. Electrolyser G

Electrolyser G differed from Electrolyser F, with the reduction of number of electrodes from 24 to 20 plates. A CAD design of Electrolyser G is shown in Figure 3.22. This gave space for use of an additional electrical connection on each of the stainless steel interconnects. A circuit diagram on Electrolyser G is shown in Figure 3.23 and an image of the constructed Electrolyser G in Figure 3.24.

This accompanied with the increase length (10 mm to 30 mm) and diameter (4 mm to 6 mm) of the SS316 screws gives rise to better heat distribution through the electrical connections, especially considering the higher currents (> 200 A) expected and the corresponding heat produced.

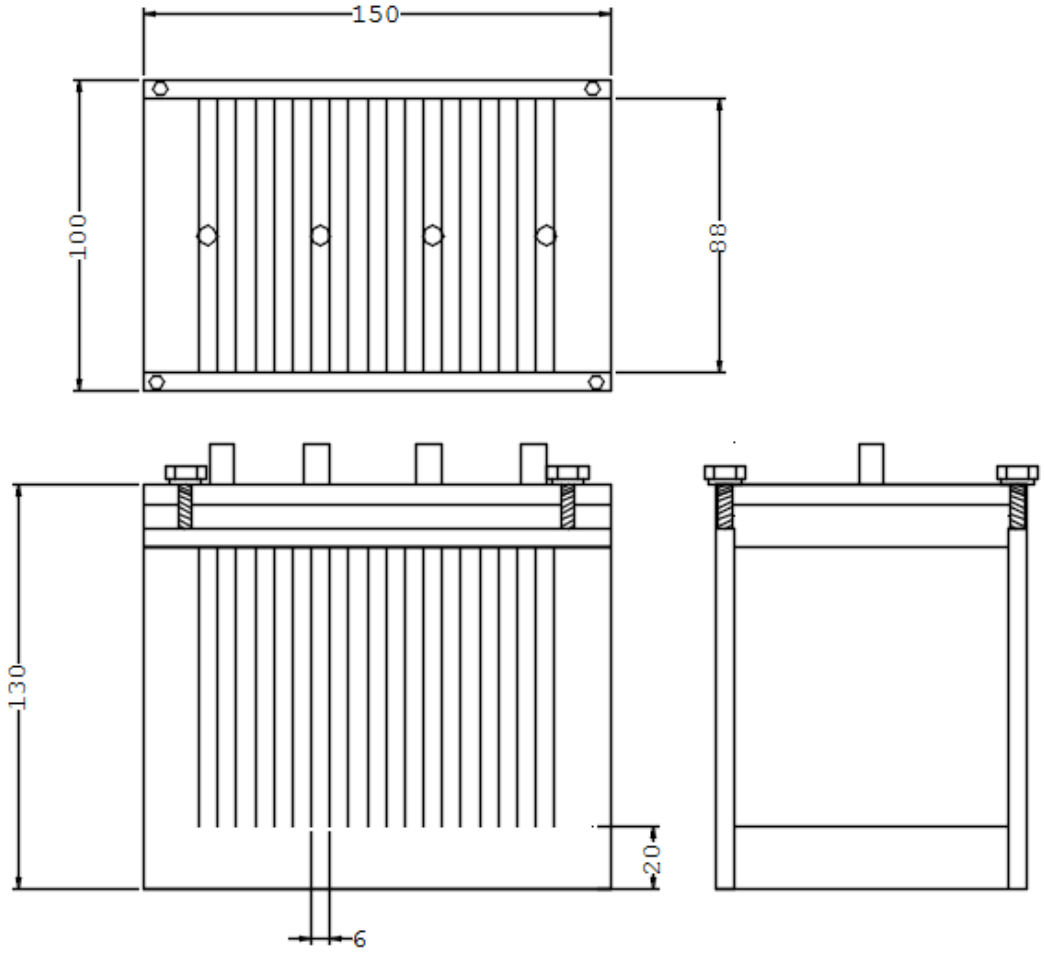

Figure 3.22: Electrolyser G CAD Design of 20 100mm x 100mm x1mm electrodes with 6mm spacing between electrodes

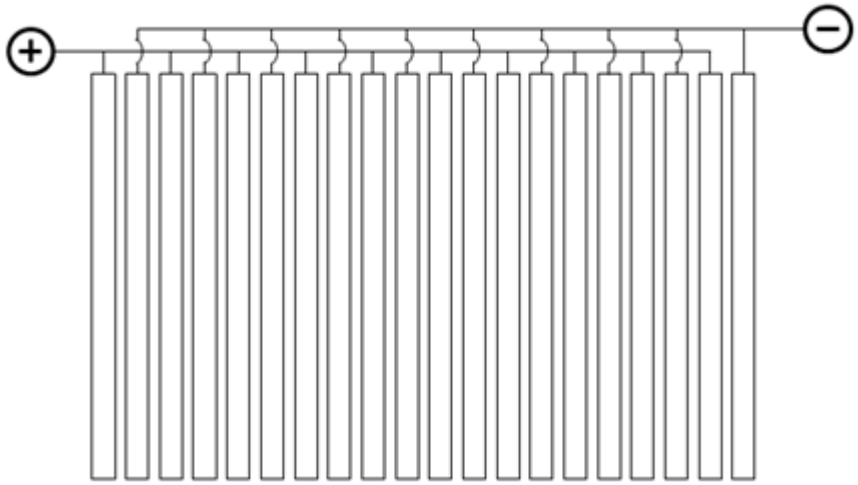

Figure 3.23: Electrolyser G Circuit Diagram

An additional pair of nylon nozzles was added into the electrolyser lid, taking the total number to four. This will aid flow of electrolyte solution and aid the removal of HHO gas formed from the stack, thus keeping the internal pressure at a minimum and reducing the risk of explosion. Figure 3.24 shows the experimental setup for Electrolyser G.

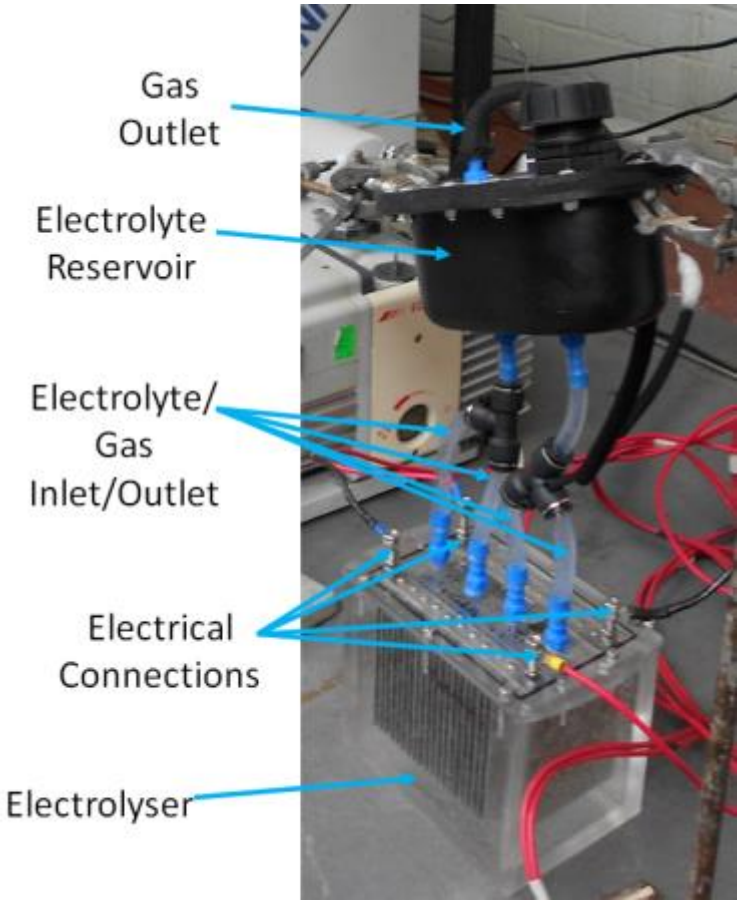

Figure 3.24: Electrolyser G and Apparatus Setup

3.2.1.6. Electrolyser H & I

Two electrolysers (Electrolysers H & I) were built in a Perspex casing consisting of six nickel (201) electrodes (100 mm x 100 mm x 1 mm) (total electrode surface area = 1206 cm^2) in a unipolar configuation with a fixed separation distance of 6 mm. There is a clearance of 20 mm from the bottom of the Perspex vessel to the bottom of the nickel electrodes. Electrolyser H is the above mentioned electrolyser stack without titanium (Grade I (ASTM B265)) chips, whilst Electrolyser I has the titanium chips in the bottom of the vessel. An image and CAD of the electrolyser is shown in Figure 3.25.

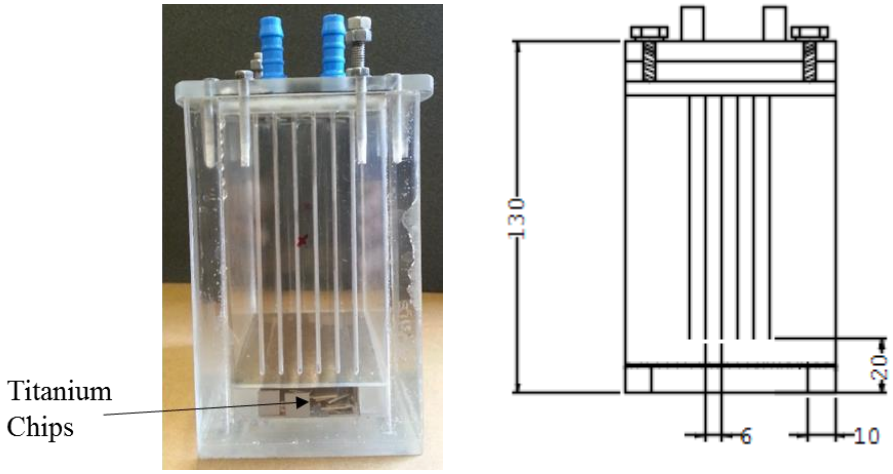

Figure 3.25: Image and CAD of Electrolyser I (dimensions in mm)

In this case titanium chips (10 mm x 10 mm x 1 mm) must be added (240 cm^2 total surface area) to ensure that the electrode material is protected from corrosion. The titanium chips will be held at the bottom of the reaction vessel under a nickel mesh to ensure they do not interact with the electrochemical reaction. The specified dimensions were chosen for this feasibility study to maximise the surface area in the small volume available at the underside of the vessel, and if proven further research could be conducted on varying geometries and loadings of titanium in the system. A larger size of titanium chips would limit the surface area of titanium available in the vessel and the subsequent electronegativity of the titanium. The titanium does not participate in the electrochemical reaction and must be kept out of physic contact with the nickel electrodes.

The potassium hydroxide (≥85% KOH basis, pellets) was mixed with a specific volume of Type II Deionised Water (Millipore Distilled Water Purification System (Rios Doi3)), to produce a predetermined concentration of KOH solution. The potential was controlled

and the subsequent current measured using a direct current power supply (Thurlby Thandar Instruments QPX1200SP model).

Following the electrolysis reaction, the electrodes were prepared for SEM (JEOL JSM-6610LV), EDX (Oxford Instruments Inca 300 EDS system), and XPS (Thermo Scientific K-Alpha) analysis, and were washed thoroughly with Type I (18MΩ) water to remove any residual KOH solution, and then subsequently dried.

3.2.1.7. Electrolyser J

Electrolyser J was leased to the University of Birmingham by commercial supplier of water electrolysers to produce hydrogen for fuel cell vehicle refuelling in April 2011. Before being implemented in the refuelling system, the electrolyser was continually tested in collaboration with the manufacturer.

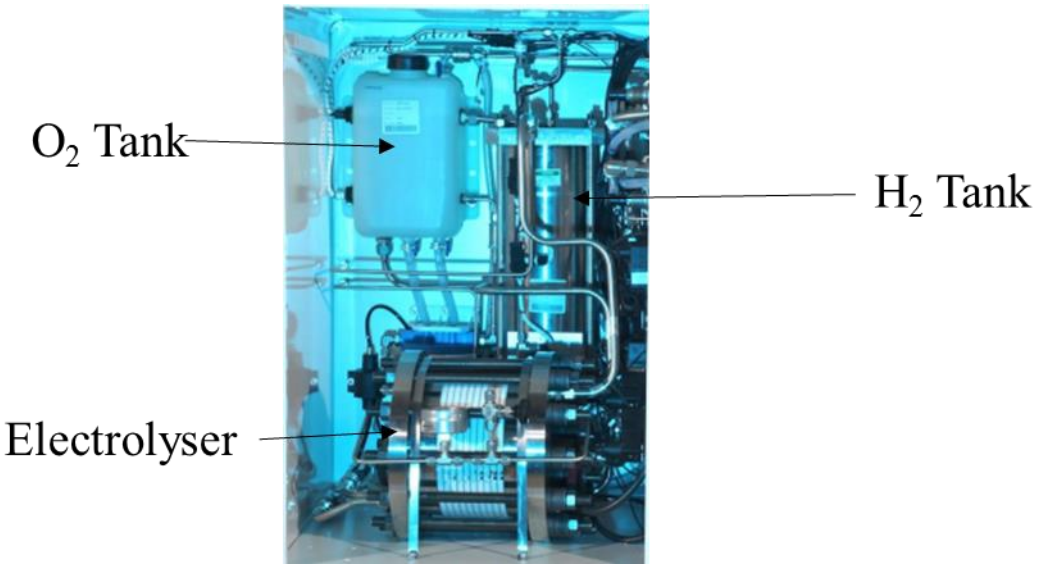

Figure 3.26: Image of Electrolyser J

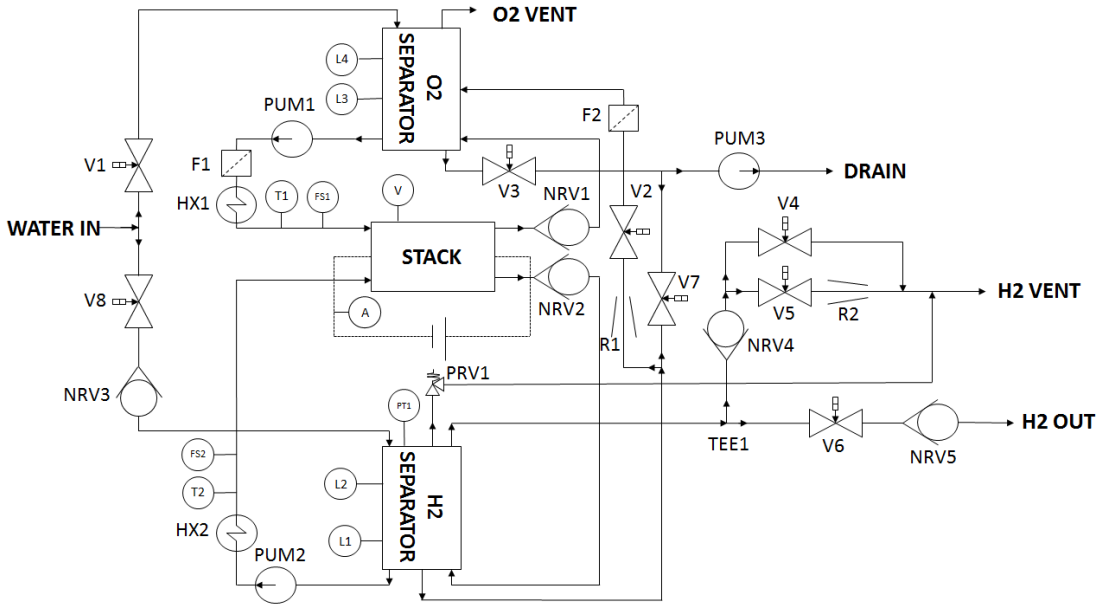

Figure 3.27: P&ID of Electrolyser J

Description of Process

Start-up Sequence

Upon operation, the control system opens valves V1 and V8 to fill the oxygen (O_2) separation tower and hydrogen (H_2) separation tower with water, stopped by closing the valves when the water reaches level sensors L4 and L2 respectively. To ensure that no pressure head builds up whilst filling the H_2 separation tower, V4 is opened (the O_2 separation tower is already open to the atmosphere). A timer for each fill identifies any blockage in the water lines. Pumps 1 and 2 are activated and the lines through the electrolyser stack are also filled with water.

The O_2 separation tower is then emptied by opening V3 and activating pump 3 (again with a timer to identify any blockage in the drain line) and refilled back to the level of L4. To empty the H_2 separator, the electrolyser is briefly powered on with V4 now closed to create sufficient hydrogen head pressure (at 19 V to evoke a lower hydrogen production rate than full capacity at maximum potential) which when V7 is opened, causes water to drain from the H_2 separation tower. The H_2 separator is then refilled back to the level of L2, then V7 is opened for 15 seconds to drop the water level in the H_2 separation tower slightly below L2.

System Pressure Check Sequence

After the water purge, the voltage to the electrolyser stack is ramped up to approximately 17-19 V where V6 is closed in order to build up pressure in the H_2 separation tower. At various pressures up to 13 bar, the power to the stack is stopped, and the pressure monitored for any change (due to a pressure leak). The power is shut-down for 60 seconds, whilst the pressure is measured using PT1, and presuming there is no change in the H_2 pressure, power is reintroduced to the stack and the pressure increases again. Once achieving 13 bar pressure and the 60 seconds pressure testing completed, the pressure is released by venting the gas through V5 (slow vent). When the pressure is down to 0 bar, V5 shuts and the system is ready to start producing its H_2 gas product.

Gas Generation

The control system then moves into the operational mode and commences electrolysis and starts to pressurise the hydrogen system, whilst oxygen is vented to the atmosphere. The hydrogen produced in the electrolyser stack is channelled to the H_2 separation tower along with the flowing water (used to provide cooling) and can be vented either through V4 or V5 (fast and slow vent respectively) or used to fill a vessel connected externally or provide a continuous flow of product hydrogen. The pressure at which the product hydrogen exits the electrolyser is controlled by a back pressure regulator (BPR) at a pressure of up to 14 bar, as chosen by the user. This will influence the pressure consistently seen by the H_2 separation tower, pipes and hydrogen producing side of the electrolyser. It is measured using PT1, a compact high pressure OEM pressure transmitter. The prevent over-pressurisation, the separating vessel is fitted with a safety relief valve set at 18 bar. Unless the system is shut down (see below), either by the user or automatically due to a fault, electrolysis will continue until the system pressure reaches a user defined target pressure (maximum 15 bar), at which the power supply will be turned off by the control system (when control logic is implemented), halting electrolysis and the system will remain in a standby state at pressure.

Unless a shut-down is instigated, the electrolyser will produce hydrogen (or be in the standby state at its target pressure) in operational mode for a defined period of time – currently set at 24 hours. After this time period, the system automatically enters a water purge mode, to replace the water in the system.

Water Circulation

Under current operational parameters, the maximum temperature that can be reached by the water in the vessel is 60^{o}C before stopping electrolysis. When the temperature reaches 50^{o}C, a heat exchanger loop is activated to reduce the temperature.

Water Repatriation

During electrolysis, as protons migrate from the anode to the cathode, they drag water molecules with them. This phenomenon is referred to as electro-osmotic drag, and results in a build-up of water in a hydrogen separator. Whilst in operational mode and above 3.5 bar, V2 is opened to return water to the O_2 tower through a electro-osmotic drag water repatriation loop. This creates a pressure drop that can be up to 1 bar, depending on the system pressure, with a frequency of up to 6 per hour. Although the actual frequency depends on the system conditions, the frequency is relatively predictable and monitoring this can identify leaks in the system not picked up by the pressure transducer due to pressure loss.

Depressurisation

As above, the control system returns the hydrogen bearing components to ambient pressure at a slow rate (approximately 6.5 minutes from 15 bar to 1 bar) by opening the restricted vent V5 and finally V4, before the system stops at ambient pressure. This can be caused by an error detected by the control system or by user intervention.

Operational Protocols

As previously mentioned, the outlet pressure of H_2 produced from Electrolyser J is controlled using a back pressure regulator (BPR). This BPR is situated outside Electrolyser J itself, and is subject to changing environmental conditions (varying temperature (approx. 5-25^oC)), unlike the electrolyser stack and separation towers which are contained within Electrolyser J and are maintained at moderate temperatures (approx. 45-55^oC).

The change in temperature results in a variance of output pressure of H_2 from the electrolyser. BPR's have a tendency to vary from the set point with varying temperature. Typically the set point pressure decreases with temperature decrease and vice-versa.

3.2.2. Electrolysis Single Cell Experimental Cell Setup

A single cell PEM Electrolysis test rig (Figure 3.28) was supplied from ITM Power plc. This consisted of two separate water/gas reservoirs and cell end plates from which an MEA (8 cm^2) can be placed into the cell for electrochemical characterisation.

The acrylic cell halves start off by having a piston each inserted. The meshes are placed on top of the piston with the sinter on top of that. The MEA is then sandwiched between the two sinters. The two half cells are then joined with screws and bolts (1 Nm force) to make the fully formed electrolysis cell ready for testing.

The cell is then connected to the 20 bar nitrogen supply to force the pistons towards one another and create a high pressure contact between the MEA, sinters and meshes. The water lines can be connected in the bottom and top of each cell half as shown in Figure 3.29. The electrical wires from the direct current power supply can then be connected to and the cell is fully assembled.

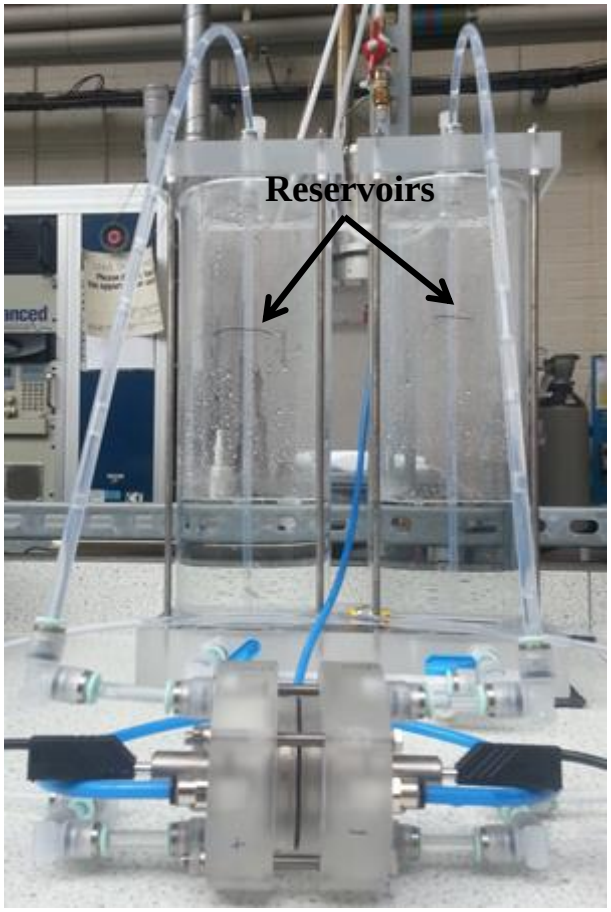

Figure 3.28: Single Cell PEM Electrolysis Test Rig

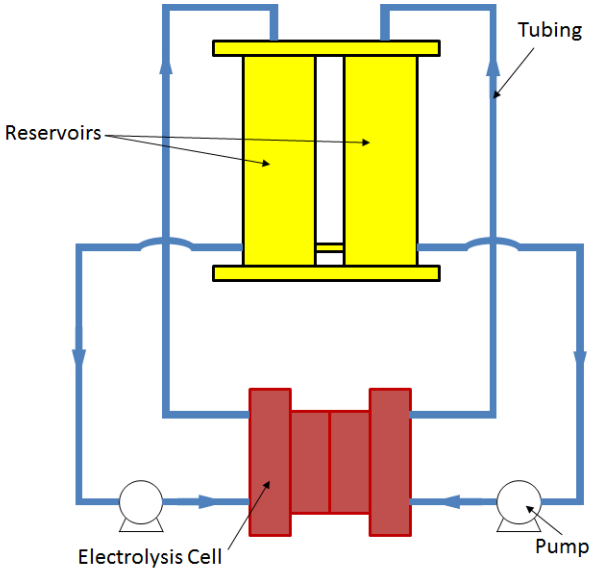

Figure 3.29: PEM Test Rig Schematic

The cell contained titanium meshes and sinter for both the anode and cathode. Once the cell was assembled the contact between the MEA, sinter and mesh was maintained by pistons subjected to 20 bar pressure of nitrogen gas (Figure 3.30).

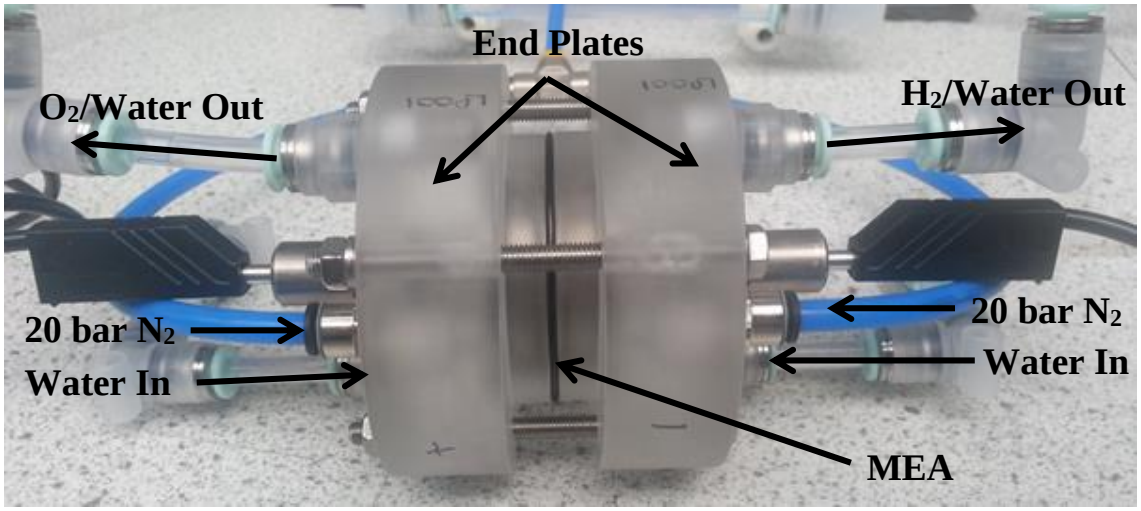

Figure 3.30: PEM Electrolysis Test Cell

3.2.2.1. Membranes

Nafion®117 – Supplied by ITM Power (Figure 3.31)

Perfluorosulfonic acid (PFSA) Nafion® membranes were supplied by ITM Power and are Nafion®117. The membranes are circular with a diameter of 50 mm (8 cm^2 active area). The catalysts on the membrane consisted of for the cathode, 3 mg/cm^2 platinum black and for the anode, 3 mg/cm^2 of a commercially sensitive ruthenium/iridium mix.

The CCMs are delivered in a dry state. They are activated ex-situ in Type I deionised water for 24 hours at 60^oC to humidify them fully.

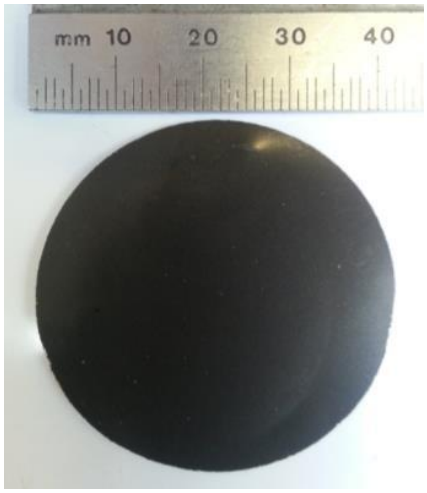

Figure 3.31: Nafion®117 based MEA (Cathode Face Up)

The standard electrolysis polarisation for the MEAs supplied is shown in Figure 3.32.

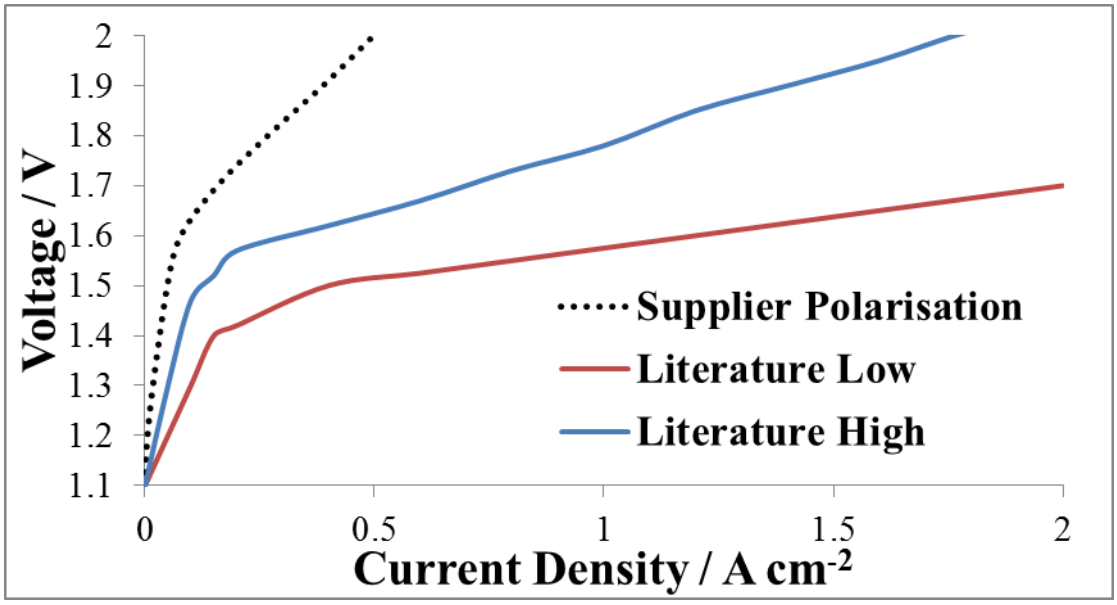

Figure 3.32: Supplier Standard Polarisation for MEAs supplied with literature data provided from [71]

This polarisation data supplied with the MEAs was compared with polarisations provided in literature [71]. It shows the standard polarisation is worse than the best polarisations in literature with a lower voltage which equivalent to more efficient electrolysis process. This is the result of the low catalyst loadings (affordable) on the MEA, which limits the efficiency of the electrolysis process.

Fumea® EF-10 – BWT FuMA-Tech GmbH (Figure 3.33)

Hydrocarbon (Fumea® EF-10) membranes were supplied by BWT FuMA-Tech GmbH. The membranes are circular (32 mm diameter) with an external gasket extending the overall dimensions to 50 mm in a square geometry. The catalysts consist of 0.5 mg/cm^2 platinum cathode & 2 mg/cm^2 iridium anode. The method of catalysts coating the membranes is proprietary of the supplier.

The CCM is delivered in a dry state. For optimum performance and minimal resistance, the CCM must be activated in-situ in the cell. The manufacturer states that the activation period takes 16-48 hours of net operation time according to the temperature and working current density of the cell.

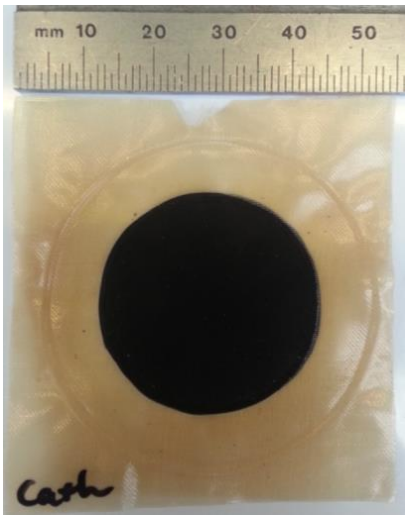

Figure 3.33: Fumea® EF-10 based MEA (Cathode Face Up)

The CCMs were activated with an applied potential across the cell of 2.0V at ambient temperature for a period of 24 hours. After 24 hours of operation the current density remains constant and therefore the CCM is now activated.

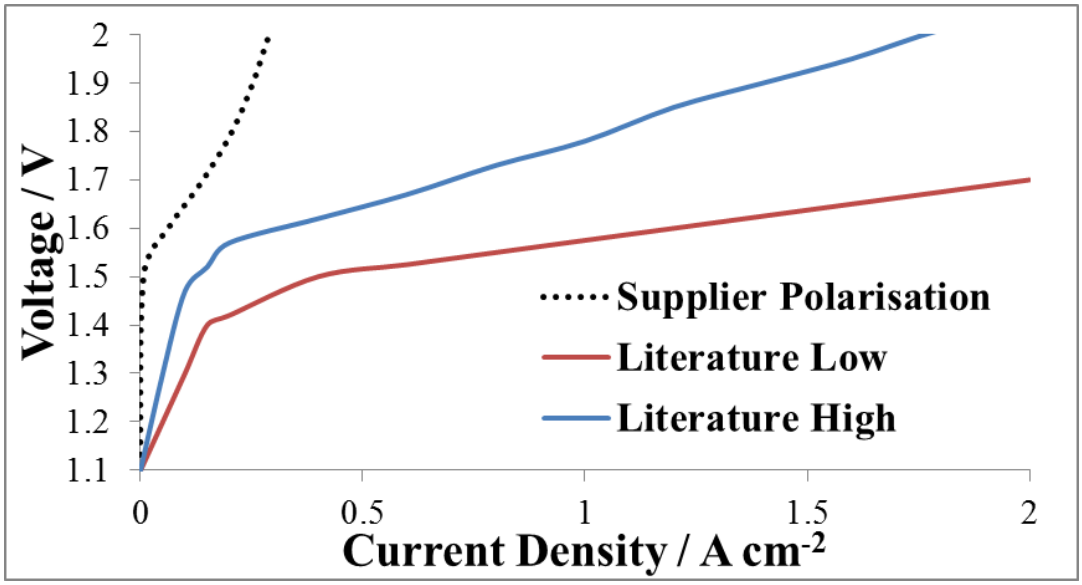

Figure 3.34: Supplier Standard Polarisation for MEAs supplied with literature data provided from [71]

The standard electrolysis polarisation for the MEAs supplied is shown in Figure 3.34. This polarisation data supplied with the MEAs was compared with polarisations provided in literature [71]. It shows the MEA performance is vastly inferior to others tested in literature. This is the result of the low catalyst loadings (affordable) on the MEA, which limits the efficiency of the electrolysis process.

3.3.2.2. Current Collectors

The current collectors were supplied by ITM Power plc and are platinum coated titanium sinter (Figure 3.35 (a)). The purpose of the current collector is to manage the flow of water to the electrocatalyst layer on the CCM, and the flow of evolved gases (hydrogen from the cathode catalyst layer and oxygen from the anode electrocatalyst layer) away

from the CCM to the gas outlets [24, 160, 161]. They are also there to maintain a distributed flow of electrical current through the electrolysis cell [28, 99].

Along with the sinter, platinum coated backing meshes were also provided with the cell (Figure 3.35 (b)). This aids the current distribution through the cell and the dispersion of bubbles from the sinter surface, thus creating a reduction in bubble overpotential.

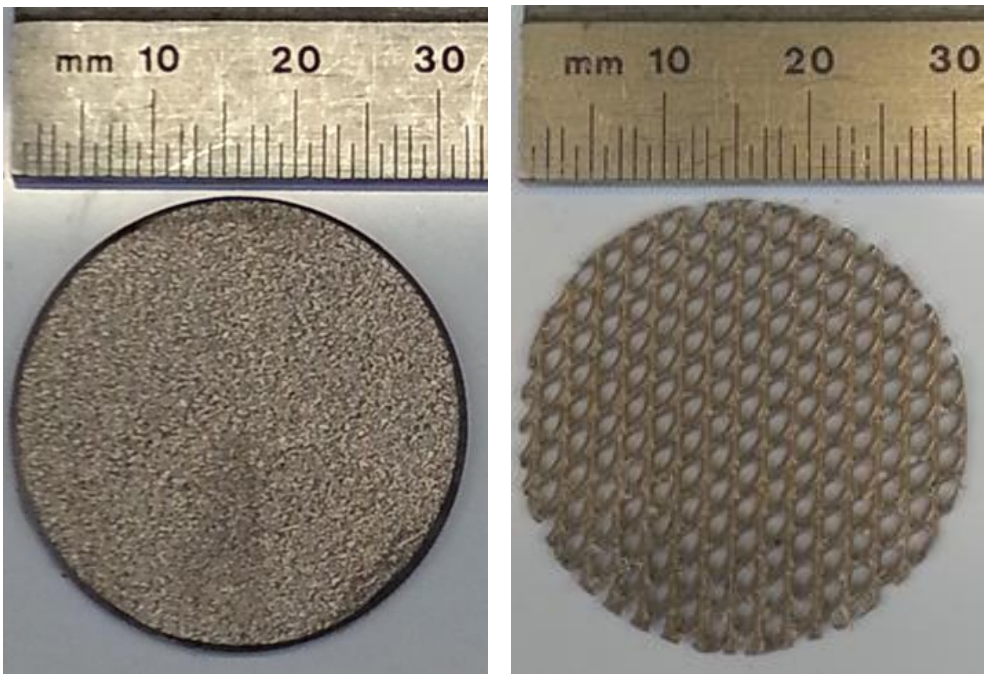

Figure 3.35: Platinum coated Titanium (a) Sinter and (b) Mesh

3.2.3. Ancillary Equipment

Peristaltic Pump

The flowrate of deionised water from the reservoirs to the electrolysis cell and back to the reservoir was controlled with a peristaltic pump (Cole-Parmer Masterflex L/S).

DC Power Supply

The potential was controlled and the subsequent current measured using a direct current power supply (Thurlby Thandar Instruments QPX1200SP model).

Millipore Rios-DI Pure Water Supply

One of the most important parameters for a PEM Electrolyser is the water supply. The water needs to be very pure de-ionised water. The water supply system selected was a Millipore RiOs-DI 3 Water Purification System. This produces Type 2 ASTM Water (10MΩ), which provides the substantially low conductivity of the water required.

Water Acidity & Conductivity Testing

Measurements were taken of the water conductivity and pH systematically to monitor the quality and purity of the de-ionised water. A Hanna Instruments Checker pH Tester (HI 98103) and a Hanna Instruments Pure Water Tester (HI 98308) were used to ensure the water in Electrolyser J was > pH 4 and the ion content in the water (conductivity) was keeping to the ASTM Type II Water. Monitoring these parameters will ensure the water entering the electrolyser is not damaging the membranes of the electrolyser which can be susceptible to long term failure with poor water quality.

Chapter 4

Characterisation & Analysis of Industrial Electrolysers

This research has been published in 4th European PEFC and H2 Forum Conference Proceedings, 2013, Chapter 10, Section A12, p17-27.

This chapter investigates the performance and efficiency of Electrolysers A - E through polarisation characterisation, gas productivity and engine performance when integrated with ICEs.

The companies that manufacture Electrolysers A – E state that when these are integrated into an ICE reductions in exhaust emissions of up to 80% and improvements in fuel economy of up to 50% are achievable [162], which is unfathomable. These values quoted do not take into account external influences on engine behaviour (driver behaviour, engine load variation), which could contribute to an increase in fuel economy. Subsequently, these electrolysers are tested on a static engine, which removes these variables so the change in engine performance is the result of the HHO addition only.

Each of the electrolysers tested herein are connected to a 12V power supply (from the engine alternator in real world application). To verify claims of engine efficiency increase and exhaust emission reduction, testing with take place at 12V also. This 12V applied to the unipolar alkaline electrolysers will result in high degradation and energy loss, but the external suppliers believe is necessary to produce sufficient yields of HHO gas. This chapter will analyse these claims.

This chapter will characterise these commercial electrolysers and then test them on a static engine to quantify any reduction in fuel consumption and exhaust emissions.

4.1. Electrochemical Characterisation

All four electrolysers underwent electrochemical analysis to characterise current flow, gas productivity, and system efficiencies. All alkaline electrolyser experiments were completed using 0.1M KOH solution.

4.1.1. Polarisation Analysis

The electrochemical characterisation analysis for each electrolyser was completed and subsequent current densities are presented in Figure 4.1.

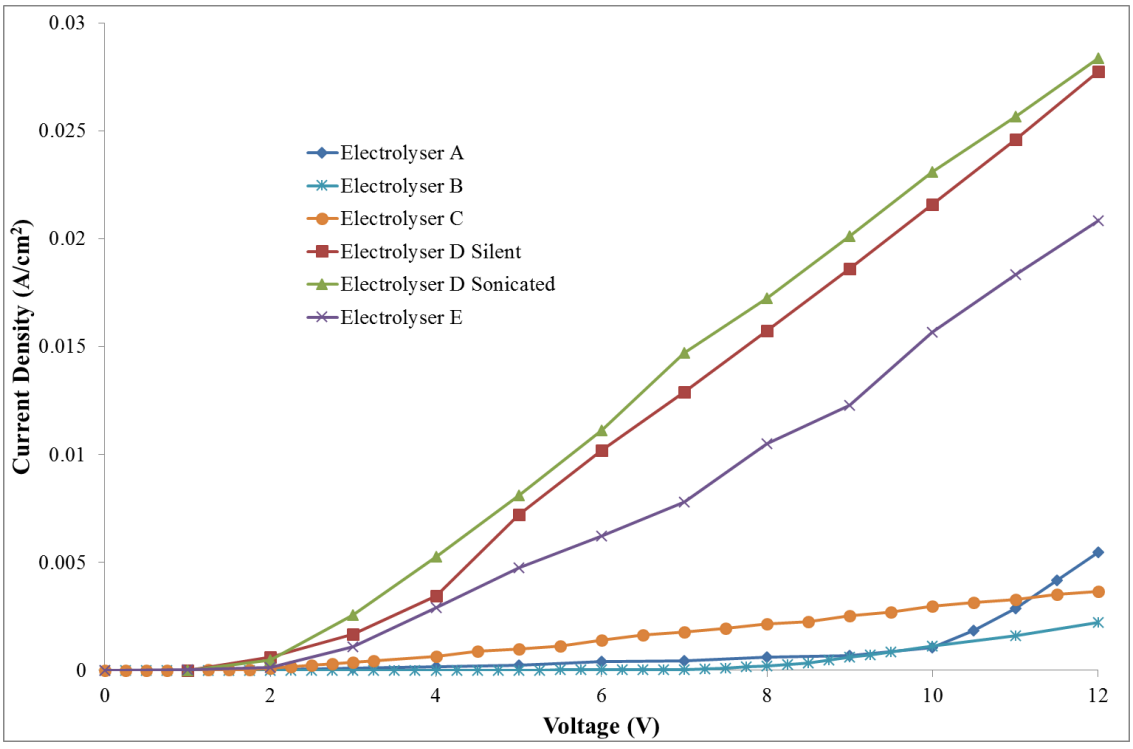

Figure 4.1: Polarisation for all Electrolysers at 25ºC, 0.1V scan rate, 0.1M KOH, 1 atm pressure

Figure 4.1 shows both modes of the Electrolyser D demonstrates the highest polarisation as a function of electrode surface area. This is a result of the very small electrode surface area and the use of carbon electrodes, which the other electrolysers do not have. Electrolyser E exhibits good electrochemical performance, achieving 0.02 A/cm^2 at 12V operating potential, when compared to Electrolysers A-C. Electrolysers A, B & C exhibit poor current densities with increasing potentials which is the result of low current flows (high overpotentials) and large surface areas.

4.1.2. Gas Productivity

As well as analysing the electrochemical performance, the gas evolution rate must be analysed as it is vital performance parameter of an electrolyser. Figure 4.2 shows the gas productivity rates as a function of cell voltage.

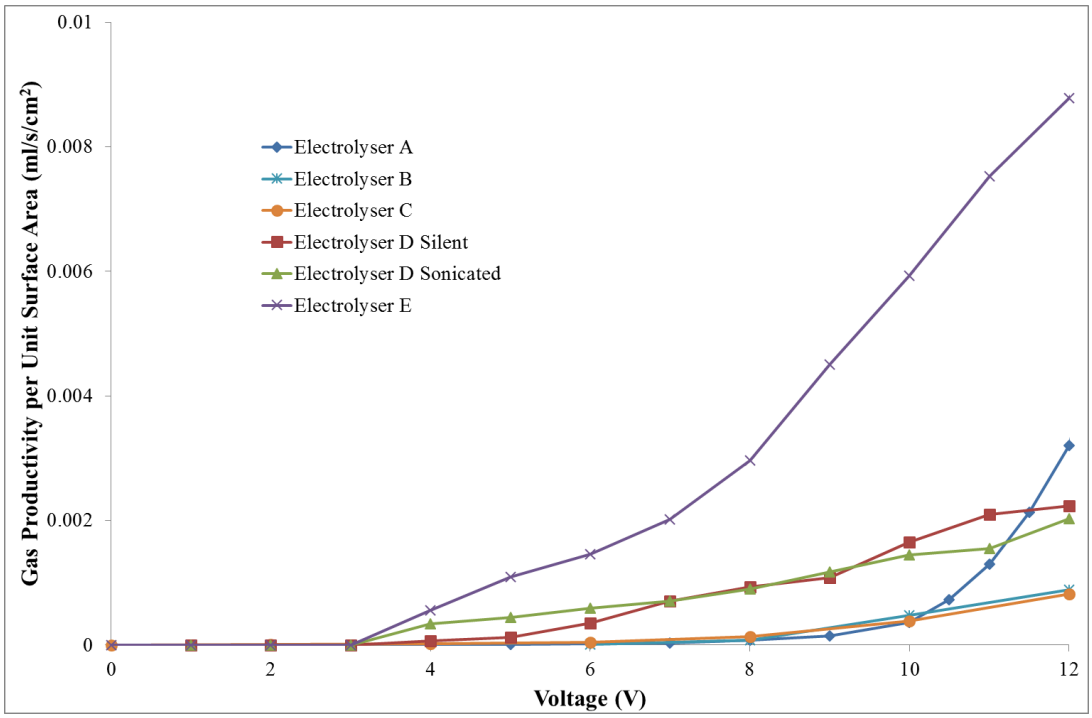

Figure 4.2: Gas Productivity Curves for all Electrolysers at 25°C, 0.1V scan rate, 0.1M KOH, 1 atm pressure

Figure 4.2 shows Electrolyser E has the highest gas production rate as a function of cell potential when compared to the other electrolysers. This is expected to be the result of either reduced bubble overpotential from increased electrolyte flow through the cell removing bubbles from the electrode surfaces or improved build quality of the electrolyser. Both Electrolysers B & C have low gas productivity rates as a function of surface area and is likely to be the result of increased electrode spacing (ohmic overpotential), since it's the largest electrolyser of all. This cannot be confirmed though.

Electrolyser A only begins to exhibit gas production at higher potentials and is reflected by the low electrochemical performance, as shown in Figure 4.1, up to 8 V. Electrolyser D exhibits very low quantities of gas evolution, which is a direct result of the very small electrode surface area, in spite of its very impressive electrochemical performance as shown in Figure 4.1.

4.1.3. Faradays 1st Law of Electrolysis

The electrochemical performance and the gas productivity of the electrolysers can be compared and analysed as a function of each other, which is Faraday's First Law of Electrolysis. Figure 4.3 shows the data for each electrolyser tested.

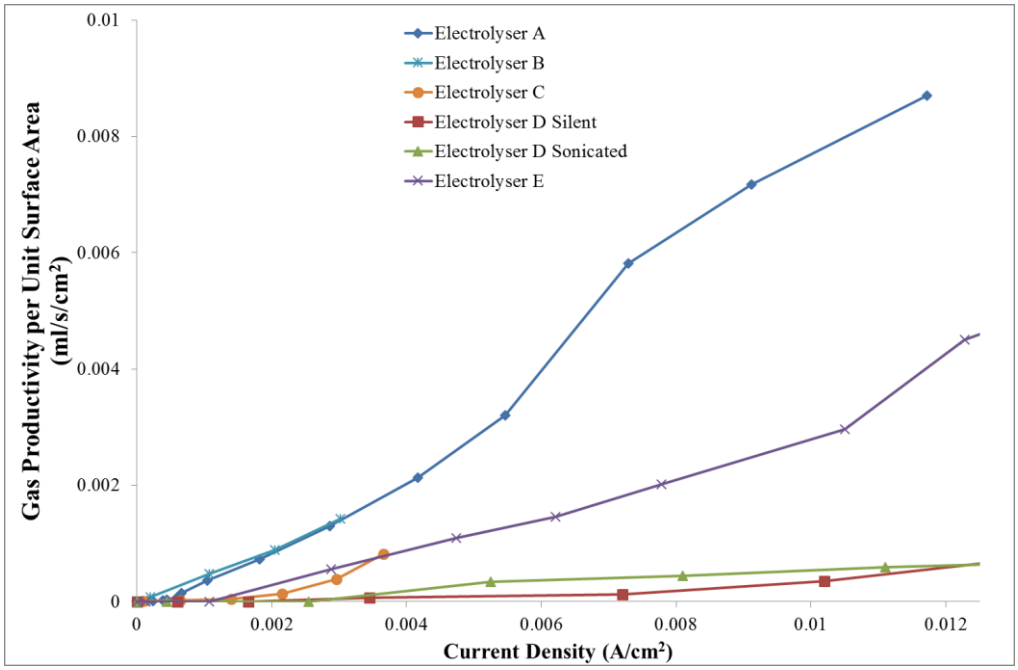

Figure 4.3: Faraday Plots for all Electrolysers

Figure 4.3 shows Electrolyser A demonstrates the highest gas output per unit surface area as a function of current flow in the electrolysers. This is a desirable trend in electrolysers, as it shows a high gas yield from a low electrical energy input. Electrolysers B, C & E exhibit slightly lower rates of gas evolution for current flow, and Electrolyser D is the lowest rate of them all (<0.001 ml/s/cm^2) so has poor gas productivity per unit surface area as a function of electrical current flow per unit electrode surface area.

4.1.4. Electrical Efficiency

The electrical efficiency of the electrolysers was calculated using Eq. 3.1. Figure 4.4 shows these efficiencies for each electrolyser as function of cell potential.

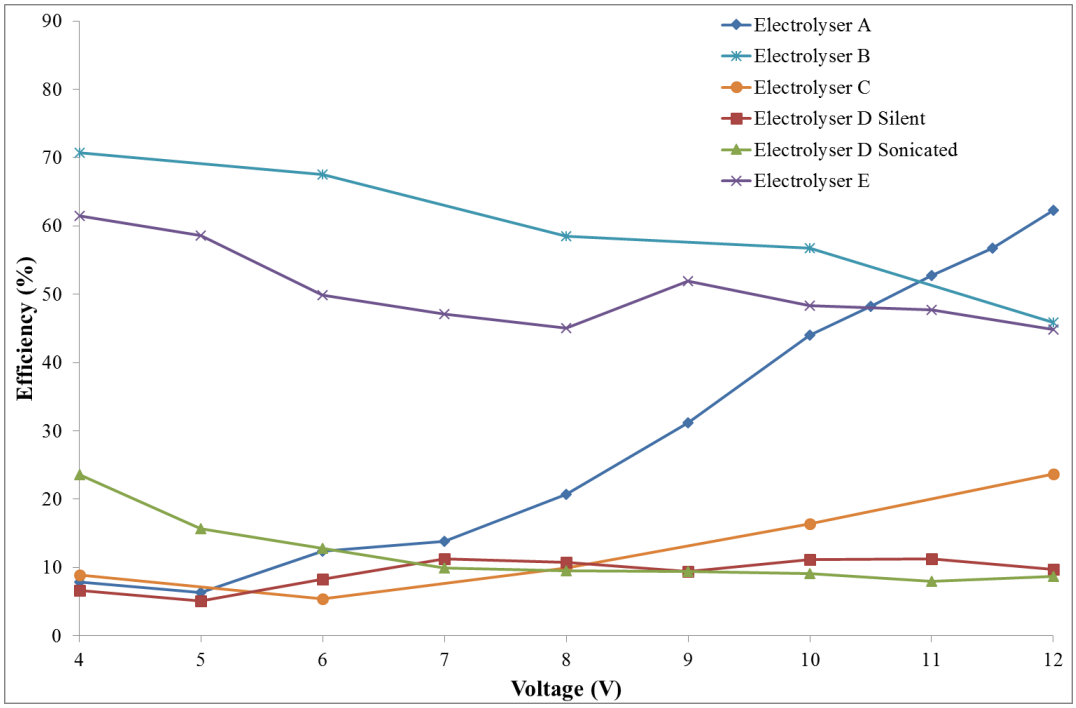

Figure 4.4: Electrical Efficiency Curves for Electrolysers at 25ºC, 0.1V scan rate, 0.1M KOH, 1 atm pressure

Figure 4.4 shows Electrolyser B exhibits the best efficiency values for an electrolyser when compared to the others. It exhibits textbook electrical electrolyser efficiency behaviour as a function of voltage [22, 27, 45, 65, 163], along with Electrolyser E electrolyser which has slightly lower efficiency values. Electrolyser D shows poor efficiency (< 10%) in both modes, which is the result of low gas evolution rates per unit surface area from the electrolyser at 12 V potential.

Electrolyser A exhibits uncharacteristic behaviour with an increasing electrical efficiency as a function of cell voltage, achieving an efficiency of approx. 65% at 12 V. The same can be said for Electrolyser C, except this only increases as high as approx. 20% efficiency, but goes against the expectant trend of a decreasing electrical efficiency with

increasing cell potentials. Literature has shown efficiencies of commercial electrolysers as 50-80% [25, 27, 45-47, 49, 61, 64, 163, 164], which only Electrolysers B & E achieve. The performance of the remaining commercial electrolysers is not up to this standard.

4.2. Engine Testing

Electrolysers C & E underwent testing on an ICE to quantify the improvements in performance and reduction in exhaust emissions as contractually obliged by the project sponsors. Testing these two electrolysers under identical operating conditions (12 V fixed potential, 0.1M KOH electrolyte solution) will show the difference in effect on the ICE performance as a result of its introduction the combustion system. All research experiments on the ICE were operated for 30 minutes before measurements or until a constant engine power and emissions reached a constant value for 15 minutes.

4.2.1. Electrolyser C

Electrolyser C was connected to the ICE as shown in Figure 3.11. The operating parameters for this engine performance analysis are shown in Table 4.1.

Table 4.1: Engine Operating Parameters for Electrolyser C Engine Testing

Engine speed (rpm)	Imep (bar)	Air Intake flow rate (l/min)
1500	3	517

4.2.1.1. Instability without the water trap

Water (moisture) is undesirable in an ICE as it will decrease the engine temperature and subsequently reduce the engine efficiency and exhaust emissions in steady state

conditions. As shown in Figure 4.5 it is believed small quantities of water is carried into the ICE from the electrolysis product gas, which has an adverse effect on the oxidation of NO to NO_2. The adverse effect of water in ICEs has been well documented in literature and the essential nature to remove has been recorded [142, 143, 145, 146, 165, 166].

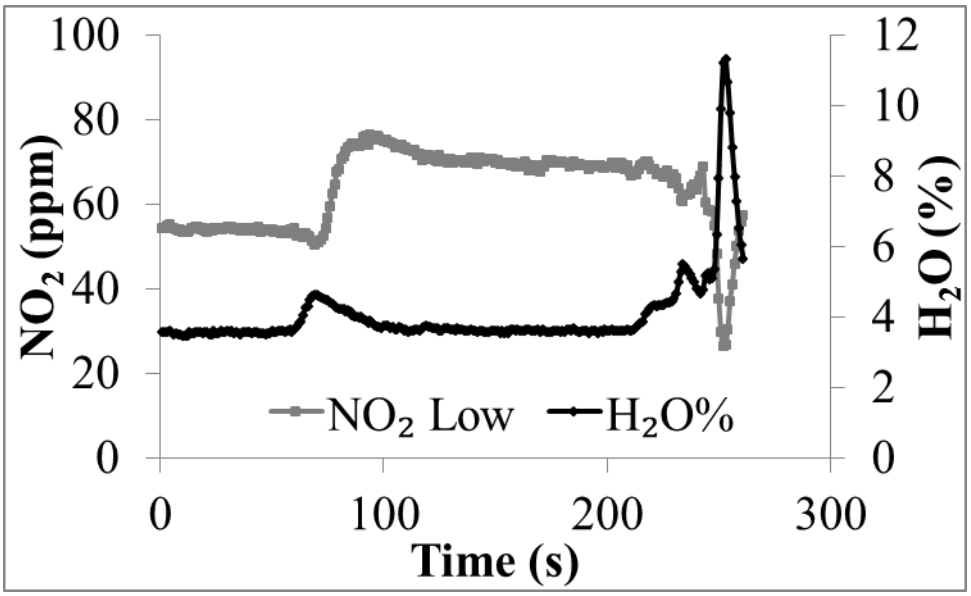

Figure 4.5: Engine H_2O Instability without Water Trap

The electrolyser was activated 180 seconds into the experiment. Within a minute of this, there is a visible increase in H_2O content in the exhaust emissions, which further increases to 11.5 mass% in the exhaust. As a result a water trap was added between the electrolyser gas outlet and the air intake pipe. This water trap as shown in Figure 4.6 collects moisture from any gases that pass through it and the results from the identical operation of the engine as shown in Figure 4.7.

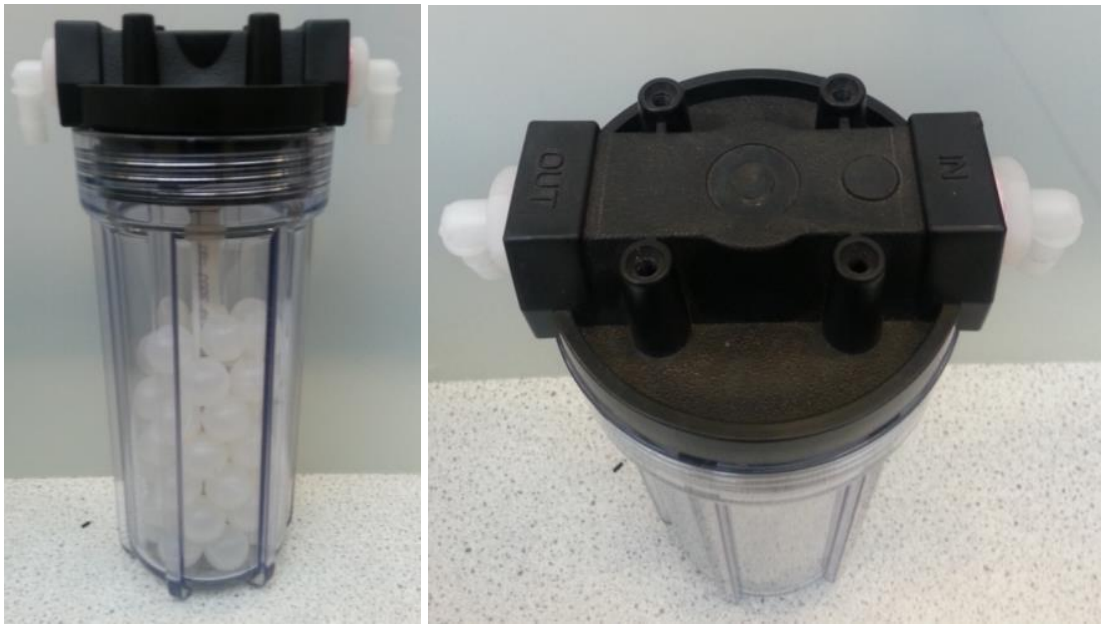

Figure 4.6: Image of commercially supplied water trap made up of Silica spheres

The electrolyser was again activated at 3 minutes into the experiment and the NO_2 emissions increase as expected from the oxidation of NO and NO_x to NO_2 (due to added oxygen from HHO in the engine).

This experiment with the water trap integrated keeps the H_2O content fixed at 4 mass% through 25 minutes of operation, thus proving the water trap is eliminating water vapour from reaching the engine from the electrolyser. The water trap after the experiment is shown in Figure 4.8.

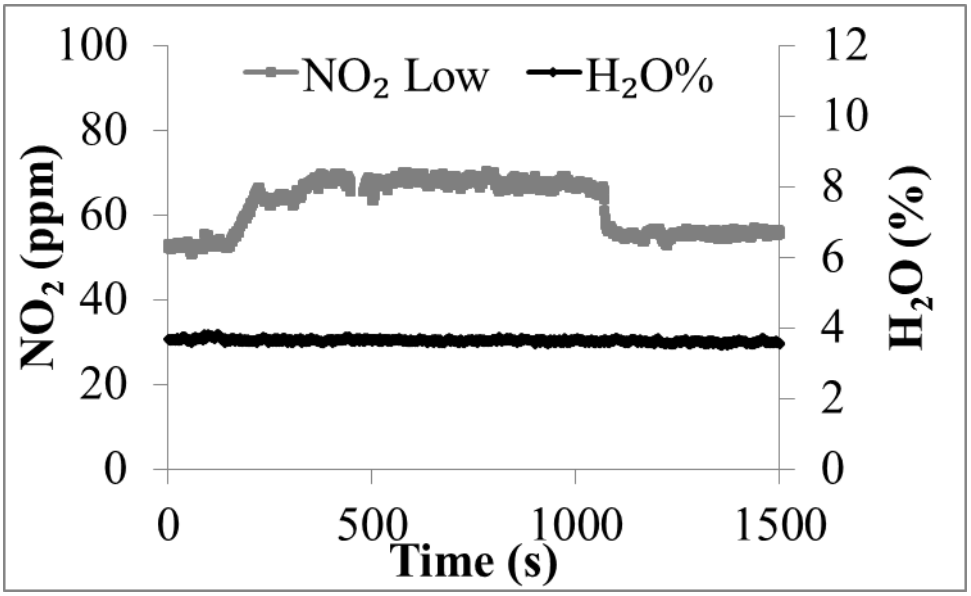

Figure 4.7: Engine H_2O Levels with Water Trap

Figure 4.8: Water Trap after Engine Integration with Red Line marking Water Level

4.2.1.2. Combustion Properties

Figure 4.9 shows the variance in cylinder pressure and rate of heat release with the electrolyser in off and on mode. This is an important characteristic of an ICE because it will show any variation in liquid fuel replacement (fuel input reductions), with the only variable in the system being the quantity of HHO injected into the ICE.

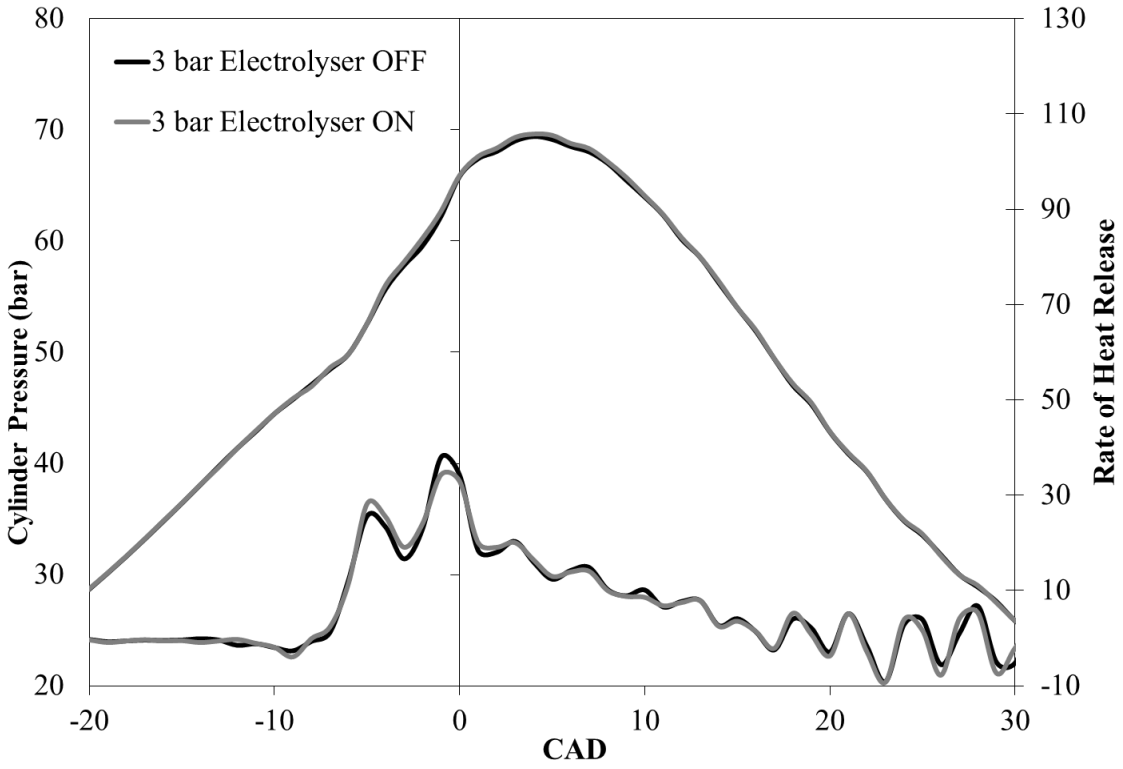

Figure 4.9: Liquid Fuel Replacement for Electrolyser C at 3 bar pressure and 1500 rpm

Figure 4.9 shows no significant difference on pressure and rate of heat release in the ICE through varying the crankshaft angle degree (CAD). This shows the introduction of an electrolyser to the system is having no effect on the combustion properties of the ICE.

4.2.1.3. Brake thermal efficiency

Brake thermal efficiency is defined as brake power of a heat engine as a function of the thermal input from the fuel. It is used to evaluate how well an engine converts the heat from a fuel to mechanical energy. Figure 4.10 shows the variance in brake thermal efficiency with the electrolyser in off and on mode.

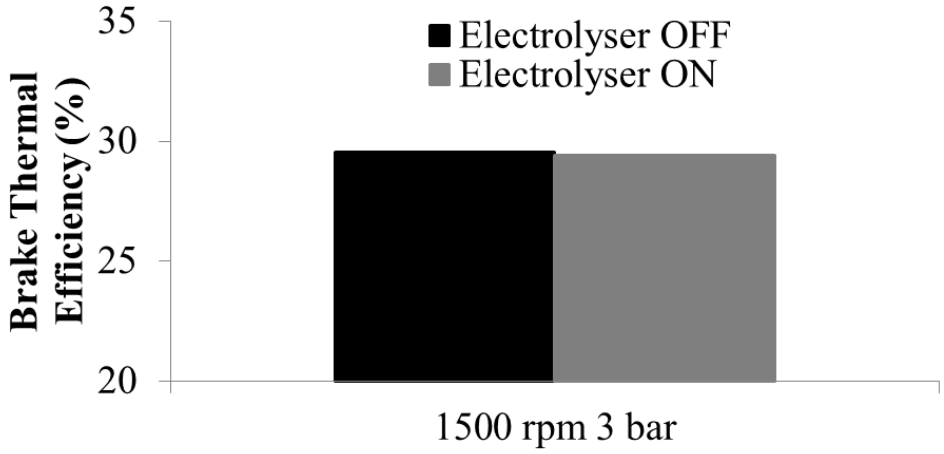

Figure 4.10: Brake Thermal Efficiency for Electrolyser C

Figure 4.10 shows Electrolyser C is having negligible effect on the brake thermal efficiency, which is mimics the data shows for liquid fuel replacement in the ICE.

4.2.1.4. CO_2 and H_2O emissions

The exhaust emissions of CO_2 and H_2O were analysed for the standard engine setup and with the electrolyser integration. The percentage composition for both of these emissions is shown in Figure 4.11. The results show no significant effect on H_2O and CO_2 emissions as a result of adding the electrolyser into the system.

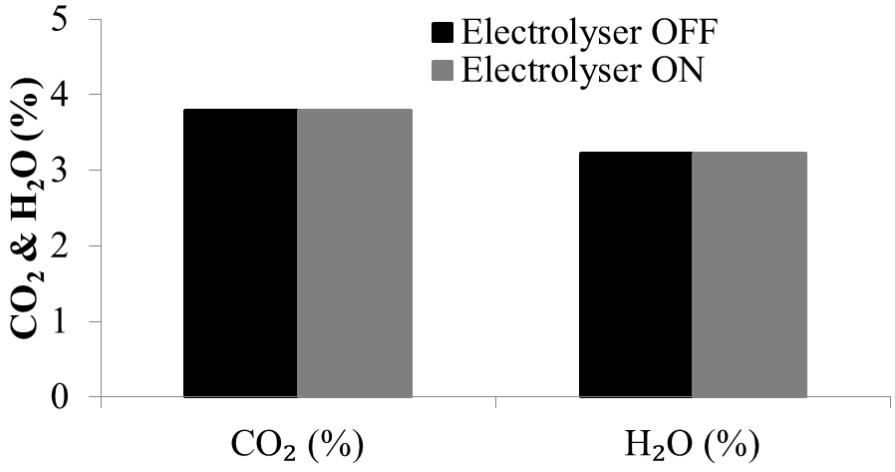

Figure 4.11: CO_2 & H_2O Engine Emissions for Electrolyser C

4.2.1.5. NO, NO_2 and NO_x emissions

The nitrous oxide exhaust emissions are a suitable indicator of the presence of hydrogen in the combustion process. When hydrogen is present, it is expected to show a drop in NO emissions and an increase in NO_2 emissions due to the high flammablility of the combustion process which results in a more complete combustion of NO to NO_2. Figure 4.12 shows the emissions changes for the electrolyser in off and on mode.

Figure 4.12 shows a small decrease in NO emissions when the electrolyser is operational, which shows a small quantity of hydrogen is present in the combustion chamber of the ICE. This is further evident by the small increase NO_2 emissions when the electrolyser is on. The overall NO_x exhaust emissions have no change with the two variations in NO and NO_2 emissions cancelling each other out.

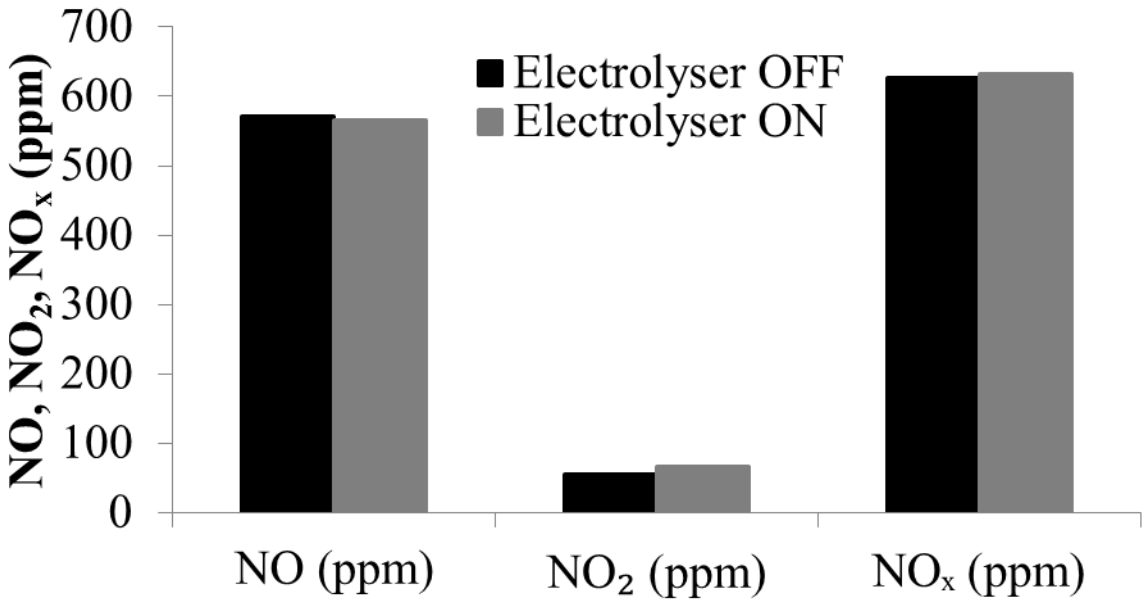

Figure 4.12: NO, NO_2 & NO_x Engine Emissions for Electrolyser C

4.2.1.5. THC and CO emissions

The total unburnt hydrocarbon (THC) and CO emissions were measured and with hydrogen present in the combustion chamber, the higher combustability of the fuel/air mixture should result in less unburnt hydrocarbon. Figure 4.13 shows the variance in these exhaust emissions for the two experimental set ups.

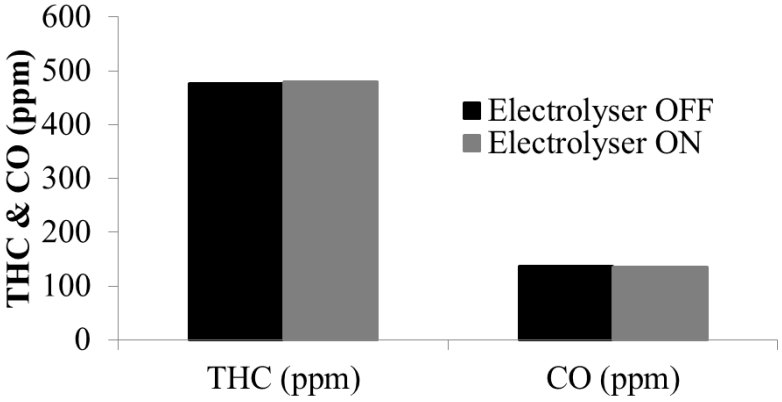

Figure 4.13: THC & CO Engine Emissions for Electrolyser C

Figure 4.13 shows no significant effect on THC between the two sets of data and the CO slightly decreases (around 2%) with the implementation of an electrolyser to an engine.

4.2.1.6. Conclusions

The engine testing results from integration of Electrolyser C shows negligable of effect on the engine performance and exhaust emissions. This is a result of low HHO flowrate from the electrolyser as shown in Figure 4.2 and is much lower to those found in literature [137, 138, 162]. Electrolyser E will now be tested on an ICE, because as shown in Section 4.1.2 it has a higher gas ouput than Electrolyser C.

4.2.2. Electrolyser E

Electrolyser E was connected to the ICE as shown in Figure 3.11. The operating parameters for this engine performance analysis are shown in Table 4.2. Two engine speeds and two Imeps were tested for this electrolyser. All experiments were carried out at 12 V fixed potential across the electrolyser and used 0.1M KOH electrolyte solution.

Table 4.2: Engine Operating Parameters for Electrolyser E Testing

Engine speed (rpm)	Imep (bar)	Intake flow rate (l/min)
1200	3	402
1200	5	402
1500	3	517
1500	5	517

4.2.2.1. Combustion

Figure 4.14 shows the variance in cylinder pressure and rate of heat release with the electrolyser in off and on mode for (a) 1200 rpm and (b) 1500 rpm. Experiments have

been completed on Electrolyser E with a 4 V potential supply (equivalent to 0.06 LPM HHO flowrate) and a 12 V potential supply (equivalent to 0.2 LPM HHO flowrate).

Figure 4.14 shows a maximum 2.25% saving for Electrolyser E using a 12V voltage supply compared to 0.5% fuel saving when the electrolyser is operated at 4V supply. This shows the introduction of an electrolyser to the system is having a small effect on the combustion properties of the ICE.

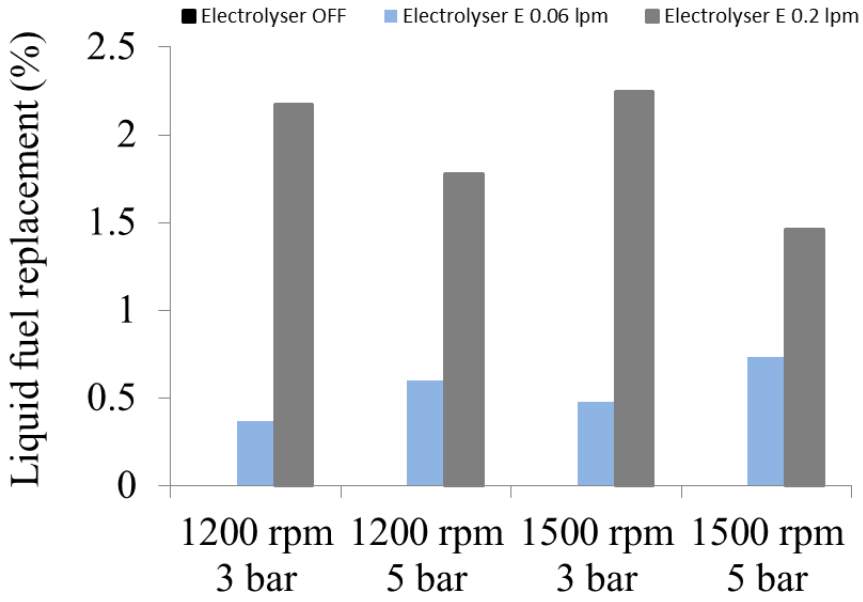

Figure 4.14: Liquid Fuel Replacement Analysis for Electrolyser E

4.2.2.2. Brake thermal efficiency

Figure 4.15 shows the variance in brake thermal efficiency with the electrolyser in off and on mode for both engine speeds and Imep. It shows between 0.6-1% increase for break thermal efficiency when the electrolyser is activated for both engine speeds and

Imep. At low load, there is no improvement in thermal efficiency and at high load there is a slight improvement (less than 1%).

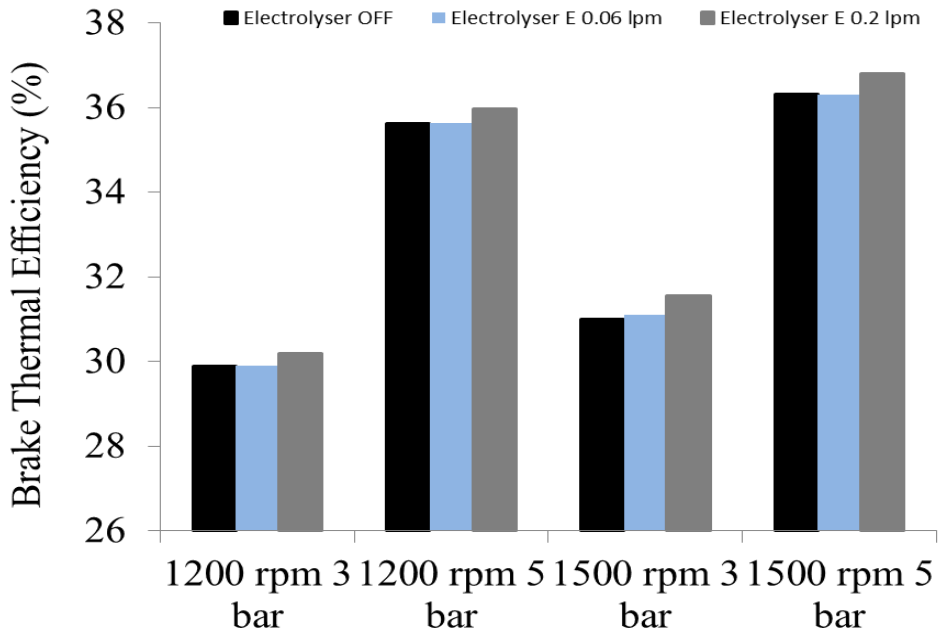

Figure 4.15: Brake Thermal Efficiency for Electrolyser E

4.2.2.3. CO_2 and H_2O emissions

The exhaust emissions of CO_2 and H_2O were analysed for the standard engine setup and with the electrolyser integration. The percentage composition for both of these emissions is shown in Figure 4.17 for all engine settings.

Figure 4.16 shows CO_2 slightly decreases ($\leq$ 2% for all engine conditions). This is much smaller quantity of CO_2 exhaust emission savings as currently reported in industry. Figure 4.17 shows no significant effect on H_2O for all engine speeds and Imep.

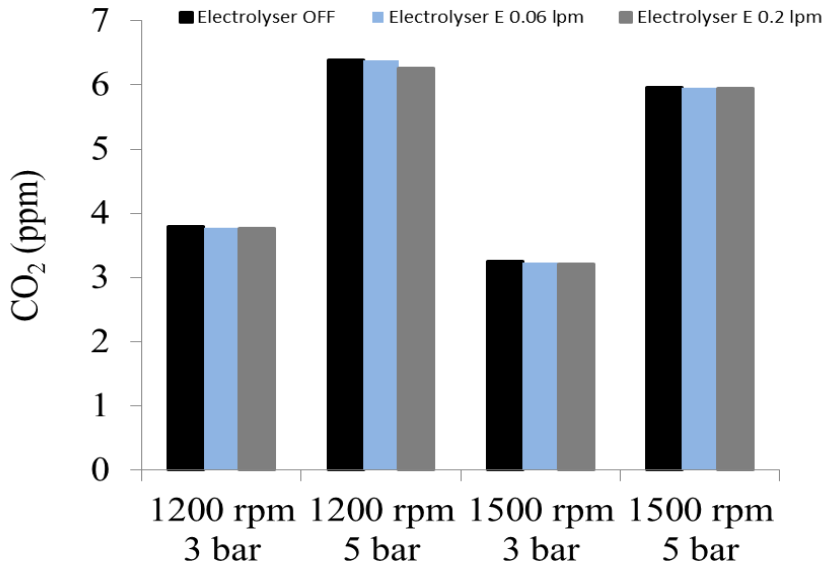

Figure 4.16: CO_2 Engine Emissions for Electrolyser E

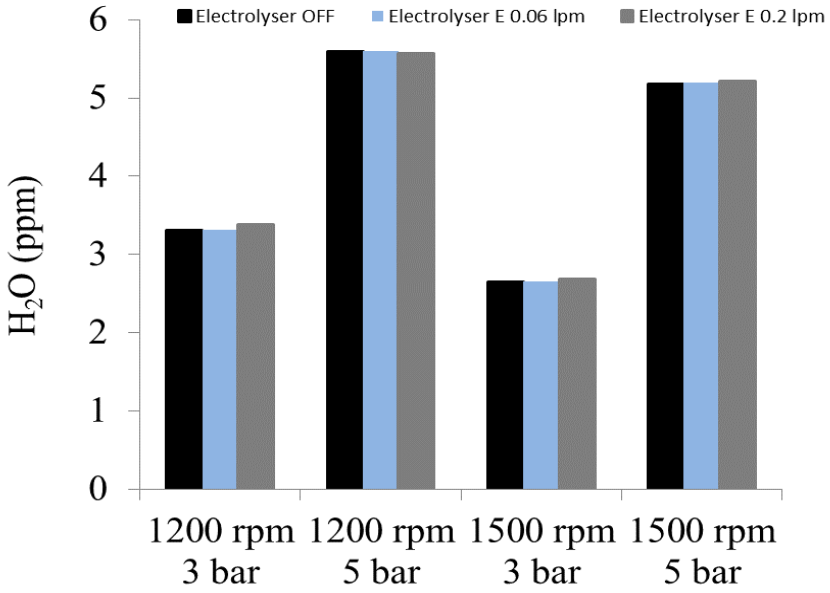

Figure 4.17: H_2O Engine Emissions for Electrolyser E

4.2.2.4. NO, NO_2 and NO_x emissions

Figure 4.18 shows the NO, NO_2 and NO_x emissions changes for the electrolyser in off and on mode for all varying engine operating parameters.

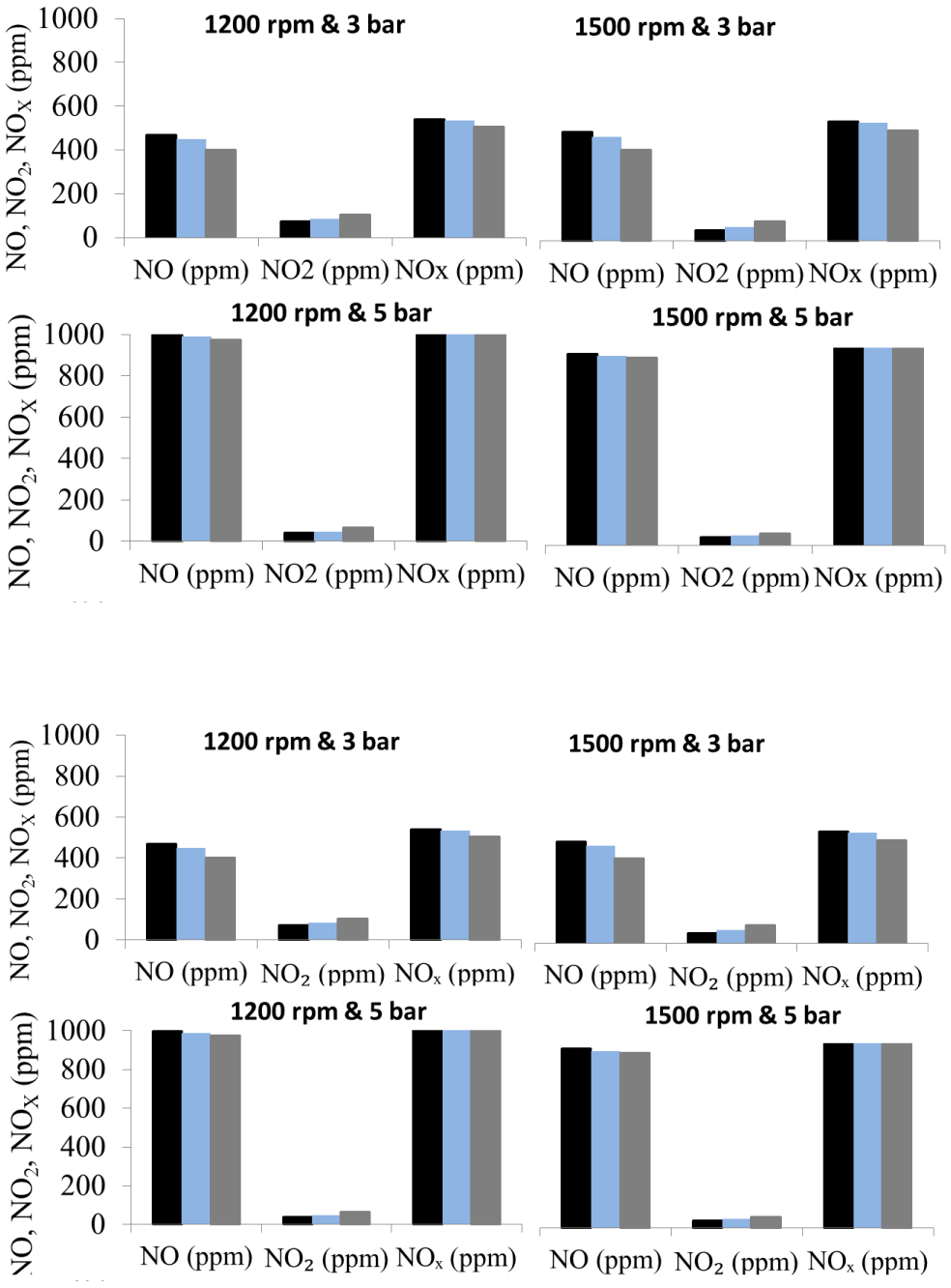

Figure 4.18: NO, NO_2 & NO_x Engine Emissions for Electrolyser E

Figure 4.18 shows that NO decreases and NO_2 increases for all engine conditions. These changes however have no net effect on NO_x emissions (no penalty on NO_x emissions). These reductions in NO and increase in NO_2 emissions are greater than for Electrolyser C, which is to be expected from the higher input of HHO gas in the air intake pipe from Electrolyser E.

4.2.2.5. THC and CO emissions

Figure 4.19 shows the variance in THC and CO exhaust emissions for the electrolyser off and on modes as well as the four different engine settings.

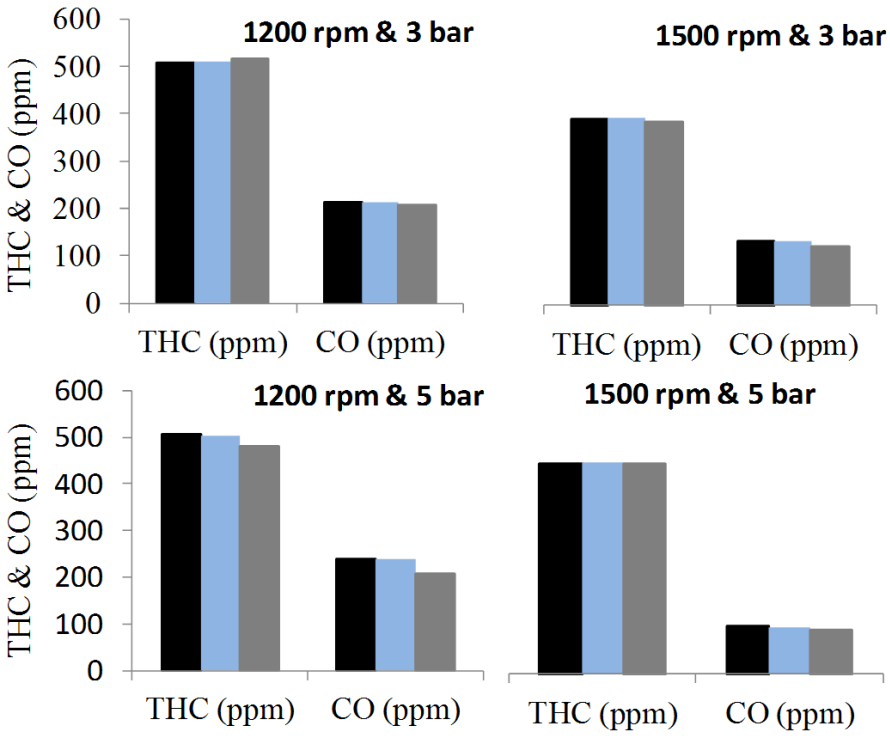

Figure 4.19: THC & CO Engine Emissions for Electrolyser E

The results in Figure 4.19 show no significant effect on THC content in the exhaust emissions from the introduction of Electrolyser E to the system. The CO emissions

slightly decrease (up to 5% for all engine conditions) with the introduction of HHO gas into the air intake pipe. This is the result of a higher oxygen content in the combustion chamber (from the HHO) oxidising CO to CO_2.

4.2.2.6. Engine Testing Conclusions

The results in Section 4.2.2.3 & 4.2.2.5 show very small reductions in CO and CO_2 emissions for Electrolyser E, but the reductions are greater than that seen with Electrolyser C (Section 4.2.1.3 & 4.2.1.5) in the same experimental procedure. The greater decrease in NO emissions in Electrolyser E than Electrolyser C is further evidence that more hydrogen is present during the combustion process and therefore larger HHO productivity rates are needed to reduce these gaseous exhaust emissions further.

4.3. Chapter Conclusions

The electrochemical performance of 4 different commercial electrolysers was analysed. The analysis of these electrolysers has found low efficiencies and subsequent low gas production rates from every electrolyser tested. These are summarised in Table 4.3 for a 12V input which is consistant with a engine alternator.

Table 4.3: Summary of Electrolyser Performance

Electrolyser	Current Density @ 12V (A/cm^2)	Gas Flowrate @ 12V (ml/s)	Efficiency @ 12V (%)
A	0.006	1.2	68
B	0.002	4.0	50
C	0.0035	3.9	25
D	0.028	0	10
E	0.02	5.2	48

Electrolysers C & E were tested on a static ICE and showed no change in efficiency and exhaust emissions. This is the result of the low HHO gas flowrates generated by the commercial electrolysers characterised. A higher flowrate of HHO gas into the ICE is required to observe a change in engine characteristics.

Electrolyser E was redesigned, built and characterised electrochemically before analysis on an ICE to quantify any improvement in engine efficiency and exhaust emissions.

Chapter 5

Alkaline Electrolyser Redesign, Construction & Testing

This research has been published in International Journal of Low-Carbon Technologies (2013). DOI: 10.1093/ijlct/ctt034

The aim of this project (continuing on from Chapter 4) was to improve the reductions in exhaust emissions. This can be achieved, as shown in literature, through the application of a higher flowrate of HHO gas. The end user has Electrolyser E to be utilised on a static engine on a wood-chipper, used 40 hours a week, which is supplied with a 12 V potential from the engine alternator.

As shown in literature, flowrates of > 20 LPM of hydrogen into diesel combustion engines have utilised to achieve reductions in NOx emissions by approximately 25%. The fixed size and dimensions of the electrolyser designed herein, as well as the fixed 12 V potential input from the engine alternator limit the design parameters for this.

The expensive cost and limited timeframe for engine testing allowed only testing of the Electrolysers C and E in the first instance, and then finally for Electrolyser I. In ideal circumstances (with time and cost not a factor) engine testing would have been conducted on bottled hydrogen and oxygen gas at varying flowrates to determine the peak requirement to maximise reduction in engine emissions.

This chapter redesigns Electrolyser E to an identical footprint and minimal economic cost, whilst increasing the production rate of HHO gas at 12V operation. Firstly areas of potential electrochemical improvement in the electrolyser need to be identified, which includes the material, geometry and spacing of the electrodes. The purpose of this study is to identify sources of resistance in the electrolyser which can be reduced/eradicated,

and consequently increase the electrochemical performance. The re-engineering of this electrolyser should result in increased reaction kinetics and high HHO gas yield for injection into an ICE.

Once an improvement in electrochemical performance has been found in a single cell, an electrolyser stack will be constructed with the number of cells maximised to fit in the desired footprint and at reasonable economic cost. This prototype electrolyser will then be characterised electrochemically and be tested on an ICE under identical conditions as shown in Section 4.2.

The results of the engine testing will be directly compared to those shown in Section 4.2.2 with varying flowrates and with synthetic/baseline (bottled) hydrogen gas. This will identify the necessity of oxygen (which already exists in the air intake flow) in the HHO gas, and whether direct addition of hydrogen into the air intake pipe is more worthwhile in terms of reducing the exhaust emissions from the ICE.

5.1. Materials Development

5.1.1. Electrodes

The activation overpotential is a source of resistance in electrolysis from the need for the energy input requirement to be greater than the activation energy on the electrode surface. The lower this activation energy the more efficient the process is. As a result research on

varying materials was conducted to see which metals have the lowest activation overpotential. There are two methods for characterising this activation overpotential.

The first method uses linear sweep voltammetry (LSV). This involves the use of three electrodes (working, counter and reference electrode). The working electrode is the material of choice for which we are trying to calculate the activation overpotential. The counter electrode, consisting of platinum produces the opposite charge to the working electrode, thus enabling a current to flow between them. The reference electrode is a stable electrode consisting of a material that has a well-known electrode potential. This is shown in Figure 5.1.

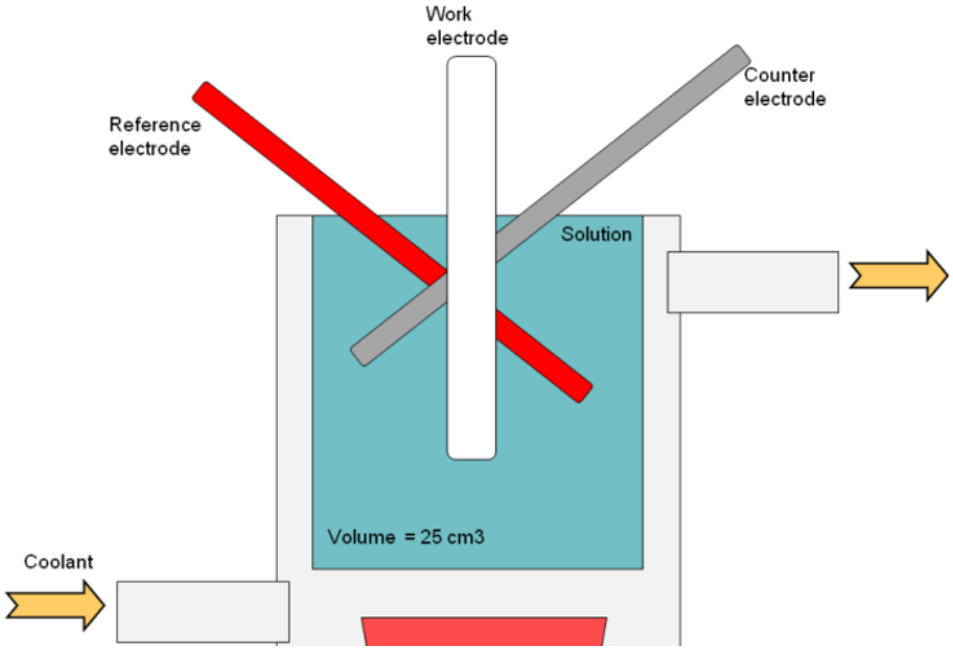

Figure 5.1: Equipment Setup for Linear Sweep Voltammetry (LSV)

The experiments would be carried out in 25 cm^3 0.1M KOH solution, and for a fixed current density (since overpotential varies with current density), the activation overpotential can be characterised for that electrode material.

A second method for characterising activation overpotential is to calculate the decomposition potential for each electrode material in 0.1M KOH solution. This is much more economical and practical for the project and an example is shown in Figure 5.2.

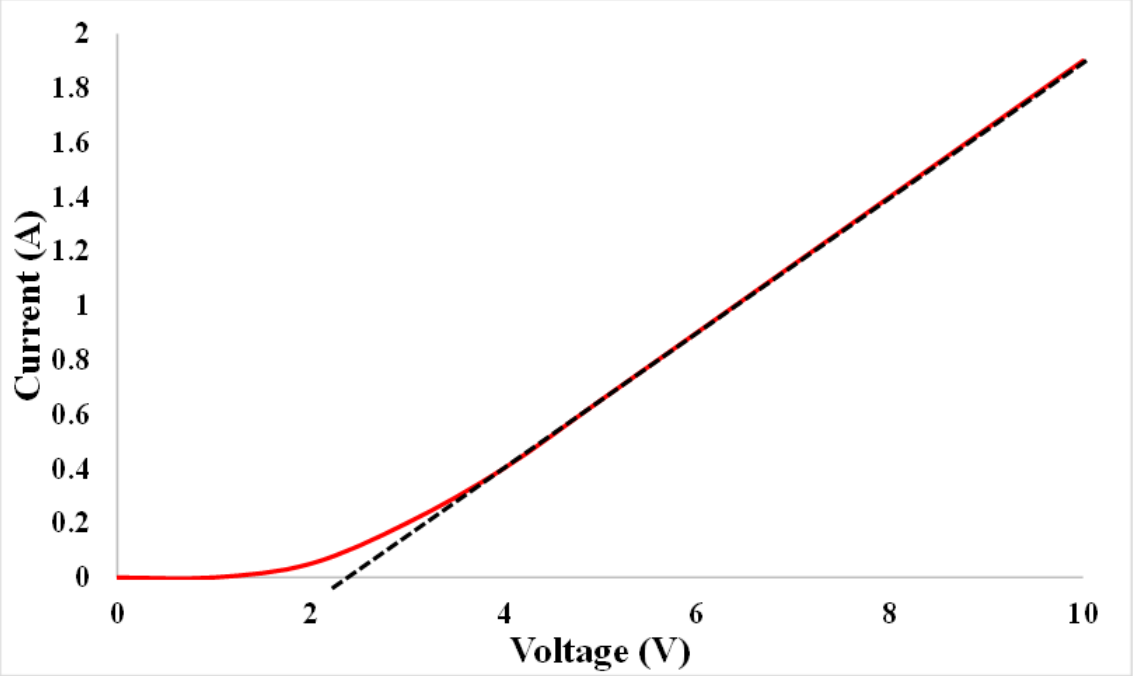

Figure 5.2: Schematic for measurement of decomposition potential from polarisation curve for various electrode materials

The value where the gradient intersects the x axis can be subtracted from the OCV (1.23V) to give the resultant overpotential. The separation distance between the two electrodes will be kept constant at 10 mm, therefore keeping the value of ohmic

overpotential constant throughout all the experiments. A reference point of platinum wire will be used. The change in overpotential values for different electrode materials will then only be as a result of the activation overpotential.

A list of materials for experimentation is in Table 5.1, along with its corresponding real-world trading material cost (based on data from Metalexchange.com as of 1st February 2015). The metals with a cost < £100/kg (except platinum) will undergo further characterisation due to their excellent conductive properties as well as evidence of use in electrolytic processes in literature.

Table 5.1: Raw Material Costs

Material	Cost (Metal Exchange)	Electrical Conductivity from Literature (x10^6 Siemens/m) [167]	Purchase Options	References
Platinum	£29049/kg	9.3	Biologic	[63, 72, 73]
Palladium	£18231/kg	9.5	Biologic	[73, 168]
Gold	£28304/kg	44.2	Biologic	[45, 169]
Iron	£2.81/kg	10.1	Biologic, Mini-Science	[51, 73]
Silver	£390/kg	62.1	Biologic	[51, 72]
Nickel	£9.85/kg	14.3	Biologic, Mini-Science	[27, 49]
Graphite	£1.64/kg	5.9	Biologic, Mini-Science	[170-172]
Lead	£1.24/kg	4.7	Mini-Science	[51]
SS316	£1.82/kg	1.32	Mini-Science	[49, 72]
Magnesium	£3.01/kg	10	Mini-Science	[45, 51]
Titanium	£12.48/kg	2.4	Min-Science	[173]
Copper	£3.61/kg	58.5	Mini-Science	[45, 51, 63, 72, 73, 168, 169]
Aluminium	£1.31/kg	36.9	Mini-Science	[49, 72]
Tin	£11.98/kg	8.7	ScienceCompany	[45, 72]
Zinc	£1.41/kg	16.6	Mini-Science	[51]

This was completed using a simple experimental procedure as shown in Figure 5.3. The electrodes of choice were placed 10 mm apart for each experiment, thus keeping the ohmic resistance constant. The concentration was kept constant at 0.1M KOH for each experiment which kept the concentration overpotential constant.

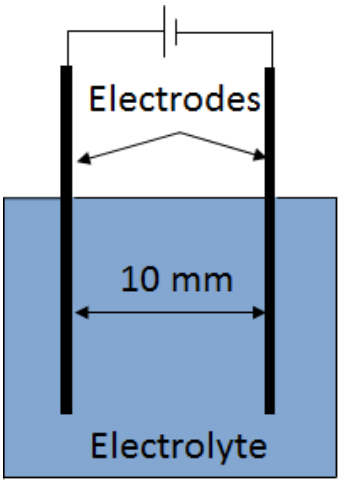

Figure 5.3: Experimental setup for various electrodes to be tested in 0.1M KOH solution at standard temperature and pressure

5.1.2. Electrode Material Cost-Benefit Analysis

From the objectives of this work it was paramount to use an electrode material which had excellent electrochemical properties and had a good resistance to corrosion from persistent contact with an alkaline environment. As well as this, the material of choice had to be cost effective; therefore an evaluation of cost versus electrochemical performance was carried out.

The electrochemical performance was then plotted as a function of material cost (decomposition potential / raw material cost (in £/kg) as shown in Table 5.1) for each electrode material. This is shown in Figure 5.4.

From calculating the decomposition potential for each electrode from their respective current-voltage curve and then plotting this as a function of the material cost, we can see that relatively cheap metals such as zinc, iron and brass exhibit good cost effective electrochemical behaviour.

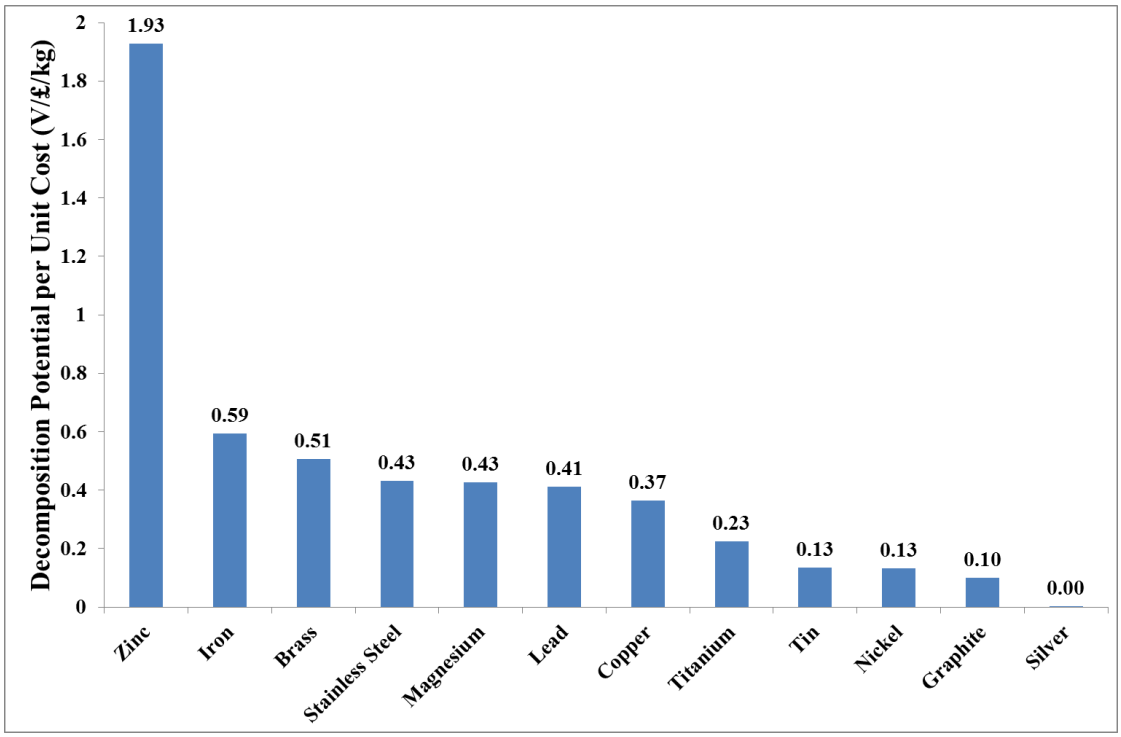

Figure 5.4: Decomposition Potential as a function of raw material cost for various electrode materials

This method of analysis represents a crude evaluation of electrode materials which will be operating at high efficiencies (low potentials), but in reality these materials will be

operated at a 12V potential supplied from the engine alternator. Each electrode material had a potential of 12V applied across it and the current per unit area (current density) was recorded. This is shown in Figure 5.5.

This shows that silver exhibits a high current flow at 12V. Silver, however is extremely expensive (£717.83/kg) and is not economically viable for this electrolyser design. The next three materials which exhibit good current flow are iron (mild steel), nickel and stainless steel (SS316). As well as having high current flow when 12 V is supplied to the electrodes, all three materials have economical unit costs which make them suitable towards meeting the project objectives.

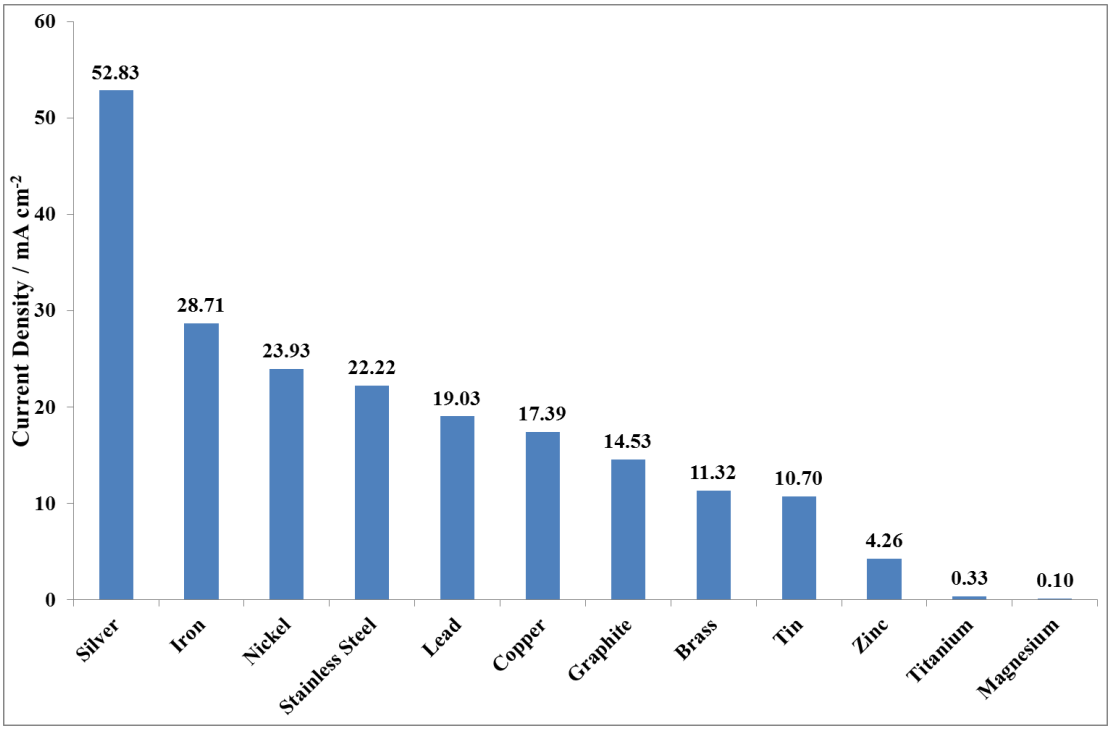

Figure 5.5: Current Density for Various Materials at 12V Operation

These three potential electrode materials have been selected for further testing due to their electrochemical properties as just mentioned and will undergo degradation testing to characterise their resistance to a caustic alkaline environment.

5.1.3. Electrolytes

There are many available electrolytes available for water electrolysis. They are in either liquid or solid form. Since the objective is to produce an alkaline electrolyser, a liquid electrolyte will be used. Acids and salts can be also be used as electrolytes, but the disadvantage of using acidic electrolytes is the rapid degradation and corrosion of the electrodes, which is undesired.

The use of salts, such as sodium chloride, can produce chlorine gas on the anode as a result of a more favourable (lower) half-cell potential. For this electrolyser, we want to produce hydrogen and oxygen respectively, therefore choices of electrolyte will mainly be focused on basic solutions.

In Table 5.2 is a list of potential electrolytes, their cost and the anodic product from the electrolysis reaction.

Table 5.2: Electrolyte Costs (SA – Sigma Aldrich 1st February 2015)

Electrolyte	Electrolyte Cost	Anode Product	References
NaOH	£26.30/kg (SA)	Oxygen	[27, 45]
KOH	£19.80/kg (SA)	Oxygen	[27, 45]
KNO_3	£1730/kg (SA)	Oxygen	N/A
Urea	£47.80/kg (SA)	N_2 & CO_2	[174]
LiOH	£212/kg (SA)	Oxygen	[175]
RbOH	£1000/kg (SA)	Oxygen	N/A
CsOH	£1250/kg (SA)	Oxygen	N/A
$Ca(OH)_2$	£6380/kg (SA)	Oxygen	N/A
$Sr(OH)_2$	£628/kg (SA)	Oxygen	N/A
$Ba(OH)_2$	£69/kg (SA)	Oxygen	N/A
NH_3	£1511/kg (SA)	Nitrogen	[174]
Na_2CO_3	£3960/kg (SA)	O_2 & CO_2	N/A
$Mg(OH)_2$	£37.20/kg (SA)	Oxygen	N/A

From the list of electrolytes above, the cost per kg of the electrolyte does not make it economically feasible for the majority of electrolytes to be used. For the purpose of this study only two electrolytes will be tested. They are sodium hydroxide (NaOH) and potassium hydroxide (KOH) which are the most commonly used in industry.

Polarisation on a 25cm^3 solution of 0.1M NaOH and 0.1M KOH was conducted with the use of platinum electrodes (surface area 5.93cm^2) and a fixed electrode separation distance of 10mm.

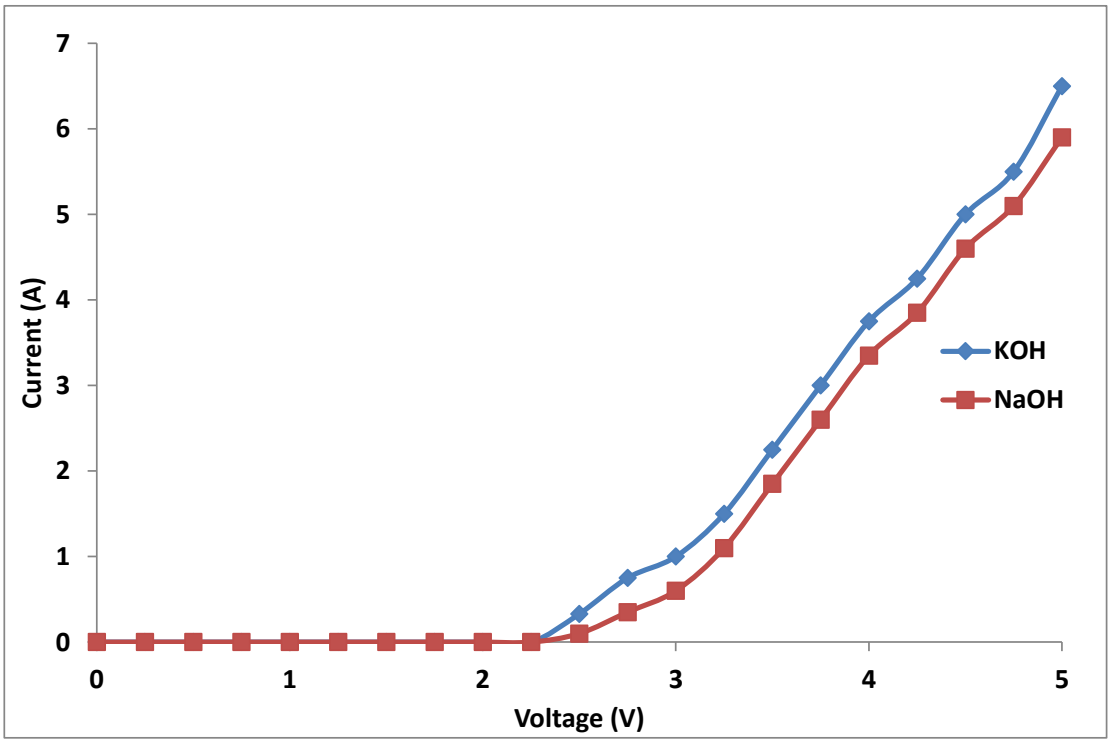

Figure 5.6: Polarisation at 25°C, 0.1V scan rate, 0.1M KOH, 1 atm pressure

Figure 5.6 shows that a KOH solution of the same concentration of NaOH solution has a higher polarisation and shall consequently be used throughout the rest of the experimentation since the only variance in the experimental procedure was the electrolyte.

5.1.4. Comparison of Experimental Results to Literature

The electrodes and electrolytes tested herein will be ranked in performance and compared to that in the literature. Table 5.3 shows the ranking of electrodes/electrolytes based on that in literature and based on the current density values measured from experimentation.

Table 5.3: Conductivity Comparison of Experimental and Literature Data

Electrodes & Electrolytes	Literature Conductivity Ranking (minus unused metals)	Experimental Conductivity Ranking
Platinum	10^{th}	N/A
Palladium	9^{th}	N/A
Gold	3^{rd}	N/A
Iron	7^{th} (5^{th})	2^{nd}
Silver	1^{st} (1^{st})	1^{st}
Nickel	6^{th} (4^{th})	3^{rd}
Graphite	12^{th} (8^{th})	7^{th}
Lead	13^{th} (9^{th})	5^{th}
SS316	15^{th} (11^{th})	4^{th}
Magnesium	8^{th} (6^{th})	11^{th}
Titanium	14^{th} (10^{th})	10^{th}
Copper	2^{nd} (2^{nd})	6^{th}
Aluminium	4^{th}	N/A
Tin	11^{th} (7^{th})	8^{th}
Zinc	5^{th} (3^{rd})	9^{th}
NaOH	2^{nd}	2^{nd}
KOH	1^{st}	1^{st}

There is a difference in ranking of conductivity for electrodes tested and that present in literature. The experimental rankings are close to the values in literature in the majority of cases, however SS316 performed much better experimentally than has been suggested, and, copper and zinc performed worse in the experimentation than provided in literature.

5.1.5. Electrolyser Stack Development (Electrolysers E & F)

From the predefined goals after the analysis of Electrolyser E, the objective was to design a new state of the art electrolyser of the same footprint (size) of the existing electrolyser (2000 cm^3). Since the electrical input to the electrolyser would need to remain constant (12 V), it was clear that the surface area of electrodes would need to increase.

From redesigning the electrolyser and utilising the full volume of the electrolyser it has been possible to increase the electrode surface area from 600 cm^2 to 5000 cm^2. This has been achieved by removal of 'neutral' plates which were found in Electrolyser E, which served no purpose in the electrolyser and were a source of unnecessary resistance.

Two prototypes (Electrolysers F & G) were designed and built for subsequent testing and analysis. Details of both are found in Section 3.2.1.5.

5.2. Experimental Results & Analysis

5.2.1. Stack Electrochemical Characterisation

5.2.1.1 Polarisation Analysis

This was conducted for SS316 and nickel plates, since iron is known to have high degradation characteristics [176]. Each electrode material was analysed as new (unpolished) and with pre-cleaned surfaces (polished). The polishing technique is explained in Section 5.2.2.1. The results were then compared plotted with the results from Electrolyser E from Section 4.1. Figure 5.7 shows that for the same electrolyser size (an important parameter of the project objectives) there has been an increase in current flow for the same potential. When 4 V is applied to the stack, there has been a 1500% increase from the commercial electrolyser to the improved design presented here.

This does not take into account the surface area of the electrodes, where in this case this analysis is carried out for Electrolyser F (24 x SS316 plates) and Electrolyser G (20 x nickel plates). This drastic increase in current flow has been attributed to the increase in the surface area of electrode (600 → 5000 cm^2).

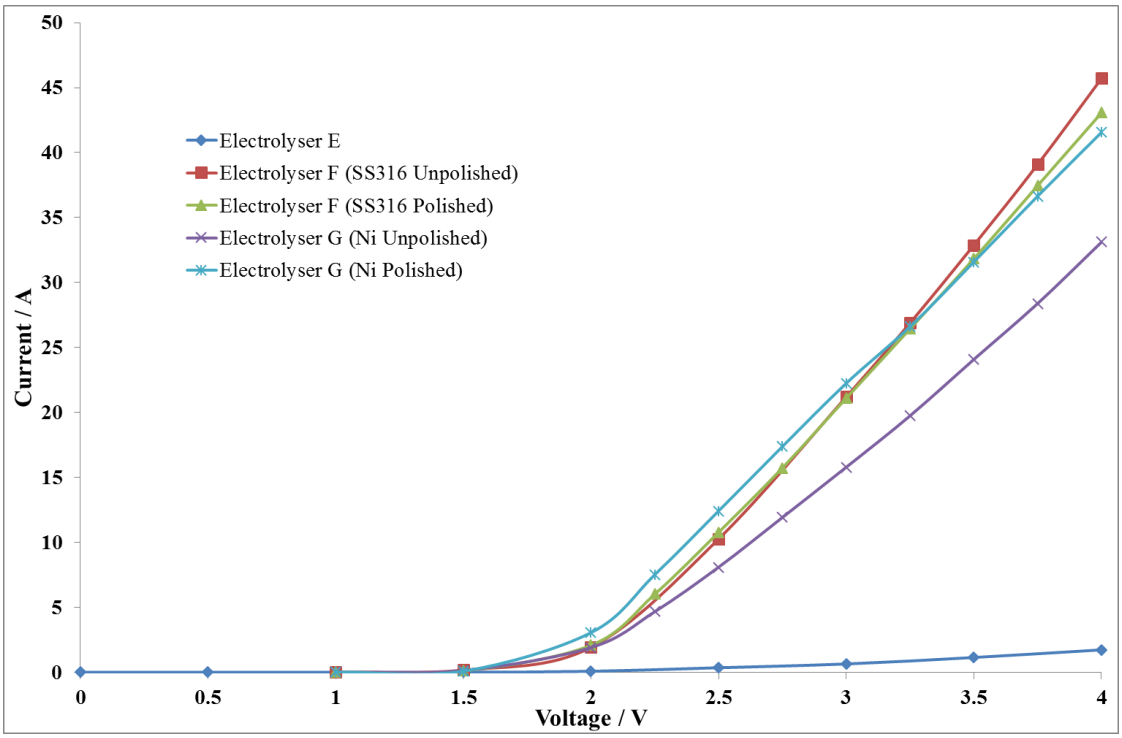

Figure 5.7: Polarisation as a function of Current at 25°C, 0.1V scan rate, 0.1M KOH, 1 atm pressure

To analyse this further, we can electrochemically characterize the electrolyser stacks as a function of the electrode surface area (current density). This is shown in Figure 5.8.

Figure 5.8 shows a smaller enhancement in terms of current density at a fixed potential. At a 4 V stack voltage, there is a 267% increase in performance from the commercial

electrolyser to the new design for both electrode materials. This enhancement observed can be attributed to the decrease in resistance in the electrolyser system.

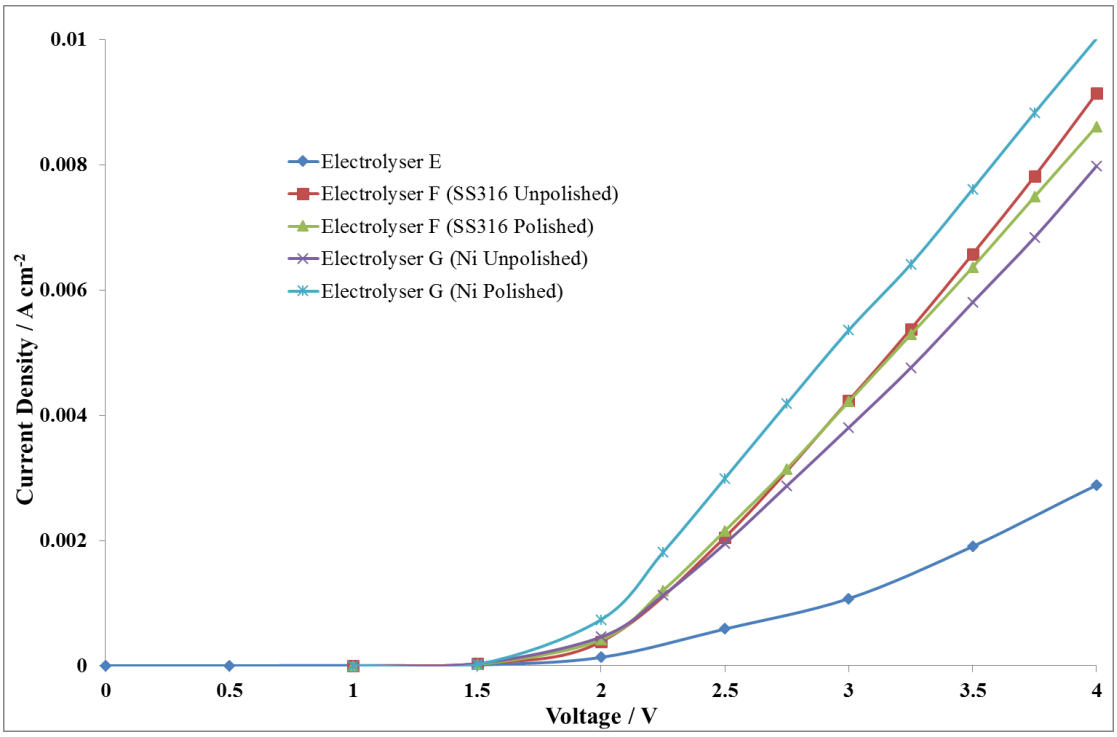

Figure 5.8: Polarisation as a function of Current Density at 25ºC, 0.1V scan rate, 0.1M KOH, 1 atm pressure

It is believed the reduction in resistance is a result of the smaller separation distance between the electrodes (reducing the ohmic resistance), and the removal of 'neutral' plates in the electrolyser, but increased the resistance in the commercial electrolyser.

5.2.1.2. Gas Productivity

Figure 5.9 shows the comparison in gas productivity from Electrolyser E to the new design. This increase at 4 V from ≈ 0.5 ml s^{-1} to 5 ml s^{-1} is a 10-fold increase. It also shows the polished electrode surfaces exhibit a higher gas production rate than the

unpolished electrode surfaces. This is a result of decreased surface tension (smoother electrode surfaces from a polishing process) which results in the removal of the oxide layer of the electrode, resulting in the increase in the electrode surface area for bubble nucleation.

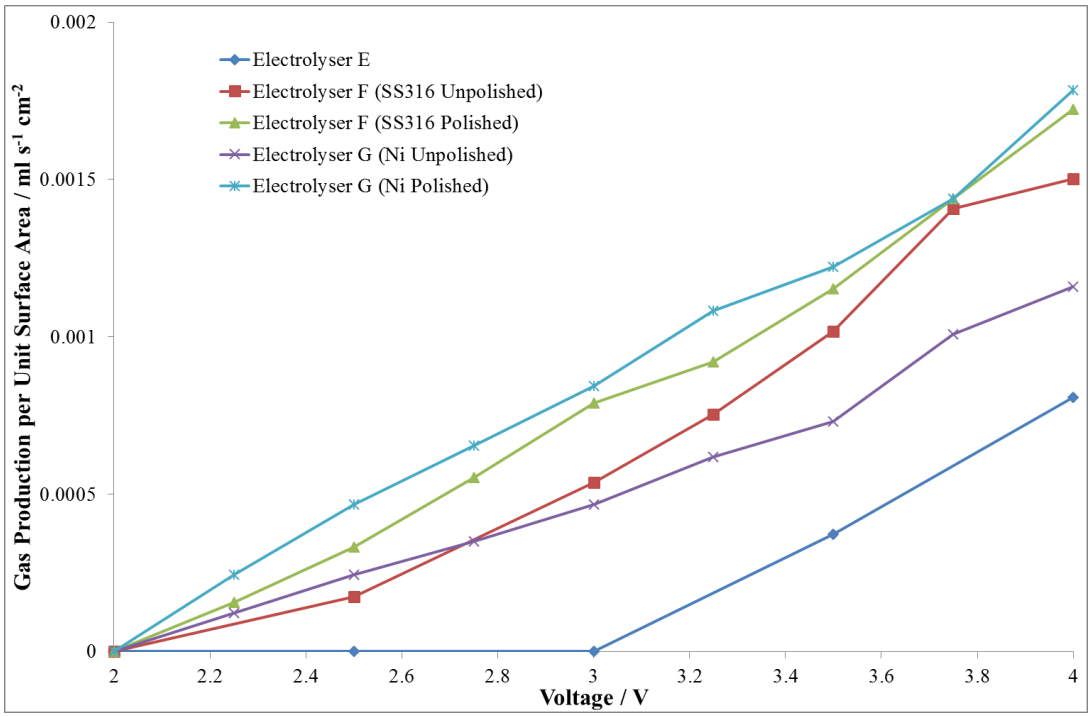

Figure 5.9: Electrolyser HHO Production Rate at 25°C, 0.1V scan rate, 0.1M KOH, 1 atm pressure

The increase in gas productivity from electrode surface polishing can also be attributed to oxide layer removal. These increase the resistance in the electrolyser, since it limits the number of active reaction sites available for bubble nucleation and slows kinetics depending on the thickness of the non-conductive layer.

5.2.1.3. Faraday's 1st Law of Electrolysis

Current flow per unit surface area is directly proportional to the rate of gas evolution. This is Faraday's first law of electrolysis. Figure 5.10 shows this relationship as recorded from the improved electrolysers, for both electrode materials and surface characteristics. The graph shows the directly proportional relationship between current density and gas productivity. To accomplish a higher gas productivity for effective catalytic behaviour in the combustion engine, a large current density is required to achieve these flow rates. This can be achieved by increasing the number of charge carriers, which conversely increases the rate of electrode degradation, by increasing the potential applied to the electrolyser or increasing the electrode surface area further.

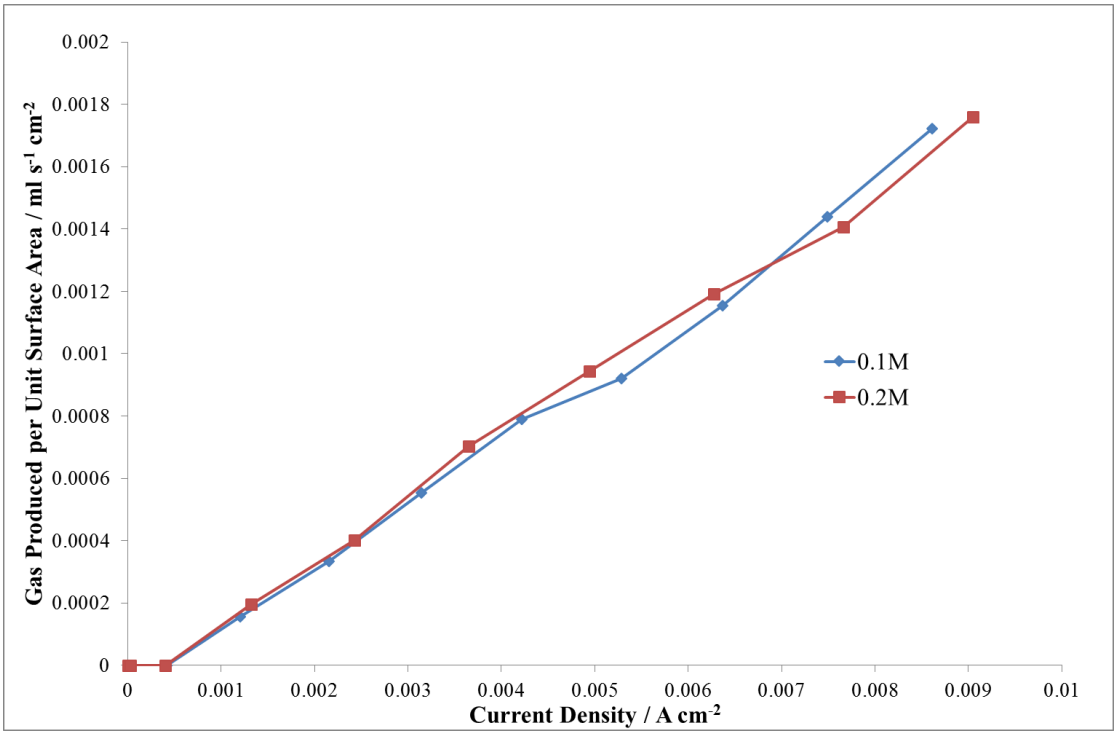

Figure 5.10: Current Density vs Gas Productivity per surface area at 25°C, 0.1M & 0.2M KOH, 1 atm pressure

The rate of HHO gas evolution can be quantified as a result of current flow through the electrolyser. Figure 5.10 shows a production rate of 2.66 ml/sHHO/A for 0.1M KOH and 1.41 ml/sHHO/A for 0.2M KOH.

5.2.1.4. Performance Projections

Equipment limitations meant that the operating current was restricted to 50 A. As a result, the operating potential has only been able to achieve 4 V. An experimental measurement from the application of a 12V to the electrolyser during engine testing, produced a 200 A current (green x on Figure 5.11) demonstrating a linear relationship between voltage and current and gas productivity, the data can be extrapolated up to 12 V and a projection can be made on the resultant current and HHO gas production. This is shown in Figure 5.11.

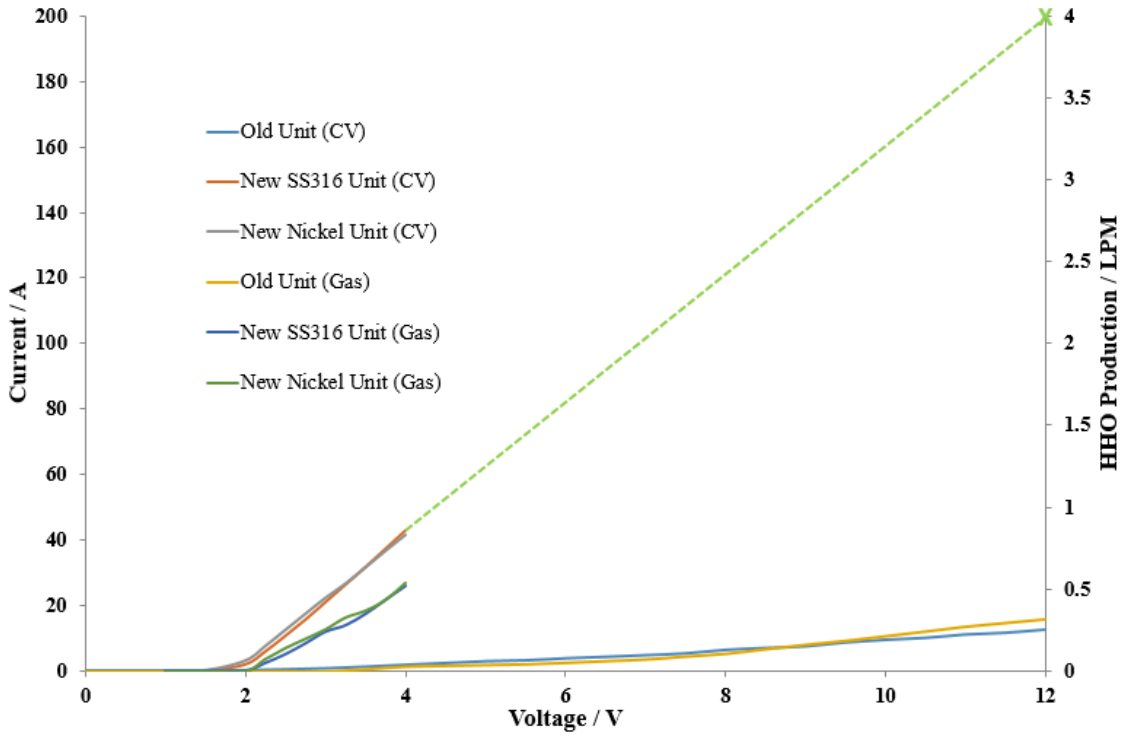

Figure 5.11: Performance Projections at 25ºC, 0.1V scan rate, 0.1M KOH, 1 atm pressure

Assuming the electrolyser obeys Faraday's 1st law of electrolysis the HHO gas flow rate from a 12 V applied potential is approximately 3.5-4 LPM.

5.2.2. Degradation Studies

The lifetime of the electrolyser needs to be maintained, so it achieves the specified 2500 hour operation. To analyse this rates of degradation were studied in in-situ (in electrolysis mode), and ex-situ (material degradation in the absence of electrolysis). One process uses the application of metal polish to the electrodes to increase electrode kinetics, and the current degradation analysis of the electrolyser over a fixed period of time.

5.2.2.1. In-situ Analysis

This research uses the application of metal polish to the electrodes to remove/decrease the thickness of the non-conducting layer. Stack polarisation and current degradation at fixed potential are measured over time.

Stack Lifetime

To analyse the performance of the electrolyser lifetime, the current variation can be measured at a fixed potential over time. Figure 5.12 shows the current degradation in the electrolyser for SS316 and nickel for a period of 7 hours.

This shows that there is a decrease in current flow over the seven hours of operation, seen by the negative gradient for the two electrode materials. The current decreases by 11% for the SS316 and 3% for the nickel over the seven hours.

Using the gradient of the data points, we could approximate the time it takes until zero current occurs assuming that rate of degradation remains constant. For SS316 this is approximately 53 hours and for nickel this is 242 hours. A fivefold lifetime extension can be found for using nickel electrodes instead of SS316.

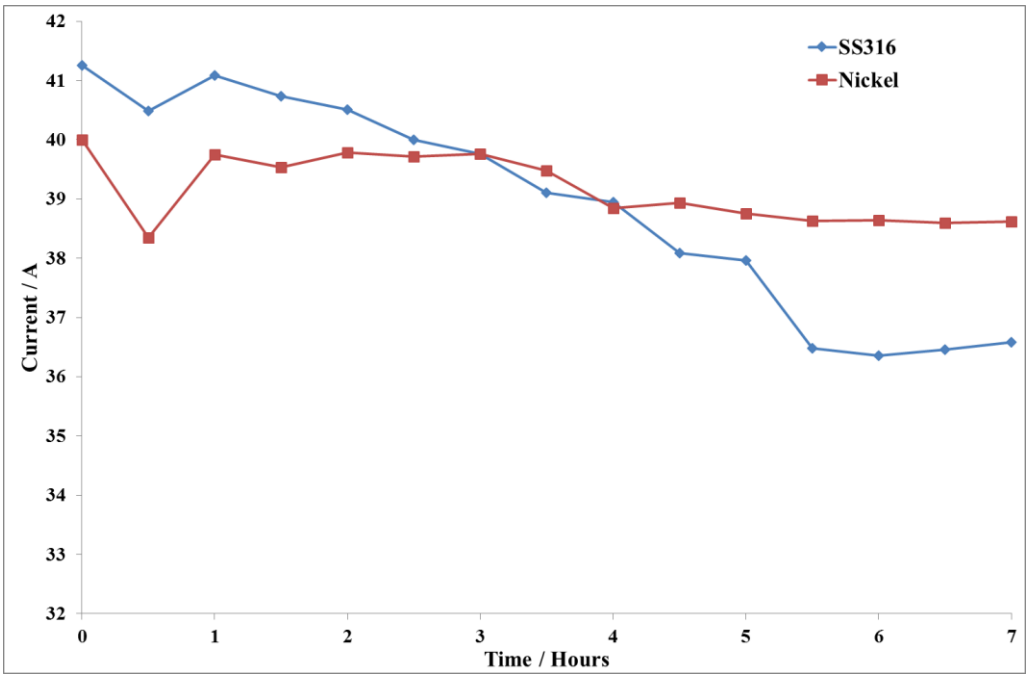

Figure 5.12: Current Degradation Analysis for SS316 and Nickel, at 25°C, 4V, 0.1M KOH, 1 atm pressure with fixed electrode surface area of 100cm^2 for both SS316 and nickel.

Electrode Surface Cleaning

To increase the lifetime of the electrolyser the surfaces of the electrodes were cleaned after use. The hand polishing of a solution (ingredients: C8-10 alkane/cycloalkane/aromatic hydrocarbons, quartz, kaolin, C12-20 saturated and unsaturated monobasic fatty acids, aqua and ammonium hydroxide) for 15 minutes to the plates should remove the oxide content on the plates, thus reducing the resistance in the electrolyser unit. The cleaner surface is expected to give rise to a higher rate of bubble evolution as a result of a higher utilisation of electrode surface area. Analysis of the effect that polishing the plates has on nickel is presented in Figure 5.13.

It shows for two concentrations that polishing the plates increases the flow of current between the plates, and subsequently increases the rate of HHO gas production for varying potentials Figure 5.14.

From these figures we can detect the enhancement in polarisation as a result of electrode surface cleaning. This is subsequently mimicked by the increase in HHO gas evolution rate as a result of the increase in electrolyte concentration and resultant increase in current.

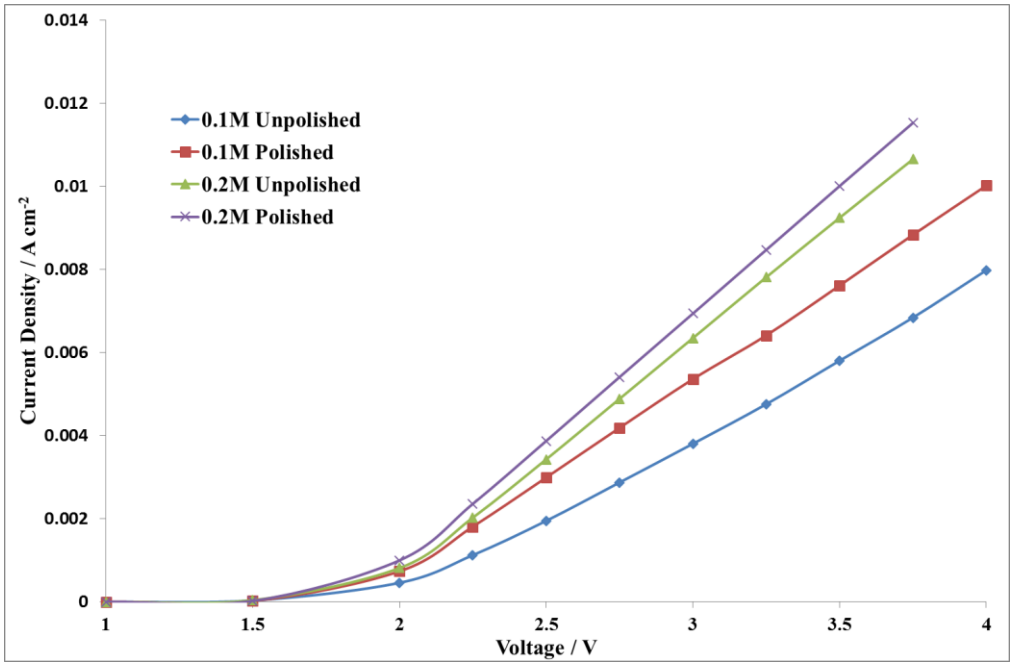

Figure 5.13: Polarisation of Polished and Unpolished Nickel Electrodes at 25ºC, 0.1V scan rate, 1 atm pressure

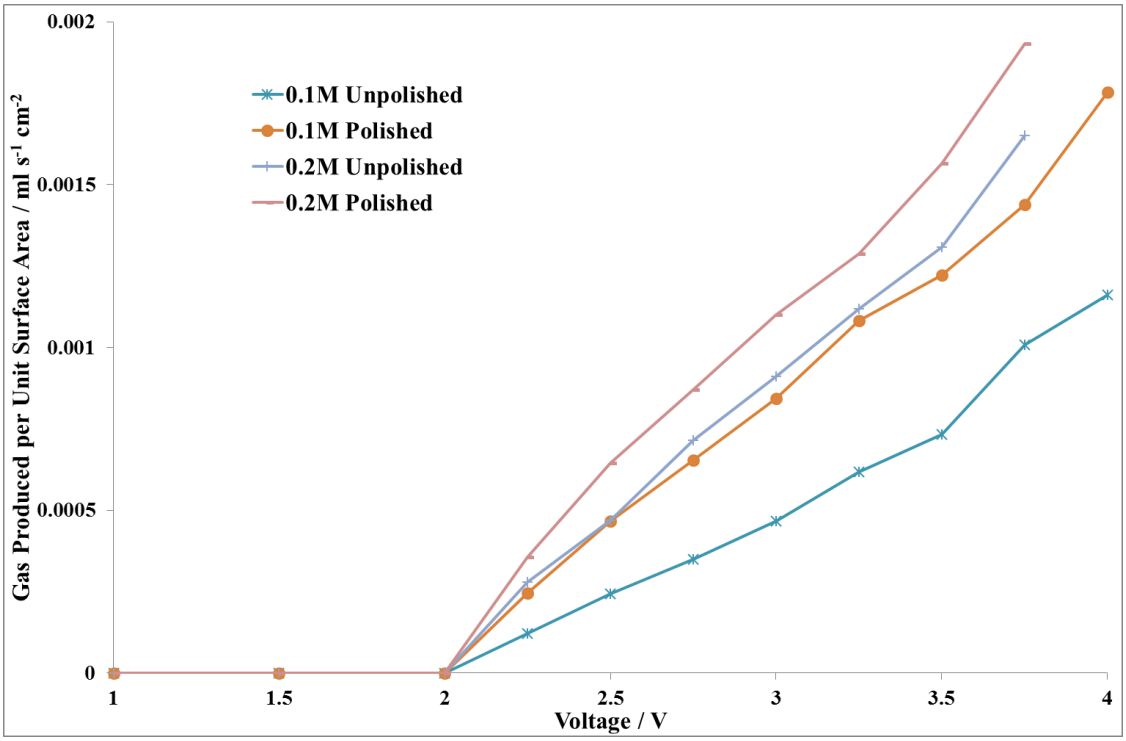

Figure 5.14: Gas Evolution Rate of Nickel Electrodes at 25ºC, 0.1V scan rate, 1 atm pressure

The effect of surface polishing can be further characterised by mimicking how the electrolyser would be operated in the outside world. This involves conducting a current degradation evaluation over an eight hour period, then deactivating the electrolyser and leaving the KOH solution in the electrolyser overnight (16 hours and consistent with real world operation), and then turning the turning the power on for another three hours (mimicking usage the next morning). After this duration, the electrodes are polished and the current degradation at a fixed potential continued for a further three hours. This was completed for two fixed potentials and is shown in Figure 5.15.

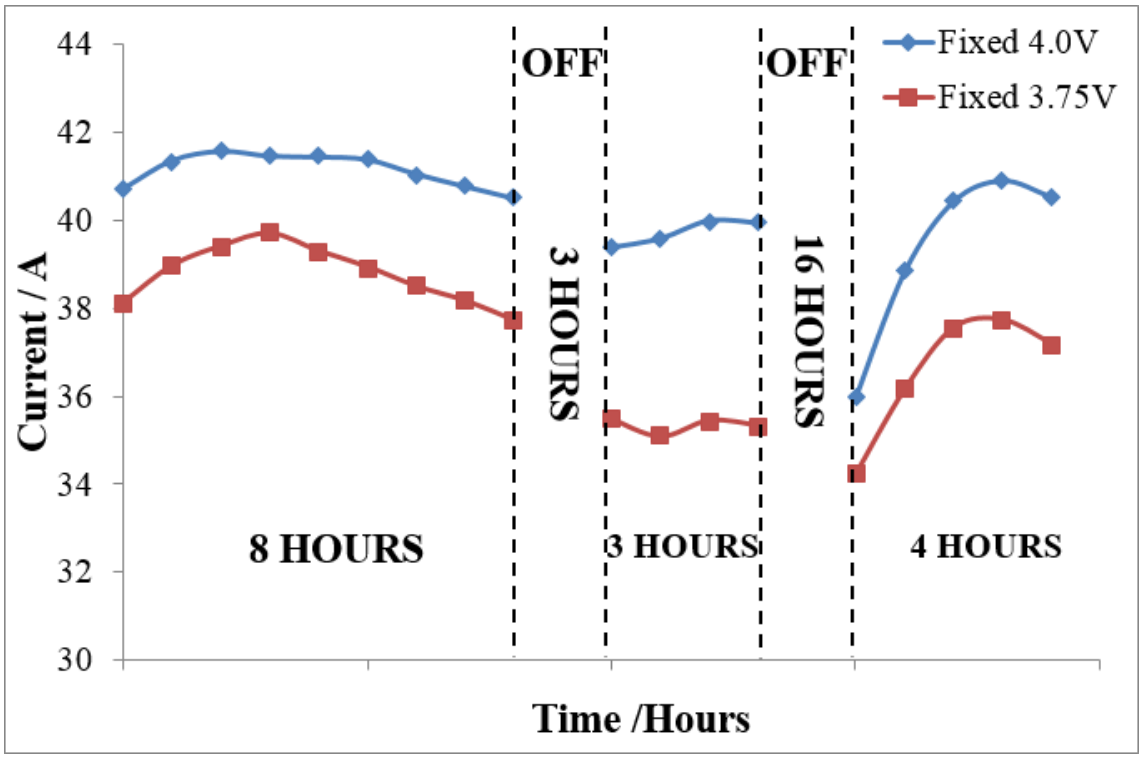

Figure 5.15: Electrochemical Degradation of Nickel Plates at 4 V & 3.5 V, 25°C, 0.1M KOH, 1 atm pressure

Figure 5.15 shows the long term electrolytic behaviour of the electrolyser incorporating electrode cleaning and systematic 'no power' periods to simulate real world utilisation of the electrolyser in industry.

In the first phase of the experiment, the data shows a steady increase in current over time during start up. At the end of the first phase the electrolyser is shutdown and left in solution for 3 hours. In the second phase, a decrease in current is observed upon start up due to the now cold electrolyte temperature. This current flow increases at a slower rate than previously stated due to the presence of the recently increased oxide content on the surface, and the increase in electrolyte temperature and is carried out for three hours.

At the end of the second phase of experimentation, the electrolyser is left for 15 hours in shutdown mode, and electrolyte present in the electrolyser, the expected increase in the quantity of the oxide content on the surface should result in a decrease in current flow. This is shown in the third part of Figure 5.15. The starting current is lower than seen in the first phase of the experiment, but once again rises over time due to the decreasing resistance as a result of temperature increase in the electrolyte.

Figure 5.15 shows the electrochemical behaviour of an electrolyser in application which includes an eight hour working day, on/off cycles and an inactive period in the time outside the normal working day. Reducing the evolution of the oxide content on the electrode is imperative to the lifetime and electrochemical performance of the alkaline electrolyser.

5.2.2.2. Ex-situ Analysis

As well as analysing the degradation rates of the electrodes whilst electrolysis is in progress, there are significant periods of time (at least two thirds of a day) when electrolysis will not be happening. During this period of time, the electrodes are in contact with caustic electrolyte, causing corrosion to them. This degradation is characterised and methods of corrosion reduction are discussed in order to increase electrode lifetime.

The first analysis involved selecting three electrode materials from the initial electrochemical material testing, which had a beneficial electrochemical performance and sufficient cost analysis for this electrolyser to be economically viable. The three metals that were selected were mild steel, SS316 and nickel.

Each of these metals was subject to three different concentrations of potassium hydroxide (KOH), two different temperatures, and each of these for four varying experimental durations. These are shown in Table 5.4.

Table 5.4: Degradation Analysis Experimental Parameters

Parameters:			
3 x Electrode Materials	3 x Concentrations	2 x Electrolyte Temperatures	4 x Experimental Duration
• Mild Steel	• 1M KOH	• 25°C	• 0 Days
• Stainless Steel	• 2M KOH	• 80°C	• 5 Days
• Nickel	• 5M KOH		• 10 Days
			• 20 Days

Each sample for each experiment would undergo scanning electron microscopy (SEM) to observe any defects/damage to the metallic surface of the electrode. This would be

expected to show that an increase in electrolyte concentration, electrolyte temperature, and exposure duration, increases the rate of electrode degradation.

Scanning Electron Microscopy (SEM)

For each metallic sample a timeline of SEM images can be displayed for increasing durations, concentrations and operating temperatures. This will show the rate of electrode surface degradation.

Figure 5.16 shows the surface degradation for mild steel. The control sample (start of experiment), shows a very uniform smooth surface, whereas after 10 days subjected to 1M KOH at 25^{o}C, iron leaching is evident on the surface of the sample which is localised. After 20 days this leaching is evident with a much larger surface coverage in the same concentration and temperature. This leaching after 20 days of being subject to concentrated KOH solution makes mild steel unsuitable as a material of choice for an alkaline electrolyser.

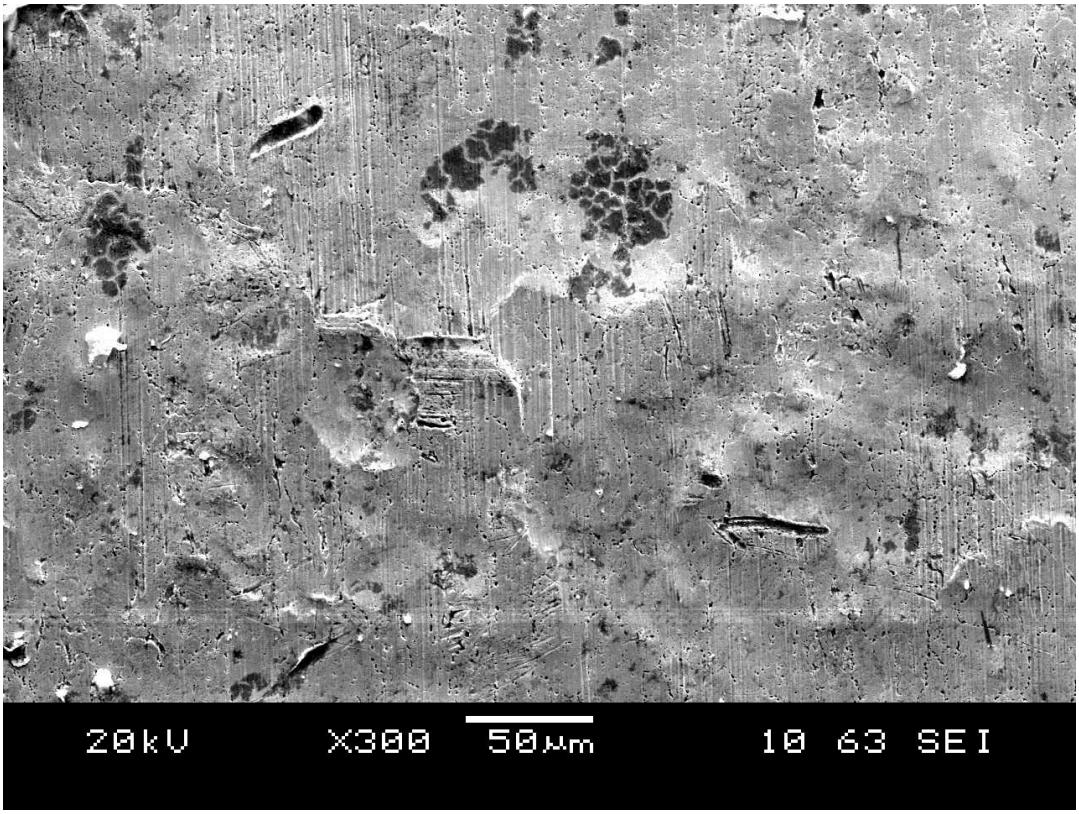

Initial

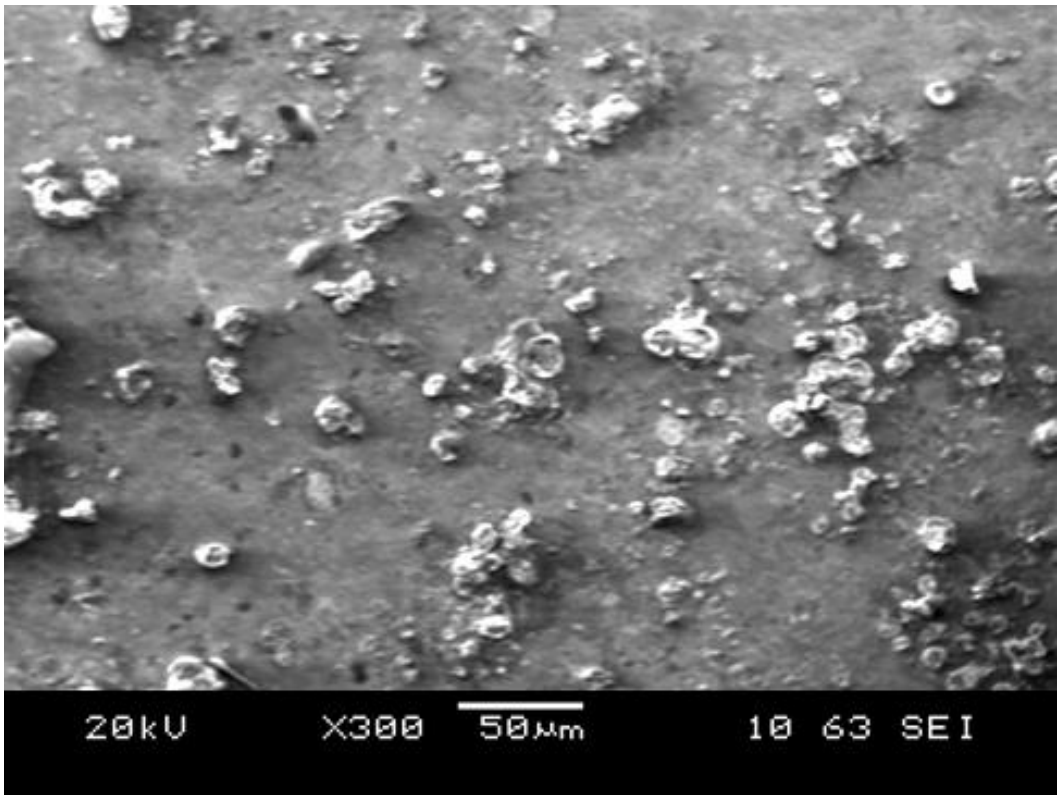

10 Days

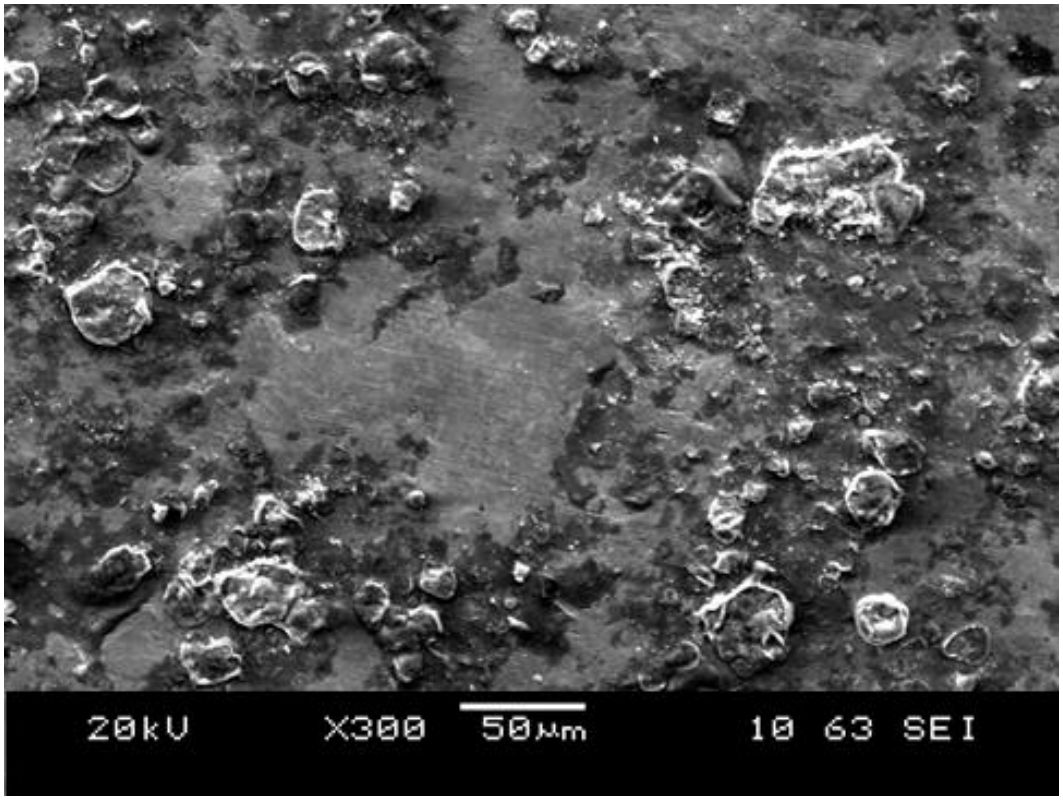

20 Days

Figure 5.16: SEM Images of Iron Electrode Surface

Figure 5.17 shows the surface degradation for stainless steel. The control sample (start of experiment), shows a uniform smooth surface with the grain boundaries clearly defined. After 10 days of being subjected to 1M KOH at 25^{o}C, minor iron leaching is evident on the surface of the sample.

After 20 days this leaching is visible on the surface in the same concentration and temperature. This is not as severe as seen on the surface of the mild steel, but this leaching after 20 days of being subject to concentrated KOH solution makes stainless steel unsuitable as a material of choice for an alkaline electrolyser.

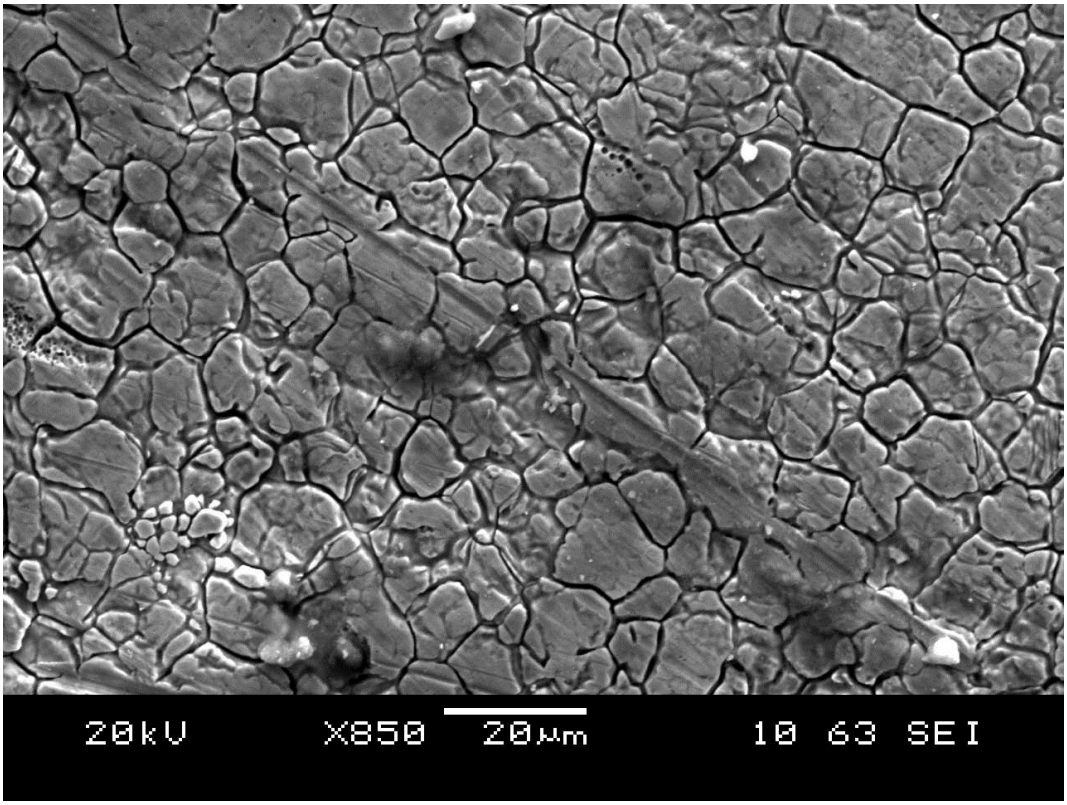

Initial

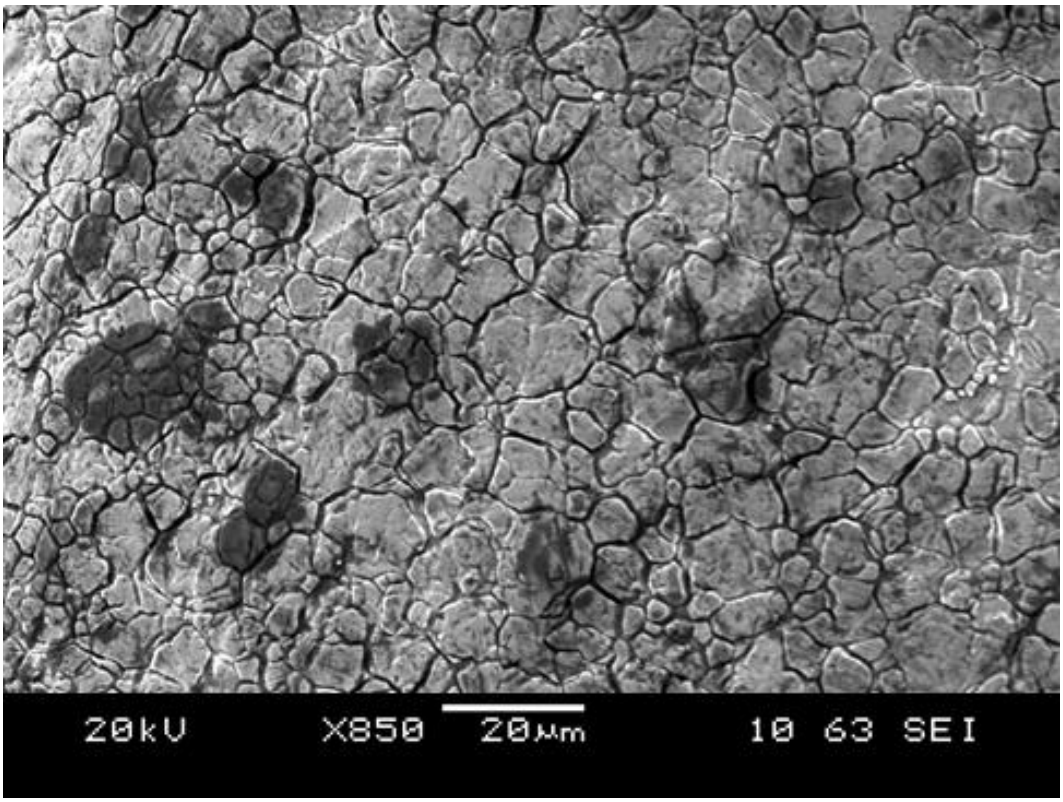

10 Days

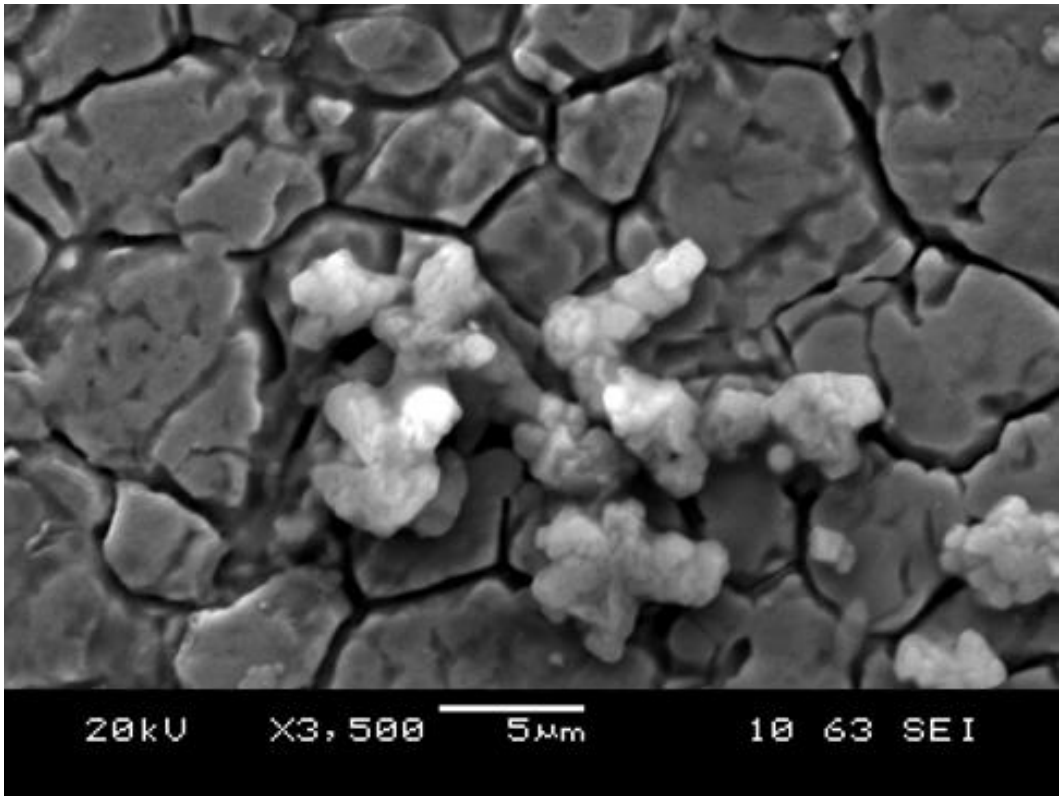

20 Days

Figure 5.17: SEM Images of SS316 Electrode Surface

Figure 5.18 shows the surface degradation for nickel. The control sample (start of experiment), shows a uniform smooth surface. After 10 days of being subjected to 1 M KOH at 25^{o}C, no surface corrosion is evident on the surface of the sample.

After 20 days leaching is still not visible on the surface in the same concentration and temperature, unlike on the mild steel and stainless steel. This resilience to corrosion/leaching after 20 days of being subject to concentrated KOH solution makes nickel a suitable material of choice for an alkaline electrolyser, when compared to the degradation properties of mild and stainless steel.

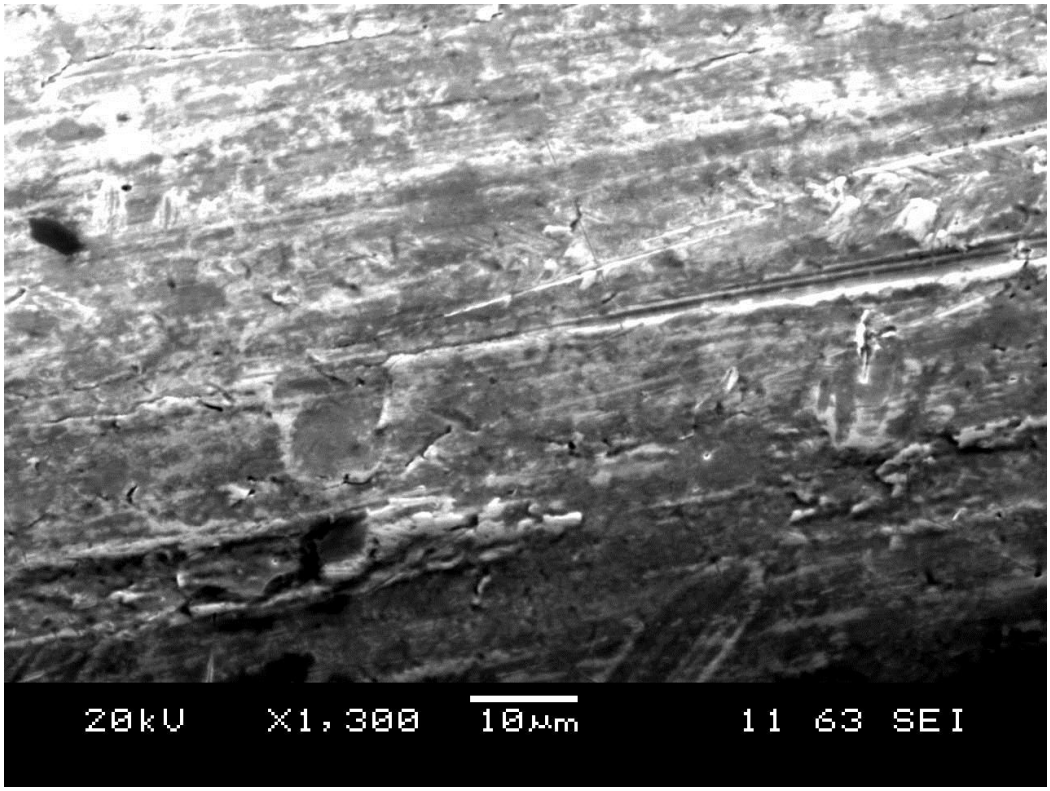

Initial

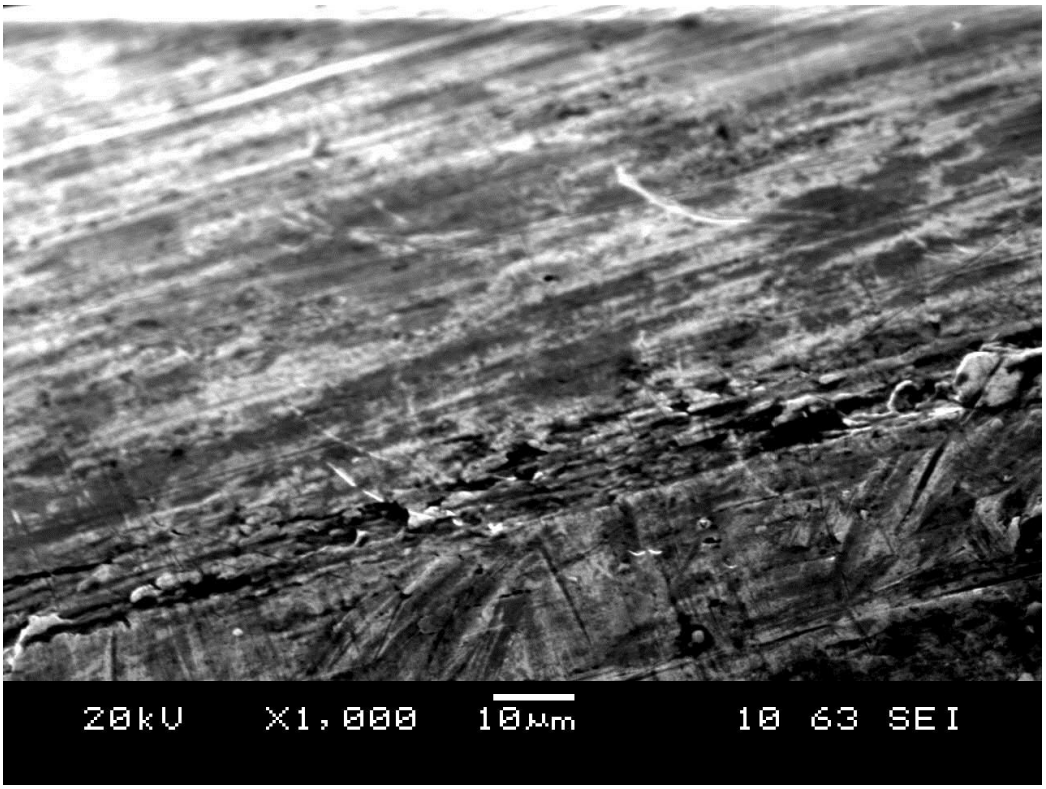

10 Days

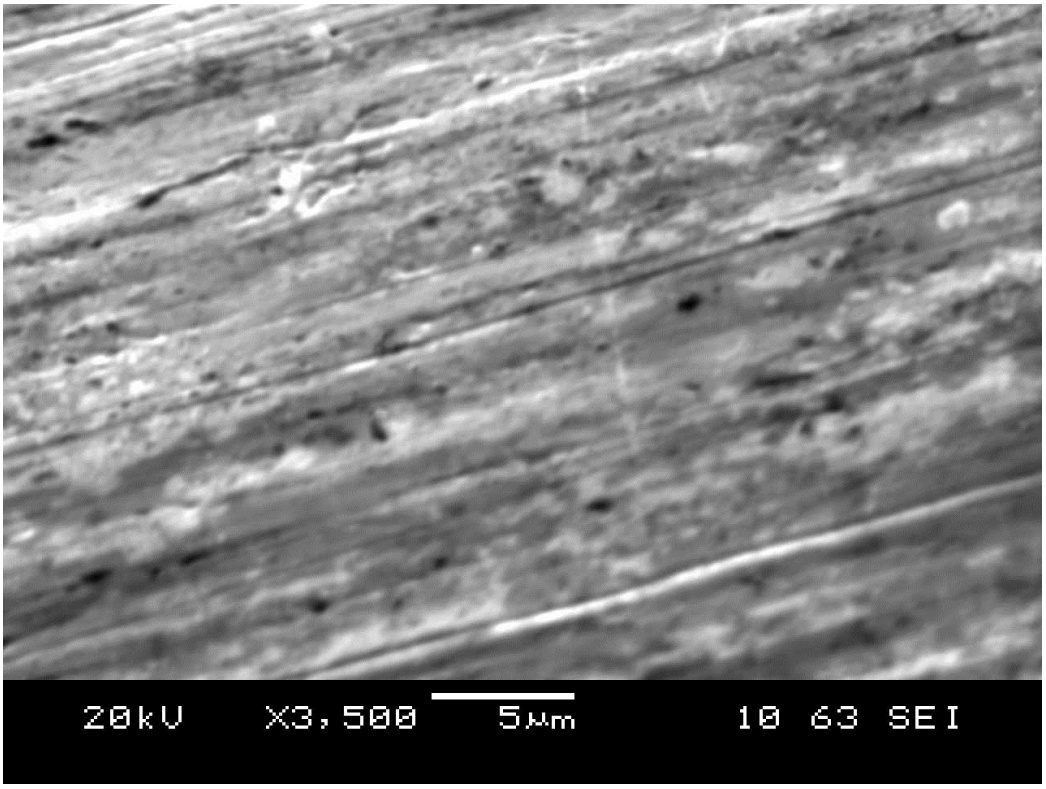

20 Days

Figure 5.18: SEM Images of Nickel Electrode Surface

5.2.3. Engine Testing

The engine testing procedure is in Section 3.1.11. The analysis shows data from the Original Unit (Electrolyser E) at 0.1 & 0.3 LPM HHO output (Section 4.2.2.) and compares this from the engine analysis of Improved Unit (Electrolyser G) at 0.1 & 0.3 LPM HHO output. The analysis also compares the HHO from the Original and Improved Electrolyser against bottled (simulated) hydrogen from a gas cylinder (Material Number 290631-L-C). The gas inlet characteristics are shown in Table 5.5. In the extended study from Chapter 4, experiments were performed at a constant engine speed of 1500rpm and the engine load of 3bar indicated mean effective pressure (Imep), representing 40% maximum load.

Table 5.5: Engine Experimental Fuel Additives

	HHO Flowrate (LPM)	**H_2 Flowrate (LPM)**	**H_2 Intake Concentration (ppm)**
Electrolyser Off	0	0	0
Electrolyser E 0.06 LPM H_2	0.1	0.066	120
Electrolyser E 0.2 LPM H_2	0.3	0.2	400
Electrolyser G 0.4 LPM H_2	0.6	0.4	800
H_2 simulated 0.4 LPM H_2	-	0.4	800
H_2 simulated 1 LPM H_2	-	1	2000
Electrolyser G 5 LPM H_2	7	5	10000
H_2 simulated 5 LPM H_2	-	5	10000

5.2.3.1. Liquid Fuel Replacement

The reductions in the mass of the injected liquid diesel fuel when HHO was inducted are shown in Figure 5.19. This liquid fuel replacement is a direct effect of the hydrogen contained in the HHO flow as it has been previously reported in [137] and [138] for spark ignition engines and in [162] for compression ignition engines. Liquid fuel replacement was less than 1% when the power to run the electrolyser was 10% of the engine output power. When the energy input to the electrolyser was increased up to reach a similar power to the engine output power (i.e. 100% fuel penalty), the HHO flow from the electrolyser also increased, but still the liquid fuel replacement was limited to 2-3%. At medium engine load the liquid fuel replacement was slightly higher than that at high load as a result of the lower engine fuel consumption, while the HHO flow was kept constant. These reductions were calculated without including the fuel/power needed to produce the hydrogen in the electrolyser. In any case the liquid fuel replacement was small to justify

the significantly high electrical power used in the electrolyser. Further improvements in the electrolyser are needed in order to obtain acceptable power consumption and HHO production (i.e. improved efficiency).

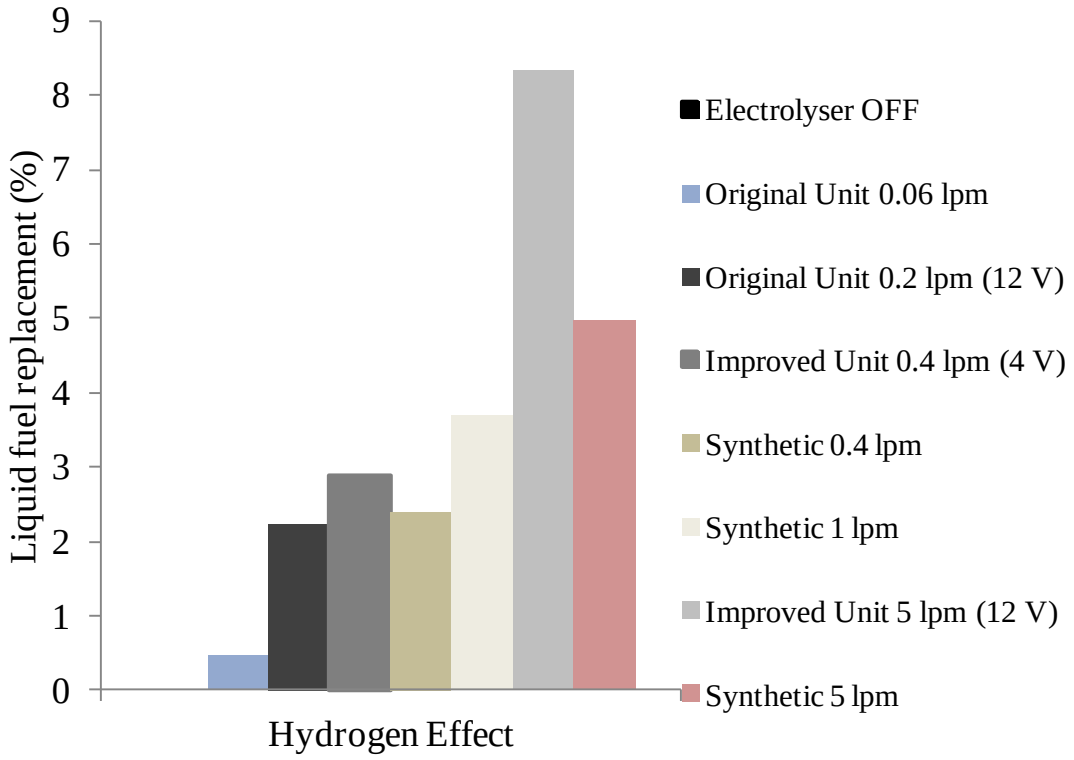

Figure 5.19: Liquid Fuel Replacement

The results of Electrolyser E are also shown in Figure 5.19. Liquid fuel replacements were higher than Electrolyser E. In the case of the improved unit the liquid fuel replacement of around 3% was obtained when the electricity to run the electrolyser was around 10% of the engine output power. When the electrolyser input power was increased up to the limits of the unit (i.e. similar to the engine output power) an 8% liquid fuel replacement was obtained. As in the case of the original unit, the power needed to calculate liquid fuel replacement was not considered.

5.2.3.2. Brake Thermal Efficiency

This liquid fuel replacement resulted in shorter liquid fuel injection duration and hence shorter combustion duration. In addition, the high flame speed, low ignition energy and wide flammability limits of hydrogen favoured mixture oxidation, reduced combustion duration, [177-180] and allowed more combustible mixture to be converted to useful work. The shorter combustion duration also resulted in reduced time available for heat transfer to the cylinder wall and thus may reduce heat loss which in turn would increase the thermal efficiency (Figure 5.20) [181]. The increase in brake thermal efficiency is limited to 1%, even though the energy required to produce HHO in the electrolyser was not considered in the calculations. The overall brake thermal efficiency will consequently be lower.

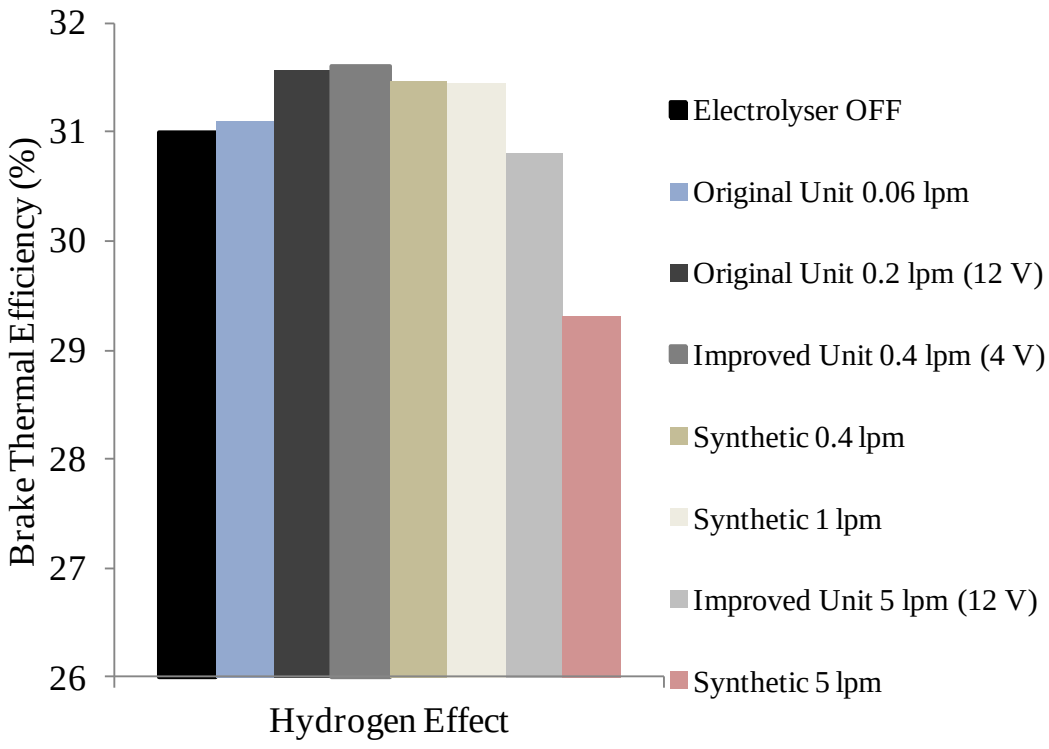

Figure 5.20: Brake Thermal Efficiency

Brake thermal efficiencies using HHO and synthetic hydrogen were compared for the same intake hydrogen concentrations. It is suggested that this is a result of the oxygen content within the HHO, even though it has to be noted that the oxygen flow within the HHO was much lower than the oxygen flow in the air intake. In the case of synthetic hydrogen, the increase in brake thermal efficiency due to hydrogen was partly compensated by a reduction in the volumetric efficiency as a result of the intake air replacement by hydrogen. In the case of HHO, the intake air replacement was higher compared to synthetic hydrogen (for the same intake hydrogen concentration) but the monoatomic HHO increased the combustibility of the fuel-air mixture.

Therefore, it is believed that in HHO a double benefit was obtained (hydrogen and oxygen benefits) in comparison with synthetic hydrogen. It should be noted that the oxygen effects within the HHO are limited as the HHO flow was very small in comparison with the air intake.

5.2.3.3. CO_2 & H_2O Emissions

Another advantage of using hydrogen is the decrease in CO_2 engine out emissions which is the most abundant greenhouse gas. In the case of Electrolyser G, as hydrogen concentration was increased, CO_2 engine out emissions were further reduced as a result of the reduction in carbon through liquid fuel replacement by hydrogen (Figure 5.21). Therefore, the reductions in CO_2 emissions were higher when more liquid fuel was replaced.

A maximum CO_2 reduction of around 8% was reached corresponding to the maximum HHO flow from the electrolyser unit. As in the case of liquid fuel replacement, the CO_2 benefits are limited by the HHO flow which can be efficiently produced in the device. It has to be noted that the CO_2 produced to operate the electrolyser was not included in these calculations. It is clear that the overall CO_2 emissions will be higher. On the other hand H_2O emissions increased as hydrogen was replacing the liquid fuel.

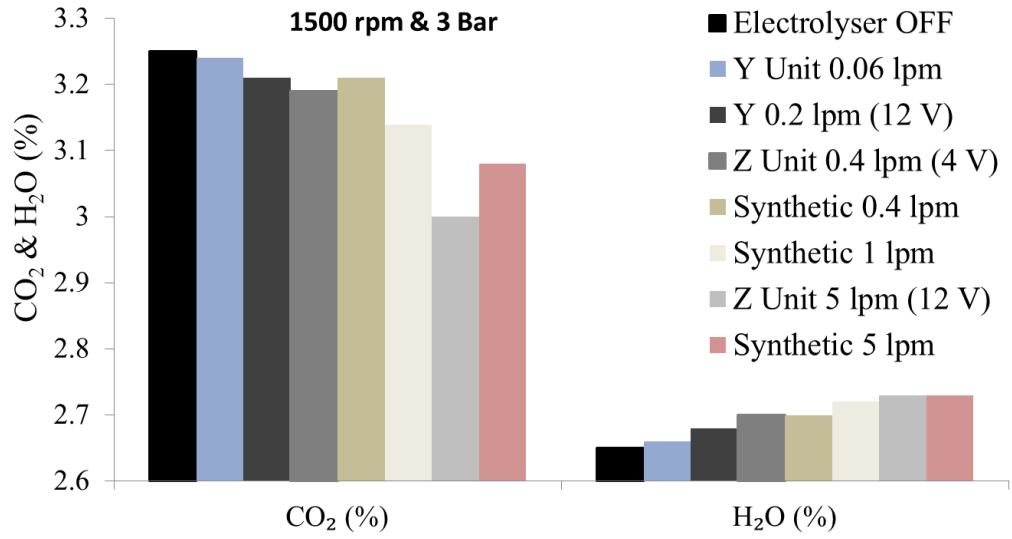

Figure 5.21: CO_2 & H_2O Emissions Analysis

5.2.3.4. NO, NO_2 & NO_x Emissions

In terms of NO and NO_2 distribution, it can be seen from Figure 5.22 that in overall, the addition of HHO and hydrogen into the engine significantly reduced the NO while increased the NO_2 engine emissions compared to diesel fuel. Despite increasing NO_2, the large drop in NO emissions contributed to the reduced NO_x emissions. As shown by [182], small addition of H_2 reduced the NO_x due to its combustion characteristics [165,

166]. However, it is also widely reported that high hydrogen concentrations or the application of hydrogen at high load can increase NO_x emissions.

This has been studied in the case of 5 bar imep with Electrolyser E and when 1% (i.e. 5 LPM) synthetic hydrogen intake concentration was used at 3 bar imep with the Electrolyser G. Therefore, hydrogen addition should be limited in terms of NO_x emissions. NO_x emissions were similar for HHO and synthetic hydrogen for the same hydrogen concentration, even though the oxygen content of HHO. In this case the effect of the oxygen within the HHO was negligible in comparison with the oxygen of the intake.

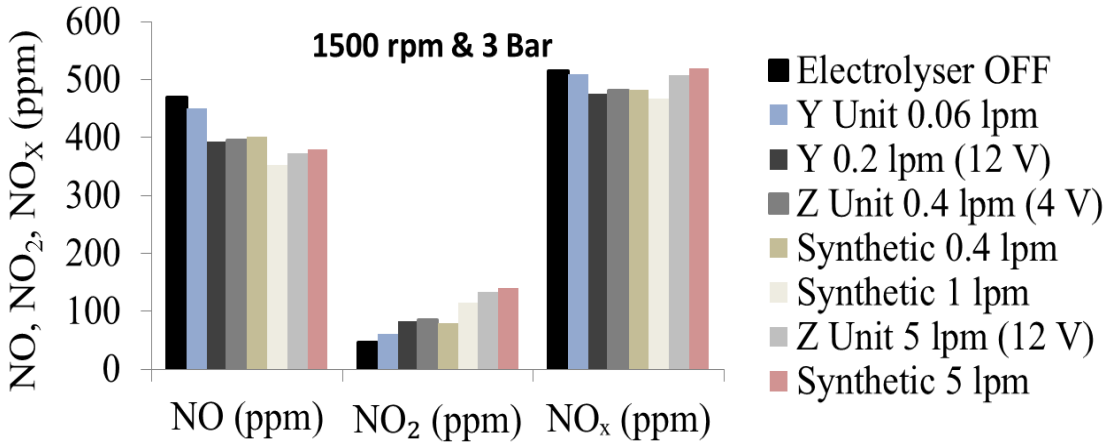

Figure 5.22: NO, NO_2 & NO_x Emissions Analysis

The increase of NO_2 with hydrogen addition was via the oxidation of NO with HHO [183]. Therefore, the introduction of hydrogen present in the reformate increased the HHO level, as shown experimentally in [184] and numerically in [185] which in turn resulted in the increase in the NO_2 emissions. As NO_2 has a higher soot oxidation

potential at low temperature (150ºC-400ºC) than oxygen [186], the increase in the engine out NO_2/NO_x ratio with HHO could be considered an additional potential benefit of the HHO addition in the case of diesel particulate filter passive regeneration [187].

5.2.3.5. THC & CO Emissions

The CO and THC emissions are shown in Figure 5.23. The addition of HHO decreased CO emissions because the hydrogen replaced some of the liquid fuel in the combustion process. The CO reductions for Electrolyser G are higher than for Electrolyser E as a result of the higher HHO flow.

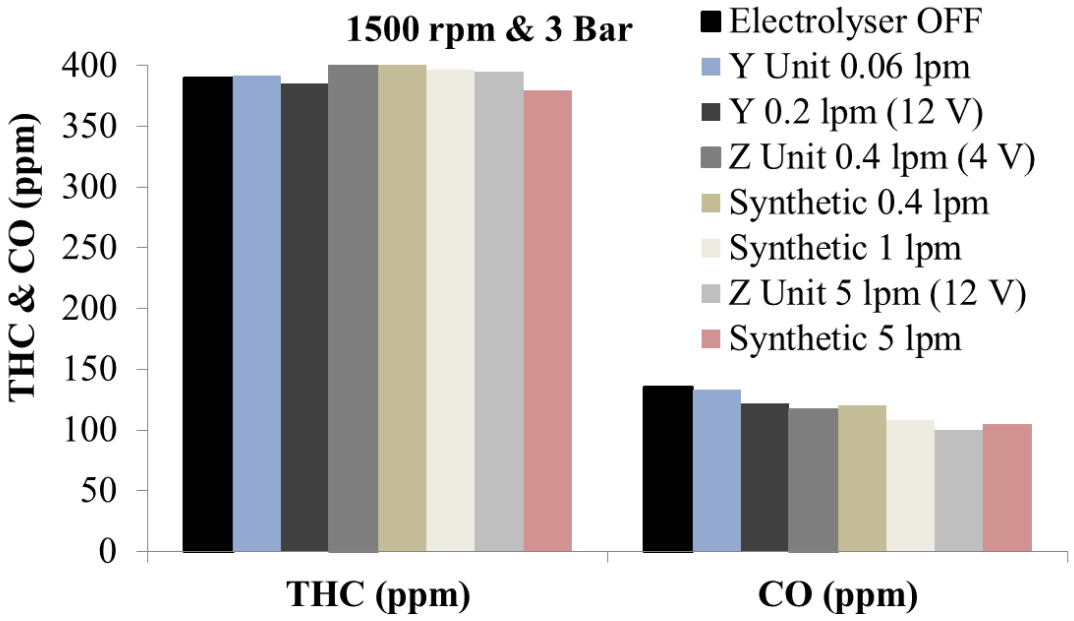

Figure 5.23: THC & CO Emissions Analysis

The CO reductions in the case of HHO were higher than in the case of synthetic hydrogen when the same hydrogen intake concentration is compared. In contrast to hydrogen

addition HHO did not reduce the oxygen intake concentration which could lead to incomplete combustion when a high fraction of hydrogen is applied especially at high load [145]. Therefore, it is suggested that the emission benefits of HHO not only were due to the beneficial combustion properties of hydrogen but also to the oxygen effect resulting in lower CO engine out emissions. In any case the CO reductions were limited (around 20-25%) due to HHO flow which was produced by the electrolyser unit. In terms of THC, there was not a clear effect of HHO and synthetic hydrogen. It is suggested that the quantity of HHO and hydrogen additions in all the conditions was not enough to significantly reduce THC emissions.

5.2.3.6. Engine Testing Conclusions

The addition of HHO gas produced by an electrolyser in compression ignition engines has been shown to partly replace non-renewable conventional diesel fuel and has slightly improved engine brake thermal efficiency. In addition, potential emission benefits in terms of carbonaceous gaseous emissions (especially CO and CO_2) and NO_x have also been obtained. These benefits were higher than those obtained using synthetic hydrogen due to the monoatomic structure of HHO i.e. there was not any atomic bonds needed to be broken (in H_2 and O_2) before combusting into water.

The hydrogen and oxygen never go into a diatomic state. Consequently HHO gas had more energy as these bonds never formed. This unstable state of H_2O vapour, more energy is achieved compared to hydrogen combusting with oxygen. The oxygen atoms evolving

with hydrogen results in a lower auto-ignition temperature than that of diatomic hydrogen.

In any case the benefits were restricted by the level of the HHO flow which can be efficiently produced by the unit in terms of the needed energy to operate the electrolyser. It is suggested that higher HHO flows will result in further increases in liquid fuel replacement and brake thermal efficiency and reductions in CO and THC emissions as a result of the hydrogen combustion benefits and the incorporation of oxygen in the HHO. On the other hand, these higher HHO concentrations could result in an increase in NO_x emissions and a considerably higher fuel/energy penalty to produce HHO in the electrolyser.

5.3. Conclusions

This chapter explained the development and characterisation of an alkaline electrolyser for on demand hydrogen generation. Its objective was to produce at least 4 LPM of HHO gas, using cost effective materials, whilst not increasing the footprint of the device.

Three metals (mild steel, stainless steel and nickel) were analysed using electrochemical and electron microscopy techniques to determine the best electrochemical performance and least surface degradation impacts. Iron exhibited poor resistance to degradation, with iron leaching evident from the microscopy analysis. Stainless steel exhibited moderate resistance to a caustic environment with minor iron leaching found. It and nickel both

exhibited good electrochemical performance, with the latter exhibiting no visual surface degradation when subjected to an alkaline environment.

An alkaline electrolyser was built using nickel plates (Electrolyser G), which was characterised up to a potential of 4V for bench testing, and projections were made for electrochemical performance at 12V, which was expectant to be between 200-250A but in fact was closer to 400A; a one hundred-fold increase from the initial unit in Chapter 3.

This improved performance in engine mode was achieved with notable results on the effectiveness of HHO in internal combustion engines. The objective of producing an alkaline electrolyser which produces a higher HHO yield at similar economic cost to the original Electrolyser E was achieved and this subsequently decreased CO and CO_2 exhaust emissions.

Electrochemical performance testing over extended periods of time indicated a non-conductive layer on the surface of the electrodes, and the degradation in current flow over time was quantified. A method for removal of the oxide content and subsequent characterisation of the electrodes with and without the oxide highlighted the increased electrochemical performance when the oxide was removed.

It is also worth considering the high voltage applied to the nickel electrodes (12V) may change the phase and composition of the nickel. Pourbaix diagrams for nickel, which maps out the phases of an aqueous electrochemical system, show that for an applied voltage above 2 V in an alkaline system (pH >10) exists nickel oxide hydroxide (NiOOH).

Future research is needed in this field to determine what effect this phase has on the electrolyser performance and suggests, given no financial constraints, a bipolar alkaline electrolyser with a lower operating voltage per electrolysis cell would reduce degradation.

The high current flow in the electrolyser, when 12 V is applied, will drastically increase the rate of degradation of the electrodes in the electrolyser even though nickel has a reasonable resistance to corrosion from an alkaline environment [46, 176]. As a result of this the mechanisms for the degradation of nickel electrodes in an alkaline solution will be researched and methods to lower the rate of electrode degradation investigated.

Chapter 6

Reduced Degradation of Nickel Electrodes using an Oxygen-Getter in Alkaline Electrolysers

This research has been published in Materials for Renewable and Sustainable Energy, Volume 27 (3), 2014. DOI: 10.1007/s40243-014-0027-4

This chapter focuses on reducing the high degradation rates of electrodes existent in alkaline electrolysers. As shown in Chapter 5, the real-world application of Electrolyser G has an operating power of 2.5kW (given 12V power supply). Reduction of this subsequent electrode degradation will increase the lifetime and cost-effectiveness of operation and is of paramount research priority in industry [23, 188-192].

The mechanisms and characteristics of electrode degradation is a vastly researched area, especially in the field of alkaline electrolysis [45, 61, 62, 189-194]. These involve the reduction of electrolyte concentration and the use of electrocatalysts on the electrode surface to maintain high levels of electrochemical performance [62, 194-197].

One potential method of degradation reduction which has not until this moment been utilised in the field of electrolysis is the use of an 'oxygen getter'. An example of an oxygen-getter is titanium or an alloy of it in the form of either sponge or chips. The purpose of the oxygen-getter is to provide sacrificial protection (having a higher affinity to oxygen) to the electrode material from the alkaline solution during electrolysis [198].

The utilisation of an oxygen-getter already exists in the manufacture of turbine blades. These turbine blades, made of a nickel based super alloy, have a ceramic core to create the air flow channels for cooling when in operation and require removal after casting. The ceramic core is dissolved from the inside of the turbine blade by high temperature (approx. 200^{o}C), pressure (400 bar) and concentration (> 10 weight%) potassium

hydroxide (KOH) solution [198]. This caustic KOH solution would ordinarily degrade the nickel based superalloy, thus compromising its integrity. The prevention of damage to the turbine blades has been achieved by the introduction of titanium to the system, which stops the cast metal from undergoing corrosion from the caustic KOH solution.

This principle will be applied for testing in an alkaline electrolyser to draw oxide formation away from nickel electrodes to the sacrificial titanium, which has no involvement in the electrolysis reaction. Alkaline electrolysers similarly operate in high temperatures (40-90^{o}C), pressures (< 30 bar) and concentrations (20-30 weight%), making a feasibility study appropriate [71].

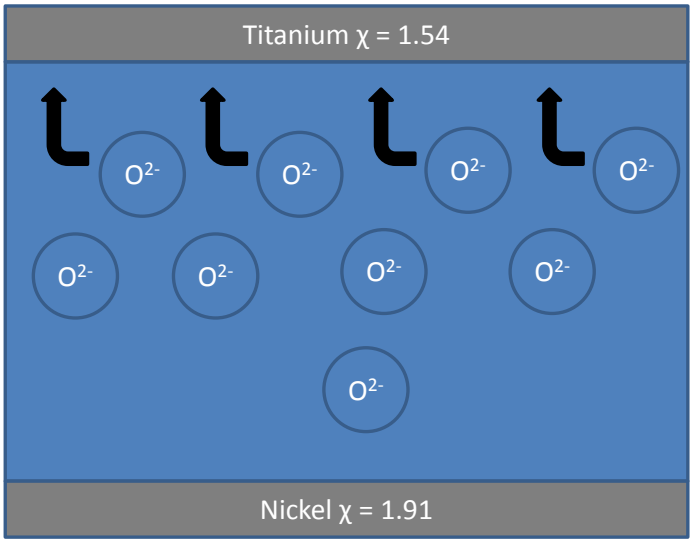

Figure 6.1: Schematic of Electronegativity Principle for an Oxygen Getter

Titanium exhibits a strong affinity to oxygen compared to nickel as it has a much lower electronegativity χ, hence it attracts electrons more freely. Electronegativity is the measure of an atom to attract a bonding pair of electrons. Titanium will protect the

electrodes from oxide layer formation in the alkaline solution (Figure 6.1). This enables the concentration and temperature of the aqueous solution to be increased, which in turn will increase the rate of electrolysis, without corroding the electrode itself [198].

6.1. Experimental Results & Analysis

This section is divided into two parts for determine the performance variation between Electrolysers H & I. The first section compares the differences in electrochemical performance, and the second compares the surface characteristics between the two electrolysers.

6.1.1. Electrochemical Characterisation (Polarisation)

The voltage was varied and the current flow recorded to characterise the electrochemical performance of the electrolysers. This analysis was completed for various concentrations (0.2M-1M) of KOH solution. Figure 6.2 and Figure 6.3 shows the polarisation and gas evolution rates for both Electrolysers H & I which are identical, thus proving that the two electrolysers are identical in electrochemical performance.

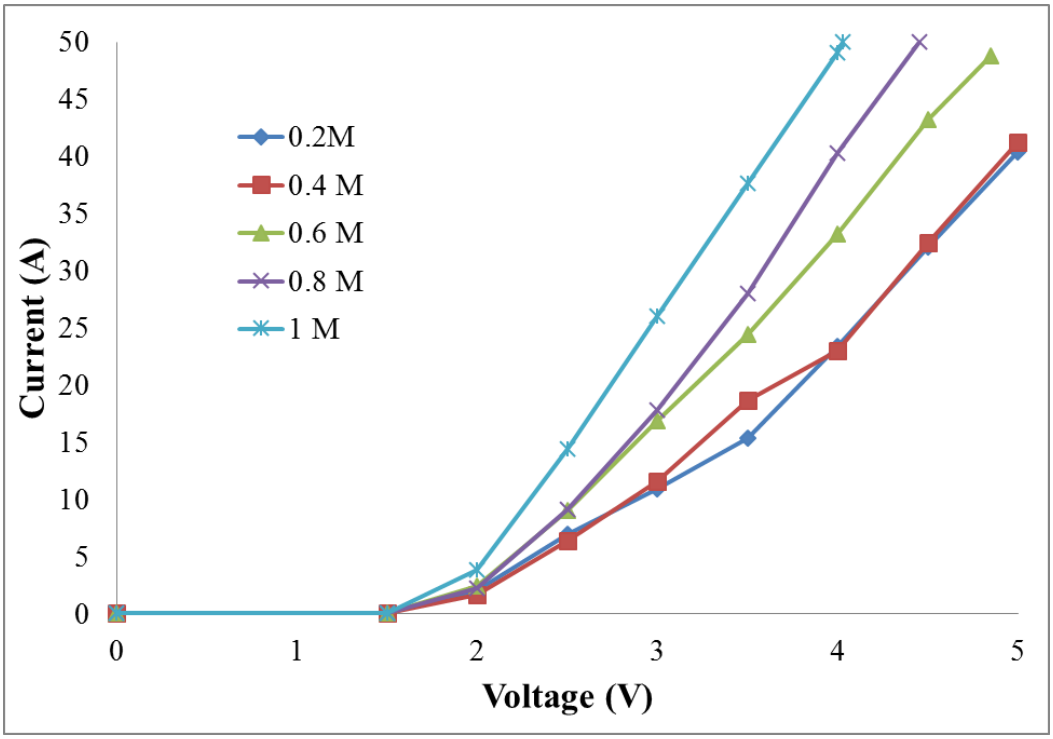

Figure 6.2: Electrolyser H Polarisation at 25oC, 0.1V scan rate, 1 atm pressure

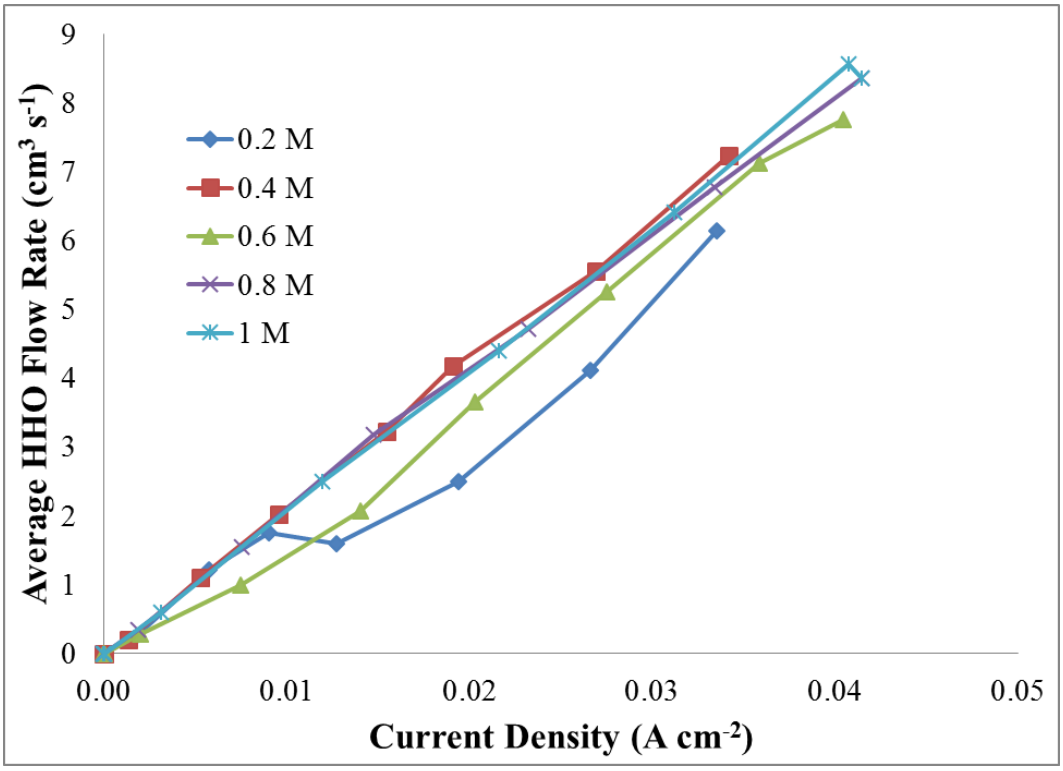

Figure 6.3: Electrolyser H Gas Productivity at 25ºC, 0.1V scan rate, 1 atm pressure

Using the same methodology for 0.2M-1.0M KOH solution, the gas production rates were measured to quantify the enhancement in the polarisation of the electrolyte solution and the corresponding production of hydrogen and oxygen (HHO) gas.

6.1.2. Electrochemical Degradation

The aim was to test both cells for a total of 10 days (two weeks), to mimic real world utilisation of an electrolyser (8 hours x 5 days a week). Figure 6.4 shows the performance for both electrolysers for the 10 day duration at constant voltage (4 V). Note that the electrolyte solution (0.1M KOH solution) was not changed throughout testing of each electrolyser, and were left in solution and in standby mode for two days between Days 5 & 6 (weekend).

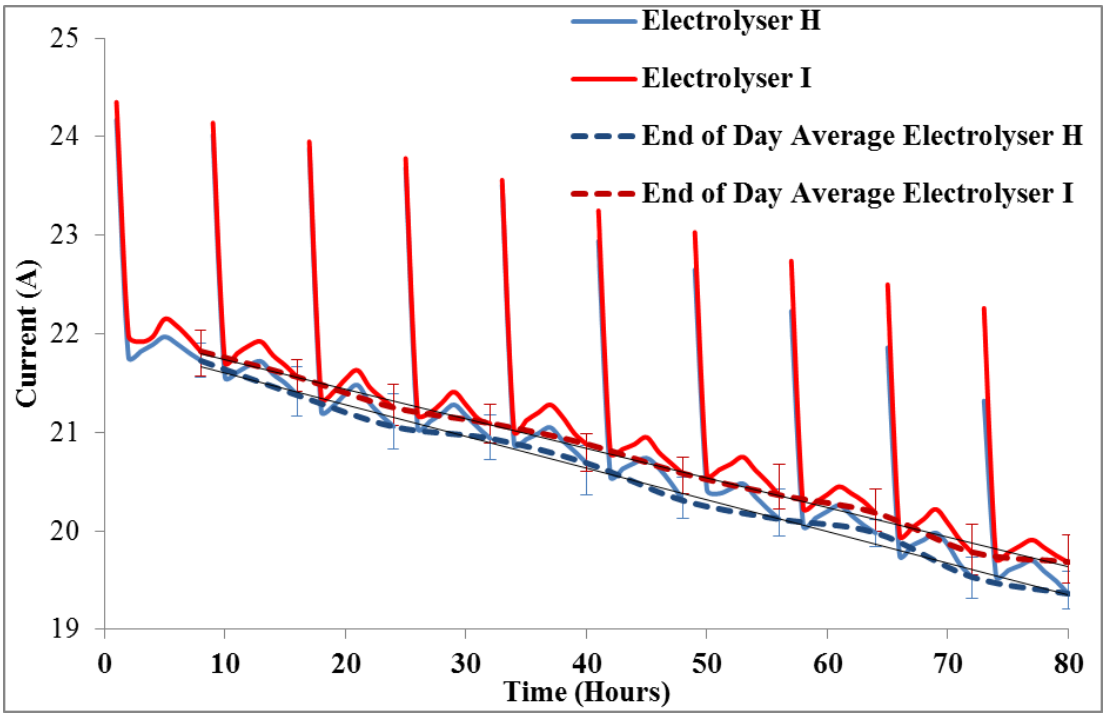

Figure 6.4: Two Week Current Degradation at 25°C, 4V, 0.1M KOH, 1 atm pressure

As discussed in Section 3.1.4 the potential step change is linked to the capacitative charging of the electrode and then the subsequent change in current over time is determined by the Cottrell equation. In Figure 6.4, the general trend shows that the current reduces over time and is an expected result due to the degradation of the nickel electrodes.

Throughout the testing, Electrolyser I, the modified cell, shows degradation to a lesser extent than Electrolyser H and the current is consistently higher, although taking into account potential errors in analysis give rise to the possibility that the performance is no superior. Although no definitive (due to possible error), it gives hope to the hypothesis that the titanium oxygen getter concept could be used in this application to help protect the nickel electrodes due to possessing a higher affinity for oxygen from degradation.

The biggest difference that the titanium chips in Electrolyser I, have appeared to make is between Days 5 and 6 where the electrodes were left in the KOH solution for 2 days to simulate the operators two rest days they are entitled to a week to mimic industrial use. After the two days of no use, the Electrolyser I current was 0.3A higher than Electrolyser H. This further supports the hypothesis showing that titanium has protected the nickel electrodes even when there is no current flow. The equations of the electrochemical degradations are:

$$\text{Electrolyser H : } y = -0.0322x + 21.927$$

$$\text{Electrolyser I : } y = -0.03x + 22.037$$

This shows they originate within 0.11A of each other, illustrating the identical nature of both electrolysers initially. Electrolyser H exhibits a current degradation rate of 32.2 mA/hour, whilst Electrolyser I shows a 30 mA/hour degradation rate. This represents a 7.3% reduction in current degradation rate. This does not take into account any error analysis data which if measured at the extremes could disprove the hypothesis stated.

Although in reality electrolysers operate for much longer than two weeks, the variation in electrochemical performance between Electrolysers H & I is evident after two weeks operation. Surface characterisation and analysis will aid discussion on the accuracy of the hypothesis and will support a better understand of the electrochemical data.

6.1.4. Scanning Electron Microscopy (SEM)

Analysis of the nickel electrode surface is important to quantify any oxide evolution on the surface. The nickel and titanium from the electrolysers will undergo image spectroscopy and surface composition spectroscopy to analyse and quantify any reduction in oxide formation as a result of introducing titanium to the electrolysis environment.

The metallic samples were split into 5 categories: Raw Nickel; Nickel from Electrolyser H; Nickel from Electrolyser I; Raw Titanium; Titanium from Electrolyser I. These were each analysed by the before mentioned techniques.

6.1.4.1. Raw Nickel

SEM images of the raw nickel were taken to provide a control sample against which the used electrode surfaces could be compared to see how the action of the electrolysis reaction affects the nickel surface. It is clear to see that from Figure 6.5, the raw nickel is clean and smooth, bar a few minor surface defects.

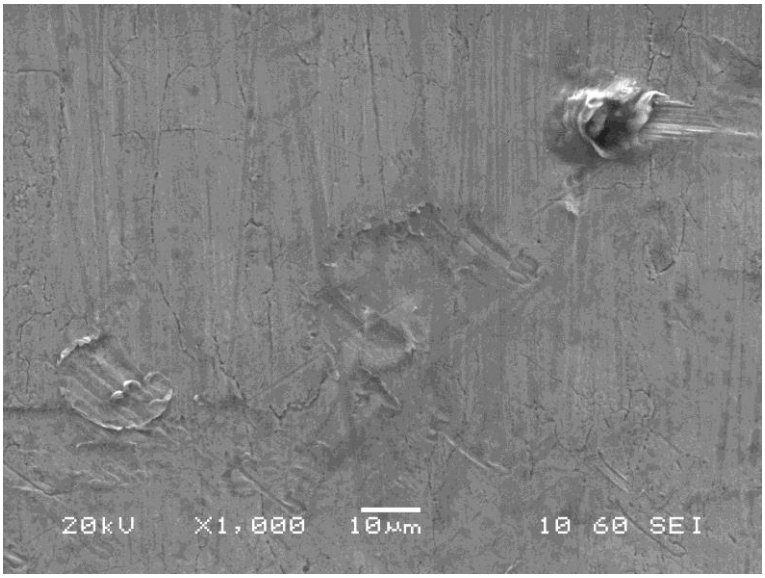

Figure 6.5: Surface image (raw nickel)

6.1.4.2. Electrolyser H Nickel

On Figure 6.6 there are a series of white deposits on the surface, each approximately 50 µm in length (to be identified by the surface chemistry characterisation). These large deposits are also surrounded by many smaller deposits of < 5 µm. The face also no longer shows the thin vertical pin-striping seen on Figure 6.6 (a&b). Instead, clear horizontal lines are seen, as well as some contouring of the surface.

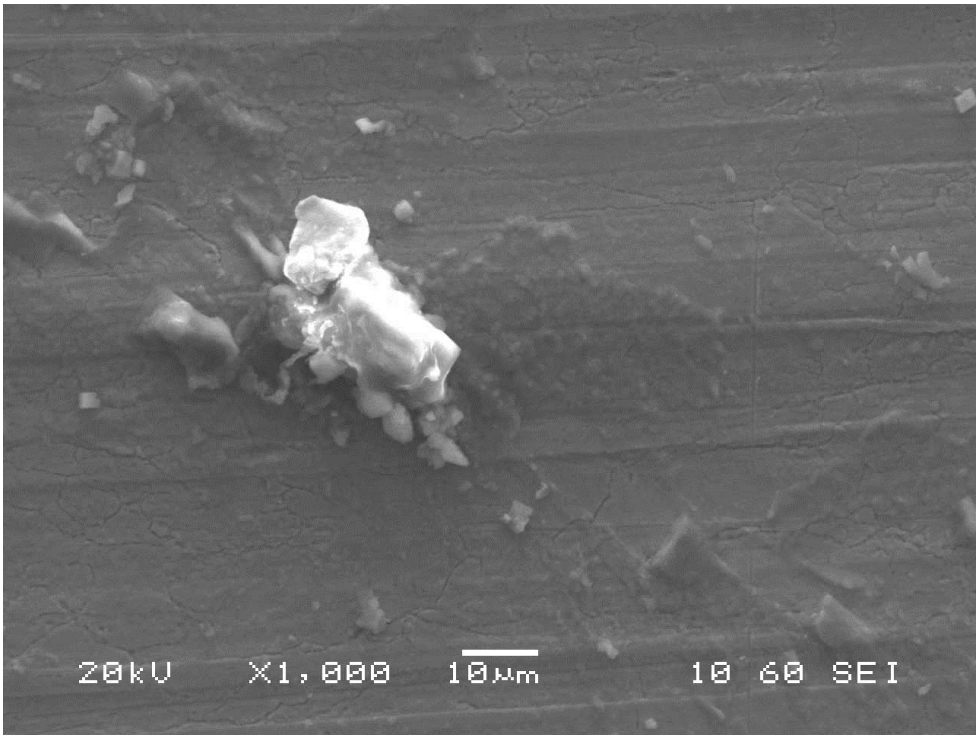

(a)

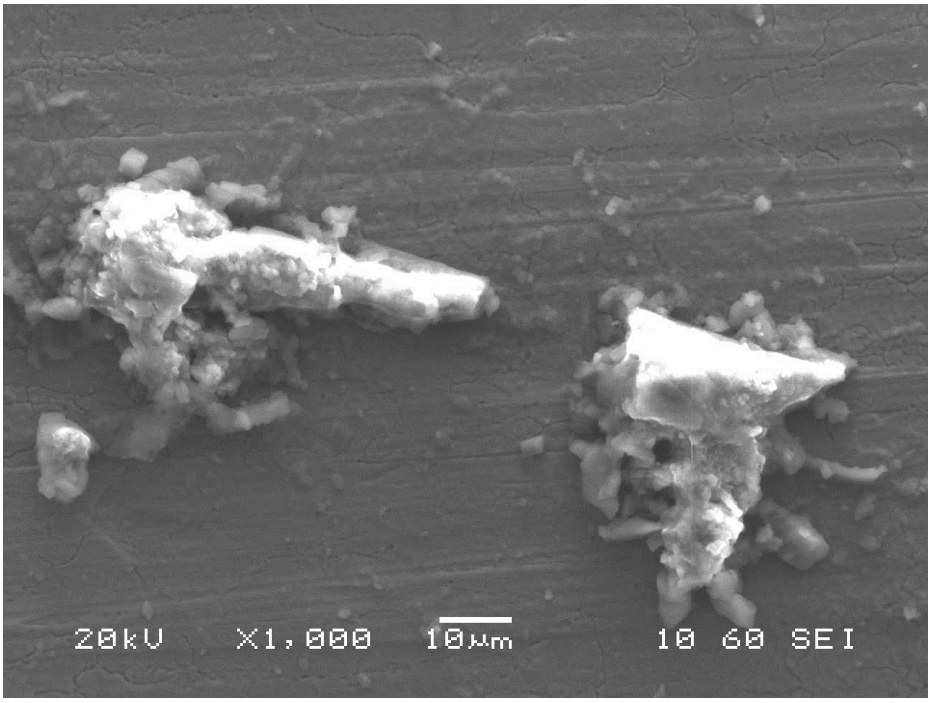

(b)

Figure 6.6: Electrolyser H (a&b) nickel surface image

6.1.4.3. Electrolyser I Nickel

On the flat face of the nickel from Electrolyser I (Figure 6.7 (a&b)), there are once again many solid crystalline deposits on the surface, although the main deposits are smaller but more numerous; the largest of those being 25 μm. The horizontal lines on this sample are more defined than on Electrolyser H.

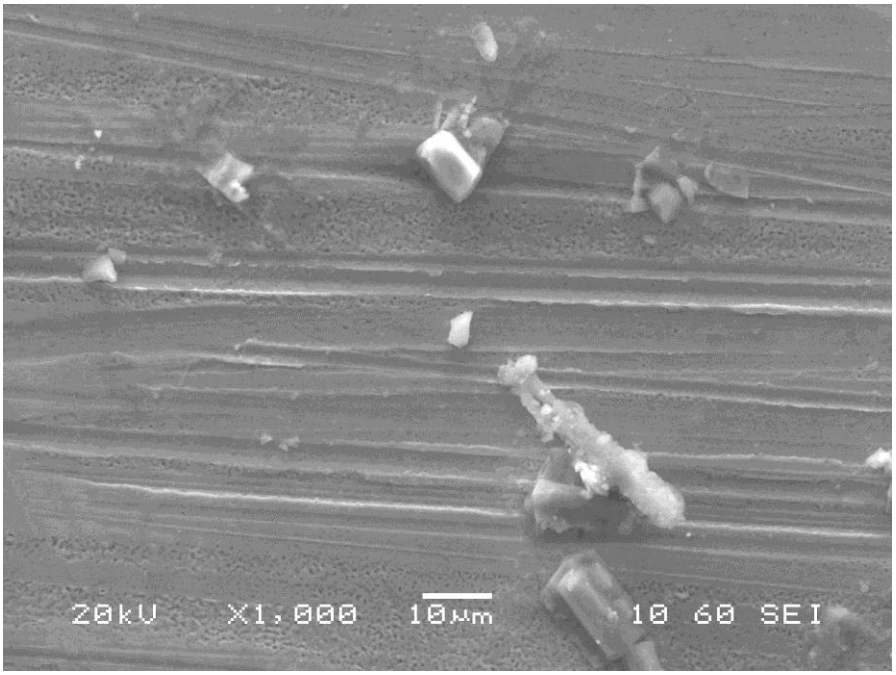

(a)

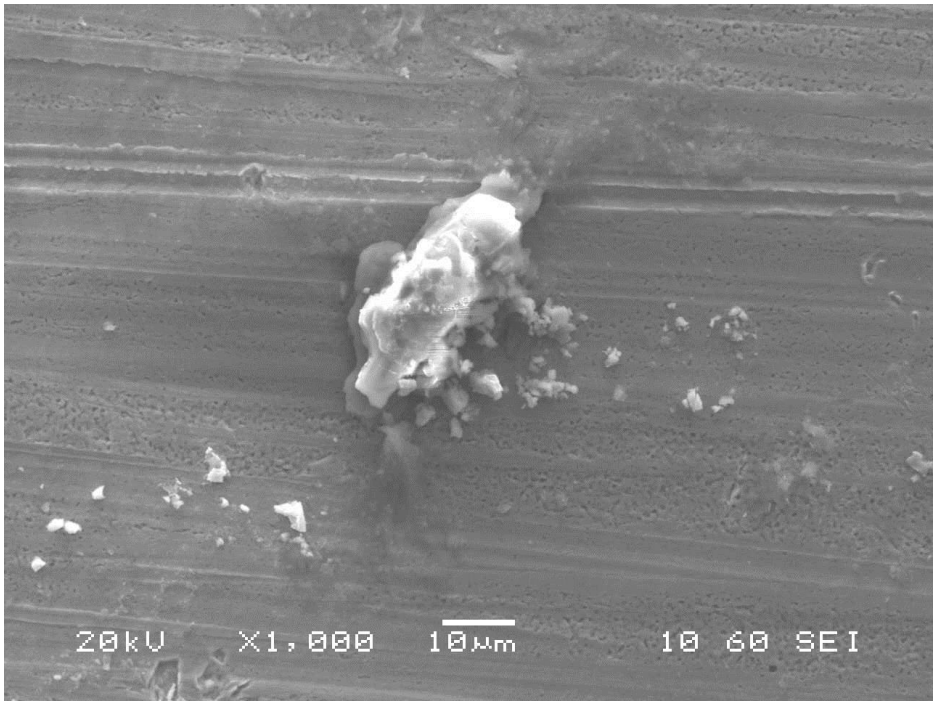

(b)

Figure 6.7: Electrolyser I (a&b) nickel surface image

6.1.4.4. Raw Titanium

Similarly to the nickel, a raw titanium sample was imaged to have a control sample against which the used titanium could be compared. The face of the raw titanium (Figure 6.8) shows some scarring and a few minor crystal structures on the surface.

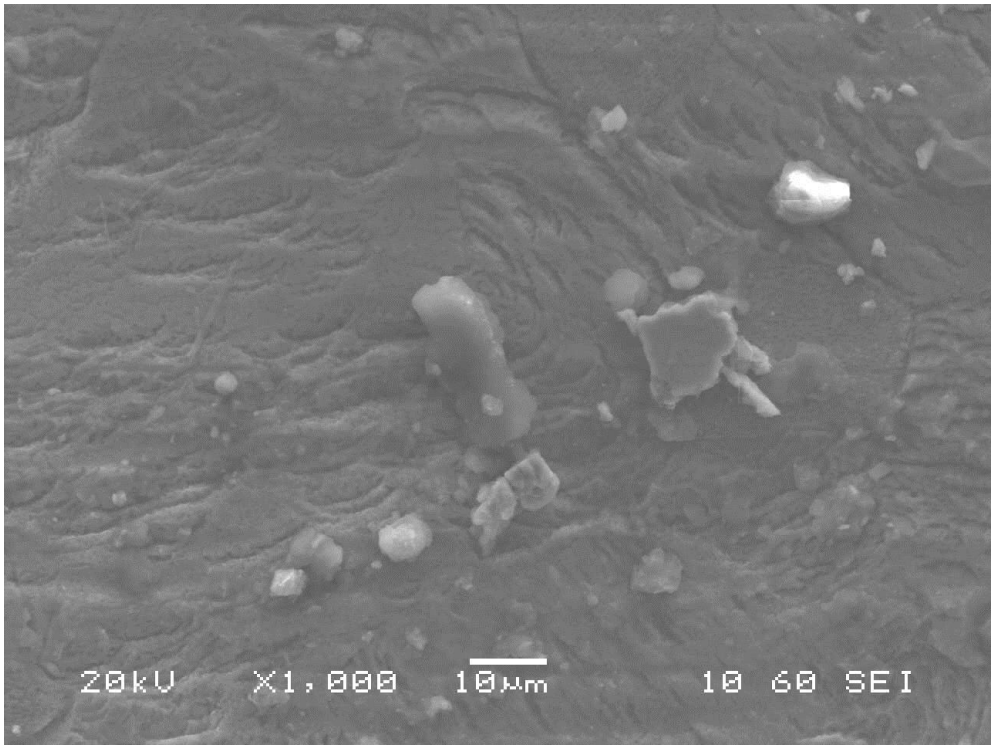

Figure 6.8: Surface image (raw titanium)

6.1.4.5. Electrolyser I Titanium

The face view (Figure 6.9) is noticeably more scarred than the raw titanium and shows deeper cervices in the surface. Any variation in surface composition will be identified by EDX.

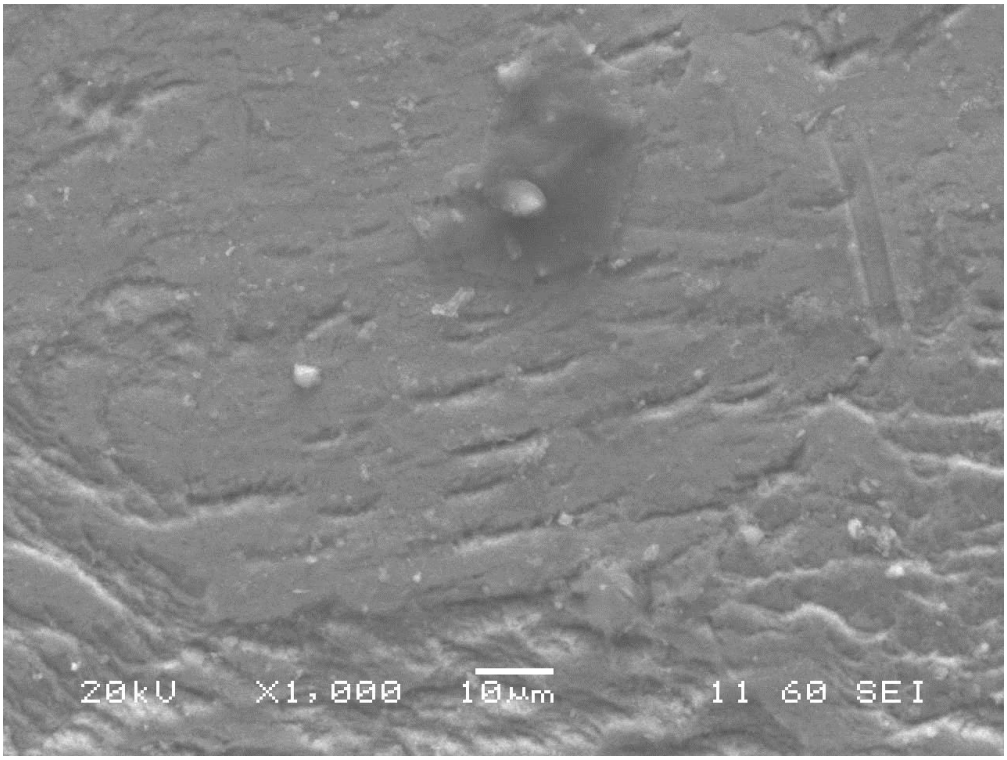

Figure 6.9: Surface image (Electrolyser I titanium)

6.1.5. Energy-Dispersive X-Ray Spectroscopy (EDX)

6.1.5.1. Nickel (1, 2 & 3)

For all nickel samples, analysis carried out at x500 magnification focused on the planar surface of each sample. Damage to the surface from the electrolysis process may have allowed other metals to be present on the surface and any deposits found (predominantly after use) would be investigated to see if this was a large increased build-up of oxide layer. The atomic% for nickel, titanium and oxygen for the nickel samples is shown in Table 6.1.

Table 6.1: EDX Elemental Composition of Nickel Samples

Sample	Atomic%					
	Nickel	**Titanium**	**Oxygen**	**Carbon**	**Silicon**	**Nitrogen**
Raw Nickel	0.40	0.00	18.2	50.08	25.03	6.29
Electrolyser H	0.21	0.00	31.1	42.27	21.14	5.28
Electrolyser I	0.27	0.01	25.9	45.40	22.71	5.71

When comparing the flat surface spectra data for the control sample, Electrolysers H & I, the main differences are the levels of nickel and oxygen. A 12.9 atomic% increase in oxygen content appears on Electrolyser H nickel compared to the unused sample, which coincides with 0.19 atomic% decrease in nickel content between the two samples.

There is a 5.2 atomic% decrease in oxygen content on the nickel surface of Electrolyser I compared to Electrolyser H showing that the presence of the titanium has reduced the quantity of oxide layer formation, helping to reduce the rate of nickel electrode degradation. This is further evident with the increase of 0.06 atomic% nickel content on the Electrolyser I nickel relative to Electrolyser H nickel.

6.1.5.2. Titanium (4 & 5)

The EDX data for raw and used titanium is shown in Table 6.2.

Table 6.2: EDX Elemental Composition of Titanium Samples

Sample	Atomic%					
	Nickel	**Titanium**	**Oxygen**	**Carbon**	**Silicon**	**Nitrogen**
Raw Titanium	0.00	0.22	27.5	44.48	22.23	5.57
Electrolyser I	0.01	0.19	32.2	41.80	20.70	5.10

Electrolyser I titanium shows an increase in oxygen content when compared to the control sample (4.7 atomic%). This shows that an oxygen layer is present, which is consistent with titanium having a higher affinity for oxygen than nickel. Analysis on the used titanium content of the samples shows a 0.3 atomic% decrease, consistent with the increased oxygen content on the titanium Electrolyser I sample.

6.1.6. X-Ray Photoelectron Spectroscopy (XPS)

To support the EDX evidence provided, the samples (1-5) also underwent XPS analysis for further verification of the surface composition. Both nickel (1-3) and titanium (4-5) samples were analysed for nickel, titanium and oxygen content on the samples. The peaks were then integrated to determine the surface elemental composition in atomic%. This is shown in Table 6.3.

Table 6.3: XPS Elemental Composition of Nickel and Titanium Samples

Sample	Atomic%					
	Nickel	**Titanium**	**Oxygen**	**Carbon**	**Silicon**	**Nitrogen**
Raw Nickel	0.36	0.01	15.0	52.12	26.02	6.49
Electrolyser H Nickel	0.19	0.02	29.5	43.25	21.63	5.41
Electrolyser I Nickel	0.26	0.02	24.5	46.32	23.17	5.73
Raw Titanium	0.01	0.12	25.0	46.01	23.07	5.79
Electrolyser I Titanium	0.02	0.09	29.5	43.32	21.66	5.41

Table 6.3 shows a 94% increase in oxygen concentration on the nickel surface from raw nickel to nickel in Electrolyser H and then a 17% decrease in when compared to nickel

from Electrolyser I. This is consistent with the analysis shown in the SEM and EDX analysis.

The metallic composition shows a 43% decrease in nickel content on the Electrolyser H nickel compared to the raw nickel samples and a 25% increase in nickel content of Electrolyser I compared to Electrolyser H nickel. The titanium content on the titanium samples decreases by 23% on the Electrolyser I titanium when compared to the raw titanium sample; consistent with the hypothesis of this paper.

6.2. Conclusions

The research in this chapter has analysed the effect of introducing titanium to the alkaline electrolysis system as a sacrificial metal. The electrochemical performance of Electrolyser H decreased at a faster rate than Electrolyser I, specifically after a 2 day stationary period mimicking real world operation. The only difference between the cells is the titanium; therefore this is the determining factor in the improved electrochemical performance of Electrolyser I when compared with Electrolyser H.

The conclusions drawn from the electrochemical analysis is backed up with the findings from the surface analysis. This also points towards a decrease in oxide layer formation on the nickel electrode in Electrolyser I when compared to Electrolyser H. The elemental composition of the surface of nickel and titanium from Electrolysers H & I has shown an increased presence of oxygen on the electrode surface. It is concluded that the presence

of titanium as a sacrificial metal in an alkaline electrolysis system with nickel electrodes, increases the electrical efficiency and decreases the rate of electrode degradation over two weeks of operation.

Future work in this field will investigate the use of metals which are more oxyphilic than titanium as they may yield better long term electrolyser performance. Research should also look at different titanium geometries, for example sponges, plates and spheres, and the effect that varying titanium loadings has on the thickness of oxide layer formation on nickel electrodes in an alkaline electrolyser. The potential utilisation of a sacrificial metal to the electrolysis system could reduce the degradation, but will not remove it. Alkaline electrolysis is the most established water electrolysis technology, but is not ideal for future wide scale commercialisation of electrolysers due to the degradation implications as discussed here and the usage of harmful caustic solutions.

PEM electrolysis technology represents a more attractive alternative to alkaline electrolysis with ultrapure water input, modular design and ability to handle variable loads (critical when linked to renewable energy sources). This technology is currently more expensive than the previous (alkaline), but the cost is reducing with decreasing PGM electrocatalyst being used. Another disadvantage to PEM electrolysis is the requirement for ultrapure water, which is another energy consuming process. There is very little research on the effect of water quality on PEM electrolysis and this investigated in the next chapter.

Chapter 7

PEM Electrolysis – Feed Water Analysis & Optimisation

PEM Electrolysis is a commercial technology that uses a solid polymer electrolyte (SPE) and ultrapure water (instead of alkaline solution) for splitting water. The use of this SPE makes the electrolyser adaptable for managing varying loads (from renewable resources), and the use of water instead of a caustic solution makes it more end-user friendly [61, 199-202]. PEM technology can meet short term goals/expectations from an electrolyser.

The disadvantages of PEM electrolysis are the high cost of the platinum group metal (PGM) which are used as catalysts to split water into hydrogen and oxygen [26, 61, 71, 200]. The high cost is down to the rarity of these platinum group metals and highlights a major problem towards the mass commercialisation of this technology. The cost of these catalysts will only increase with growing demand for them [28].

The use of the PGMs is a factor in the requirement of ultrapure water (inconvenient for domestic commercialisation). The impurities in conventional tap water deactivate the catalysts and rapidly reduce the lifetime of the system [33, 61, 71, 99, 160, 161, 199]. The purification of water is an additional cost process in the system, and an electrolyser which could operate efficiently with tap water the only input is much more appealing to the general public. As a result, this could see the use on non-PGMs in the electrolysers and subsequently reduce the cost substantially [24, 203].

The work examines the performance of identical Membrane Electrode Assemblies (MEAs) with varying purities of water to analyse the electrochemical performance and the microscopic properties after experimentation.

7.1. Feed Water Properties

For the various water qualities used, samples were taken and analysed to identify elements present in solution (ICP-MS), the organic carbon content (TOC) and the quantity of ions present in solution (conductivity). Five samples were tested, including the four in Table 7.1 from which the tap water therein is taken from our laboratory in Birmingham, U.K., and an additional tap water sample from London, U.K. was analysed. This shows the variance in water composition dependant on two different geographical locations.

Table 7.1: Basic Properties of Different Grades of Water [204]

Water Properties		**ASTM (D1193-91)**			
Contaminant	Parameter	Type I	Type II	Type III	Type IV
Ions	Resistivity at 25°C / MΩ.cm	18	10.0	4.0	0.2
	Conductivity at 25°C / $\mu S.cm^{-1}$	0.056	0.1	0.25	5.0
Acidity	pH at 25°C	-	-	-	5.0-8.0
Organics	TOC / max ppb (µg/l)	10	50	200	No Limit
Sodium	ppb	< 1	< 5	< 10	< 50
Chloride	ppb	< 1	< 5	< 10	< 50
Colloids	Total Silica / (µg/mL)	< 3	< 3	< 500	No Limit

7.2. MEA Characterisation & Analysis

7.2.1. System Optimisation

7.2.1.1. Piston Pressure

The pressure exerted by the pistons forces together and compresses the MEA, titanium sinter and mesh. The various polarisation curves from 1.5V to 3.5V for varying piston pressures is shown in Figure 7.1.

Figure 7.1 shows that the polarisation of the MEA improves with increasing piston pressure. This increasing pressure is reduces the contact resistance between the power connection, the mesh, sinter and surface of the MEA, subsequently reducing the resistance. For the remaining experimental procedures the piston pressure was maintained at 20 bar pressure to ensure good MEA/electrode contact surface area.

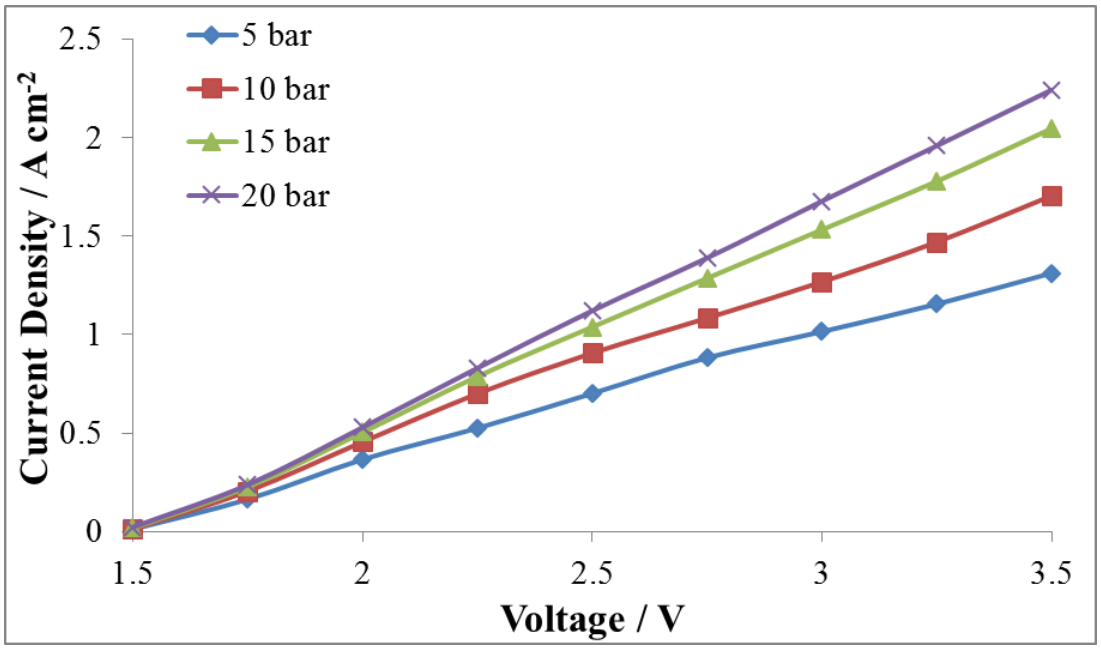

Figure 7.1: Polarisation for Varying Piston Pressure with Type I Water and 80 ml/min water flow, at 25°C, 0.1V scan rate, 1 atm pressure

7.2.1.2. Feed Water Flowrate

The feed water held in the reservoirs is pumped through the electrolysis cell as show in Figure 3.28 and exited the electrolysis cell along with the gas evolved to the reservoir vessels. The constant flow of the water to the cell keeps the MEA hydrated and enables the mechanical removal of bubbles from the electrode surfaces. The water flowrate was varied to optimise the performance and the data shown in Figure 7.2.

Figure 7.2 shows no change with in polarisation from 20 ml/min to 80 ml/min. Fluid velocities below 20 ml/min exhibit decreased performance due to occupancy of bubbles on the MEA nucleation sites. All future experiments from here on were supplied with a constant 80 ml/min of feed water to ensure sufficient flow velocity through the electrolysis cell to keep the MEA hydrated and operational efficiency high.

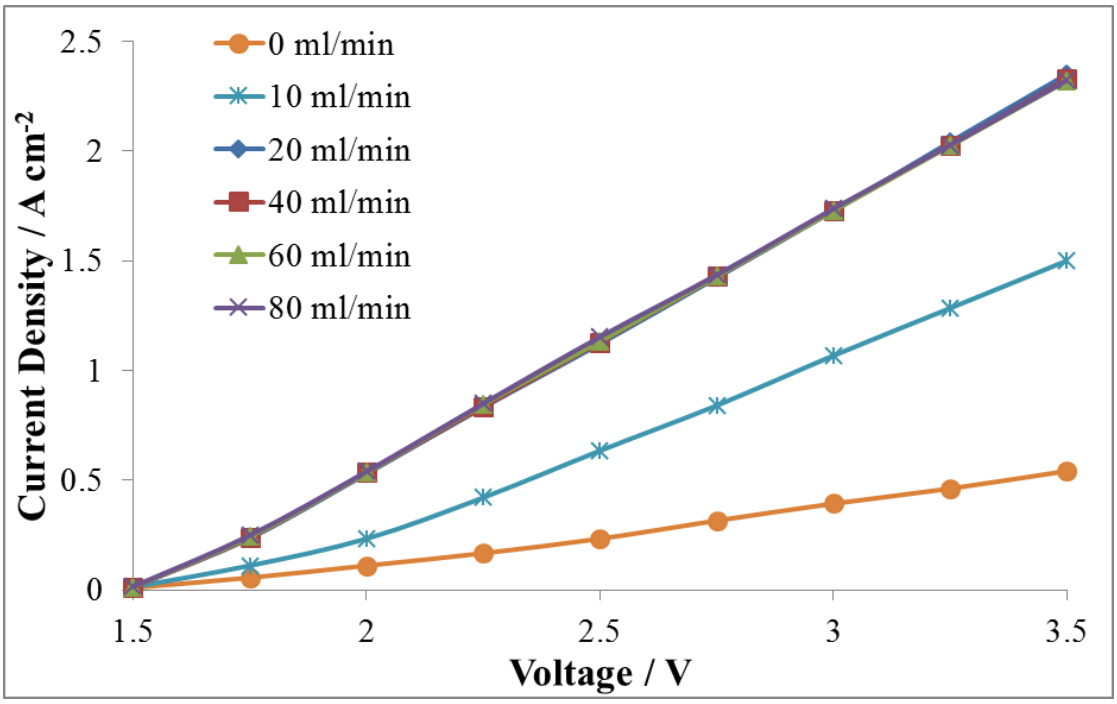

Figure 7.2: Polarisation Varying Water Flow with Type I Water and 20 Bar Piston Pressure at 25ºC, 0.1V scan rate, 1 atm pressure

7.2.2. Inductively Coupled Plasma Mass Spectroscopy (ICP-MS)

Figure 7.3 shows the quantity of the cations present in each water sample. The data shows no measurable cation content in 18 MΩ and 10 MΩ water; therefore suitable for long term operation in current PEM electrolysis technology. Water with a resistance of 1 MΩ shows small quantities of sodium and calcium ions present, which will hinder the long term performance of a PEM electrolyser using this grade of water as the feedstock.

The tap water samples show a significantly different cation content for tap water accessed in differing geographical locations. Shown here by the significantly higher cation content in tap water obtained in London, U.K. and Birmingham, U.K.

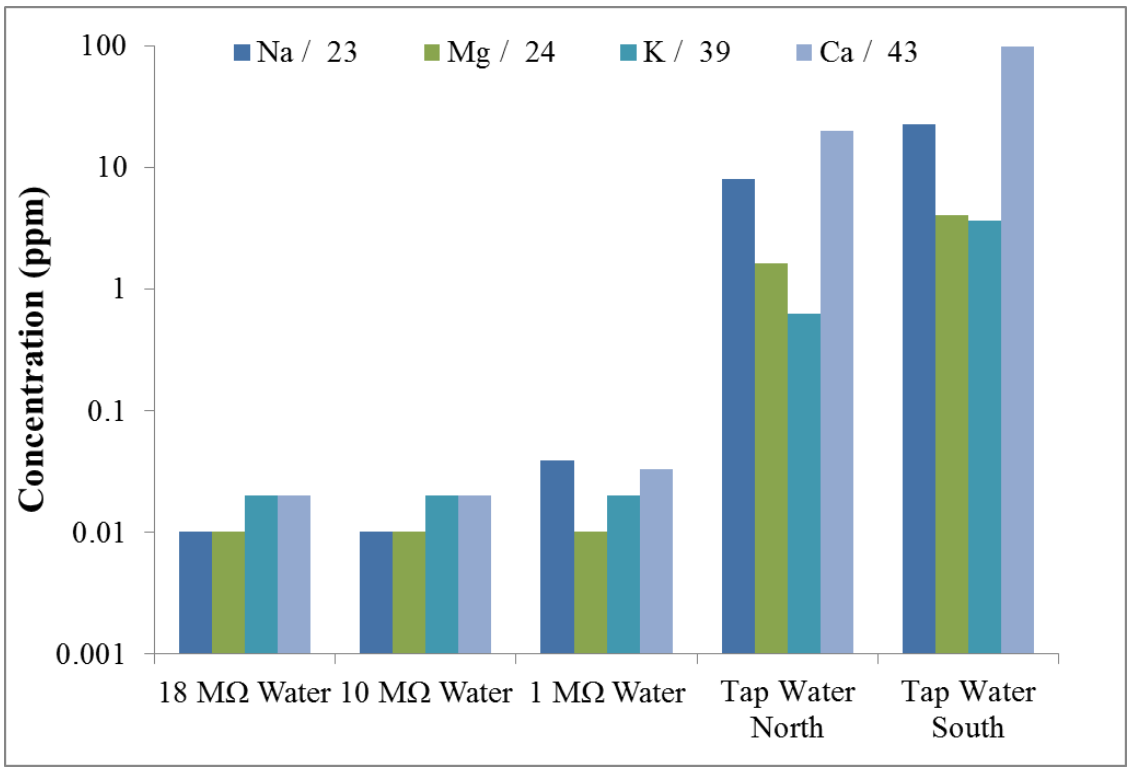

Figure 7.3: ICP-MS Analysis for 5 different water qualities

7.2.3. Total Organic Carbon (TOC) Analysis

Figure 7.4 shows the non-purgeable organic carbon (NPOC) for the five different water samples. The data shows a very low NPOC for 18 MΩ & 10 MΩ water making it suitable for use in current PEM electrolysis technology. Increasing the conductivity of the water to 1 MΩ results in an increase in TOC to 6.7 mg/L, which is less desirable for use with current PEM technology as the presence of the organic carbon will degrade the performance of the electrolyser over time (build-up of carbons on the nucleation sites will irreversibly decrease the performance).

Figure 7.4 shows the two tap water samples exhibit much higher quantities of NPOC than the purified water samples which is to be expected. The high presence of organic carbons in the water makes it incompatible with current PEM technology, and if applied would reduce the performance of the electrolyser in a very short period of time.

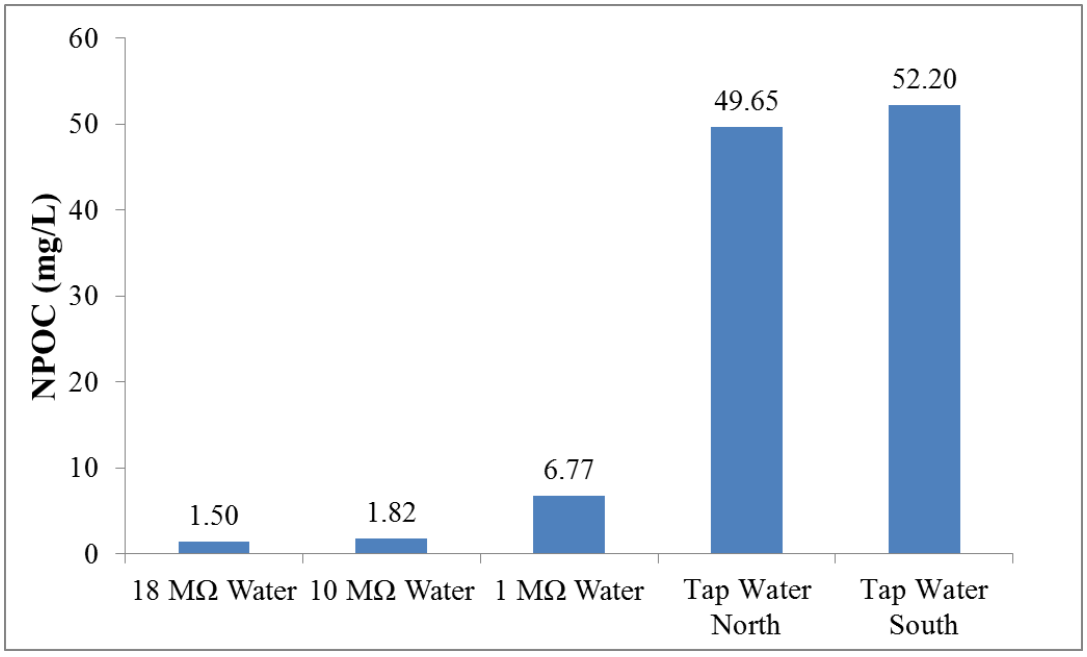

Figure 7.4: NPOC Analysis for 5 different water qualities

The analysis complied in this section on the quality of various water sources will be further investigated through the experimentation of a PEM electrolysis cell with these different water qualities.

7.2.4. Membrane #1 - Nafion®117

7.2.4.1. Polarisation

The MEAs were characterised in various grades of water as mentioned previously. The voltage across the PEM electrolysis cell was varied and the subsequent current flow measured and converted to current density (A cm^{-2}). This is shown in Figure 7.5.

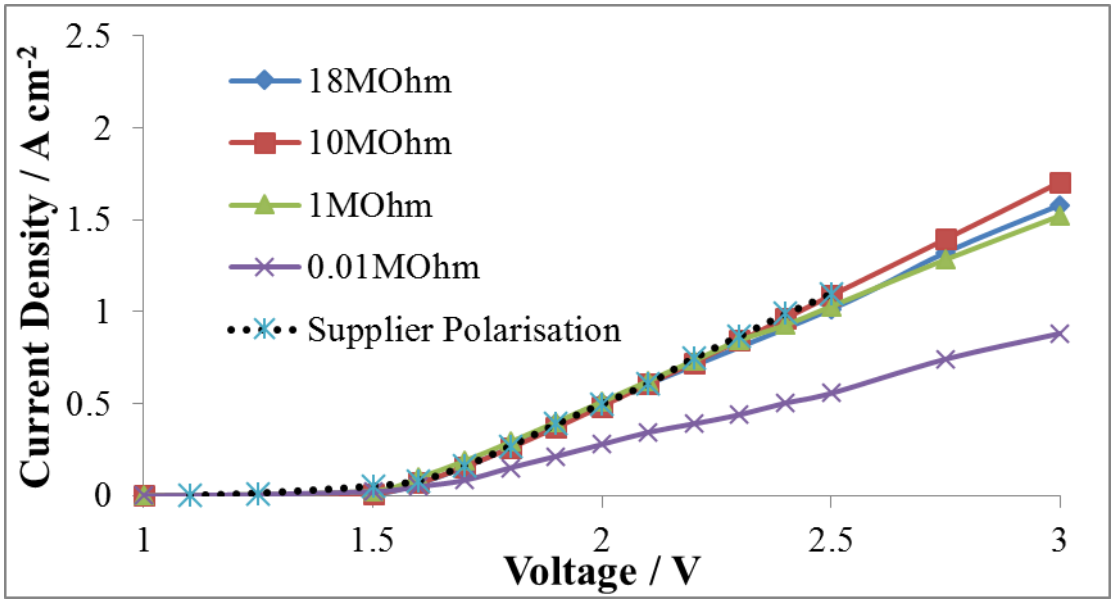

Figure 7.5: Nafion®117 based MEA Polarisation at 25°C, 0.1 V scan rate, 1 atm pressure, 20 bar piston pressure, 80ml/min water flowrate

The purified water samples show similar electrochemical behaviour which expected due to the low ion content in the water and haven't been subjected to prolonged exposure with

ions in the water. This exposure will decrease the electrochemical performance over time, whereas this experiment was only a 30 minute polarisation. The polarisation with 18MΩ deionised water mimics that provided from the supplier and is outside of the PEM electrolyser performance recorded in literature, due to the low catalysts loadings [22, 31, 71, 91, 92, 201, 205-207].

Figure 7.5 showed a decreased polarisation with tap water. This is believed to be the result of cation build up subsequently blocking the nucleation sites and increasing the resistance in the electrolysis cell. This will later be confirmed in the microscopy analysis.

7.2.4.2. Electrical Efficiency

With the data collected during the polarisation, an electrical efficiency calculation for each potential and water quality was calculated. This is shown in Figure 7.6.

The data presented in Figure 7.6 shows a decrease in electrical efficiency as the applied potential across the electrolysis cell increases, i.e. the actual hydrogen gas evolution rate at the cathode is producing less than the theoretical production rate of hydrogen.

The efficiency across all four different grades of water are similar considering the variation in cation and organic carbon content, although degradation in electrolysis performance is not expected to be observed until after longer testing.

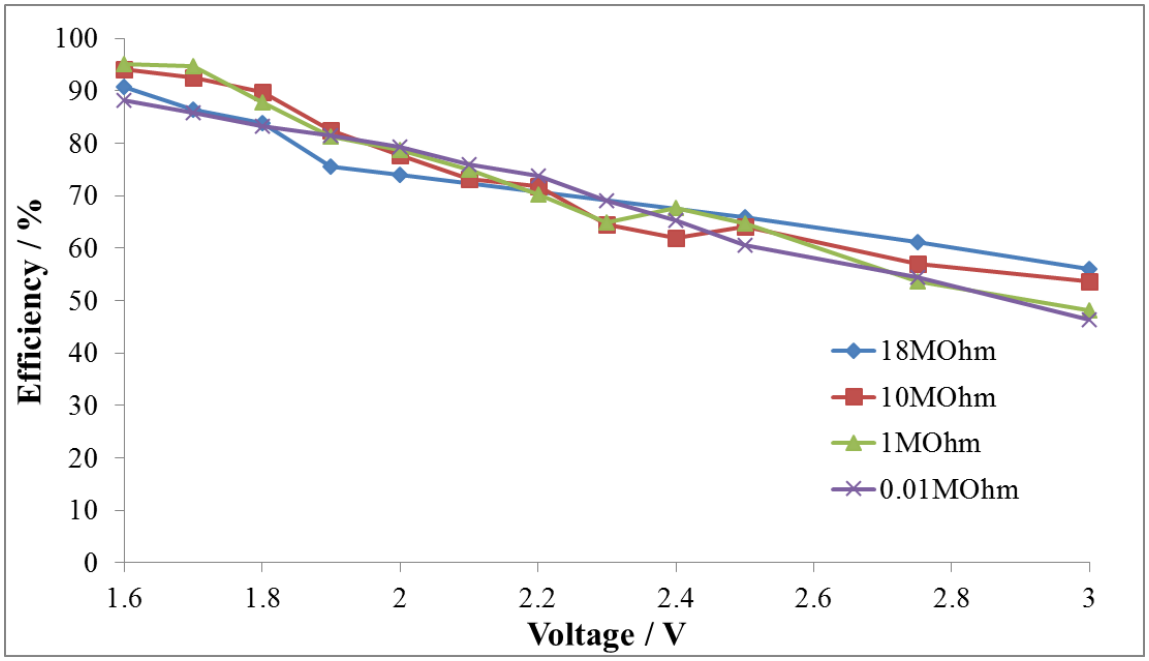

Figure 7.6: Efficiency of Nafion®117 based MEA at 25°C, 0.1 V scan rate, 1 atm pressure, 20 bar piston pressure, 80 ml/min water flowrate

7.2.4.3. Electrochemical Degradation

After initial characterisation, the electrolysis cells underwent long term degradation where the potential applied across the cell remained constant and the current flow varied with time. The purpose of this experiment is to quantify any degradation in electrochemical performance for the varying grades of water used in each experiment. The results are shown in Figure 7.7.

Figure 7.7 shows the water with a conductivity of equal to or greater than 1 MΩ maintained good electrochemical performance over the 8 hours of experimentation, with the current flow maintained with a current change with a positive gradient.

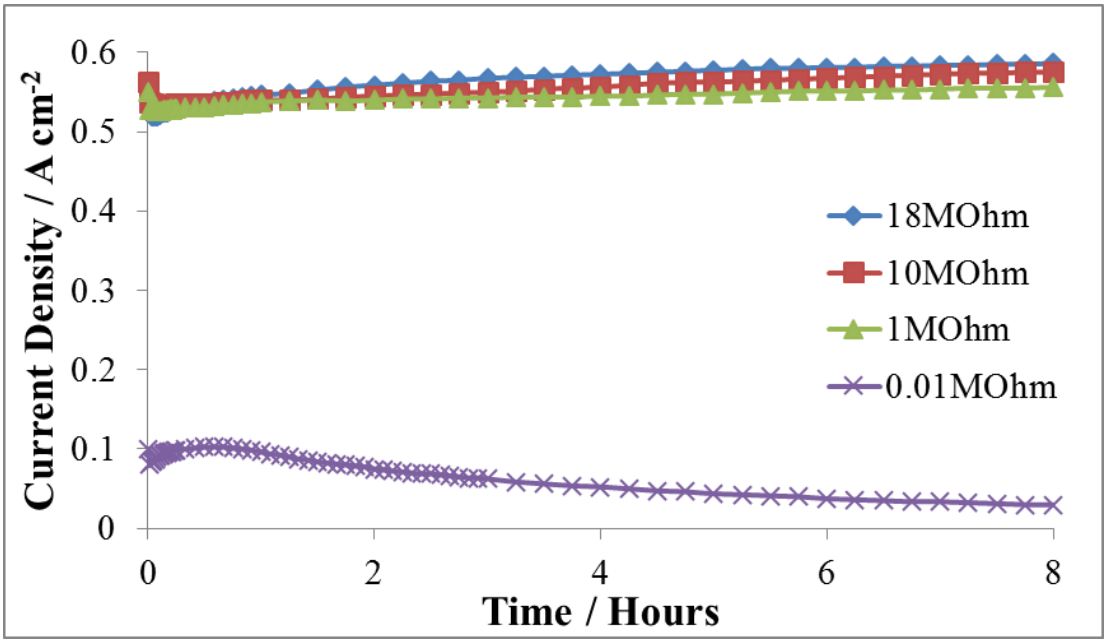

Figure 7.7: Degradation of Nafion®117 based MEA at 25ºC, 2 V, 1 atm pressure, 20 bar piston pressure, 80 ml/min water flowrate

In contrast the performance of the electrolysis cell in the tap water system is very poor. Peak voltage is achieved after 40 minutes of experimentation, from which the current decreases throughout the rest of the eight hour period. This rate of electrochemical cell degradation is unacceptable for commercial electrolysis and emphasises the scale of the problem with regards to enabling PEM electrolysis cells to function with tap water as the input. These results support those found in literature that cation poisoning of Nafion® MEAs hinders fuel cell/electrolyser performance [111, 114, 127, 135].

7.2.4.4. Scanning Electron Microscopy (SEM)

Microscopic analysis of the MEA is important to quantify degradation and anomalies on the surface. Cation build up on the Nafion® membrane limits the number of nucleation

sites available for proton exchange to occur, thus reducing the efficiency of the electrolyser. The MEAs from the electrolysis process will undergo image spectroscopy and surface composition spectroscopy to analyse any cation blockage of the porous membrane and impurity deposition on the MEA surface.

500x Pt

The lowest level of magnification on the MEAs show a planar smooth surface for the unused MEA and the 18MΩ MEA. The 10MΩ MEA shows evidence of roughness on the surface and the 1MΩ MEA exhibits increased roughness and the evolution of widening pores and cracks on the MEA. When observing the Tap Water MEA the surface roughness has increased hugely when compared to the other MEAs. The rigidness of the surface could be the result of corrosion or foreign species existent on the MEA. This will be investigated by EDX analysis in the next section.

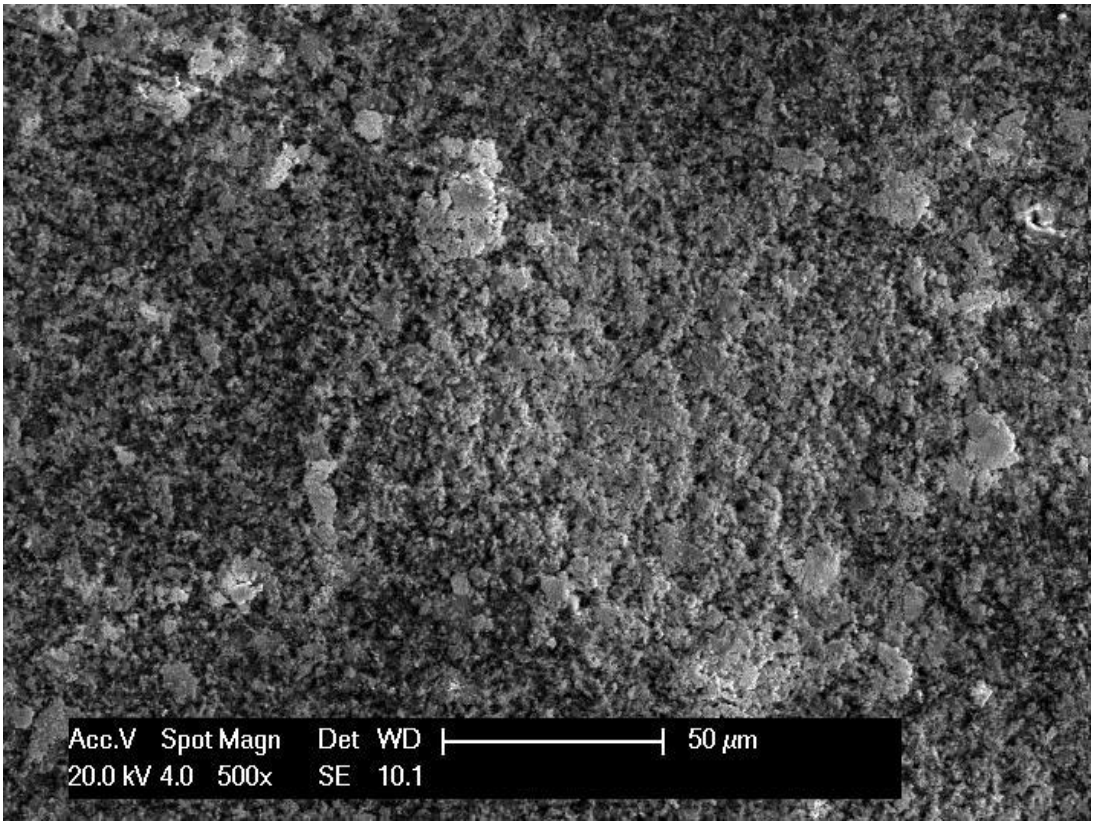
Acc.V Spot Magn Det WD 50 μm
20.0 kV 4.0 500x SE 10.1

(a)

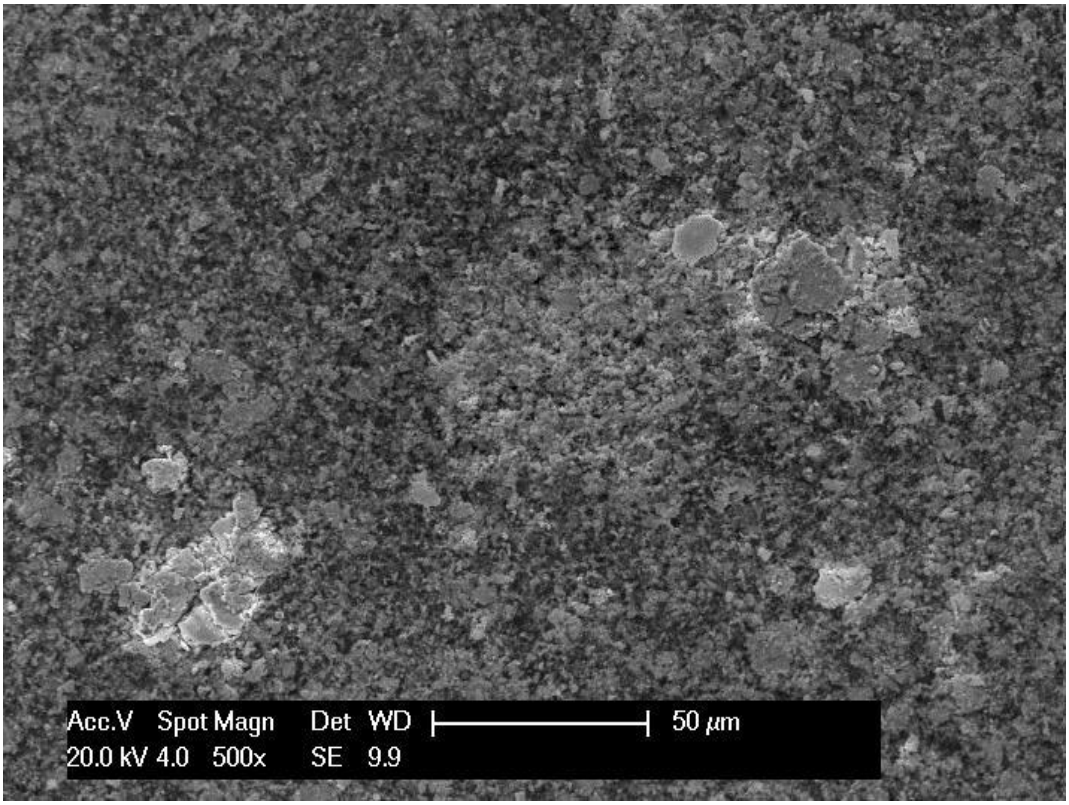
Acc.V Spot Magn Det WD 50 μm
20.0 kV 4.0 500x SE 9.9

(b)

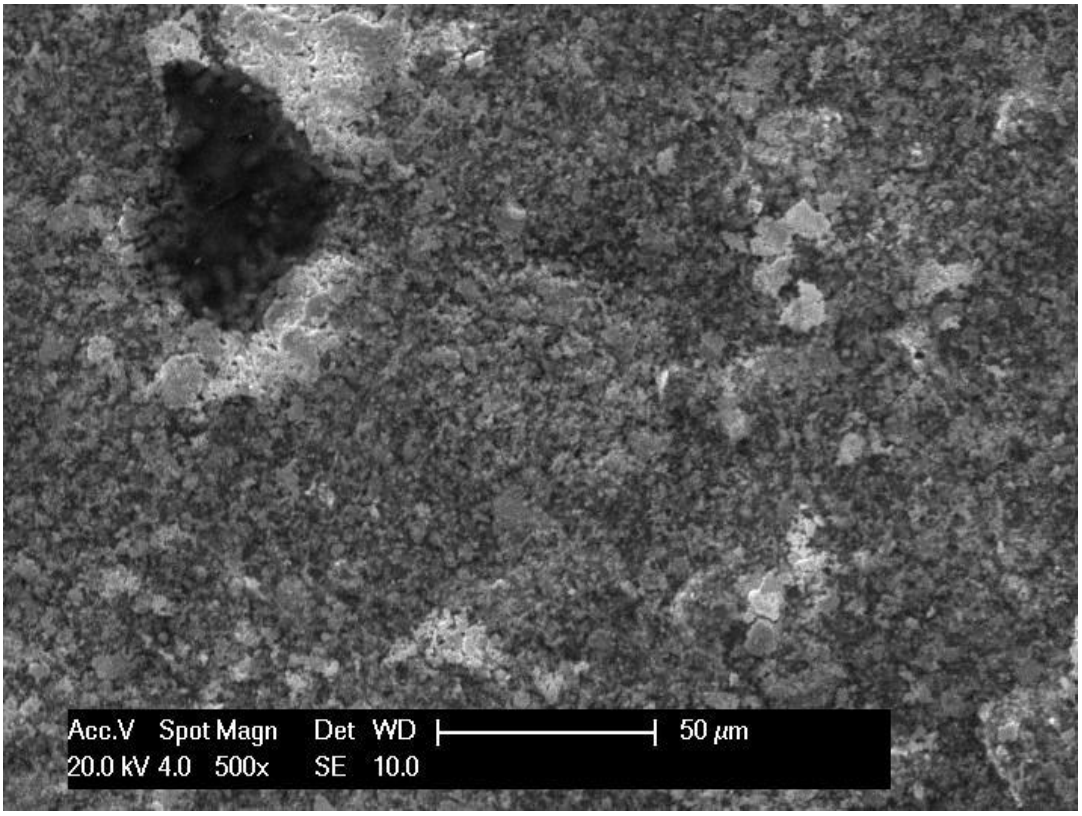
Acc.V Spot Magn Det WD 50 µm
20.0 kV 4.0 500x SE 10.0

(c)

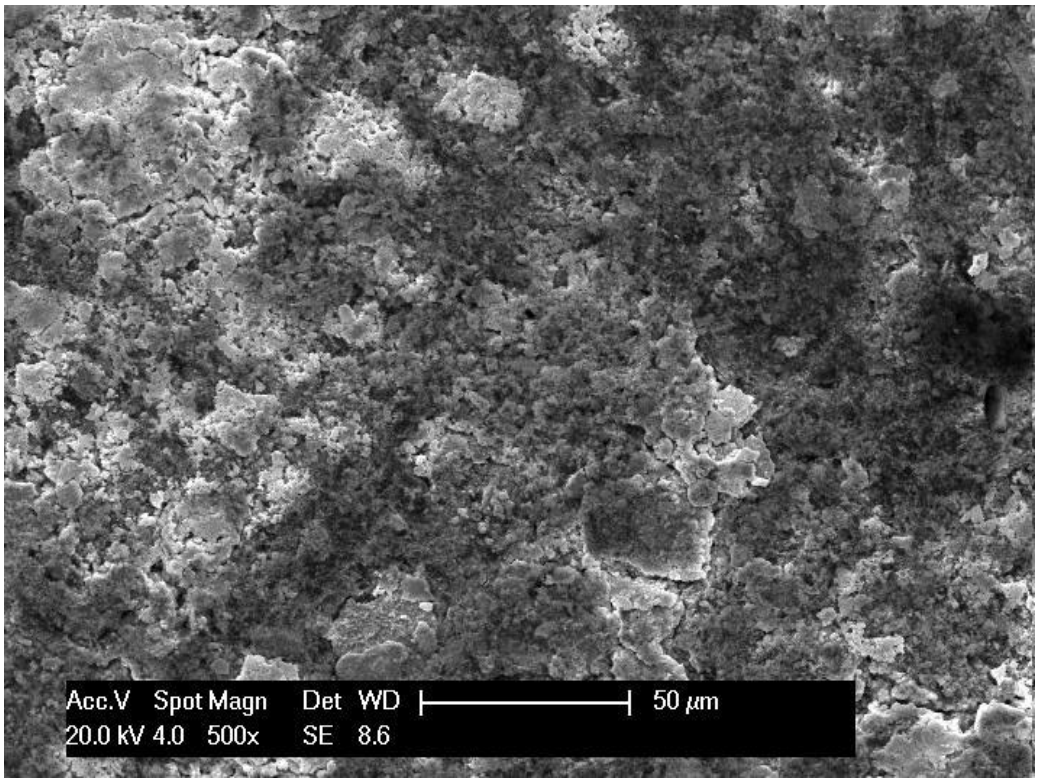
Acc.V Spot Magn Det WD 50 µm
20.0 kV 4.0 500x SE 8.6

(d)

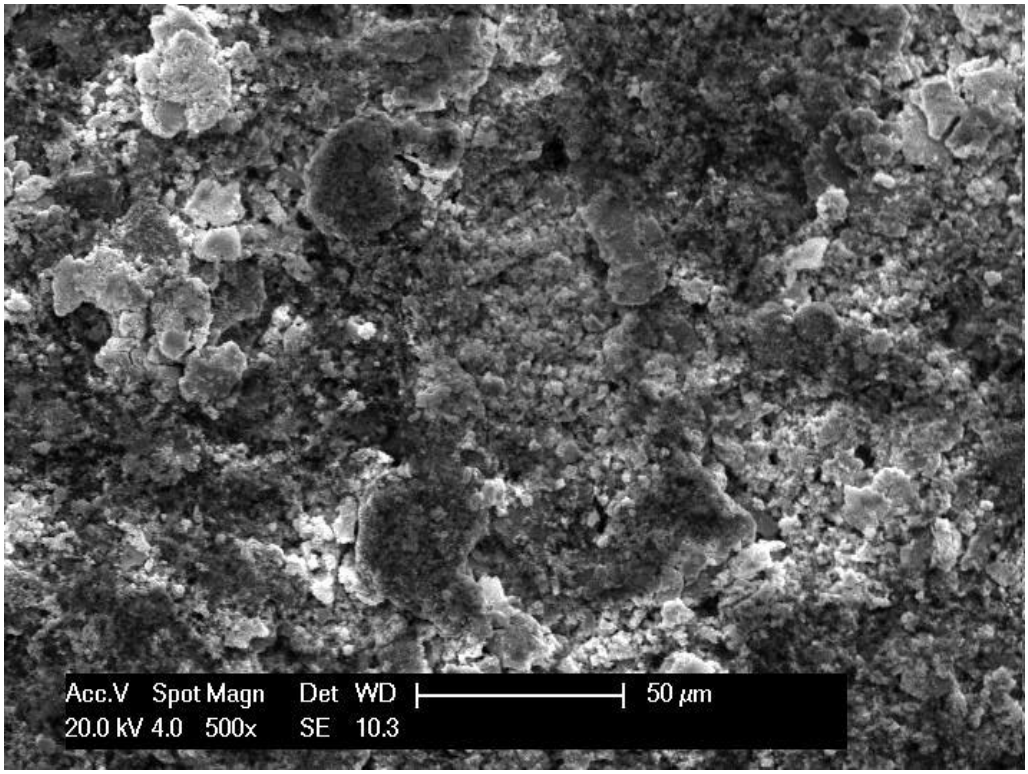

(e)

Figure 7.8: SEM 500x Magnification images of Nafion®117 cathode of (a) Unused MEA (b) 18 MΩ MEA (c) 10MΩ (d) 1 MΩ (e) Tap Water MEA

2500x Pt

When magnifying the previous images five times further, the surfaces of the MEAs appear much rougher than shown in a lower magnification. This undulating surface is characteristic of the catalyst layer which has been ultrasonically sprayed on the membrane surface. In this case the platinum black particles are the cause of the unevenness of the surface, but there is increased roughness on the Tap Water MEA when compared to the others could be the result of foreign ions on the MEA surface.

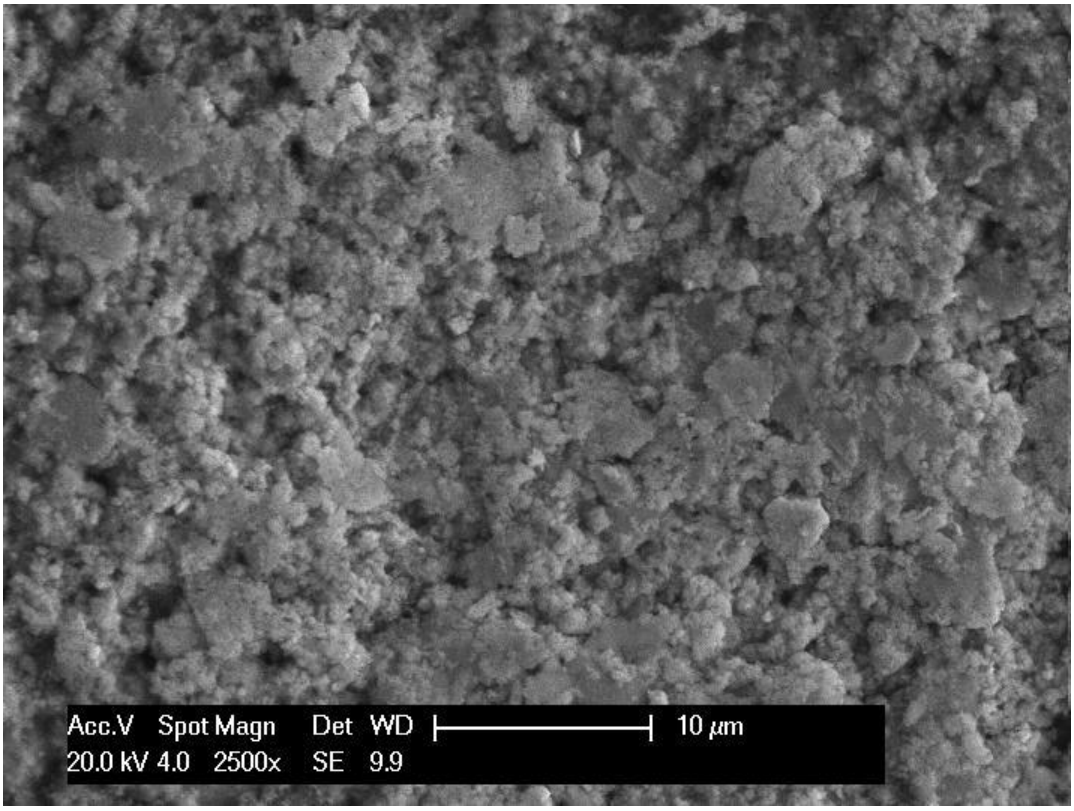
Acc.V Spot Magn Det WD 10 μm
20.0 kV 4.0 2500x SE 9.9

(a)

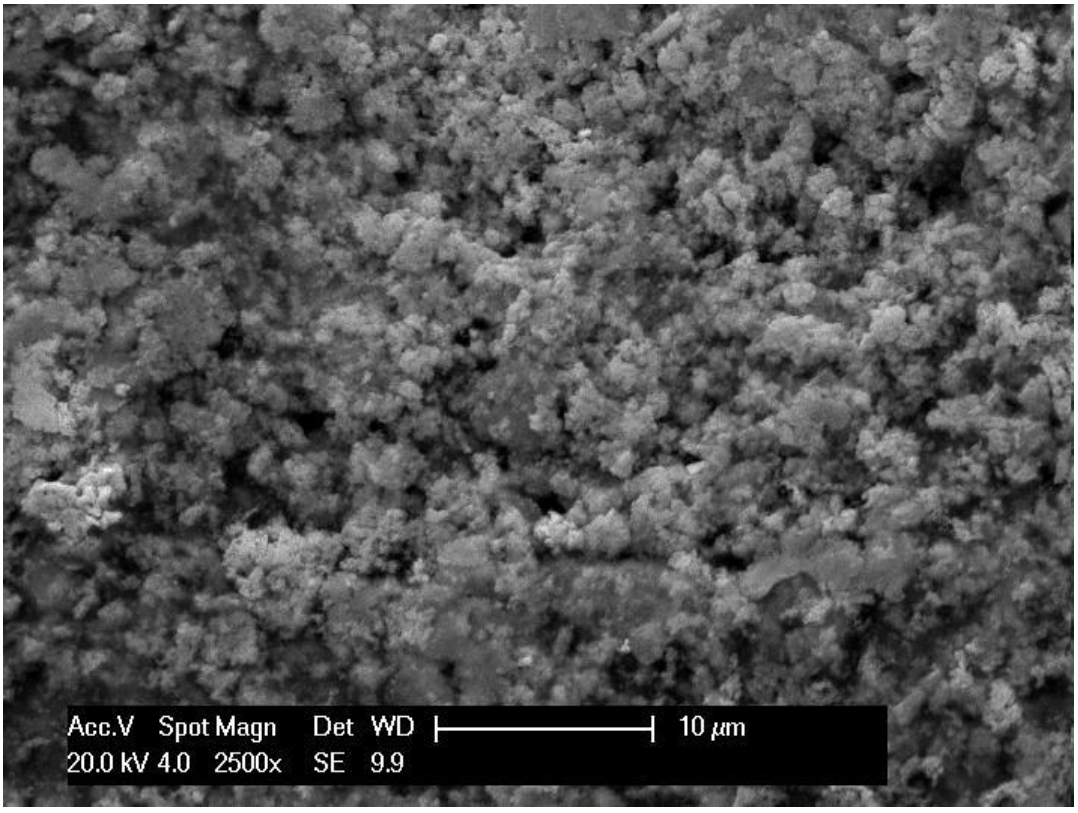
Acc.V Spot Magn Det WD 10 μm
20.0 kV 4.0 2500x SE 9.9

(b)

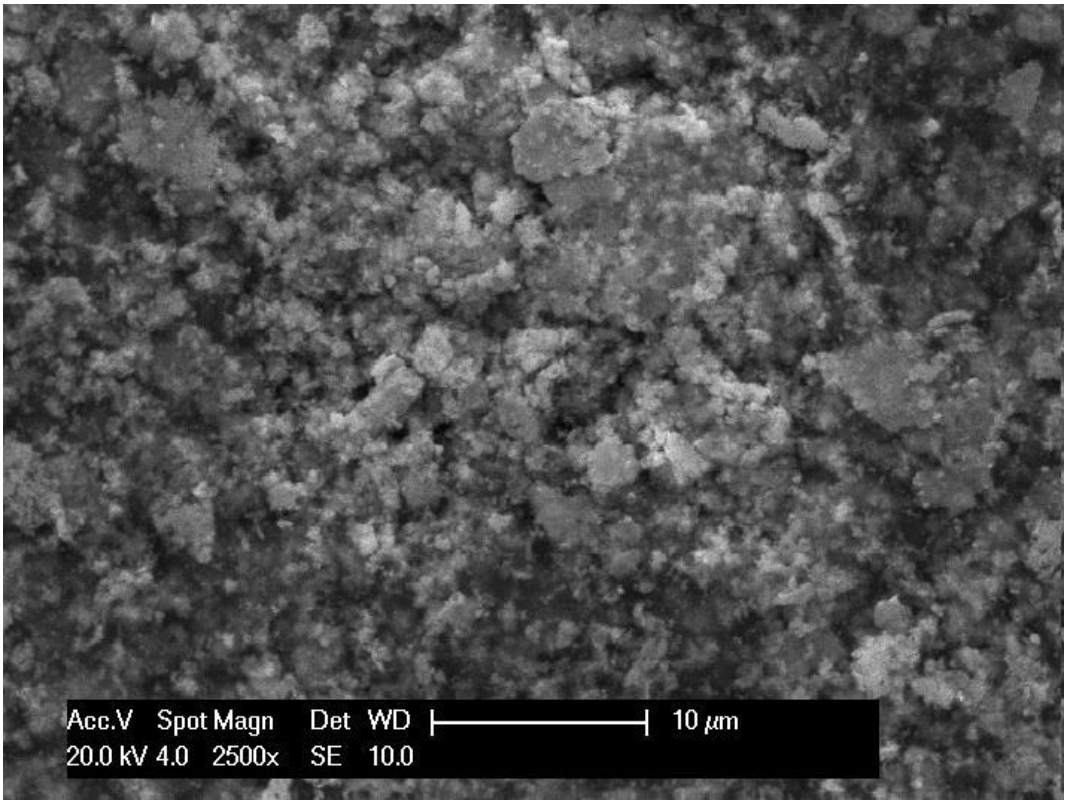
Acc.V Spot Magn Det WD 10 μm
20.0 kV 4.0 2500x SE 10.0

(c)

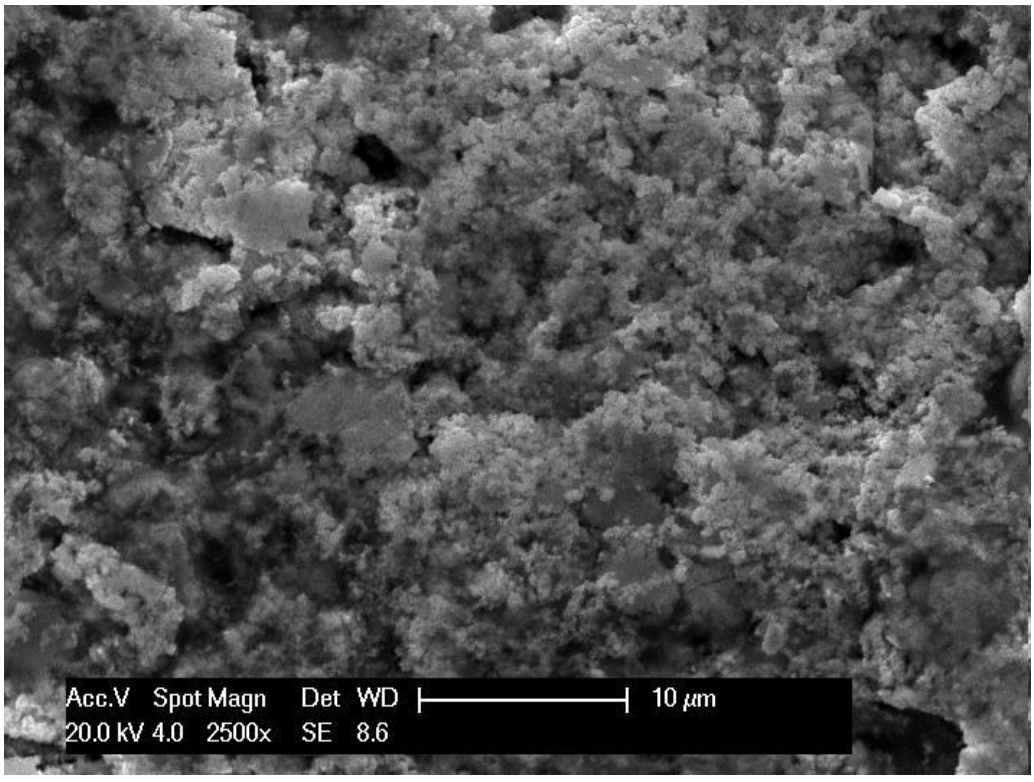
Acc.V Spot Magn Det WD 10 μm
20.0 kV 4.0 2500x SE 8.6

(d)

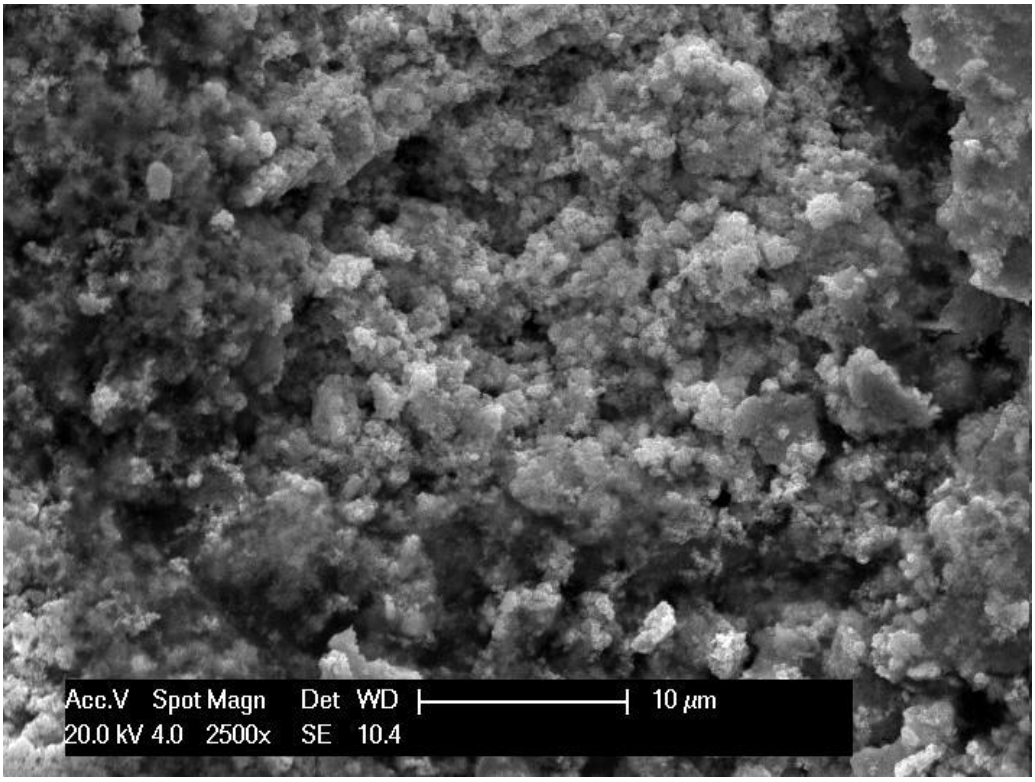

(e)

Figure 7.9: SEM 2500x Magnification images of Nafion®117 cathode of (a) Unused MEA (b) 18 MΩ MEA (c) 10MΩ (d) 1 MΩ (e) Tap Water MEA

5000x Pt

Upon further magnification of each MEA, the particulates scattered over the membrane become individually identifiable. Although minimal variation can be seen amongst the SEM images, the increase in coagulation of what is believed to be platinum particles is evident as the purity of the water used in experimentation decreases.

To analyse this images further, they will all undergo EDX analysis to identify the element composition of the MEA cathode surfaces.

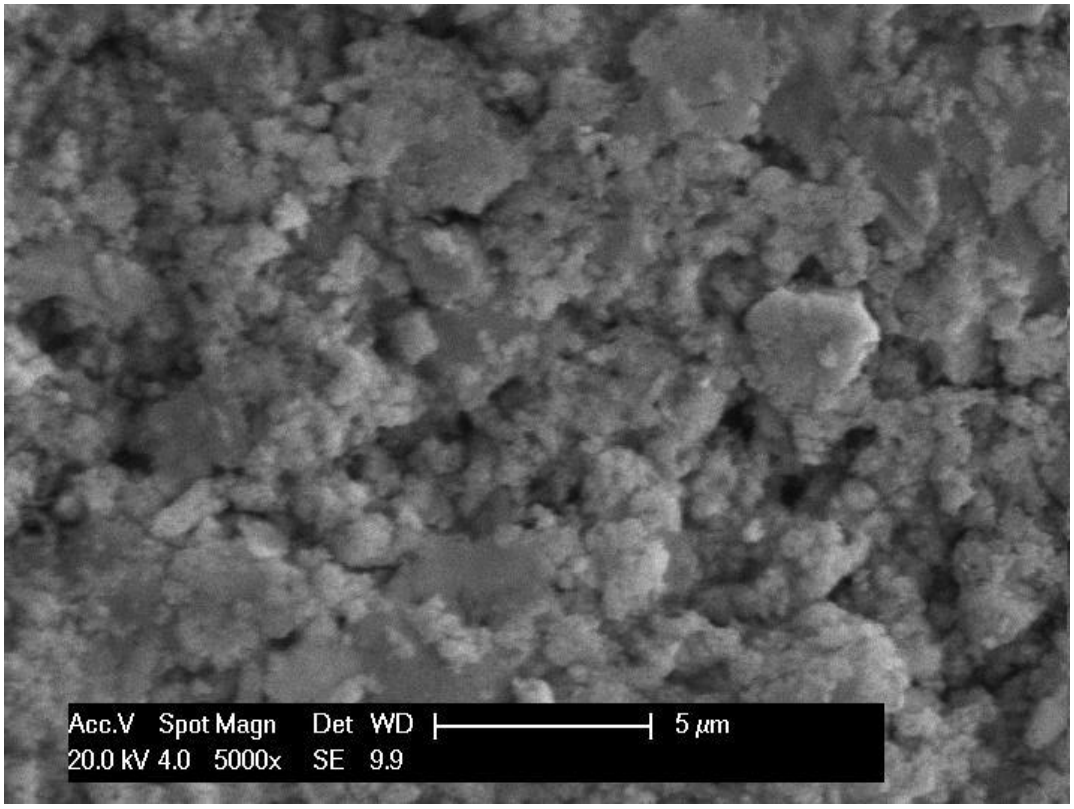
Acc.V Spot Magn Det WD 5 µm
20.0 kV 4.0 5000x SE 9.9

(a)

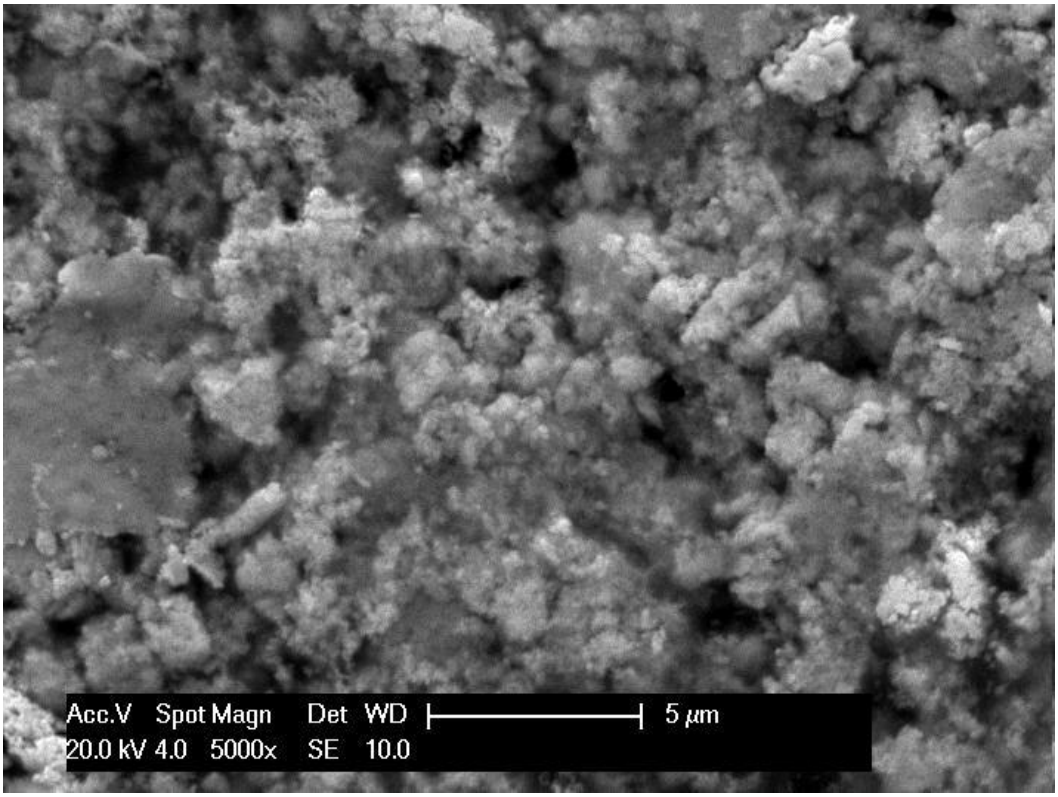
Acc.V Spot Magn Det WD 5 µm
20.0 kV 4.0 5000x SE 10.0

(b)

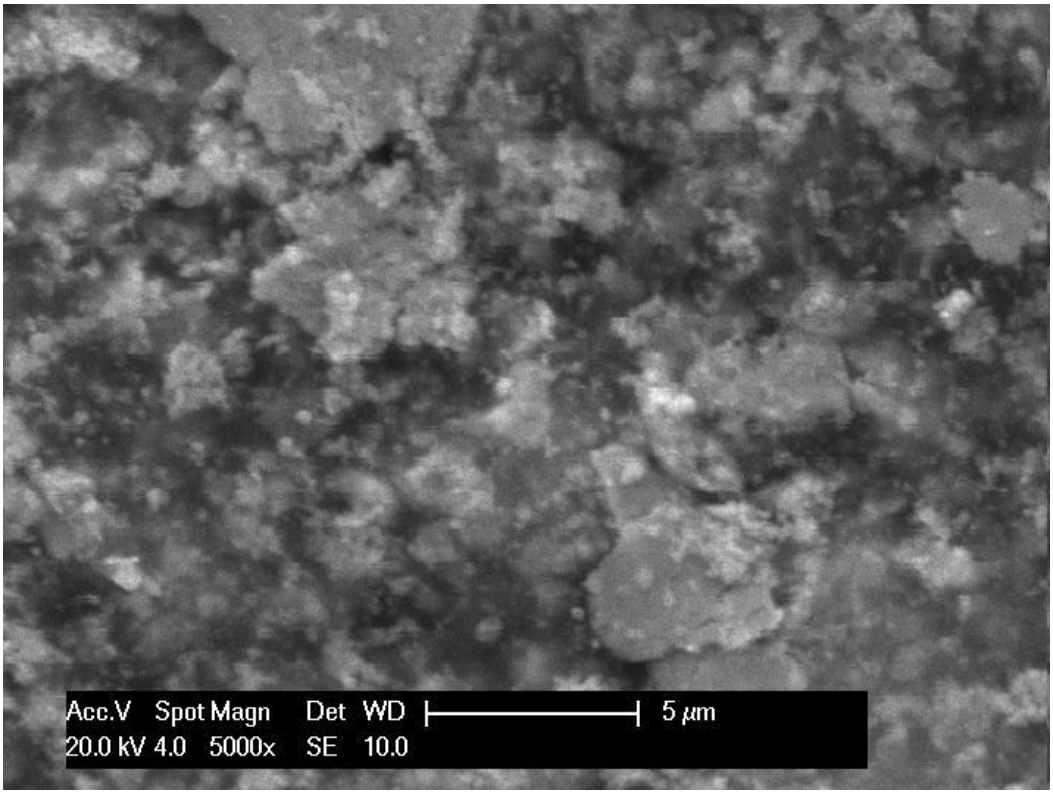
Acc.V Spot Magn Det WD 5 µm
20.0 kV 4.0 5000x SE 10.0

(c)

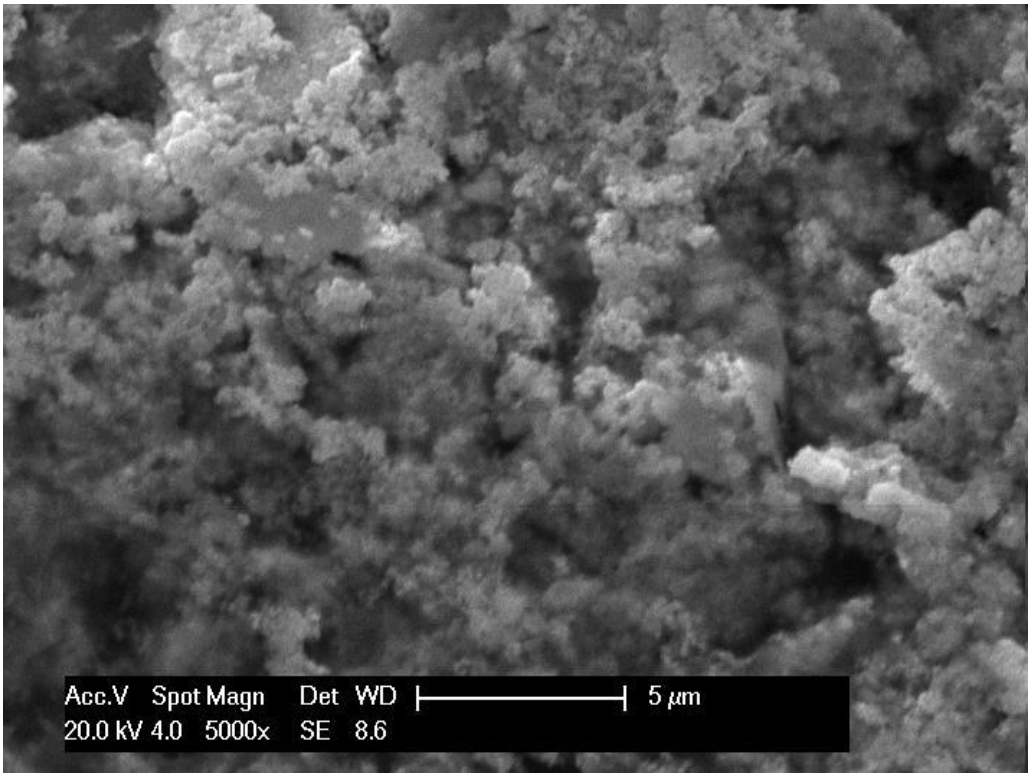
Acc.V Spot Magn Det WD 5 µm
20.0 kV 4.0 5000x SE 8.6

(d)

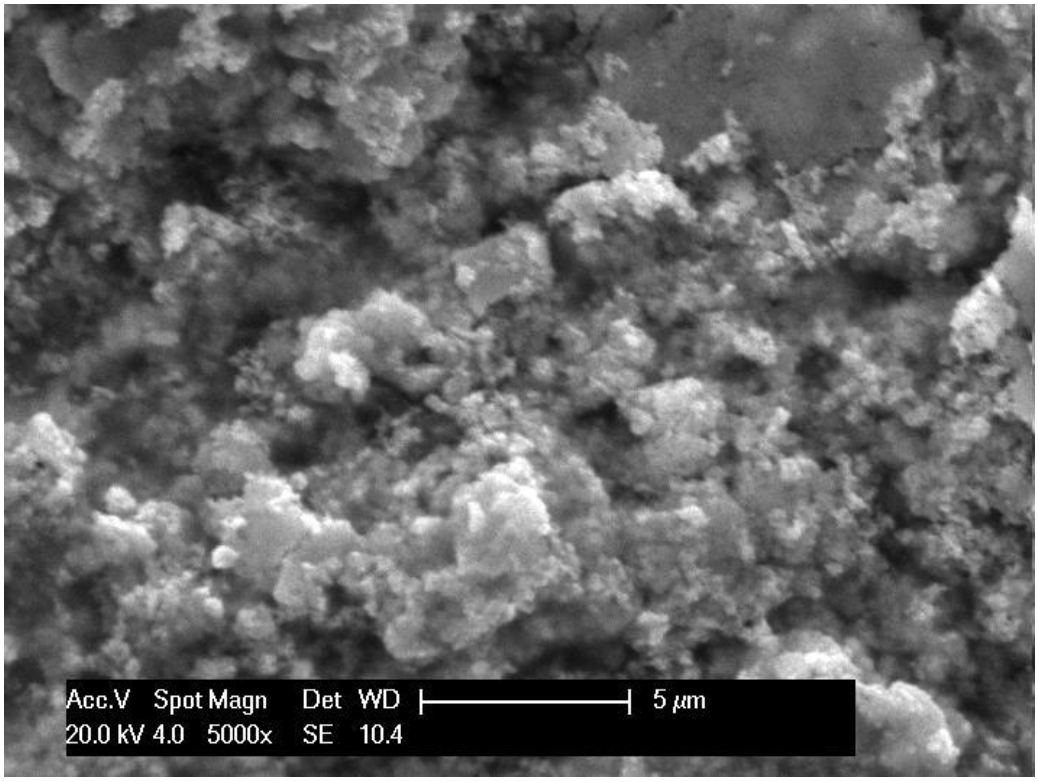

(e)

Figure 7.10: SEM 5000x Magnification images of Nafion®117 cathode of (a) Unused MEA (b) 18 MΩ MEA (c) 10MΩ (d) 1 MΩ (e) Tap Water MEA

7.2.4.5. Energy-dispersive X-ray spectroscopy (EDX)

At the lowest magnification (500x) the original elements existent in the MEA, the carbon, oxygen and fluorine from the membrane and ionomer, and the platinum from the catalyst, were analysed to measure their atomic% composition on the SEM images.

Axis Label	Corresponding MEA Sample
#1	Reference (Unused) MEA
#2	18 MΩ.cm
#3	10 MΩ.cm
#4	1 MΩ.cm
#5	Tap Water MEA

Figure 7.11 shows little change in composition of these elements, with an approximate 5 atomic% decrease in carbon with decreasing water resistivity and an approximately 3.5 atomic% increase in oxygen content with decreasing water resistivity.

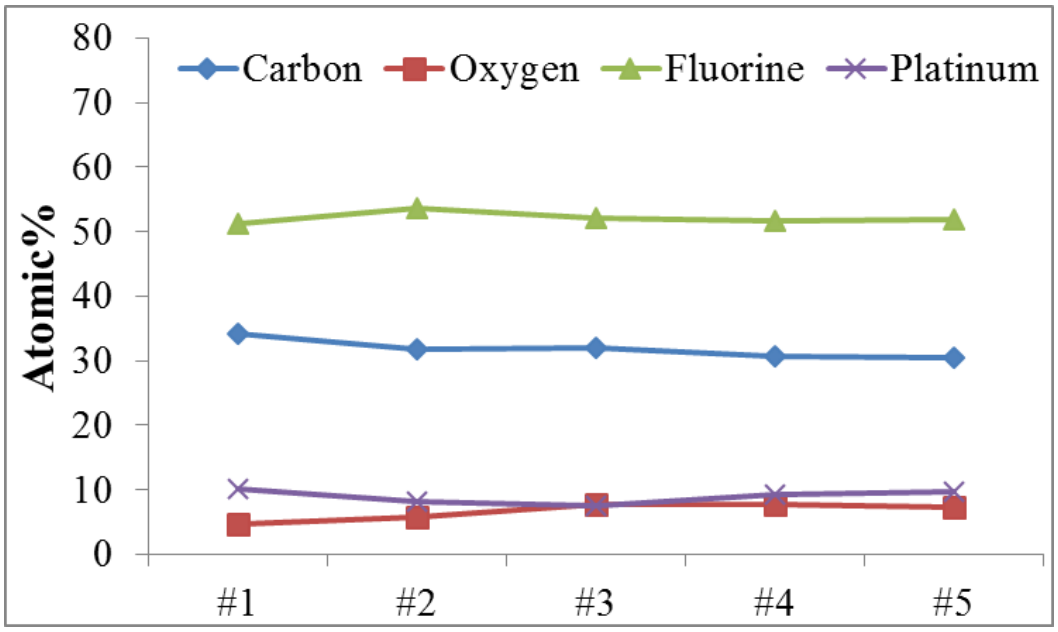

Figure 7.11: Atomic% of constituent elements found on cathode (500x) of Nafion® based MEA

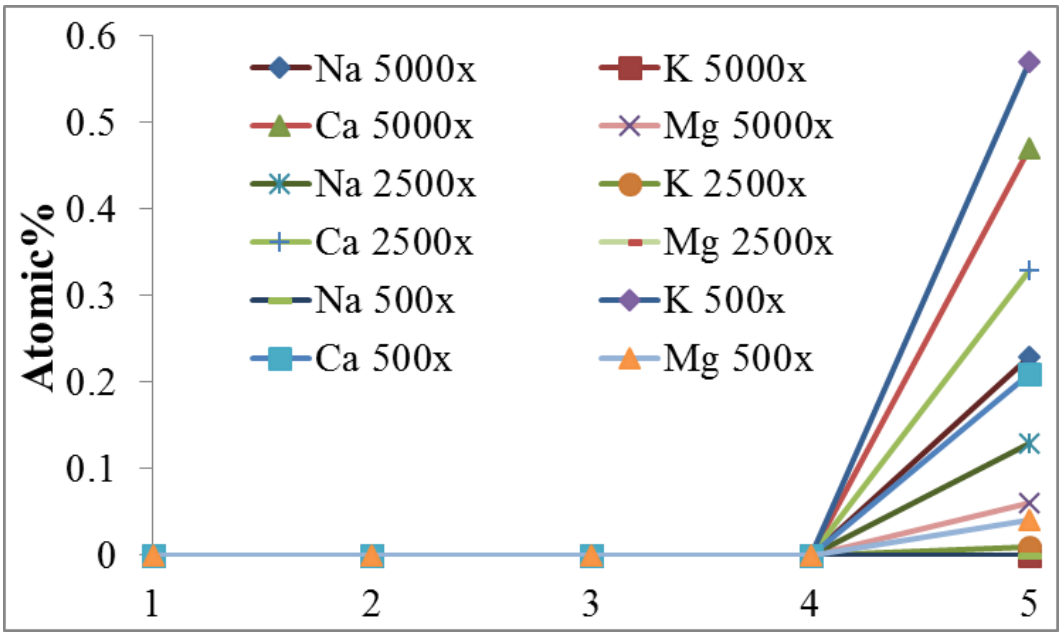

Figure 7.12: Atomic% of cations present on the cathodes of Nafion® based MEAs at all magnifications

The composition of cations (Na^+, K^+, Ca^{2+}, Mg^{2+}) typically present in impure water will be analysed to see if any of these are present on the MEA cathode surfaces (Figure 7.12). The analysis shows zero cation atomic% present on the cathode surface for the unused, 18 MΩ, 10 MΩ & 1 MΩ MEAs. Upon analysing the tap water MEA there is a sudden increase in cation composition on the cathode surface with all the cations specified present in at least one magnification.

Taking the surface composition from the tap water MEA only and measuring the cation atomic% for each magnification of the cathode surface yields the following graph. The analysis shows increasing presence of sodium and calcium with a decrease in magnification. Less than 0.1 atomic% of magnesium is present at all magnifications and the evidence of potassium decreases dramatically with increasing magnification of the MEA surface.

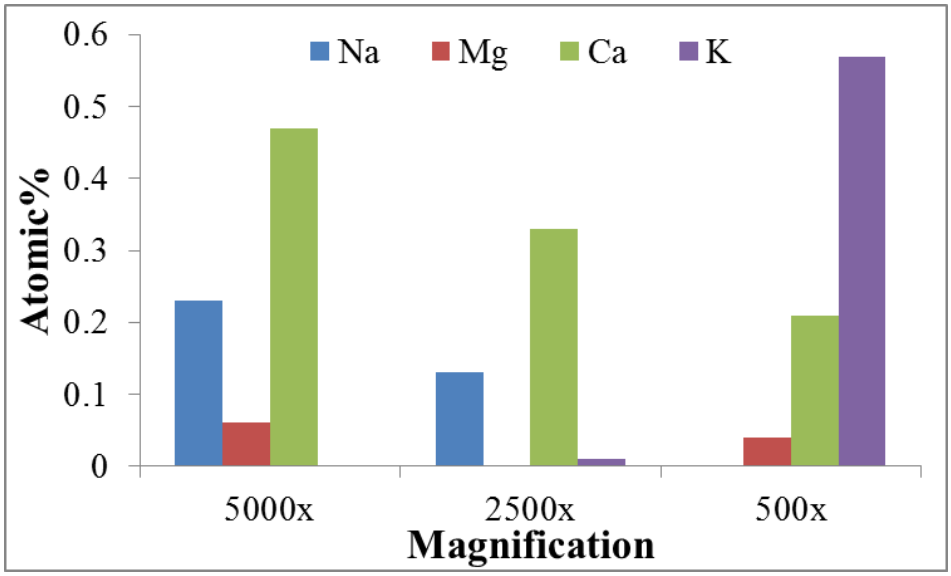

Figure 7.13: Atomic% of cation composition on Tap Water Nafion® based MEA at various magnifications

The EDX analysis has shown there to be cations present on the cathode surface of MEA subjected to tap water. The MEAs subjected to differing grades of purified water show no presence of cations commonly found in water.

7.2.5. Membrane #2 - Fumea® EF-10

7.2.5.1. Polarisation

The Fumea® MEAs were characterised in various grades of water as mentioned previously. The voltage across the PEM electrolysis cell was varied and the subsequent current flow measured and converted to current density (A cm^{-2}). This is shown in Figure 7.14. The purified water samples show similar electrochemical behaviour which expected due to the low ion content in the water and haven't been subjected to prolonged exposure with ions in the water. This exposure will decrease the electrochemical performance over time, whereas this experiment was only a 30 minute polarisation.

The polarisation showed a decreased polarisation with tap water. This is believed to be the result of cation build up subsequently blocking the nucleation sites and increasing the resistance in the electrolysis cell. This will later be confirmed in the microscopy analysis. The higher polarisation with 18MΩ water supply is still below the benchmark PEM electrolysis standard as shown in Figure 3.32 and literature [22, 31, 58, 208].

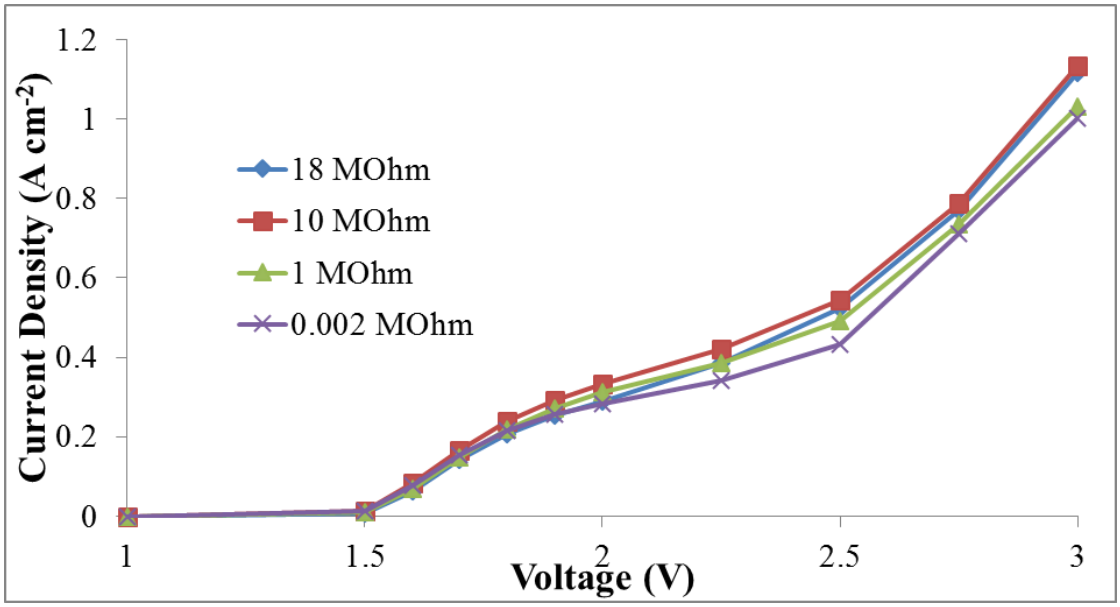

Figure 7.14: Fumea® based MEA Polarisation at 25°C, 0.1V scan rate, 1 atm pressure, 20bar piston pressure, 80ml/min water flowrate

7.2.5.2. Electrical Efficiency

With the data collected during the polarisation, an electrical efficiency calculation for each potential and water quality was found. This is shown in Figure 7.15. At low potentials the resistances (overpotentials) are lower than at higher potentials and as shown in Figure 7.15 the efficiency decreases with an increase in energy input as a result of increasing resistances in the electrolysis process.

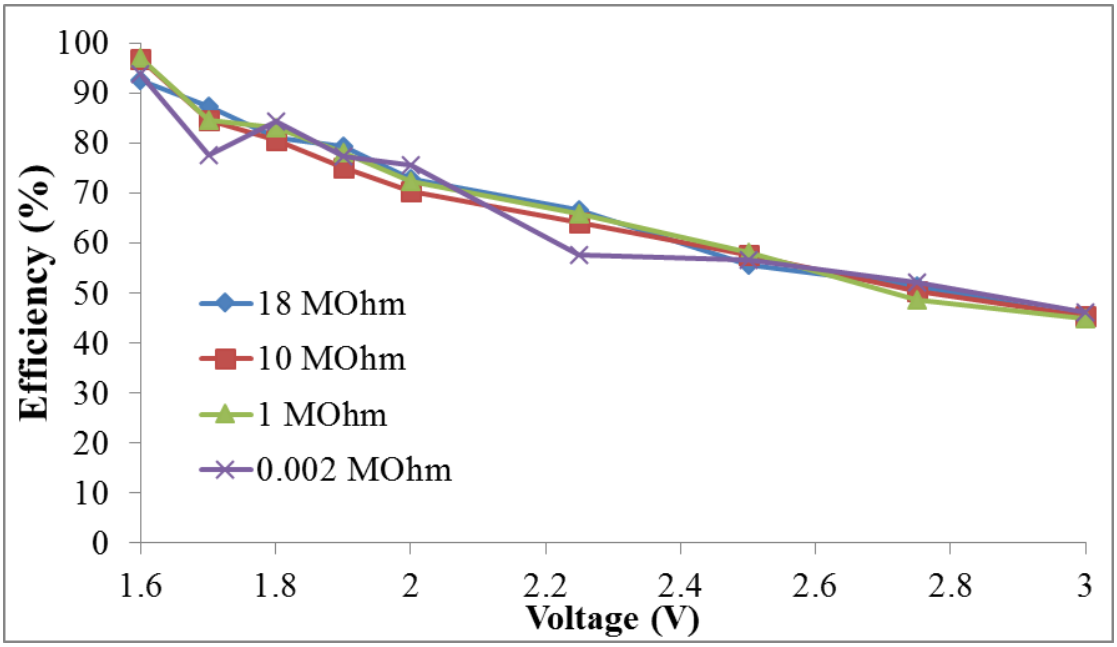

Figure 7.15: Efficiency of Fumea® based MEA at 25°C, 0.1V scan rate, 1 atm pressure, 20bar piston pressure, 80ml/min water flowrate

7.2.5.3. Electrochemical Degradation

After initial characterisation, the electrolysis cells underwent long term degradation where the potential applied across the cell remained constant and the current flow varied with time. The purpose of this experiment is to quantify any degradation in electrochemical performance for the varying grades of water used in each experiment. The results are shown in Figure 7.16.

Figure 7.16 shows the water with a conductivity of equal to or greater than 1 MΩ. It maintained a good electrochemical performance over a period of 8 hours of experimentation, when the current flow was maintained showing a positive gradient of just above 0. In contrast the performance of the electrolysis cell in the tap water system

is very poor. Peak voltage is achieved after 40 minutes of experimentation, from which the current decreases throughout the rest of the eight hour period. This rate of electrochemical cell degradation is unacceptable for commercial electrolysis and emphasises the scale of the problem with regards to enabling PEM electrolysis cells to function with tap water as the input.

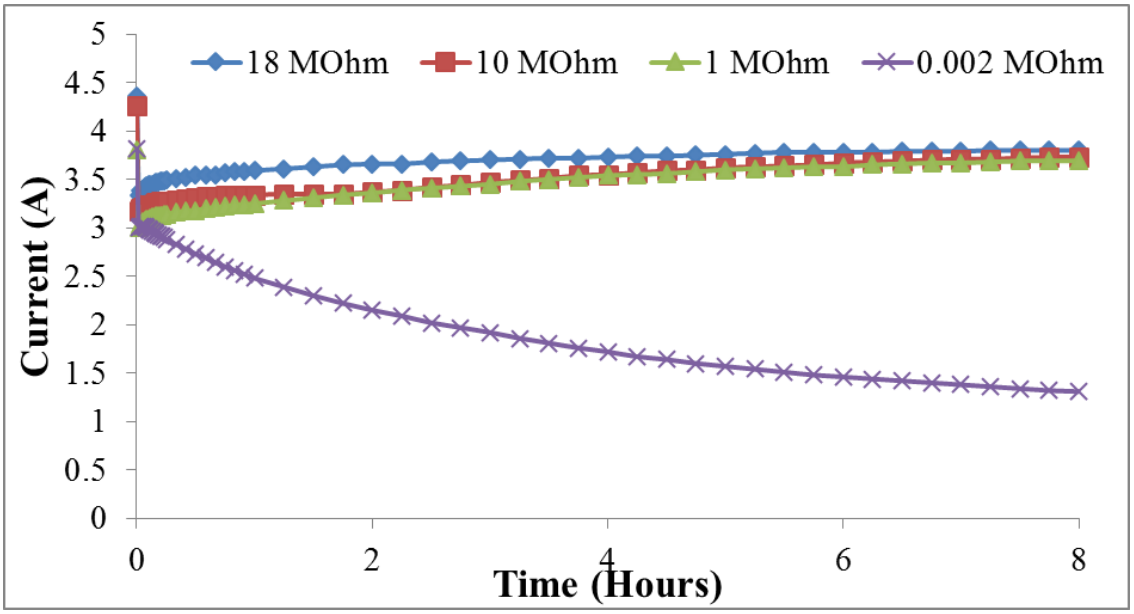

Figure 7.16: Degradation of Fumea® based MEA at 25°C, 2V, 1 atm pressure, 20bar piston pressure, 80ml/min water flowrate

7.2.5.4. Scanning Electron Microscopy (SEM)

Microscopic analysis of the MEA is important to quantify degradation and anomalies on the surface. Cation build up on the Fumea® membrane limits the number of nucleation sites available for proton exchange to occur, thus reducing the efficiency of the electrolyser. The MEAs from the electrolysis process will undergo image spectroscopy and surface composition spectroscopy to analyse any cation blockage of the porous membrane and impurity deposition on the MEA surface.

500x Pt

The lowest level of magnification on the MEAs show a planar smooth surface for the unused MEA and the 18MΩ MEA. The 10MΩ MEA shows evidence of roughness on the surface and the 1MΩ MEA exhibits increased roughness and the evolution of widening pores and cracks on the MEA. When observing the Tap Water MEA the surface roughness has increased hugely when compared to the other MEAs. The rigidness of the surface could be the result of corrosion or foreign species existent on the MEA. This will be investigated by EDX analysis in the next section.

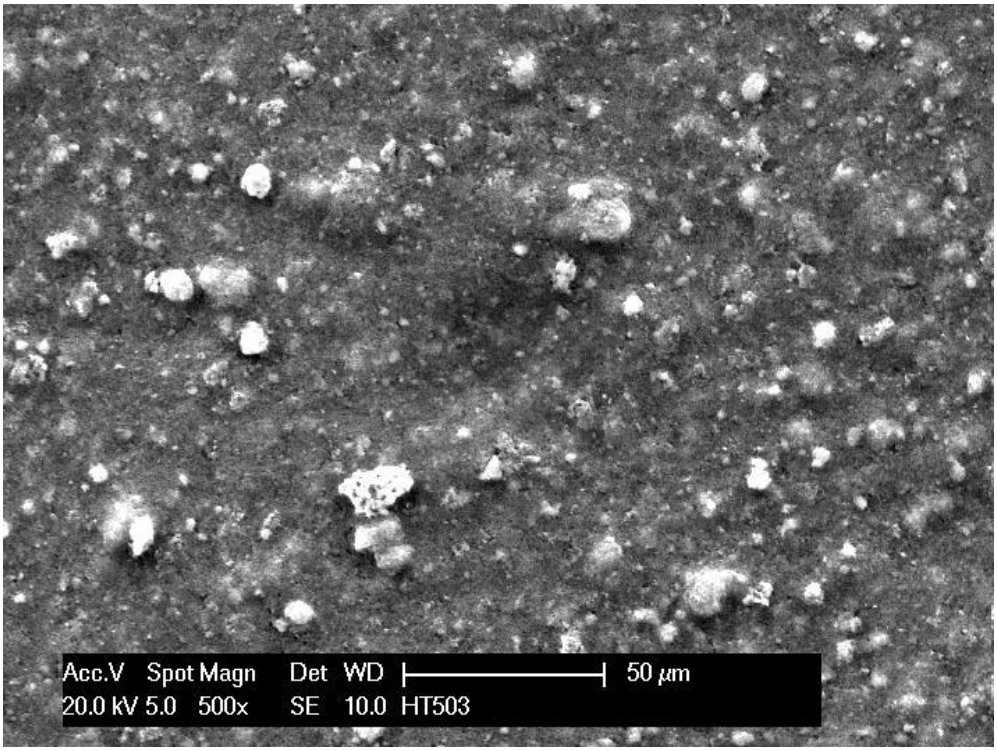

(a)

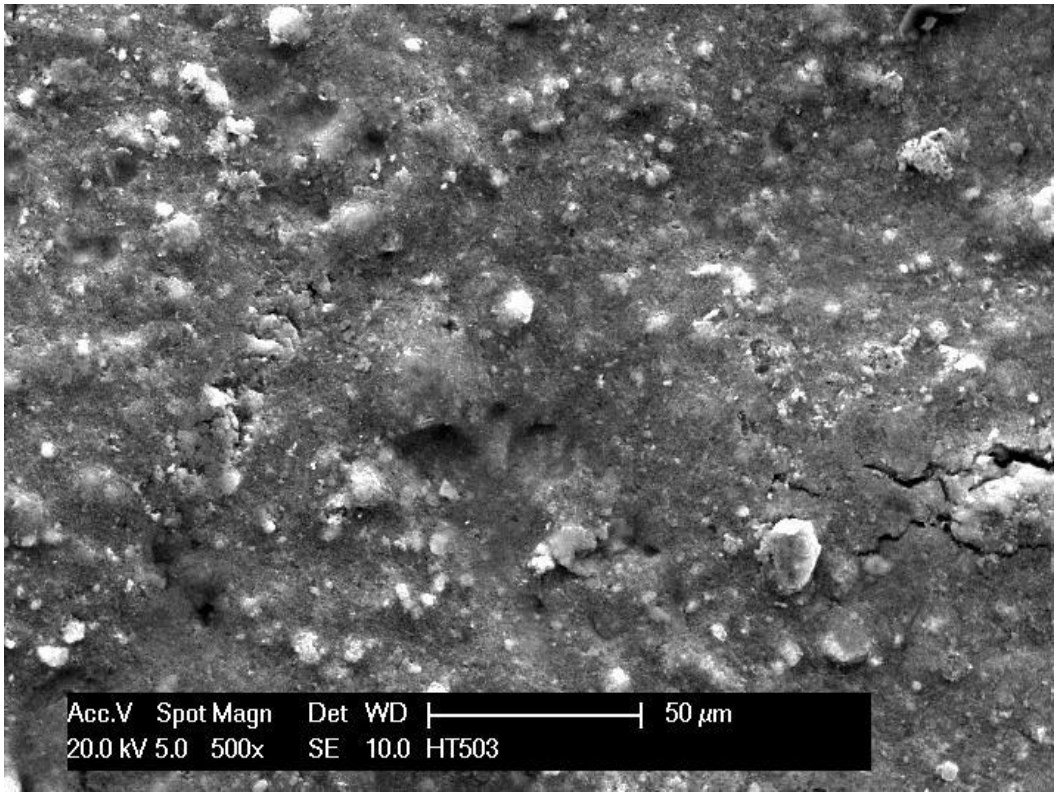
Acc.V Spot Magn Det WD 50 µm
20.0 kV 5.0 500x SE 10.0 HT503

(b)

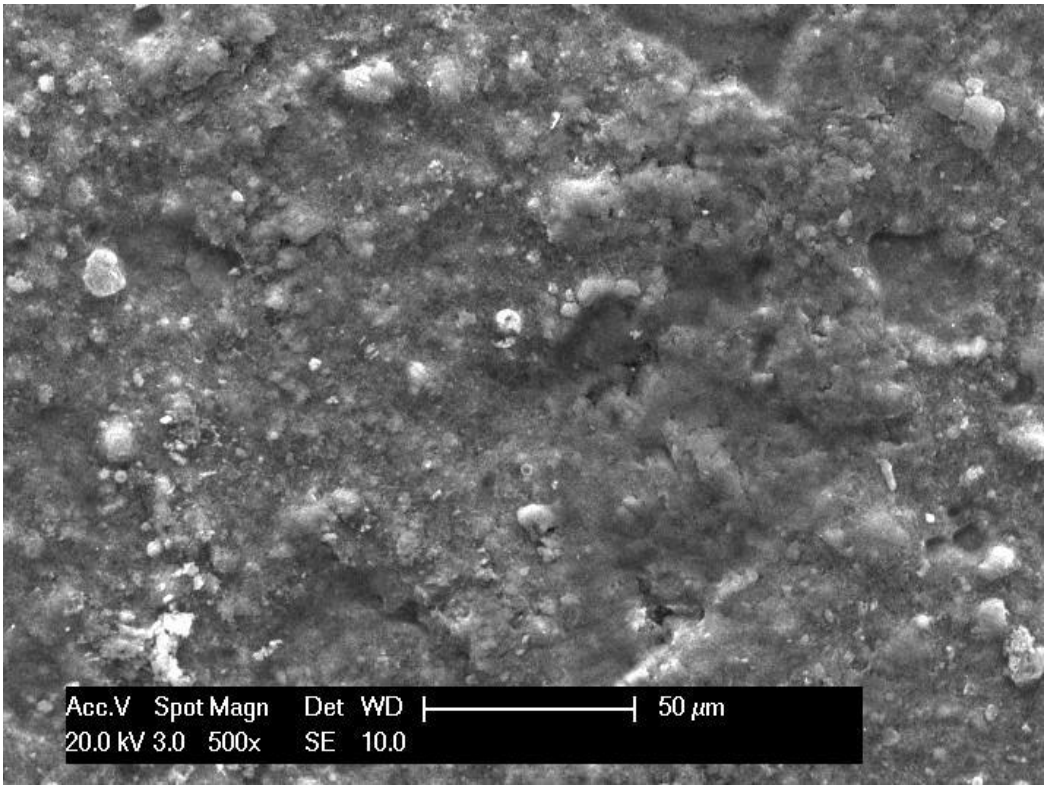
Acc.V Spot Magn Det WD 50 µm
20.0 kV 3.0 500x SE 10.0

(c)

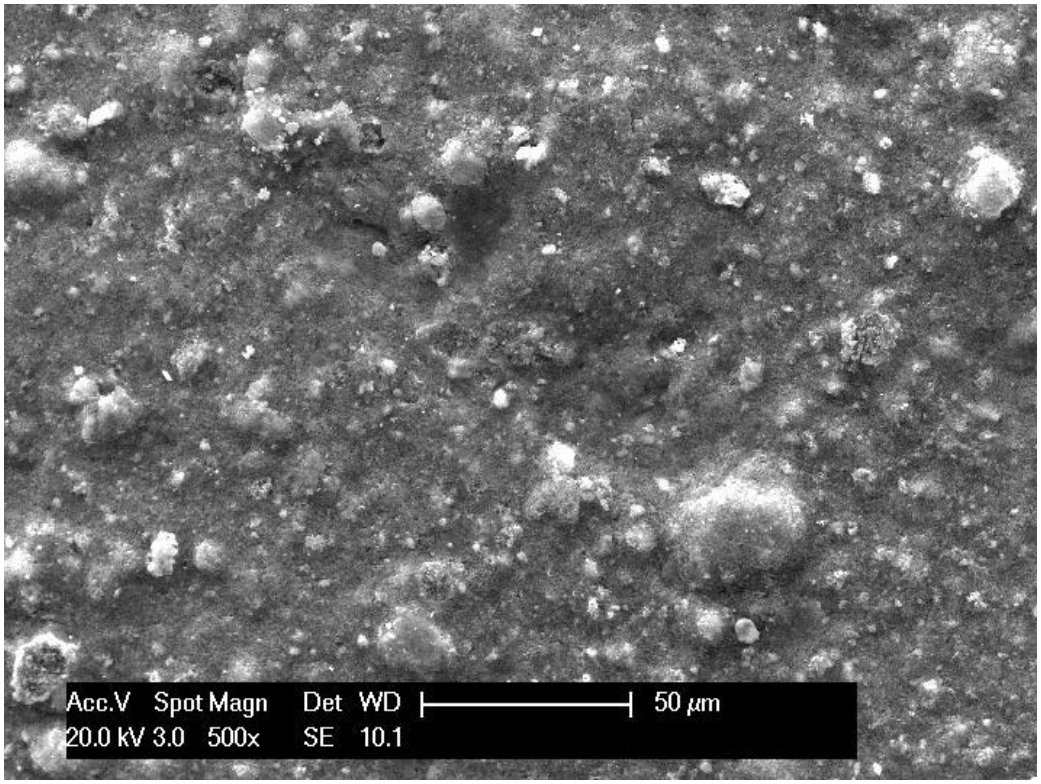

(d)

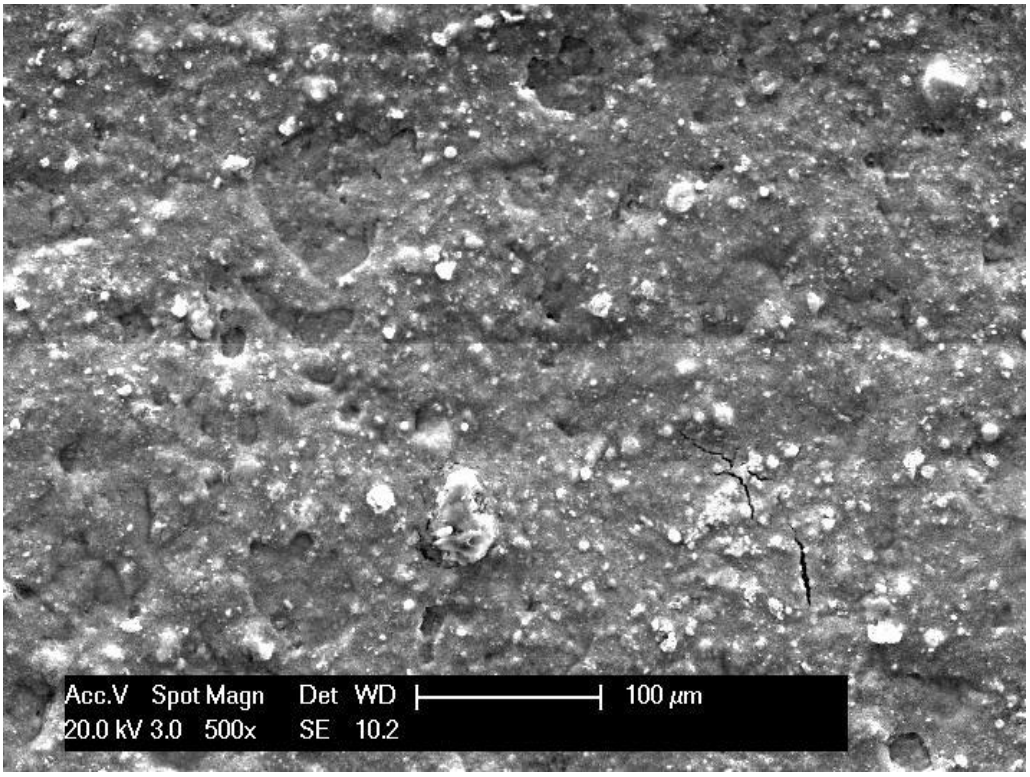

(e)

Figure 7.17: SEM 500x Magnification images of Fumea® cathode of (a) Unused MEA

(b) 18 MΩ MEA (c) 10MΩ (d) 1 MΩ (e) Tap Water MEA

2500x Pt

When magnifying the previous images further, the surfaces of the MEAs appear much rougher than shown in a lower magnification. This undulating surface is characteristic of the catalyst layer which has been ultrasonically sprayed on the membrane surface. In this case the platinum black particles are the cause of the unevenness of the surface, but the increased roughness shown on the Tap Water MEA when compared to the others could be the result of foreign ions on the MEA surface.

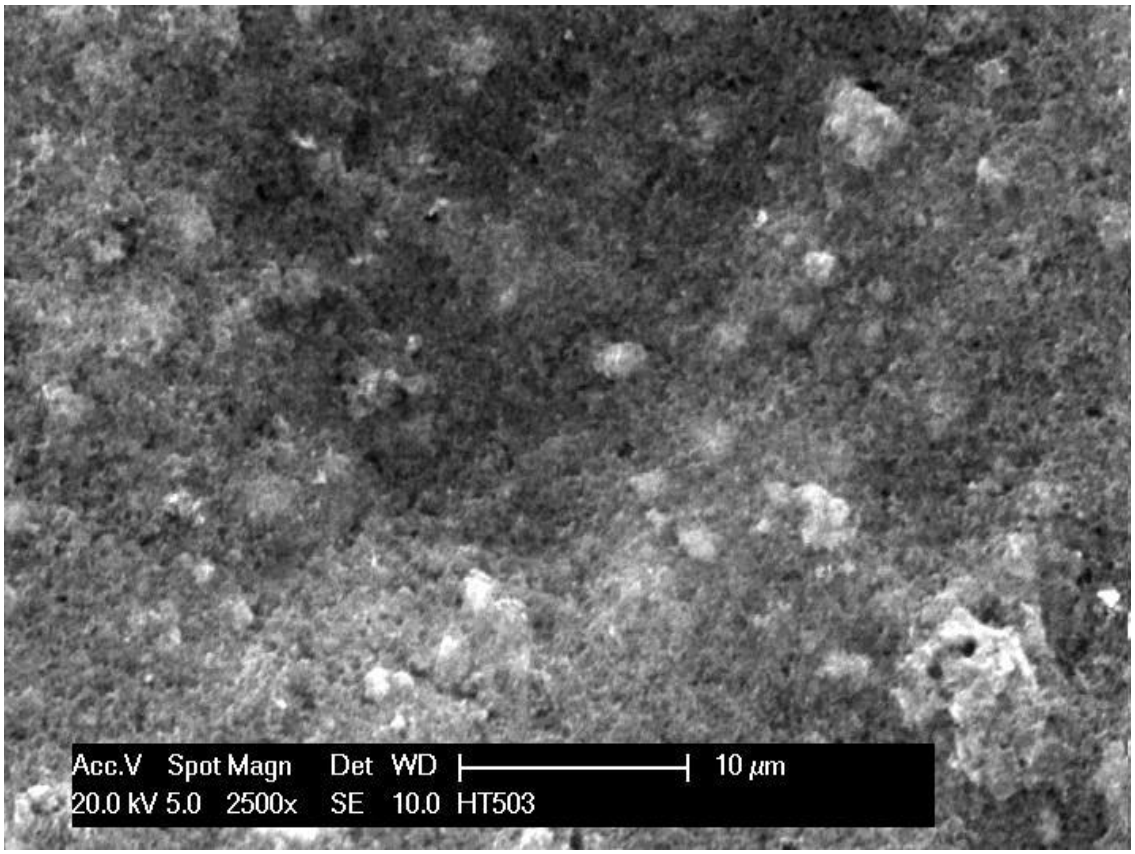

(a)

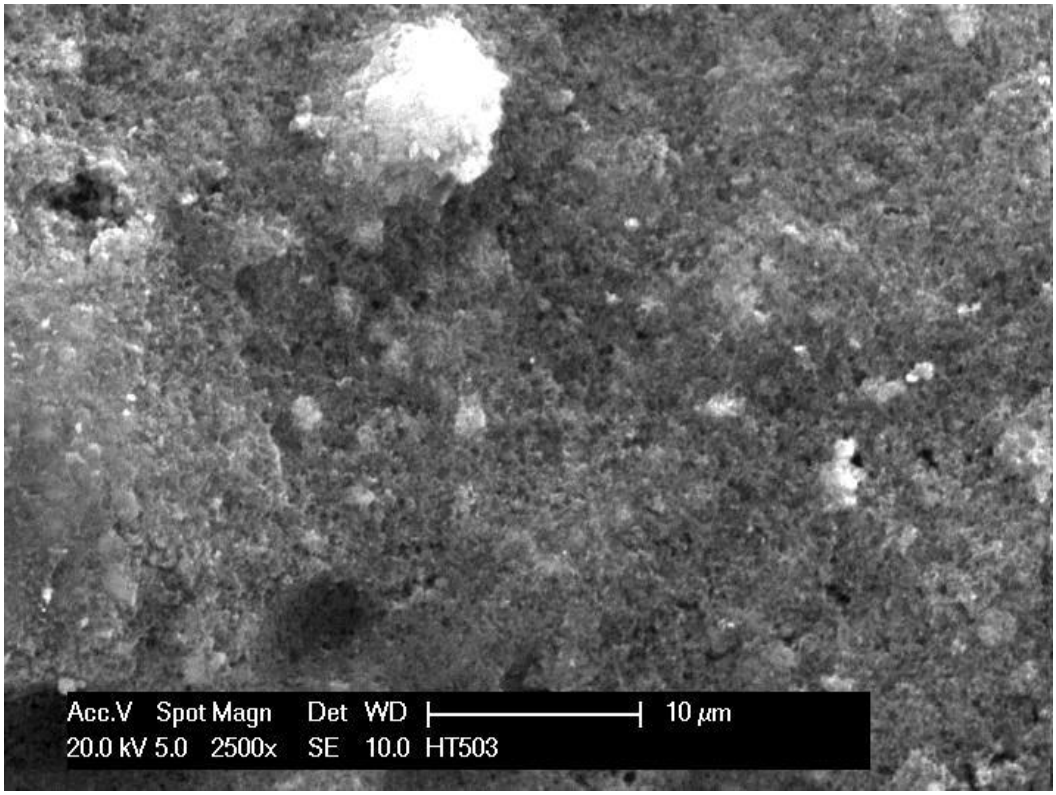
Acc.V Spot Magn Det WD 10 µm
20.0 kV 5.0 2500x SE 10.0 HT503

(b)

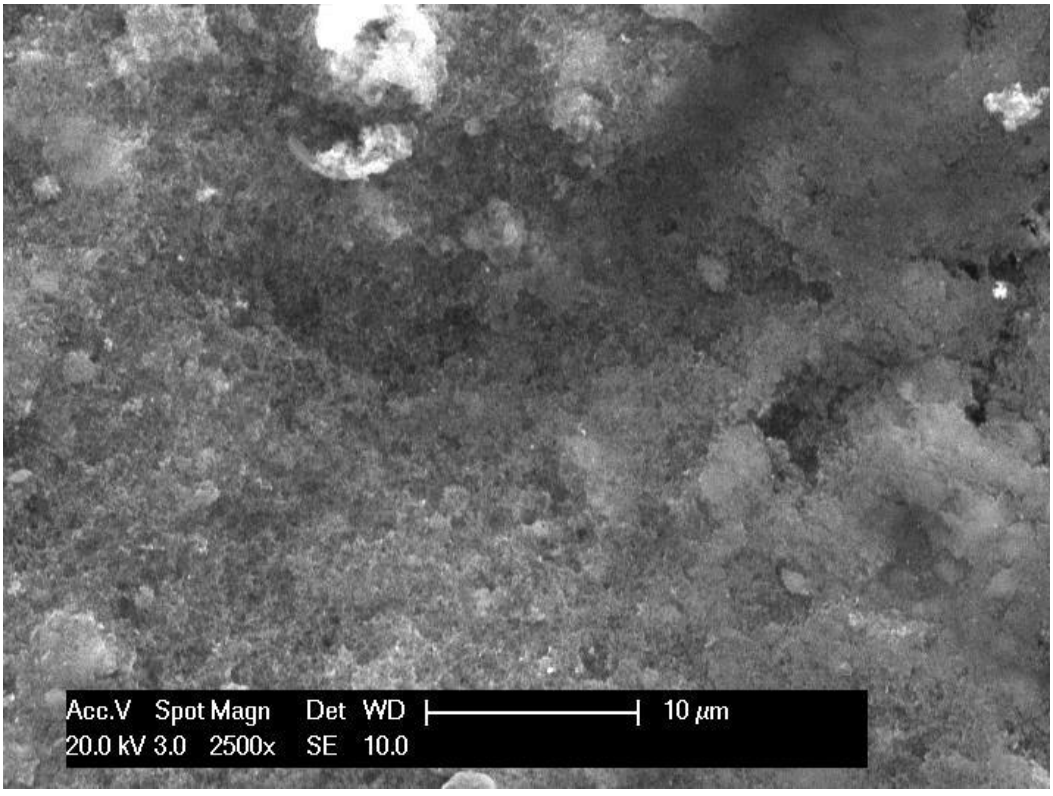
Acc.V Spot Magn Det WD 10 µm
20.0 kV 3.0 2500x SE 10.0

(c)

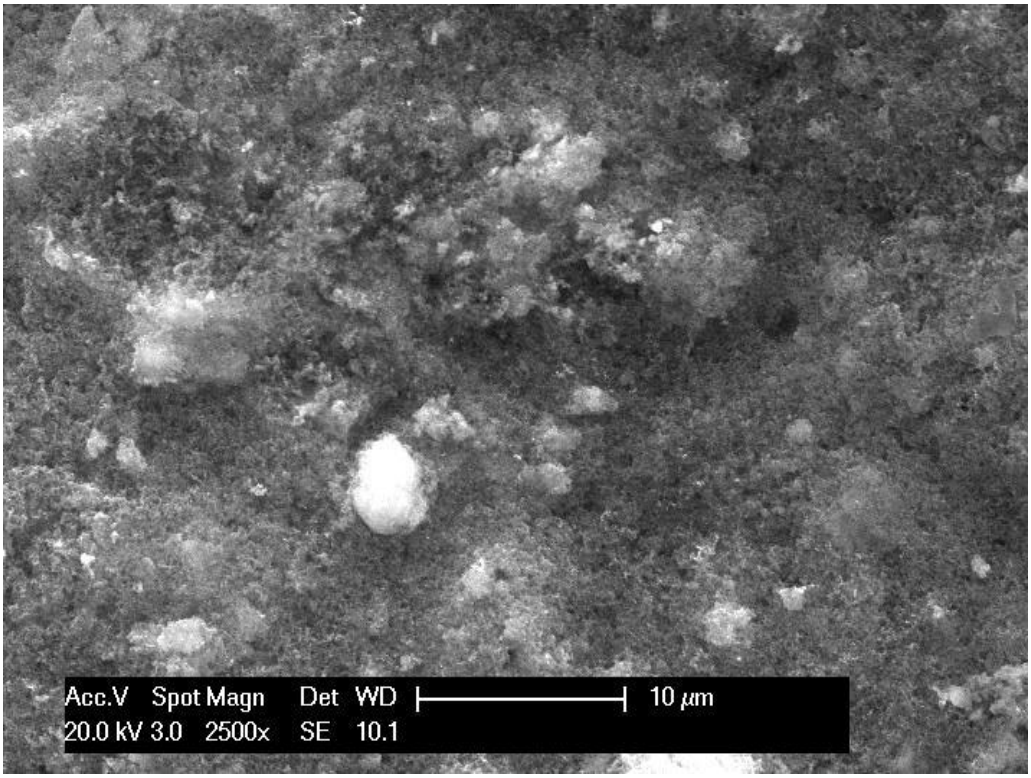

(d)

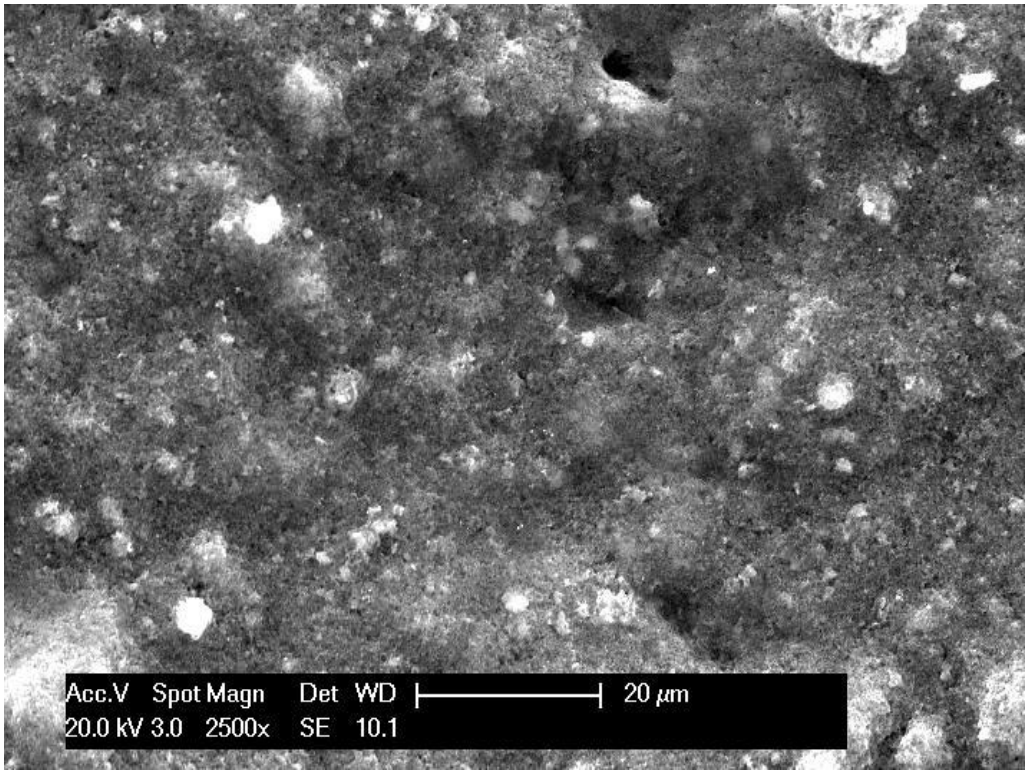

(e)

Figure 7.18: SEM 2500x Magnification images of Fumea® cathode of (a) Unused MEA

(b) 18 MΩ MEA (c) 10MΩ (d) 1 MΩ (e) Tap Water MEA

5000x Pt

Upon further magnification of each MEA, the particulates scattered over the membrane become individually identifiable. Although minimal variation can be seen amongst the SEM images, the increase in coagulation of what is believed to be platinum particles is evident as the purity of the water used in experimentation decreases.

To analyse this images further, they will all undergo EDX analysis to identify the element composition of the MEA cathode surfaces.

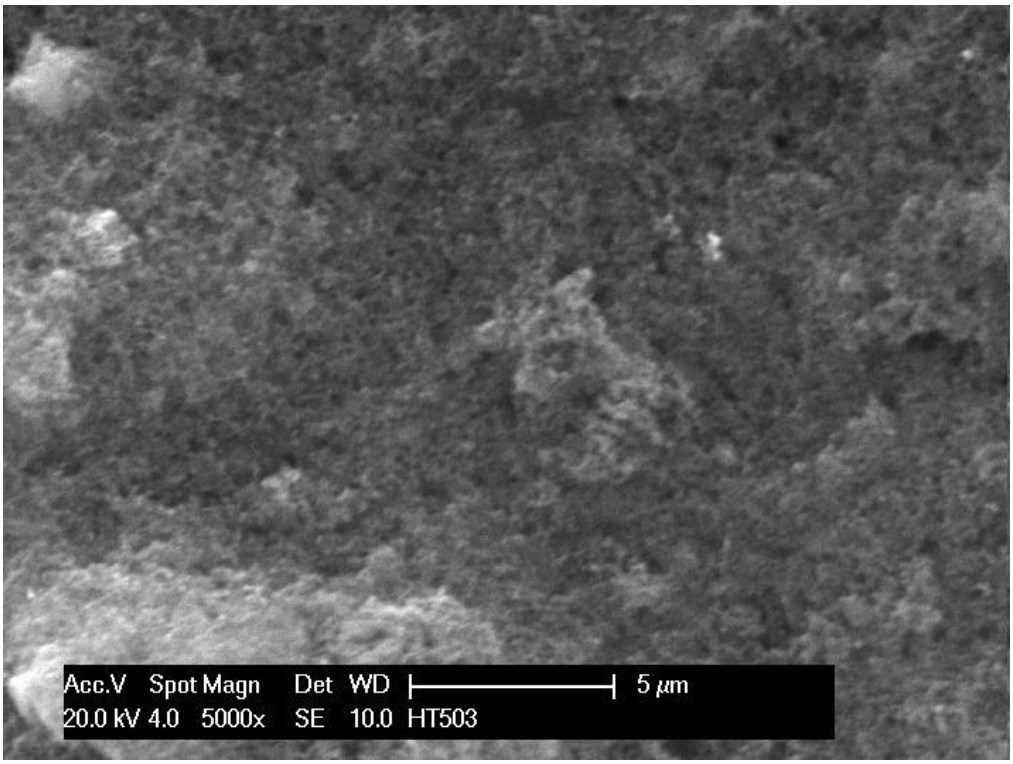

(a)

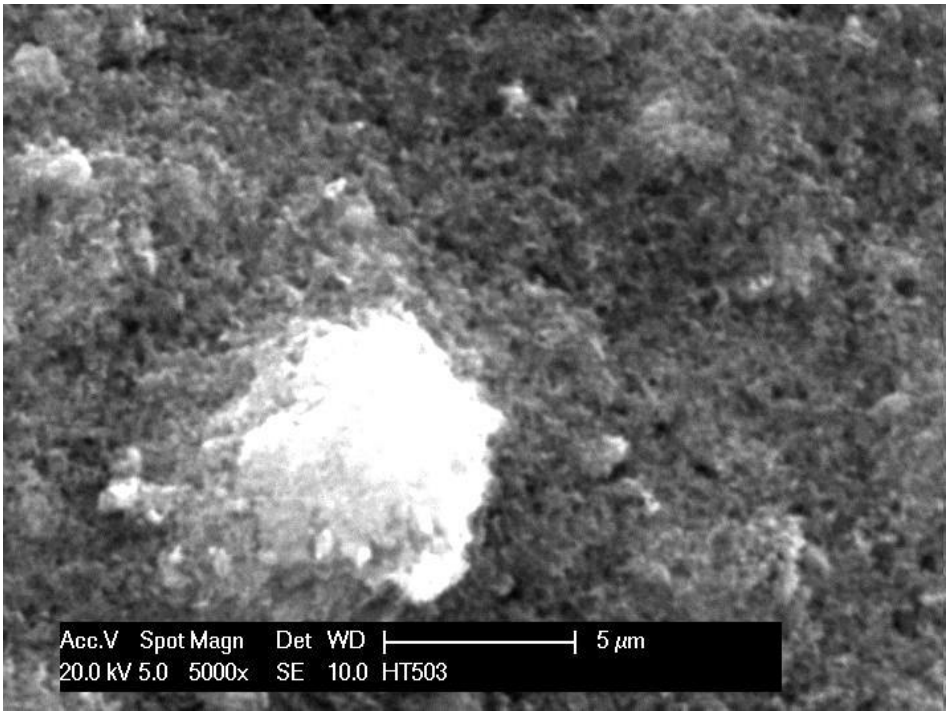
Acc.V Spot Magn Det WD 5 µm
20.0 kV 5.0 5000x SE 10.0 HT503

(b)

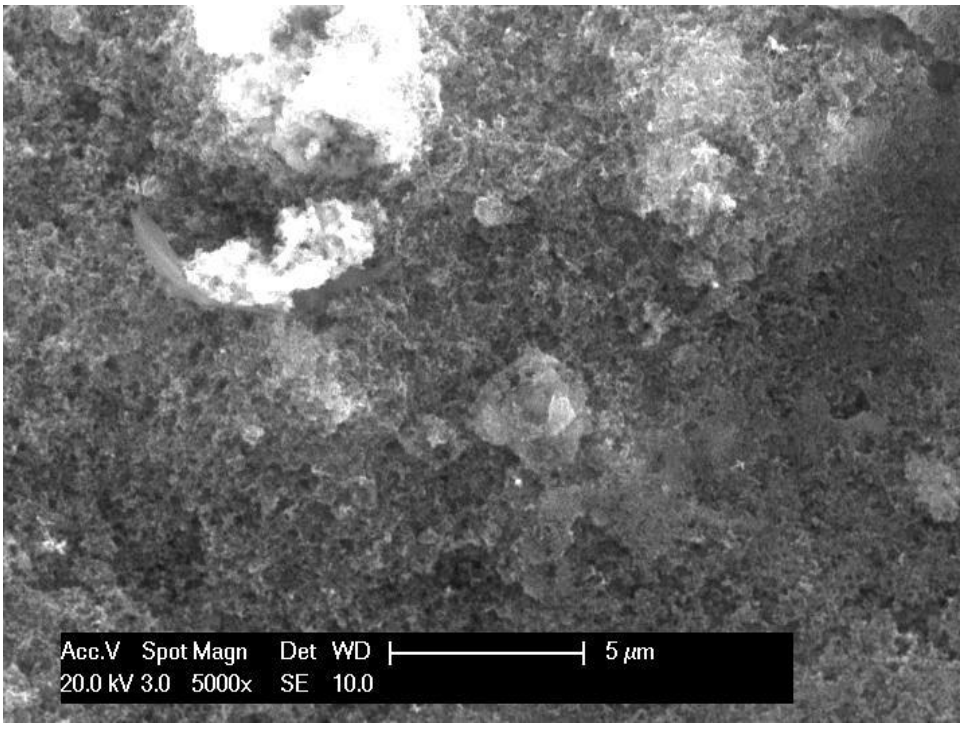
Acc.V Spot Magn Det WD 5 µm
20.0 kV 3.0 5000x SE 10.0

(c)

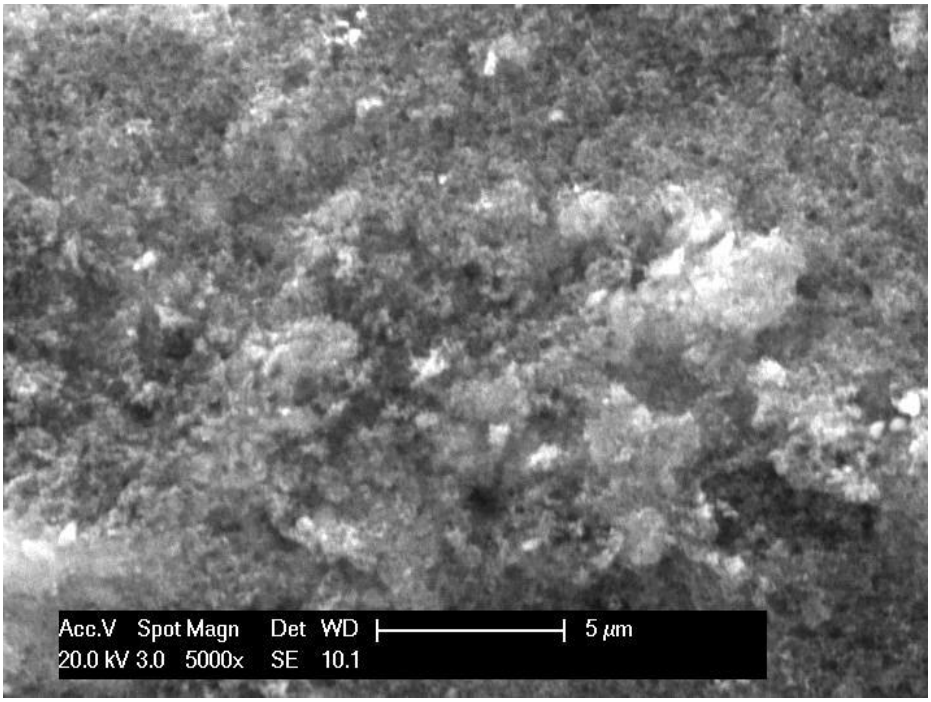

(d)

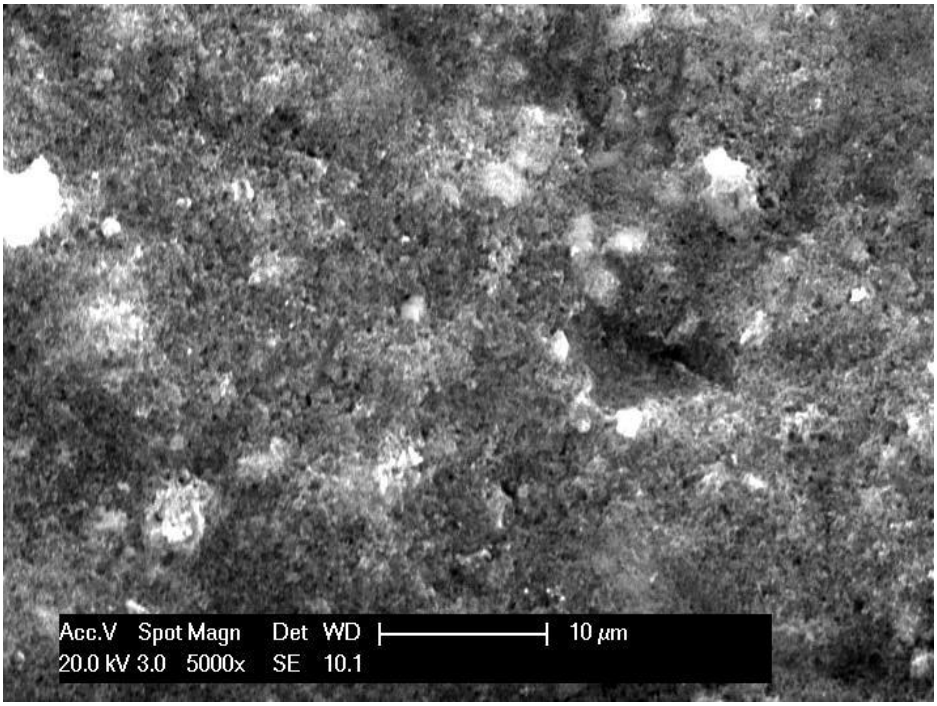

(e)

Figure 7.19: SEM 5000x Magnification images of Fumea® cathode of (a) Unused MEA (b) 18 MΩ MEA (c) 10MΩ (d) 1 MΩ (e) Tap Water MEA

7.2.5.5. Energy-dispersive X-ray spectroscopy (EDX)

At the lowest magnification (500x) the original elements existent in the MEA, the carbon, oxygen and fluorine from the membrane and ionomer, and the platinum from the catalyst, were analysed to measure their atomic% composition on the SEM images.

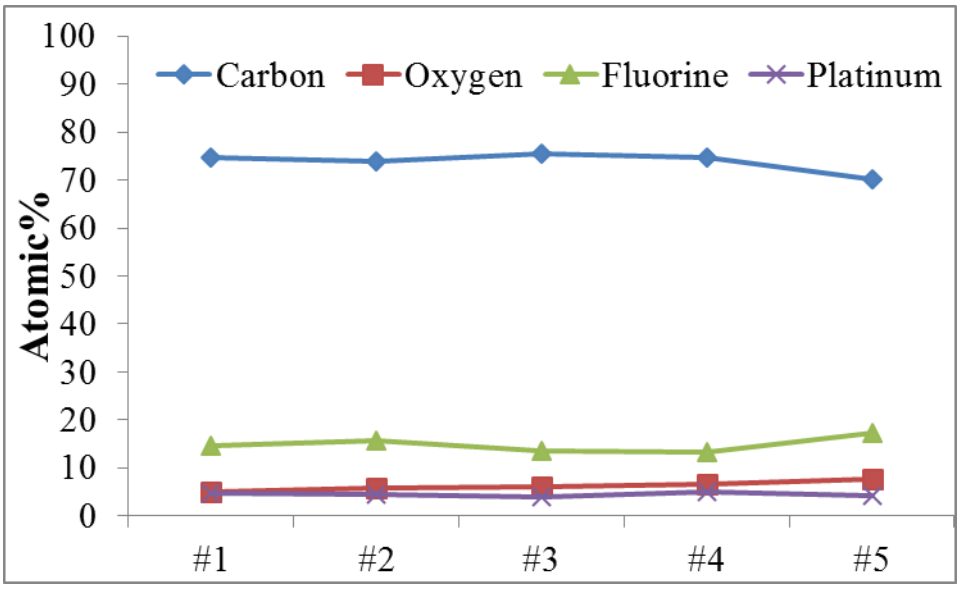

Figure 7.20: Atomic% of constituent elements found on cathode of Fumea® based MEA

The analysis shows little change in composition of these elements, with a decrease in carbon of 5 atomic% from 1MΩ to tap water. This corresponds with an increase of 5 atomic% of fluorine content for the same samples. This could be the result of damage to the catalyst layer from the tap water and the exposure of fluorine containing membrane.

The composition of cations (Na^+, K^+, Ca^{2+}, Mg^{2+}) typically present in impure water was analysed to see if any of these are present on the MEA cathode surfaces. This analysis found zero cations present on the cathode surface for all the MEA samples. This is

surprising considering the degradation in electrochemical performance from the use of tap water as shown in Figure 7.16. Relating to Figure 7.20 the exposure of membrane material through gaps in the catalyst layer may be the result of the decreased electrochemical performance as shown in Figure 7.16. This is highlighted in Figure 7.21 which shows the crack in the surface of the cathode.

The exposure of the membrane explains the increase in fluorine content on the EDX analysis. With a lack of expectant cations on the cathode, an analysis of the cation ion content on the anode of the Fumea® based MEAs was conducted (Figure 7.22).

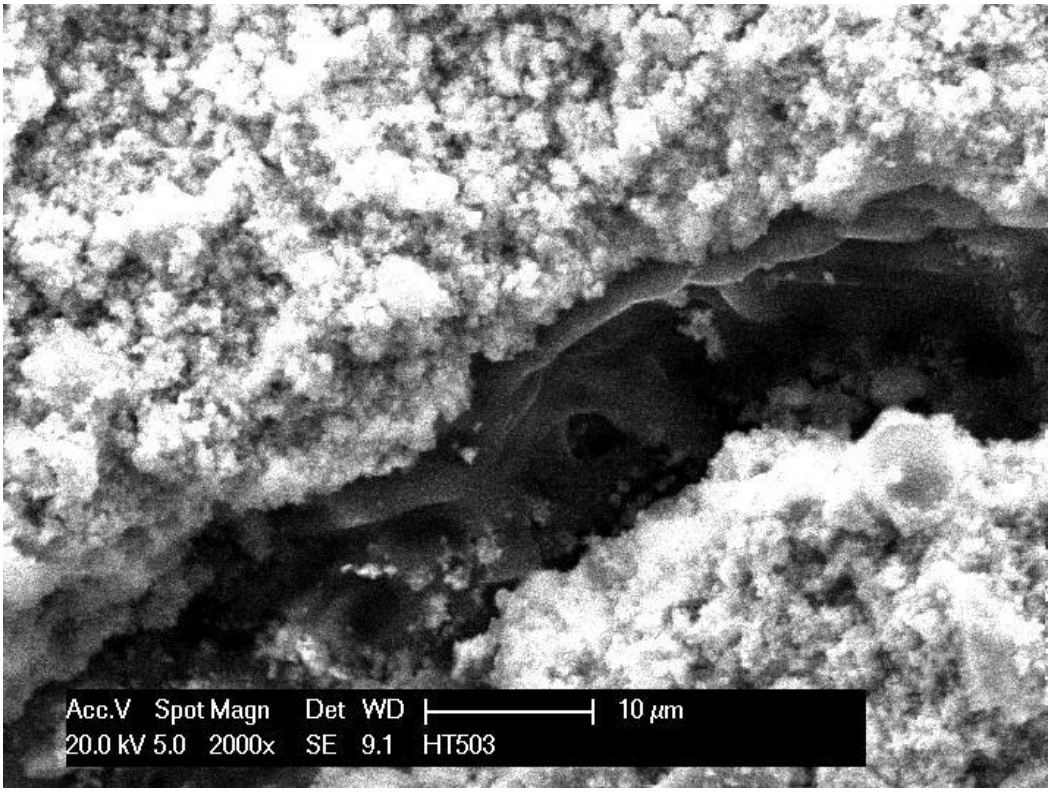

Figure 7.21: Crack in catalyst layer of Cathode of Fumea® based MEA

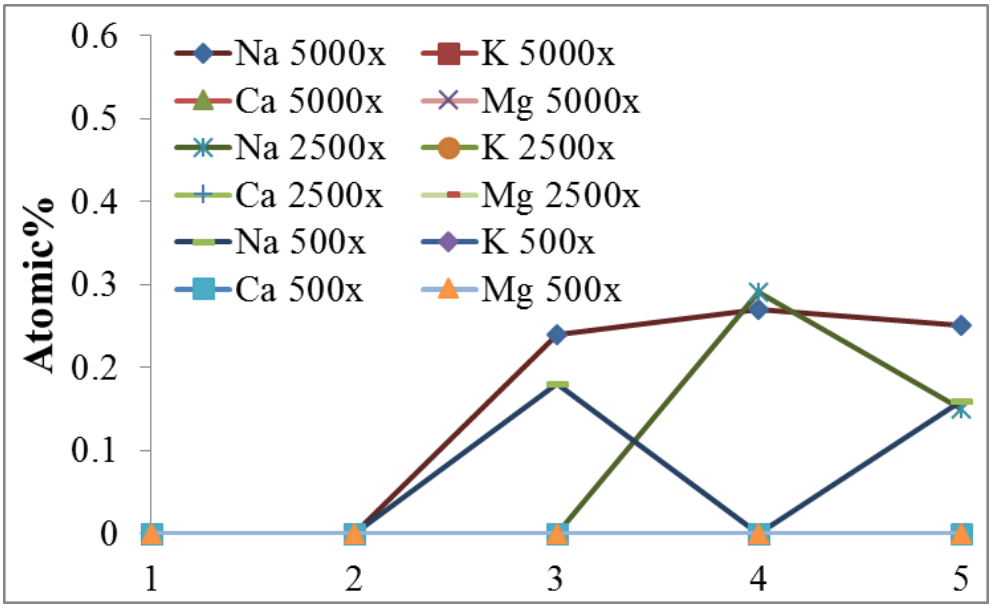

Figure 7.22: Atomic% of cation composition on Tap Water Fumea® based MEA anode

Figure 7.22 shows small quantities of sodium ion present at varying magnifications, but the shortage of potassium and especially calcium cations which are consistent in tap water give support to the hypothesis that the degradation in electrochemical performance on the Fumea® based MEAs is not a result of cation poisoning. The decrease in electrochemical performance is more likely to be a result of cracking of the MEA (Figure 7.21).

7.2.6. Comparison of Membranes

The two membrane materials have differing properties and performance related to the electrochemical reaction kinetics that occur on the MEA surface. This section shall compare the polarisation, hydrogen yield, electrical efficiency and degradation rates of both membranes in ultrapure (Type I) and domestic tap water.

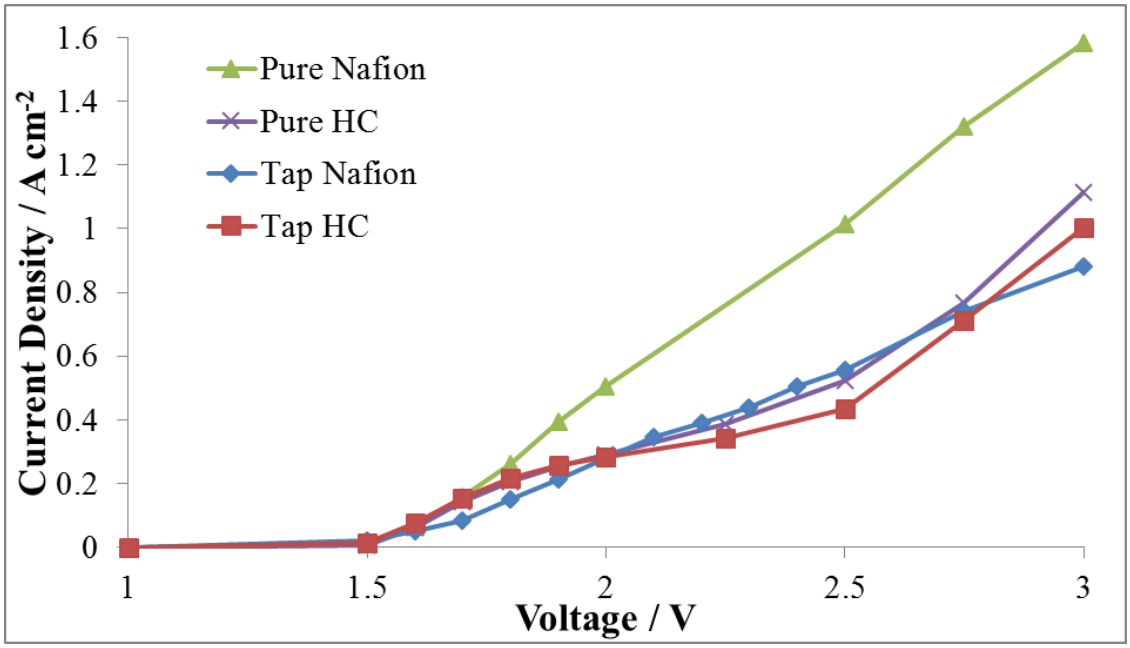

Figure 7.23: Polarisation of Nafion® and HC Membranes for Pure & Tap Water at 25°C, 0.1V scan rate, 1 atm pressure, 20bar piston pressure, 80ml/min water flowrate

Figure 7.23 shows the variation in electrochemical performance for Nafion® and HC membranes for ultrapure and tap water. There is a widening deterioration of electrochemical performance for a Nafion® membrane subjected to tap water compared to an ultrapure water feedstock. Whereas there is only a small reduction in polarisation for HC membranes when subjected to tap water compared to ultrapure water.

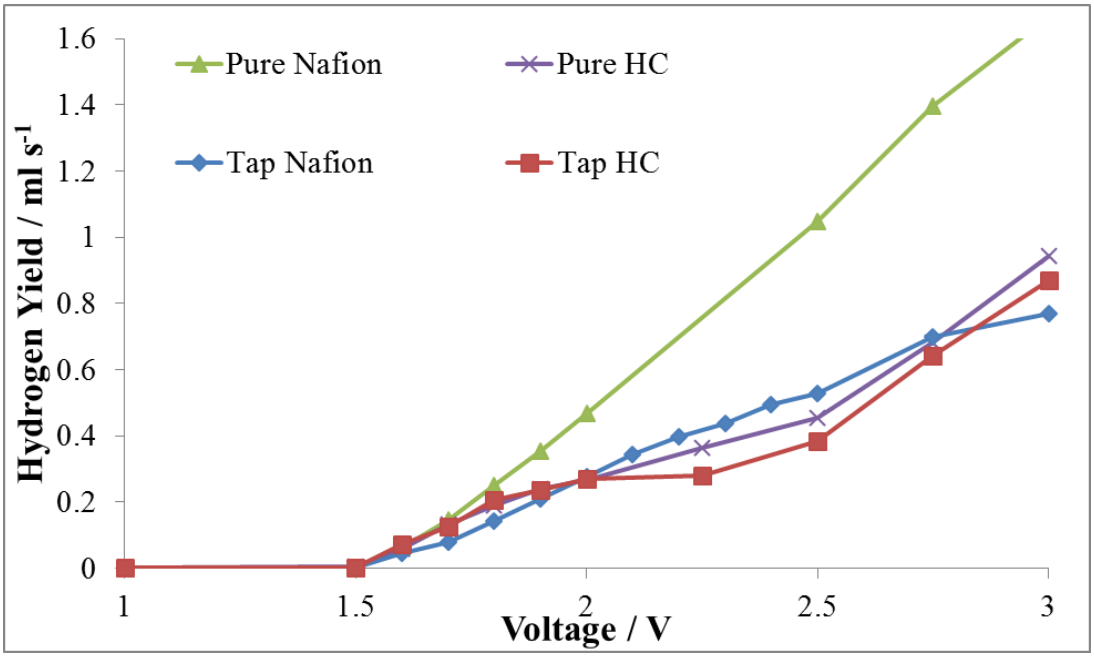

Figure 7.24: Hydrogen production rate of Nafion® and HC Membranes for Ultrapure and Tap Water at 25ºC, 0.1V scan rate, 1 atm pressure, 20bar piston pressure, 80ml/min water flowrate

Similarly to the polarisation analysis previously, the hydrogen yield from the electrolyser exhibits very familiar characteristics (Figure 7.24). There is a widening decrease in hydrogen production for Nafion® membranes in tap water than ultrapure water. Identically, the HC membrane shows minimal change in hydrogen yield for tap water and ultrapure water feedstock.

Figure 7.25 illustrates the variations in electrical efficiency for the two membranes in each grade of water. The graph shows no change in electrolysis efficiency as a result of deteriorating water quality. This is due to the fact the hydrogen yield is kept in line with the change in polarisation of the electrolysis cell. Any variation in electrochemical performance as a result of the quality of the feed water is best observed over time.

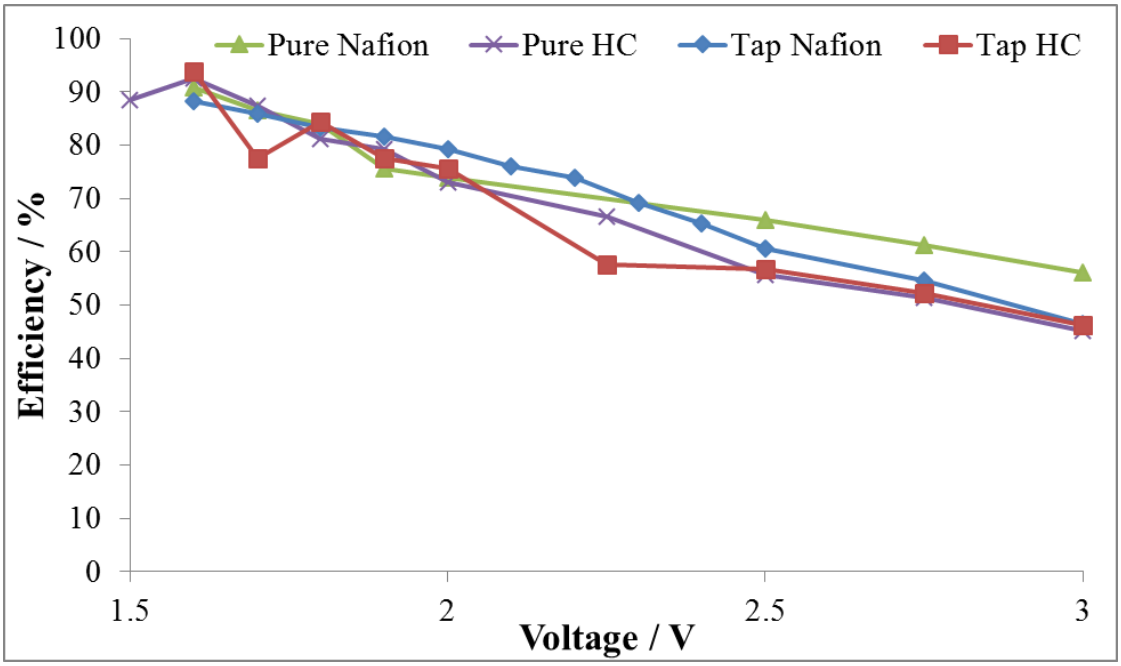

Figure 7.25: Electrical Efficiency of Nafion® and HC Membranes for Ultrapure and Tap Water at 25ºC, 0.1V scan rate, 1 atm pressure, 20bar piston pressure, 80ml/min water flowrate

Figure 7.26 highlights the major limitations of water quality on the long term performance of a PEM electrolyser. With an ultrapure water supply, both Nafion® and HC membranes exhibit good robustness and show zero electrochemical degradation over the 8 hour duration of the experiment. The current flow is still increasing for both membranes over the timeframe.

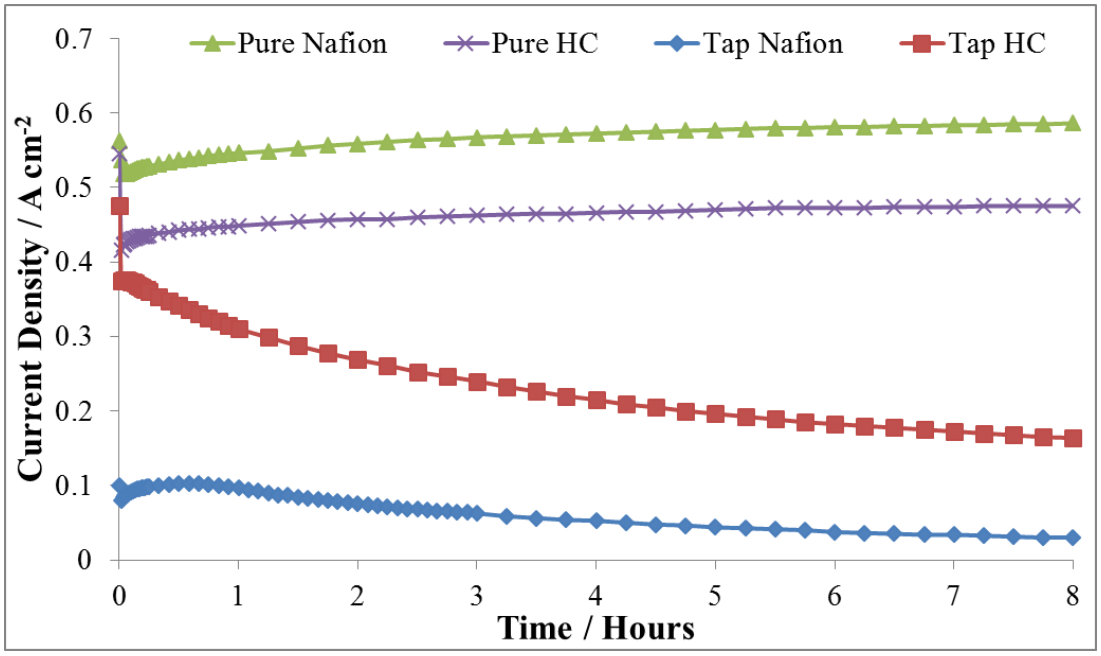

Figure 7.26: Degradation of Nafion® and HC Membranes for Ultrapure and Tap Water at 25ºC, 2V, 1 atm pressure, 20bar piston pressure, 80ml/min water flowrate

Meanwhile, the membranes subjected to tap water suffer extremely poor long term performance. The Nafion® membrane has a peak current at 35 minutes and the HC membrane at 3 minutes into the experiment, after which the dy/dx becomes negative and the current decreases over time.

The build-up of cations on the cathode surface limits the reaction kinetics and after the cations have been adsorbed onto electrode surface and the current flow is limited. This is consistent with the characteristics of electrical double layer resistance as discussed in the literature survey.

Whilst the cations in tap water are shown to be responsible for the deterioration in long term electrochemical performance, identification of which cations specifically are responsively and their quantity limits are scarcely researched. These cations in tap water shall be separately added to a PEM water electrolysis system to achieve this objective.

7.3. Cation Targeting

The impact of tap water containing several main cations on PEMs has shown to be highly detrimental to its performance. The transportation of H^+ ions through the proton conducting membrane attracts the cations previously mentioned. The larger particle size of these cations compared to a proton results in the blocking of the pores on the cathode side of the electrolysis cell. The resultant blockage limits proton transportation and subsequently reduces the efficiency and the lifetime of the electrolyser.

The identification of the four main cations present in tap water and its approximate composition are shown from the ICP-MS analysis in Figure 7.3. The aim of this section is to identify the cation(s) directly responsible for the degradation in electrolyser performance. A specific quantity of a selected cation will be added to 2 litres of Type I water and be electrochemically characterised at a fixed potential for an 8 hour duration.

The cations with the highest concentration are calcium and sodium and these are the focus of this research. For each cation the initial quantity will be consistent with that found in the tap water samples and then subsequently reduced to calculate the acceptable limit of

cation content in water in order to sustain sufficient electrolyser operation over an 8 hour period. Although the experimentation is limited by an 8 hour duration, the gradient of the data can be measured to determine the current degradation rate for a fixed voltage (2 V).

It is vital that the addition of these cations is completed without the addition of any additional cations/anions which could influence the performance of the MEA. This rules out the use compounds such as NaCl and $CaCO_3$. The cations were added in hydroxide form to the Type I water in which they dissociate into solution. With the other components of the compounds being oxygen and hydrogen (already present in water), the cations are the only new addition to the Type I water used for the electrolysis process, which is ideal for the objectives of this research.

Calcium ions showed a concentration of up to 100ppm in the tap water samples analysed in Figure 7.3. Figure 7.27 shows the performance analysis of the electrolysis cell with varying concentrations of Ca^{2+} in it starting with 100ppm.

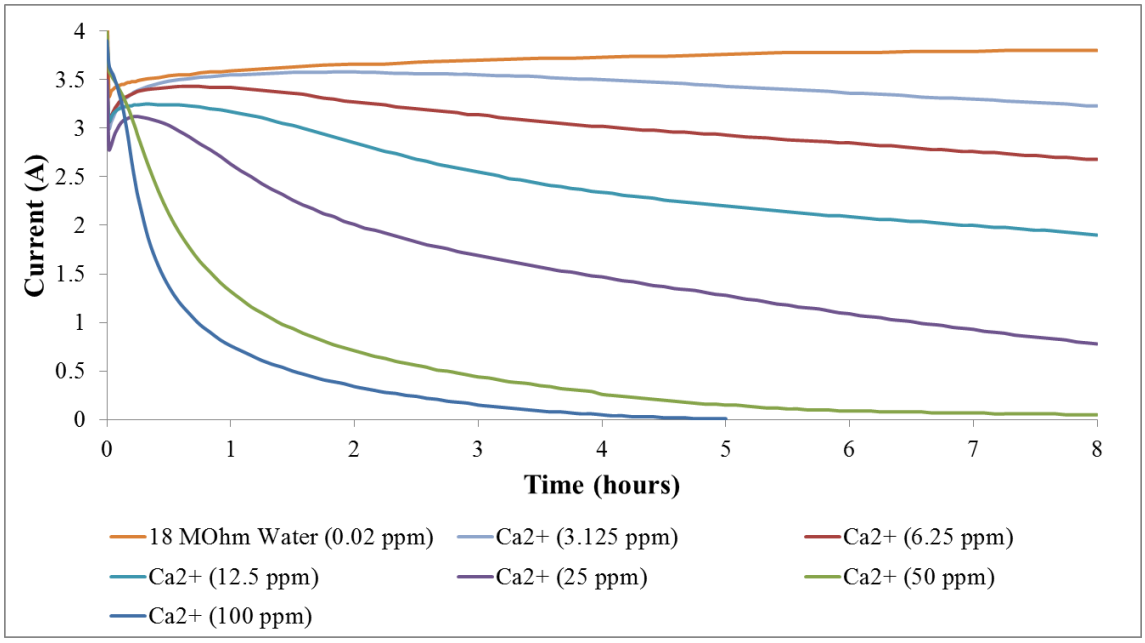

Figure 7.27: Electrolyser Degradation Performance with Calcium cation at 25ºC, constant 2V, 1 atm pressure, 20bar piston pressure, 80ml/min water flowrate

The data in Figure 7.27 shows the electrochemical degradation of the PEM electrolysis cell with 20ppm of calcium cations and less. All experiments with at least 3.125ppm of calcium cations in exhibited degradation in electrochemical performance over the 8 hour duration.

Table 7.2: MEA lifetime for varying quantities of Ca^{2+}

Calcium Concentration (ppm)	Current Degradation (Amps / Hour)
0.02	0
3.125	0.07
6.25	0.08
12.5	0.10
25	0.15
50	0.35
100	0.71

Assuming the rate of degradation remains constant, the rate of degradation between 7 and 8 hours was measured and then the current degradation to rate measured. Table 7.2 shows MEA lifetime increases with decreasing Ca^{2+} concentration in the electrolysis feedwater.

Sodium ions showed a concentration of up to 20ppm in the tap water samples analysed in Figure 7.3. Figure 7.28 shows the performance analysis of the electrolysis cell with varying concentrations of Na^{+} in it starting with 20ppm.

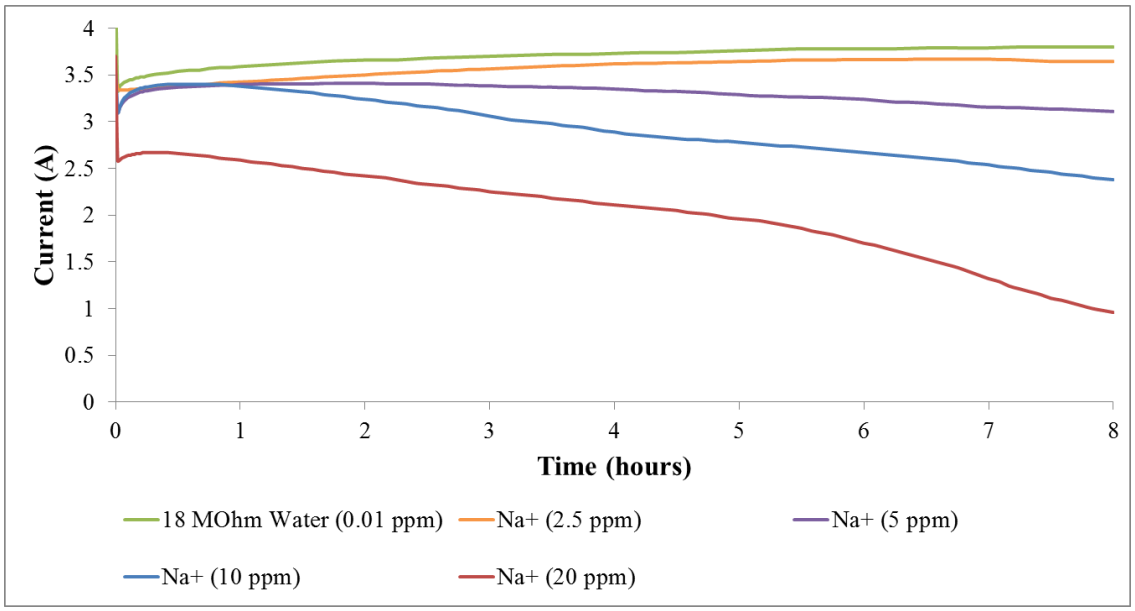

Figure 7.28: Electrolyser Degradation Performance with Sodium cation at 25ºC, constant 2V, 1 atm pressure, 20bar piston pressure, 80ml/min water flowrate

The data in Figure 7.28 shows the electrochemical degradation of the PEM electrolysis cell with 20ppm of sodium cations and less. All experiments with 2.5ppm of sodium cations in exhibited degradation in electrochemical performance over the 8 hour duration.

Assuming the rate of degradation remains constant, the rate of degradation between 7 and 8 hours was measured and then the current degradation rate was calculated.

Table 7.3: MEA lifetime for varying quantities of Na^+

Sodium Concentration (ppm)	Current Degradation (Amps / Hour)
0.01	0
2.5	0.03
5	0.05
10	0.16
20	0.37

Table 7.3 shows MEA lifetime increases with decreasing Na^+ concentration in the electrolysis feedwater. The analysis highlights the need to reduce cation content of sodium and calcium in order to allow the electrolyser lifetime requirement to increase. The ICP-MS measurement of 0.01ppm sodium and 0.02ppm in Type I water shows the minimum cation content in the purist water.

7.4. Performance Comparison to Alkaline Electrolysis

This thesis has discuss the potential of alkaline and PEM electrolysers for on demand hydrogen systems, whether this be for mobile applications (HHO generator for ICE improvement) or stationary applications (hydrogen refuelling station).

The alkaline electrolyser prototype (Electrolyser I) and the PEM electrolyser is this chapter will be compared for polarisation, hydrogen yield, electrical efficiency and long term performance. All alkaline electrolysis data is representative of 0.1M KOH solution

and polished nickel electrodes. The total electrode surface area is 4150cm^2. The PEM electrolysis data is representative of Nafion® based MEAs consistent with Section 7.2.4.1. The feed water used was Type I (18MΩ).

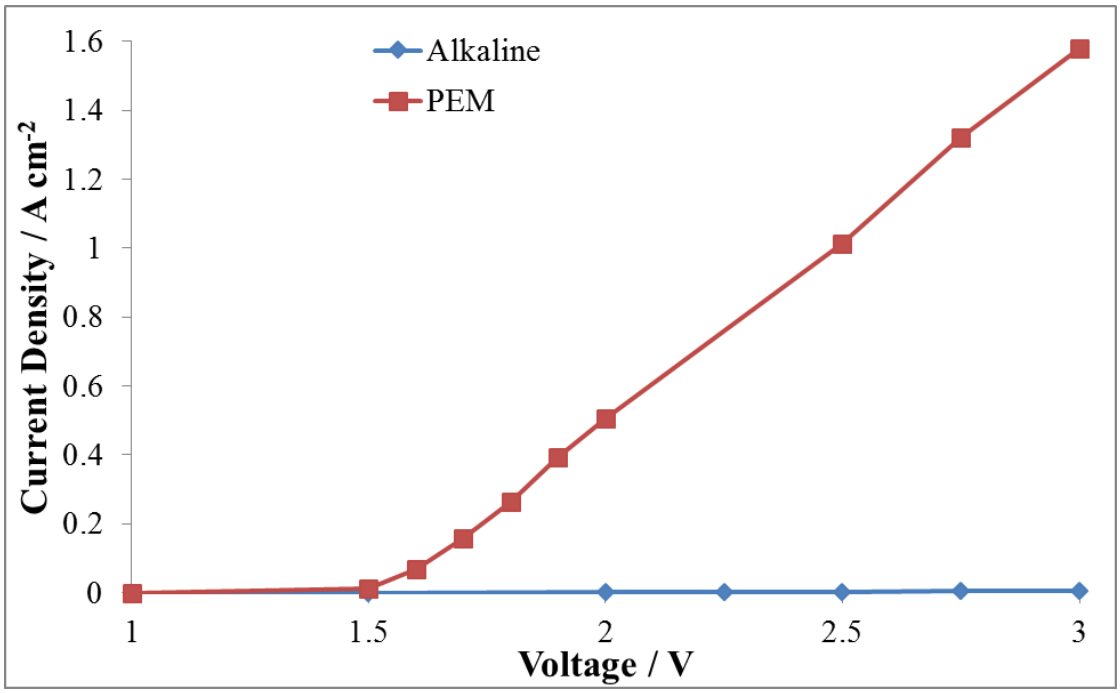

Figure 7.29: Polarisation of Alkaline and PEM Electrolysers at 25°C, 0.1V scan rate, 1 atm pressure, 0.1M KOH (for alkaline electrolyser), and 20bar piston pressure, 80ml/min water flowrate (for PEM electrolyser)

Figure 7.29 shows the difference in electrochemical performance of the two water electrolysis technologies per unit electrode surface area. The alkaline electrolyser achieves 0.005 A cm^{-2} at 3V applied potential whereas the PEM electrolyser has 1.6 A cm^{-2} at 3 V. The PEM electrolyser has a platinum catalyst which enables the higher current density comparatively. The economic cost of the PEM electrolyser is far greater than the alkaline electrolyser as a result.

Figure 7.30 shows the hydrogen yield from the alkaline and PEM electrolysers per unit electrode surface area. The alkaline electrolyser exhibits an identical trend as the polarisation with the gas produced per unit surface area significantly below that of the PEM electrolyser.

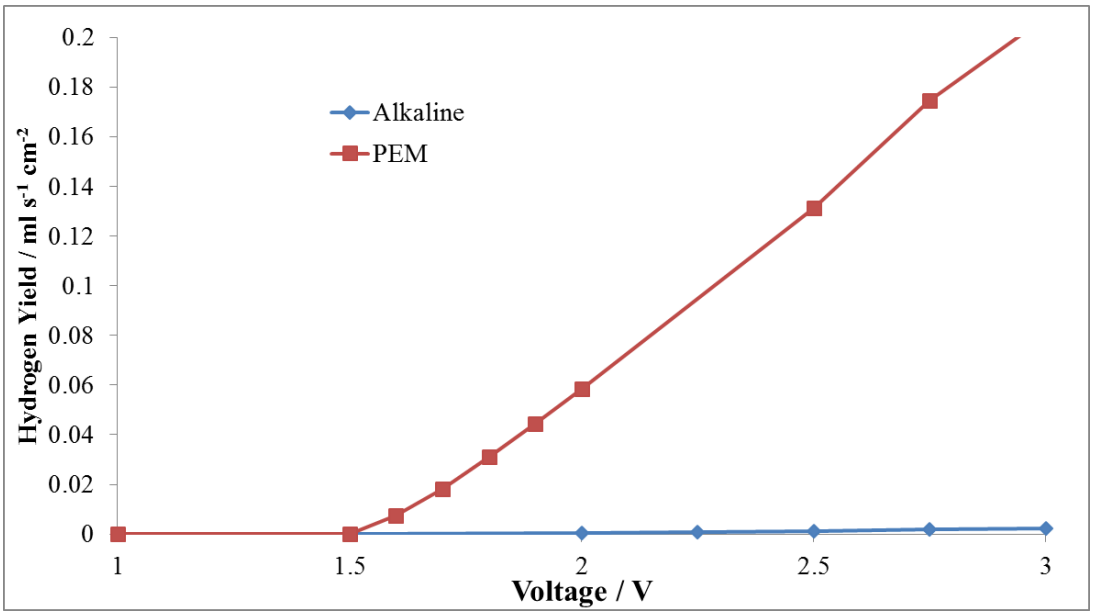

Figure 7.30: Hydrogen Productivity per unite surface area of Alkaline and PEM Electrolysers at 25ºC, Alkaline Electrolyser - 0.1V scan rate, 1 atm pressure, 0.1M KOH, PEM Electrolyser - 20bar piston pressure, 80ml/min water flowrate

Figure 7.31 shows the electrical efficiency of the alkaline and PEM electrolyser from a 1.5 to 3 V input potential. The data shows a similar performance for both water electrolysis technologies. PEM electrolysis achieves approximately 90% efficiency at 1.6 V and maintains a higher efficiency than the alkaline electrolyser until 2.5 V where the efficiencies are almost identical up to 3 V.

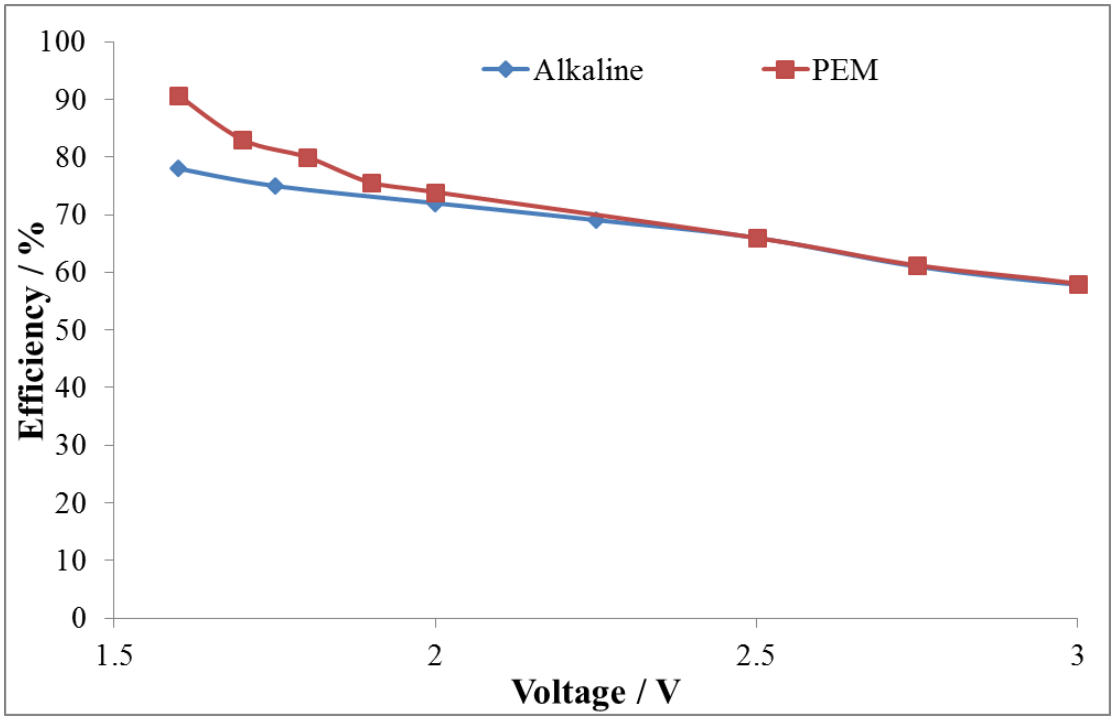

Figure 7.31: Electrical Efficiency of Alkaline and PEM Electrolysers at 25ºC, Alkaline Electrolyser - 0.1V scan rate, 1 atm pressure, 0.1M KOH, PEM Electrolyser - 20bar piston pressure, 80ml/min water flowrate

The electrolysis process is most efficient at low applied voltages as this is where overpotentials are at a minimum. The 90% efficiency at 1.6 V for the PEM electrolyser is highly desirable along with the non-hazardous feedstock required.

The long term performance for the electrolyser technologies needs to be analysed as well as the simple characterisation data presented previously. Figure 7.32 shows the long term performance data for the alkaline and PEM electrolysers.

The analysis shows that both alkaline and PEM electrolysers can support 8 hours of operation without any reduction in electrochemical performance. Whilst 8 hours is a very short period of time in reality, this research has shown the degradation in electrochemical performance possible when reaction conditions are pushed outside the comfort zone.

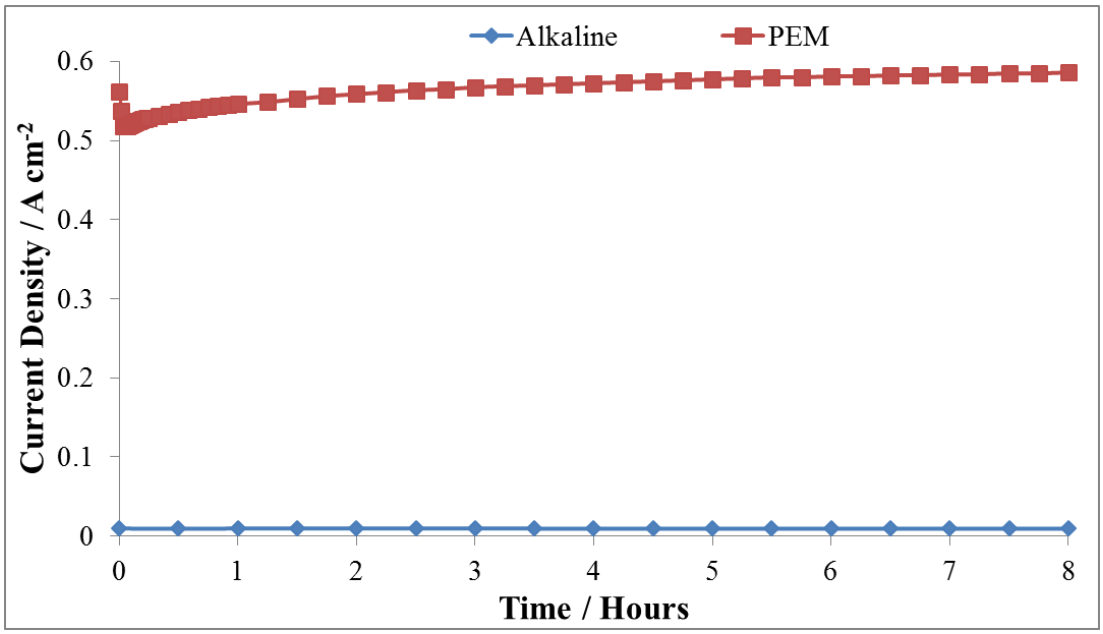

Figure 7.32: Degradation of Alkaline & PEM Electrolyser at 25°C, Alkaline Electrolyser - 1atm pressure, 0.1M KOH, constant 4V potential, PEM Electrolyser - 2V potential 20bar piston pressure, 80ml/min water flowrate

As has been previously shown (Chapter 4) alkaline electrolysis suffers from degradation when subjected to high electrolyte concentrations and high power input. The PEM electrolyser in this chapter has been shown to suffer performance deterioration when impure water feedstock is used.

The balance of power is shifting and the use of the new PEM electrolysis technology is becoming more desirable for the above reasons and the high hydrogen production rates per unit electrode surface area.

7.5. Conclusions

Feed water contamination was researched in a PEM electrolyser. Water with a resistance down to 1 MΩ has shown no electrochemical degradation over an 8 hour period for both membrane materials. The use of domestic tap water has shown very poor electrochemical performance from the PEM electrolyser with both membrane materials.

Microscopy studies of the tap water MEA after experimentation showed increased surface roughness and the presence of cations (Na^+, K^+, Ca^{2+}, Mg^{2+}) present on the cathode of the Nafion® based MEAs. This cation presence resulted in blockage of nucleation/activation sites on the MEA. The Fumea® based tap water MEA exhibited a lesser drop in electrochemical performance compared to the Nafion® based tap water MEA. The microscopy analysis of the Fumea® based tap water MEAs detected no cation presence on the cathode, but had a highly cracked surface. EDX analysis showed a drop in carbon and increase in fluorine content. This is consistent with cracking of the catalyst layer and the subsequent breaching of the membrane itself which contains fluorine.

The analysis of the data produced in this chapter supports the hypothesis of poor electrochemical performance due to cation poisoning in MEAs as previously research in

literature has shown [32, 96, 111, 113, 114, 118, 123, 127, 128, 133, 135], but the individual targeting of cations present in domestic tap water has not been previously investigated.

Calcium and sodium ions were analysed as they have the highest ppm content in domestic tap water as soon in the ICP-MS analysis. Calcium cations showed a limit of less than 3.125 ppm for an 8 hour performance consistent with Type II water. Sodium cations showed a limit of less than 2.5 ppm for an 8 hour performance consistent with Type II water. The research has shown the calcium and sodium cation content must be kept below these quantities to maintain sufficient long term performance of the PEM electrolyser.

Two water electrolysis technologies (alkaline and PEM) have been analysed in this research and the PEM electrolysis performance in this chapter has been compared with that of the alkaline electrolyser manufactured and tested in Chapter 4. The analysis highlights the improved electrochemical performance of a PEM electrolyser over an alkaline electrolyser as a function of electrode surface area.

PEM technology offers many advantages over the older alkaline technology and the marketplace for these commercial PEM electrolysers is growing in size. The ability to work at high pressures, low temperatures and with varying load conditions make them suitable for many applications which are currently in existence. Commercially available PEM electrolysers are available for integration into systems for vehicle refuelling,

synthetic methane gas injection and grid balancing. The University of Birmingham carried out a first field test of a commercial PEM electrolyser in 2011 and the next chapter details the testing of this electrolyser and its proposed integration of an onsite hydrogen production system with an existing hydrogen refuelling station.

Chapter 8

PEM Electrolyser System Integration

This research has been published in:

Energy Procedia, Vol. 29, 2012, p. 606-615. DOI: 10.1016/j.egypro.2012.09.070

&

International Journal of Hydrogen Energy, Volume 39 (14), p7460-7466. DOI: 10.1016/j.ijhydene.2014.03.003

PEM technology represents an attractive future for low temperature electrolysis for hydrogen fuel generation. This is more so than alkaline technology, because PEM technology has shown to have higher efficiencies, is highly adaptable to varying input loads, and has pure water as the only input which is much more attractive to the end user than handling caustic alkaline solutions.

The PEM electrolyser itself cannot be used to produce hydrogen fit for fuel cell vehicles (FCVs). Ancillary equipment such as a compressor and storage tanks must be integrated into a controlled system to deliver this hydrogen to refuelling stations. The options available for this process are to have the hydrogen produced at a centralised facility, which has high capital costs, low variable costs and high delivery costs. The alternative option to this would be to have the hydrogen produced onsite next to the refuelling station (distributed network).

Attractiveness of onsite hydrogen generation for vehicle refuelling represents zero carbon emissions and high financial incentives (no delivery cost) towards a decentralised/distributed energy network.

This chapter details the first field trial of Electrolyser J at University of Birmingham. This incorporated testing Electrolyser J in a lab which is considered to be a harsh operating environment (no central heating and historically an inconsistent electrical power supply).

As well as trialling the electrolyser, the end goal of the project was to design and implement an infrastructure for supplying the existing hydrogen refuelling station with hydrogen produced from Electrolyser J. The design of this proposed system is shown herein.

8.1. Experimental Results & Analysis

8.1.1. Water Analysis

Figure 8.1 contains recent measurements taken from the water used in the electrolyser. The three measurements are taken from the de-ionised water supply itself, the hydrogen tank in Electrolyser J (which is at up to 15 bar pressure), and the oxygen tank (shown in the P&ID of Electrolyser J in Figure 3.27). Figure 8.1 and shows the variation in pH and conductivity from the three sampling locations over time.

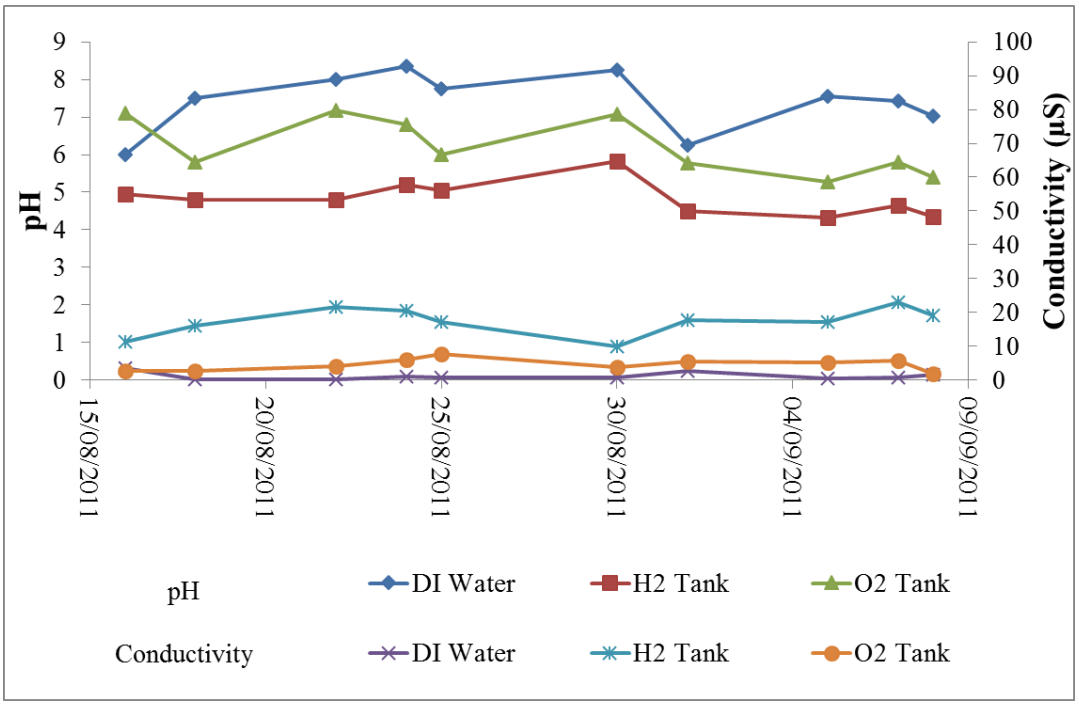

Figure 8.1: Water pH/Conductivity Analysis

The data presented shows little variation in conductivity for the three samples over time, with a conductivity of 0.1μS expected from the deionised (ASTM Type II) water.

8.1.2. Electrolyser J Testing Data

The electrolyser that was chosen to produce the high purity hydrogen was Electrolyser J (Figure 3.26). This electrolyser uses PEM technology to separate water into hydrogen and oxygen. Electrolyser J produces 10 litres per minute (LPM) of hydrogen at up to 15 bar pressure. This equivalent to approximately 1kg of H_2 produced per day. The PEM electrolyser does not use commercially common Nafion®, but uses the suppliers own membrane technology, which is a hydrocarbon based membrane, whereas Nafion® is a perfluorinated sulfonic acid (PFSA) membrane.

For the duration Electrolyser J was operational, data was collected and analysed. A sample of the data measured has been analysed. The data in Figure 8.2 can be used to analyse Electrolyser J performance. The potential (measured on the secondary y-axis) is maintained at approximately 20 V (10 cells at 2 V per cell), and when there are variations in the potential across the electrolyser stack, the current flow and H_2 and O_2 temperatures adjust as a direct result. When there is a decrease in potential (approximately 0.5 V), the current reduces by approximately 15 A (since the two electrochemical parameters are dependent on each other). The decrease in current flow results in a decrease in H_2 and O_2 temperature, visible in Figure 8.2 are due to reduction in power in the electrolyser stack and therefore the heat produced.

Table 8.1: Electrolyser J Testing Analysis

Run No.	Duration of Operation (Hours)	Notes
Electrolyser J #1 Stack #1		
1	114.5	Water Leak Shutdown Piston Pressure Decrease Observed
Electrolyser J #1 Stack #2		
2	168	Power Loss during Weekly Purge New Fuse Inserted
3	150	Water Leak Shutdown No Leak Visible
4	80	H_2 Tank Low Shutdown During Purge – Reset fixed Problem. Pressure Leak Shutdown Possible explanation: H_2 Pressure 14.9bar just before shutdown
5	96	Pressure Leak Shutdown Possible explanation: H_2 Pressure 14.9bar just before shutdown
Electrolyser J #1 Stack #3		
6	480	New Stack; Updated Software; No Dryer Present
7	597	Blown Fuses
Electrolyser J #2 Stack #1		
8	401	External Power Failure
9	171	External Power Failure
10	362	UoB Estates Shut Off; Electrolyser Stack Frozen
Total Operation Hours		2619.5
Total Hours Available		5400
Electrolyser J Utilisation		48.5%
Hydrogen Produced		≈ 109 kg

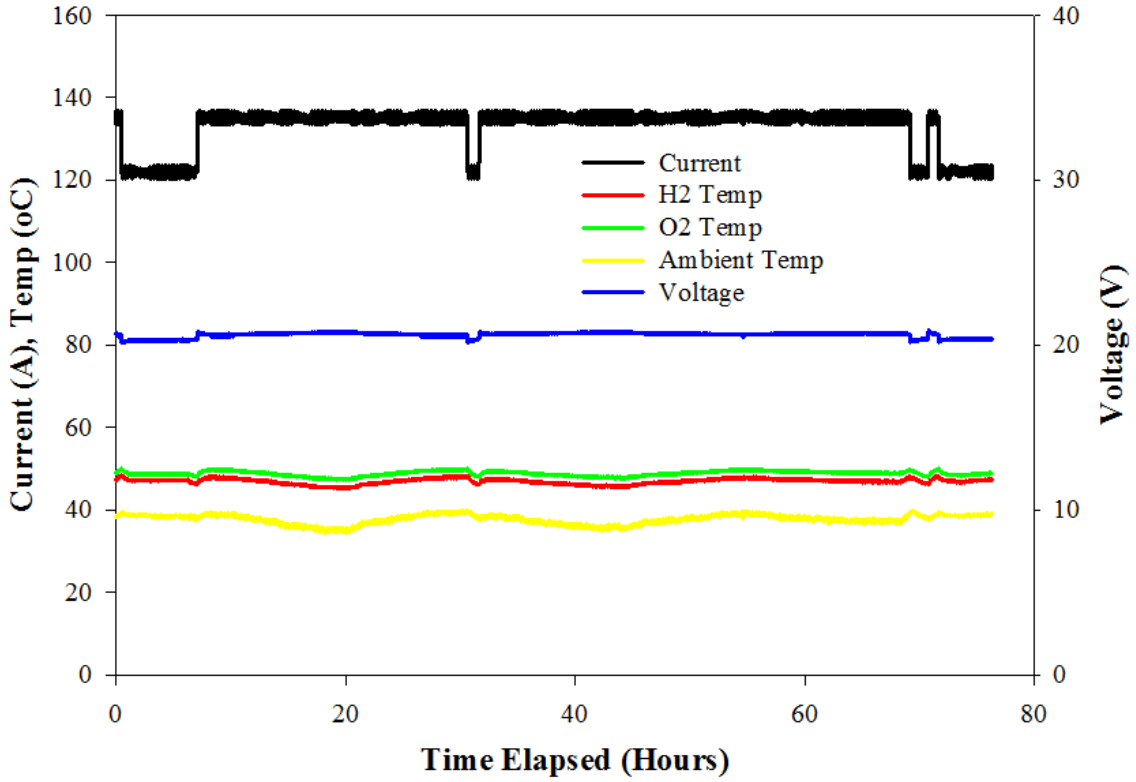

Figure 8.2: Data from Electrolyser J scenario Run 2

The data presented in Figure 8.3 shows two momentary power losses to the electrolyser stack, which stopped the flow of current and ceased the production of hydrogen. This power input deficit was only temporary and the power supply to the electrolyser stack recommenced.

It was concluded that this ten minute loss in power was when the system was going through its weekly water purge cycle, in which power to the electrolyser stack is stopped.

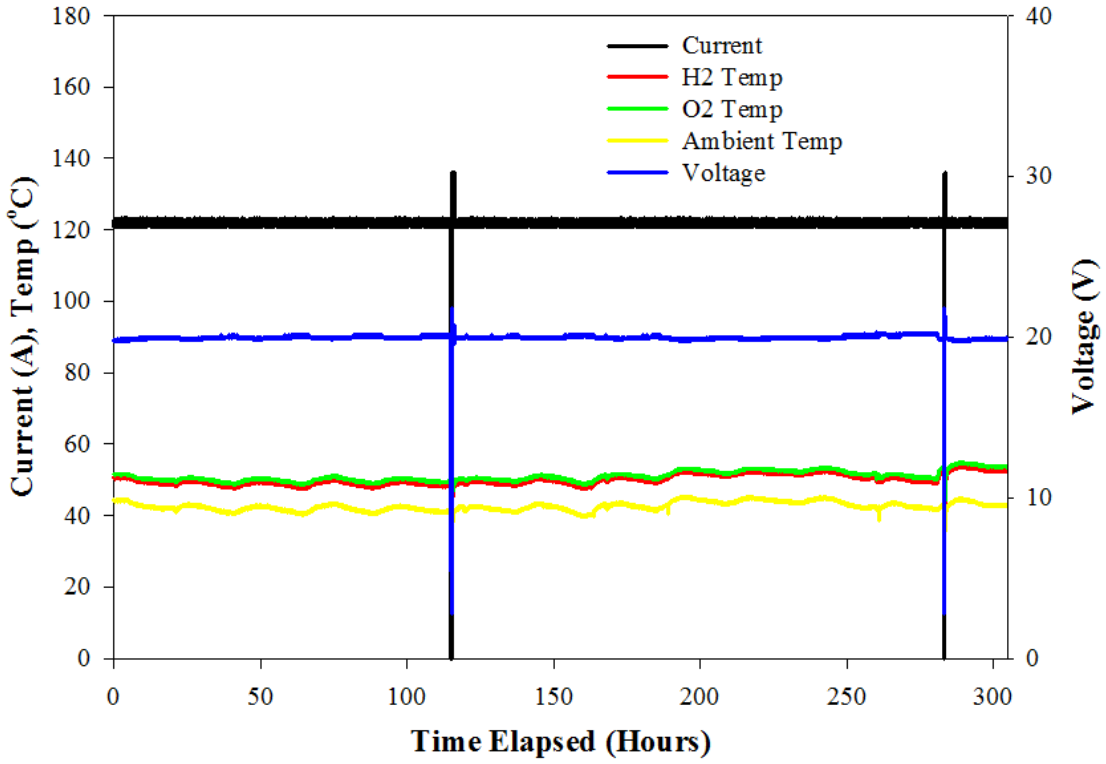

Figure 8.3: Data from Electrolyser J scenario Run 7

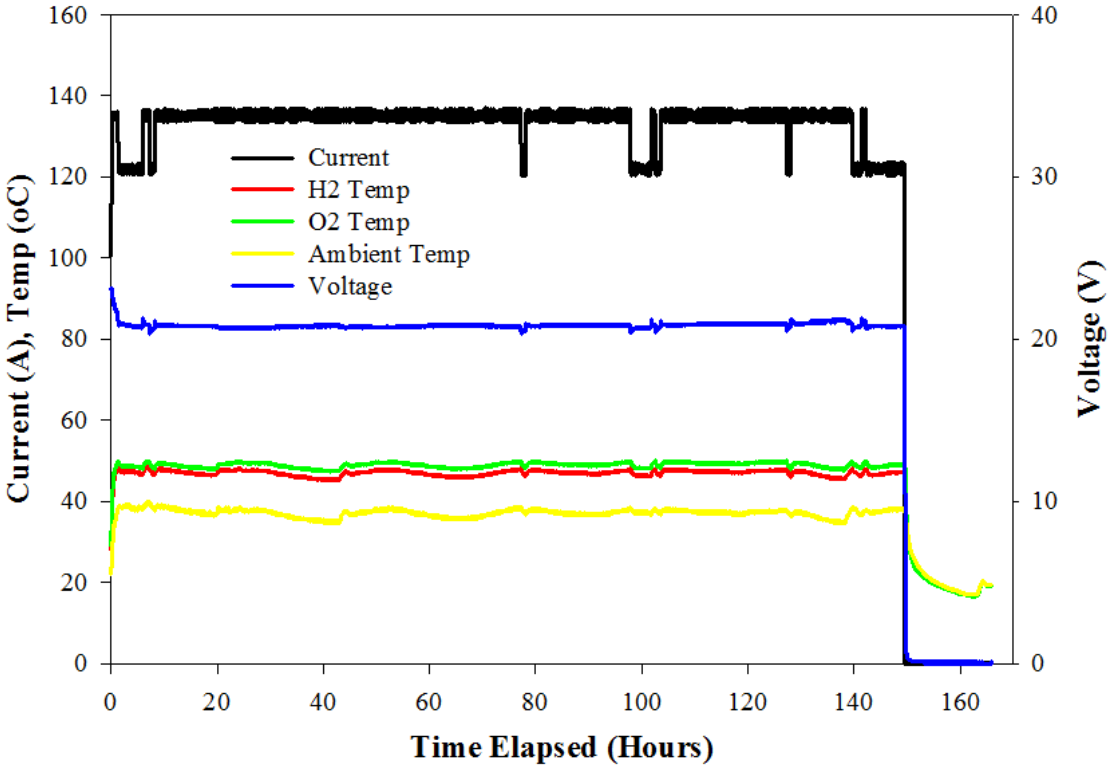

Figure 8.4: Data from Electrolyser J scenario Run 3

The data presented in Figure 8.4 shows a manual shutdown by the user. When Electrolyser J is shutdown manually using front display, power to the electrolyser stack is stopped; thus producing no current in the process. This ceases the production of output hydrogen.

With no current flow in the electrolyser stack and thus no heat production, the temperature in the electrolyser drops across all three temperature sensors until it reaches room temperature.

8.1.3. Refuelling Infrastructure Design

8.1.3.1 Project Introduction

In April 2008, The University of Birmingham launched the first permanent hydrogen refuelling station in England, U.K. This enabled the refuelling of the only fleet of (five) hydrogen fuel cell vehicles (HFCV) in the U.K at the time. The "green" hydrogen for the refuelling station was supplied off site. The ultra-high purity (99.9995%) hydrogen is a vital requirement for the polymer electrolyte membrane fuel cells (PEMFCs). This is because membrane electrode assemblies (MEAs) are susceptible to poisoning from low concentrations of impurities (carbon monoxide, sulphur etc.), and will decrease the performance and lifetime of the fuel cell irreversibly. The University aims to be the first campus in the U.K. that is carbon neutral and this project scopes to produce "green" hydrogen on-site to power the fleet of HFCVs.

Hydrogen was previously supplied from Green Hydrogen, a division of Green Gases Ltd based in Cambridgeshire, U.K. Figure 8.5 illustrates the process used to achieve high purity hydrogen gas.

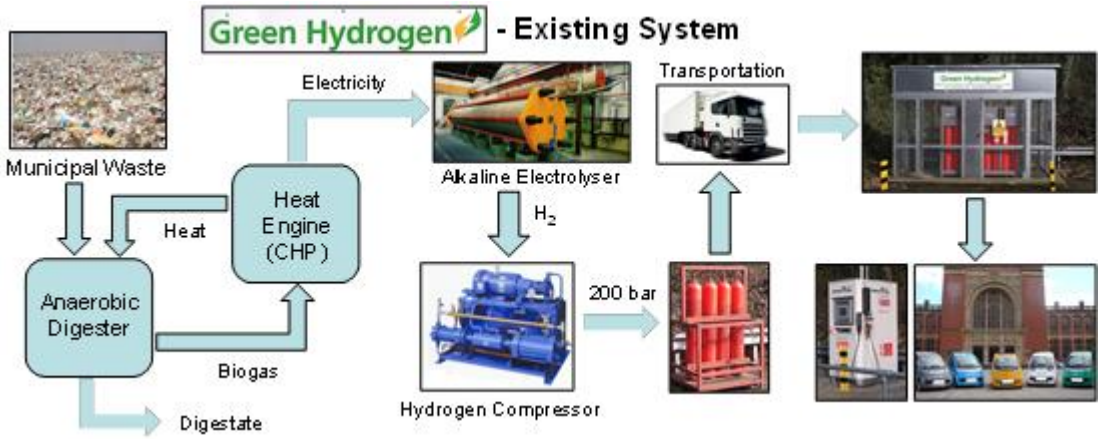

Figure 8.5: Existing Hydrogen Supply Chain at University of Birmingham, U.K.

This process oversees the conversion of municipal waste to hydrogen through an aerobic digester to produce synthetic gas (a mixture consisting of mainly carbon monoxide and hydrogen), then this combusted in a combined heat and power engine to produce electrical energy which is then used in an alkaline electrolyser to produce the high purity hydrogen gas. The gas is produced at approximately 10-15 bar, and then it is compressed to 200 bar and put into K-Type gas cylinders before transportation [209].

This process produces low levels of greenhouse gas emissions, apart from the method of transporting the cylinders to the University of Birmingham, from which a carbon footprint can be attached to the hydrogen.

Electrolysis is currently the only commercial method for producing ultra-high purity hydrogen. Electrolyser J has been purchased to produce hydrogen on-site (up to 1.25 kgH_2/day). Electrolyser J uses PEM technology, which eliminates the need for hazardous alkaline substances, to produce hydrogen. The input requirements are ASTM Type 2 de-ionised (DI) water and 240V power supply. Hydrogen is produced from the electrolyser at pressures up to 15 bar. However there is a need to integrate this unit within the existing hydrogen infrastructure. A system flow diagram of the proposed hydrogen refuelling system is illustrated in Figure 8.6.

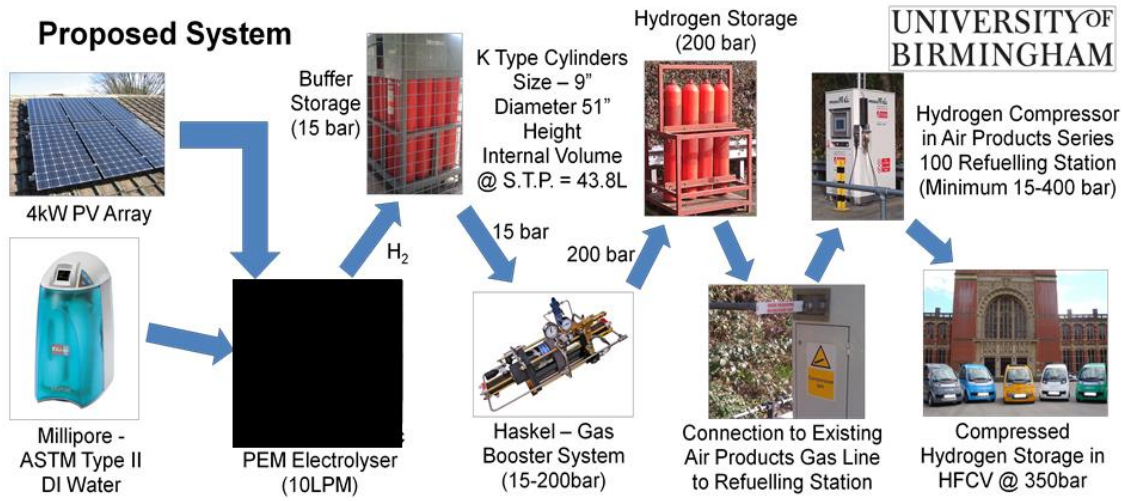

Figure 8.6: Proposed Hydrogen Supply Chain for University of Birmingham Refuelling Station

The system design involves the use of needle valves, check valves, pressure transducers, and pressure relief valves. The whole system would be controlled by a PLC control system, regulating the needle valves from the various pressure transducers in the system.

Within the HFCV, hydrogen is stored in a compressed gas tank (350bar). The Air Products Series 100 refuelling station has a built in compressor that compresses hydrogen from 200 bar (from storage, and capable of utilising the supply down to 20bar) to 400 bar (delivery). Therefore an additional compressor (Haskel International Inc.) is required to compress hydrogen from 15 bar to 200 bar.

The 200 bar hydrogen is stored in K-Type Gas Cylinders, thus by using existing cylinders no changes to the infrastructure are required. These cylinders would then be detached from the electrolyser setup and be relocated to the refuelling infrastructure, supplying 200 bar hydrogen to the Air Products Refuelling Station.

8.1.3.2 System Components

Photovoltaic Cells

Photovoltaic panels of peak rating 4kW were purchased and placed on the roof of the building (Figure 8.7). These panels were not directly coupled to the electrolyser due to the intermittency of solar energy. This 4kW is sufficient to offset the peak energy requirement of the electrolyser and the ancillary equipment.

Figure 8.7: Photovoltaic Panels Reproduced from [210]

DI Water Supply

See Section 3.2.3.

Electrolyser – Electrolyser J

See Section 3.2.1.7.

Buffer Storage

Once the hydrogen is produced in electrolyser it is placed in a 15 Bar H_2 Buffer Storage. This consists of sixteen K-Type Cylinders, each with an internal volume of 50 litres at standard temperature and pressure. The total H_2 capacity at 15 bar pressure for all sixteen cylinders is 0.8kg. This buffer store will be permanently fixed in place.

Hydrogen Compressor

Once the buffer storage of H_2 at 15 bar pressure is full, a compressor is required to pressurise the H_2 up to 200 bar pressure. The compressor that is used is a Haskell Gas Booster Pump. It is an air driven compressor that requires a compressed air supply of 7 bar pressure. The minimum inlet pressure for the compressor is 10 bar pressure and the maximum outlet pressure is 200 bar pressure. The compression rate is approximately 10.2 litres per minute (LPM), which means that the compressor operates at the same rate as the production rate of Electrolyser J. The pressure relief valve is set at 10% higher than operating pressure which is at 220 bar pressure.

High Pressure Storage

Once the hydrogen is compressed to 200 bar pressure, it is transported to four K-Type cylinders each with an internal volume of 50 litres. These four cylinders have a combined hydrogen storage capacity of 3.0 kg at 200 bar pressure. Once these four cylinders are full, they are disconnected from the compressor supply line and are attached to the existing hydrogen refuelling infrastructure to provide hydrogen to the Air Products Refuelling Station.

8.1.3.3. Health and Safety Aspects

Before the proposed system can be implemented and integrated into the existing system, the various health and safety documentation must be completed to ensure all precautions

necessary are taken to avoid risk and minimise the dangers associated with the hydrogen refuelling system.

Hydrogen requires special safety measures and handling precautions, since has many hazards. These include:

- Hydrogen burns with an invisible flame
- Vapours can spread and ignite
- Hydrogen displaces breathing oxygen in the air and so presents a risk of asphyxiation at high concentrations

All Health & Safety Information including Risk Assessments and HAZOPs are in Appendix B.

8.1.3.4. Infrastructure Planning and Piping & Instrumentation Diagram (P&ID)

The system layout is illustrated in the satellite image (Figure 8.8) and shows the Hydrogen & Fuel Cells Research Laboratories at the University of Birmingham. Shown on here is the existing location of the Air Products Hydrogen Refuelling Station, Gas Cylinder Storage and existing infrastructure. The blue represents the existing air compressor and its gas line connection to the Refuelling Station.

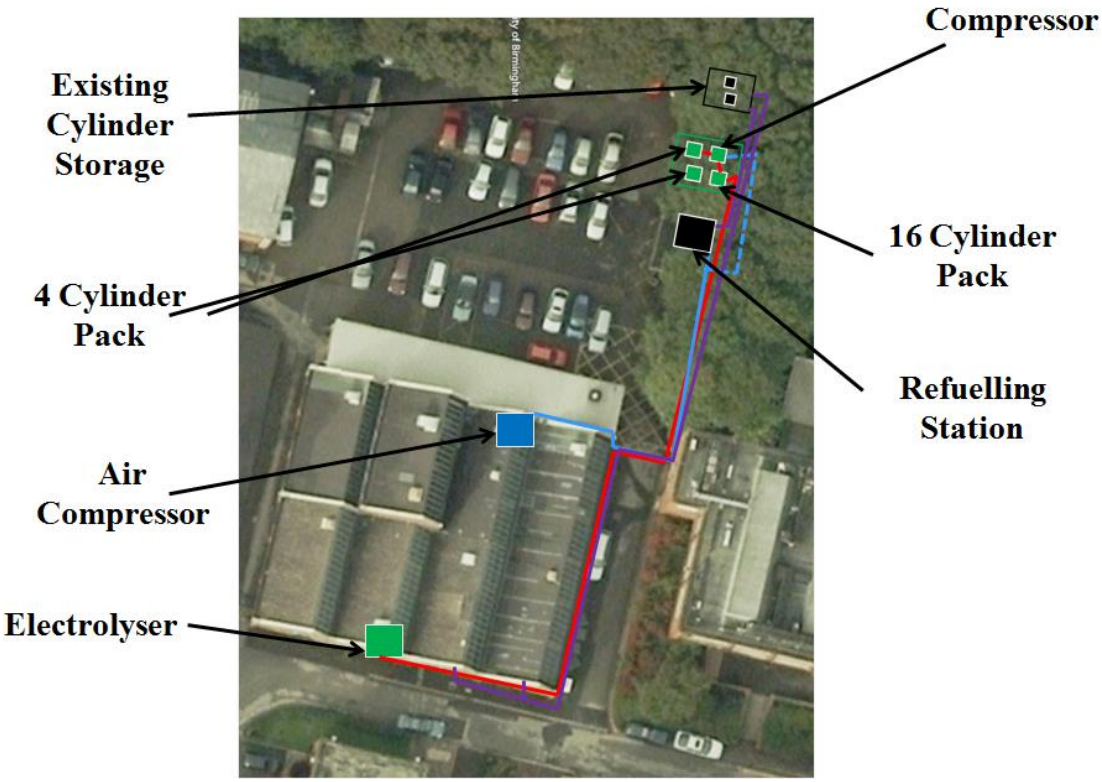

Figure 8.8: Satellite View of Proposed Hydrogen Infrastructure

The location of the new equipment is shown in green, which includes the electrolyser, gas cylinder packs, and the hydrogen compressor. The red line represents the new gas pipes (SS316 6mm ID) that are going to be implemented to connect the new equipment together. The blue hashed line shows the extension needed on the compressed air line required to supply not only the Air Products Refuelling Station, but also the hydrogen compressor, which is air-driven. What is not shown on the aerial image is the detailed use of valves, actuators, and control system, which are shown in the P&ID (Figure 8.9).

System Control Philosophy

The system operates with the electrical input to Electrolyser J and DI water provided on-demand. This produces H_2 at 10LPM up to 15 bar pressure. V1 is a manual shut off valve which is normally open, unless Electrolyser J shut off fails. H_2 fills the buffer storage when V2 is closed, and this valve opens when PT1 records a pressure of 15 bar. When V2 is open, the program logic controller (PLC) automatically opens V5, which allows compressed air to the compressor (CMP1) to compress the hydrogen from low pressure to high pressure (200 bar). This high pressure hydrogen then passed through V3 (manual shut off, normally open), and V4, which is our high pressure valve which allows us to fill the gas cylinders. To fill the high pressure cylinders takes approximately 2.5 days. Once PT2 records 200 bar pressure in the cylinder pack, V5 is closed, thus stopping supply of compressed air to the compressor, therefore halting the compression process. V4 can be manually closed, the cylinders detached and replaced with empty ones, and then V5 can open again once PT2 registers minimal pressure in the cylinders.

The cylinders containing 200 bar pressure hydrogen can be manually moved and connected to the existing hydrogen infrastructure to supply the refuelling station.

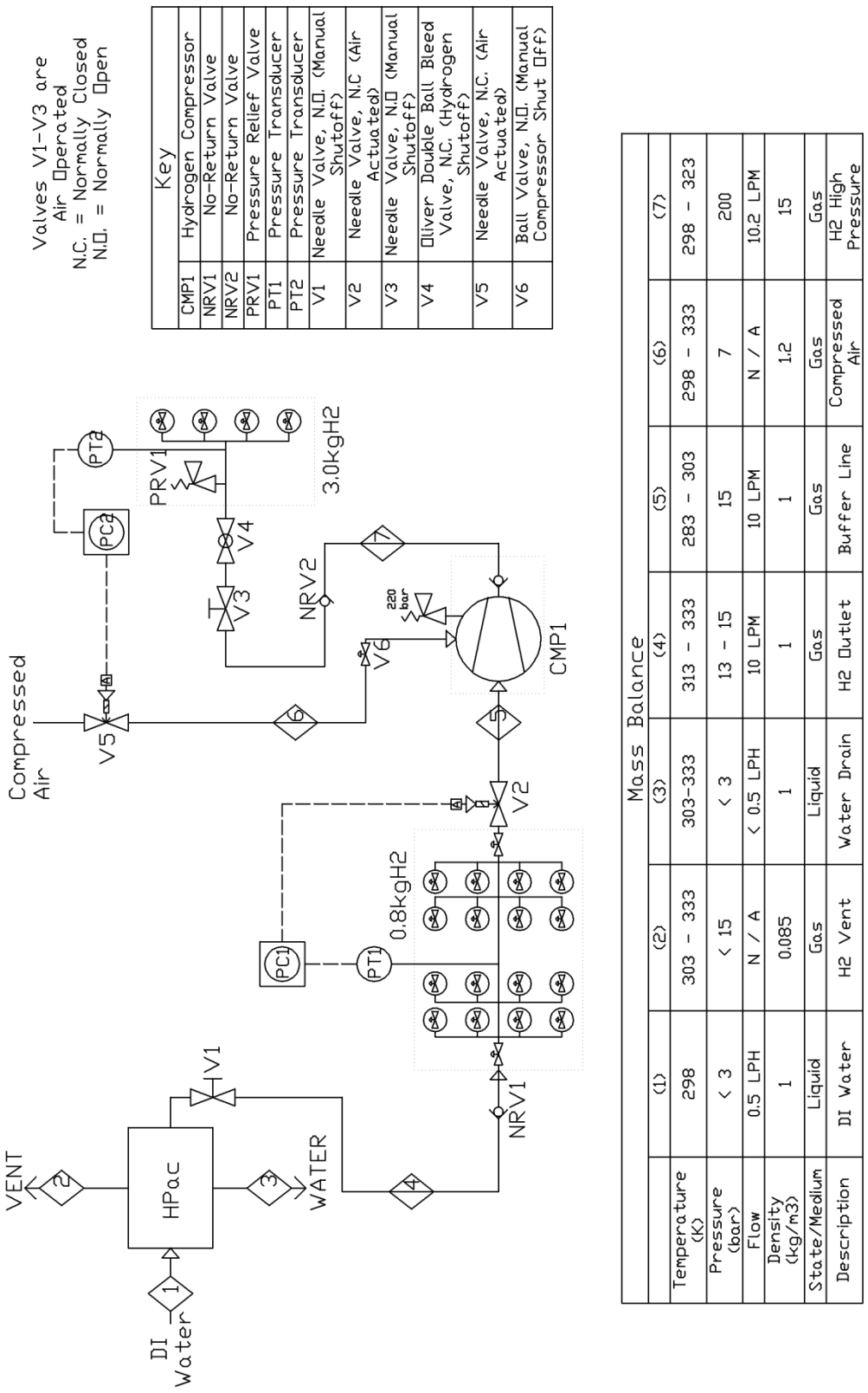

Figure 8.9: P&ID of Proposed Hydrogen Infrastructure

8.2. Conclusions

The rollout of a hydrogen refuelling infrastructure would see the implantation of onsite generation systems such as the one designed here. Rollout plans for hydrogen refuelling infrastructure are underway for U.K. (UKH_2Mobility), Germany (H_2Mobility), France (Mobilité Hydrogène France) and U.S.A. (H_2USA). An hydrogen infrastructure implementation plan conducted by the author and other students at the University of Birmingham, U.K., for the North-east U.S.A. to support FCEVs has won joint 1st place at the annual Hydrogen Student Design Contest and is found at www.hydrogencontest.org.

The results show the operation and testing of a PEM electrolyser in the first field trial of Electrolyser J with the end goal to have the hydrogen produced, supplied to existing hydrogen refuelling station at University of Birmingham, U.K. The electrolyser exhibited excellent performance under steady state (fixed load) conditions.

What is obvious from the data collected is the struggle of the electrolyser to cope with the external harsh environment the electrolyser was placed in. This laboratory had no central heating got very cold in the middle of winter. This along with the intermittent electrical supply to the laboratory highlighted the vulnerability of this new technology to non-ideal conditions for operating the electrolyser in. As a result of the circumstances surrounding this field trial and the data collected, it is evident that robustness in PEM electrolysers requires improvement for commercial rollout of such technology, thus becoming more versatile to cold temperatures and impure water supplies.

Chapter 9

Conclusions and Recommendations

Two routes for on-demand hydrogen systems have been addressed. These are through the mature alkaline electrolysis technology for mobile applications and the more recently established PEM electrolysis, which is ideal for on-demand hydrogen in stationary applications.

9.1. Alkaline – Mobile Applications

Chapter 4 addressed the existing alkaline electrolyser marketplace and characterised four commercial alkaline electrolysers which are used in the generation of HHO gas for addition to ICEs to supposedly improve engine efficiency and decrease GHG exhaust emissions. The main findings were:

- Alkaline electrolysers, most commonly sold under the general umbrella of "water to fuel" systems, exist in the public domain available for purchase which do not perform or meet the required standards to achieve the stated demands of improvement in performance.
- Major design flaws exist in the alkaline electrolysers analysed and subsequently exhibit inefficient electrochemical performance compared to that stated in public documentation.
- Electrolyser E exhibited small reductions (< 0.2%) in CO and CO_2 emissions, whilst Electrolyser C exhibited no reductions in CO and CO_2 emissions during ICE testing.
- Electrolyser E exhibited higher reductions (< 50ppm) in NO emissions than Electrolyser C (< 20ppm), highlighting the effect of increased hydrogen quantity composition in the ICE.

- One of these electrolysers will be redesigned and built to demonstrate improved performance using the same footprint and economic cost.

Chapter 5 addressed the poor performance of Electrolyser E, evaluated the reasoning behind this and then redesigned (Electrolyser I) the system accordingly to maximise HHO output with an unchanged system footprint and economic cost. The main findings were:

- Electrochemical data shows improvement in performance up to 12V operation. 200A was measured across the electrolyser during operation and the approximate flowrate of HHO gas is estimated to be 4 LPM.
- Consequently improved performance in engine mode achieved with notable results on the effectiveness of HHO in internal combustion engines.
- 8% increase liquid fuel replacement, 8% reduction in CO_2 emissions was achieved.
- The presence of oxygen as well as hydrogen as a fuel additive improves performance since the monoatomic form of HHO (unstable water vapour) results in a quicker combustion than using diatomic hydrogen which requires more energy to break the atomic bonds.

Chapter 6 investigated the high degradation rates suffered by nickel electrodes in industrial alkaline electrolysers. Low degradation rates are vital for sufficient electrolyser lifetime and the subsequent cost-effectiveness of the system. The feasibility of an

'oxygen-getter' was researched in an alkaline electrolyser to measure any improvements in electrode degradation. The main findings were:

- Improved electrochemical performance (8% lifespan increase) from introduction of oxygen-getter to the system, although further repeatability is required to reduce error margins in analysis.
- Surface analysis of the electrode highlight reduced oxide content on the electrodes (approx. 17% reduction in oxygen atomic% on nickel electrode surfaces) supporting electrochemical data found.
- Scope for further research into 'oxygen-getter' concept in alkaline electrolysers to reduce electrode degradation, including specific quantity/location/geometry of getter material with the aim of clearly proving any improvement in long term alkaline electrolysis performance.

9.2. PEM – Stationary Applications

Chapter 7 addressed the benefits of PEM electrolysis over the historic alkaline technology. The need for ultrapure water for PEM technology is an added energy requirement in the system and is undesirable for when the mass commercialisation of this technology. A PEM electrolysis cell was tested with varying grades of water purity to analyse performance degradation and the subsequent mechanisms. The main findings were:

- Performance of PEM electrolyser degraded rapidly when introduced to impure (tap) water. This was up to 95% after 8 hours operation for the Nafion® membrane and 66% for Fumea® membrane.
- Identification of high levels of cations in the water (Na^+, K^+, Ca^{2+}, Mg^{2+}) identified from ICP-MS. The presence of these cations resulted in blockage of nucleation/activation sites on MEA from microscopy and surface analysis.
- Attractiveness of cations to the vacancies in Nafion® structure make it incompatible with impure waters containing high levels of cations.
- Fumea® exhibits less performance degradation (66% vs. 95%) than Nafion® when subjected to tap water, which makes it more desirable for future commercial integration.
- A comparison of PEM and alkaline experimentation was shown. PEM is more suitable for future commercial electrolyser with increased polarisation (approx. 99.9%) and electrolyser lifetime (approx. 96%), although further research required in reducing electrocatalyst quantity and cost.
- Established PEM electrolysers are available for integration into systems for vehicle refuelling, synthetic methane gas injection and grid balancing. A first field test of a PEM electrolyser will be undertaken.

Chapter 8 addressed the integration of a commercial PEM electrolyser with a newly designed system to supply hydrogen to an existing hydrogen refuelling station at the University of Birmingham, U.K. On-site production of hydrogen represents a carbon-neutral energy generation process which leads towards a future decentralised/distributed energy network. The main findings were:

- Excellent performance of PEM electrolyser under steady state conditions. This includes the constant current flow despite a variation in ambient room temperature.
- External harsh environment highlighted the vulnerability of this new technology and this was evident from the difficulty of cold start up and the consequent regular replacement of stacks.
- Robustness in PEM electrolysers requires improvement for commercial rollout, so they become more susceptible to cold temperatures and impure water supplies.

9.3. Future Work

The research completed herein has achieved the majority of goals set out at the beginning and brought about a greater understanding of scientific principles in the process of HHO injection into ICEs, the use of materials to reduce electrode degradation in alkaline electrolysis, and the durability of MEAs in a domestic tap water environment.

Further work from that carried out in this thesis should include:

- Testing of electrolysers in 1000s/10000s of hours to test long term durability consistent with industrial operation of electrolysers to determine the mechanisms for eventual failure and ways to deter these processes.
- Analysis of non-PFSA membranes with regards to long term electrochemical performance with tap water feedstock. This includes SPEEK and PBI membranes which could pave the way for cost reduction of PEM electrolysers and ease the process of mass market commercialisation if operable with domestic tap water.
- Cyclic testing of alkaline and PEM electrolysers to test tolerance to change in input load. A regular occurrence when an electrolyser is coupled to renewable energy power sources. This is a vital requirement for the market penetration of electrolyser as an energy storage medium to produce hydrogen from intermittent renewable energy sources.
- Anion targeting in PEM electrolysis. This would identify any effect that anions, such as chlorides and sulphates have on the electrolysis reaction.
- Investigation of the use of zero gap electrodes in an alkaline electrolyser. This is in the form of an anion exchange membrane (AEM), which is only allows the

conductance of OH^- anions through it. This would be a suitable comparison with a liquid caustic electrolyte used in the alkaline electrolysis process carried out.

- Varying quantities of hydrogen, oxygen and hydroxy (HHO) gas should be injected into an ICE environment to determine the optimum level flowrate requirement of these gases and then on-demand electrolysers can be sized and built accordingly to meet this.
- Experiments on H_2, O_2 and HHO gases in an ICE should also take into account varying engine load conditions, and then the engine control unit (ECU) be programmed accordingly to communicate directly with the electrolyser to produce the optimum amount of HHO dependant on the current engine load.
- Materials and methods for improving the tolerance of MEAs to cations and anions present in domestic tap water are highly desired to remove the need water purification for the water feedstock. The removal of this process would improve the energy efficiency of the overall hydrogen generation system and subsequently the cost of the system.
- This research topic could look further at the durability of these electrolysers to sea water feedstock. This would make the technology unrestricted geographically and could theoretically be utilised in coastal areas, and in maritime and sea based military applications.
- The above aspirations of improved water electrolysis technology are required to push towards a sustainable, indefinite, non-geographically limited, cost effective fuel to power the planet in a new age of energy supply and generation.

References

1. Moriarty, P. and D. Honnery, *Hydrogen's role in an uncertain energy future.* International Journal of Hydrogen Energy, 2009. **34**(1): p. 31-39.
2. Hofmann, D.J., J.H. Butler, and P.P. Tans, *A new look at atmospheric carbon dioxide.* Atmospheric Environment, 2009. **43**(12): p. 2084-2086.
3. Cormos, C.-C., Starr, F., Tzimas, E., Peteves, S., *Innovative concepts for hydrogen production processes based on coal gasification with CO2 capture.* International Journal of Hydrogen Energy, 2008. **33**(4): p. 1286-1294.
4. Rand, D.A.J., Dell, R. M., *Hydrogen Energy - Challanges and Prospects*. 2008: The Royal Society of Chemistry.
5. Manage, M.N., et al., *A techno-economic appraisal of hydrogen generation and the case for solid oxide electrolyser cells.* International Journal of Hydrogen Energy, 2011. **36**(10): p. 5782-5796.
6. Jensen, S.H., P.H. Larsen, and M. Mogensen, *Hydrogen and synthetic fuel production from renewable energy sources.* International Journal of Hydrogen Energy, 2007. **32**(15): p. 3253-3257.
7. Zuttel, A., Borgschulte, A., Schlapbach, L., *Hydrogen as a Future Energy Carrier*. 2008, Weinheim: Wiley.
8. Holladay, J., Hu, J., King, D., Wang, Y., *An overview of hydrogen production technologies.* Catalysis Today, 2009. **139**(4): p. 244-260.
9. Gupta, R.B., *Hydrogen Fuel, Production, Transport and Storage*. 2008: CRC Press.
10. Sørensen, B., *Hydrogen and Fuel Cells - Emerging technologies and applications*. Sustainable World. 2005: Elsevier Academic Press. 450.
11. Winter, C.-J., *Hydrogen energy -- Abundant, efficient, clean: A debate over the energy-system-of-change.* International Journal of Hydrogen Energy, 2009. **34**(14, Supplement 1): p. S1-S52.
12. Lemus, R.G. and J.M. Martínez Duart, *Updated hydrogen production costs and parities for conventional and renewable technologies.* International Journal of Hydrogen Energy, 2010. **35**(9): p. 3929-3936.
13. Holladay, J.D., et al., *An overview of hydrogen production technologies.* Catalysis Today, 2009. **139**(4): p. 244-260.
14. Veziroglu, T.N. and S. Sahin, *21st Century's energy: Hydrogen energy system.* Energy Conversion and Management, 2008. **49**(7): p. 1820-1831.
15. Chen, Y., et al., *Hydrogen production from the steam reforming of liquid hydrocarbons in membrane reactor.* Catalysis Today, 2006. **118**(1-2): p. 136-143.
16. Gao, N., A. Li, and C. Quan, *A novel reforming method for hydrogen production from biomass steam gasification.* Bioresource Technology, 2009. **100**(18): p. 4271-4277.
17. Bridgwater, A.V., D. Meier, and D. Radlein, *An overview of fast pyrolysis of biomass.* Organic Geochemistry, 1999. **30**(12): p. 1479-1493.
18. Hawkes, F.R., et al., *Sustainable fermentative hydrogen production: challenges for process optimisation.* International Journal of Hydrogen Energy. **27**(11-12): p. 1339-1347.
19. Hallenbeck, P.C., *Fermentative hydrogen production: Principles, progress, and prognosis.* International Journal of Hydrogen Energy, 2009. **34**(17): p. 7379-7389.
20. Getoff, N., *Photoelectrochemical and photocatalytic methods of hydrogen production: A short review.* International Journal of Hydrogen Energy, 1990. **15**(6): p. 407-417.

21. Millet, P., et al., *Scientific and engineering issues related to PEM technology: Water electrolysers, fuel cells and unitized regenerative systems.* International Journal of Hydrogen Energy, 2010.
22. Barbir, F., *PEM electrolysis for production of hydrogen from renewable energy sources.* Solar Energy, 2005. **78**(5): p. 661-669.
23. Harrison, K., Levene, J. I., *Electrolysis of Water*. 2004, National Renewable Energy Laboratories.
24. Zoulias, E., Varkaraki, E., Lymberopoulos, N., Christodoulou, C. N., Karagioris, G. N., *A Review of Water Electrolysis.* TCJST, 2004. **4**(2): p. 41-71.
25. Floch, P.H., et al., *On the production of hydrogen via alkaline electrolysis during off-peak periods.* International Journal of Hydrogen Energy, 2007. **32**(18): p. 4641-4647.
26. Kreuter, W. and H. Hofmann, *Electrolysis: The important energy transformer in a world of sustainable energy.* International Journal of Hydrogen Energy, 1998. **23**(8): p. 661-666.
27. Ganley, J.C., *High temperature and pressure alkaline electrolysis.* International Journal of Hydrogen Energy, 2009. **34**(9): p. 3604-3611.
28. Gandía, L.M., G. Arzamendi, and P.M. Diéguez, *Chapter 1 - Renewable Hydrogen Energy: An Overview*, in *Renewable Hydrogen Technologies*, L.M. Gandía, G. Arzamendi, and P.M. Diéguez, Editors. 2013, Elsevier: Amsterdam. p. 1-17.
29. Marshall, A.T., et al., *Performance of a PEM water electrolysis cell using electrocatalysts for the oxygen evolution electrode.* International Journal of Hydrogen Energy, 2007. **32**(13): p. 2320-2324.
30. Grigoriev, S.A., V.I. Porembsky, and V.N. Fateev, *Pure hydrogen production by PEM electrolysis for hydrogen energy.* International Journal of Hydrogen Energy, 2006. **31**(2): p. 171-175.
31. Millet, P., et al., *PEM water electrolyzers: From electrocatalysis to stack development.* International Journal of Hydrogen Energy, 2010. **35**(10): p. 5043-5052.
32. Collier, A., et al., *Degradation of polymer electrolyte membranes.* International Journal of Hydrogen Energy, 2006. **31**(13): p. 1838-1854.
33. Millet, P., et al., *GenHyPEM: A research program on PEM water electrolysis supported by the European Commission.* International Journal of Hydrogen Energy, 2009. **34**(11): p. 4974-4982.
34. Linkous, C.A., et al., *Development of new proton exchange membrane electrolytes for water electrolysis at higher temperatures.* International Journal of Hydrogen Energy, 1998. **23**(7): p. 525-529.
35. Grigoriev, S., V. Porembsky, and V. Fateev, *Pure hydrogen production by PEM electrolysis for hydrogen energy.* International Journal of Hydrogen Energy, 2006. **31**(2): p. 171-175.
36. Nieminen, J., I. Dincer, and G. Naterer, *Comparative performance analysis of PEM and solid oxide steam electrolysers.* International Journal of Hydrogen Energy, 2010. **35**(20): p. 10842-10850.
37. Stuart, P.A., et al., *Solid oxide proton conducting steam electrolysers.* Solid State Ionics, 2008. **179**(21-26): p. 1120-1124.

38. Jin, C., et al., *La0.75Sr0.25Cr0.5Mn0.5O3 as hydrogen electrode for solid oxide electrolysis cells.* International Journal of Hydrogen Energy, 2011. **36**(5): p. 3340-3346.
39. Ni, M., M. Leung, and D. Leung, *Technological development of hydrogen production by solid oxide electrolyzer cell (SOEC).* International Journal of Hydrogen Energy, 2008. **33**(9): p. 2337-2354.
40. *The Hydrogen Economy – Opportunities, Costs, Barriers and R&D Needs*. Committee on Alternatives and Strategies for Future Hydrogen Production and Use, ed. N.R.C. USA. 2004.
41. Smith, J.M., H.C.V. Ness, and M.M. Abbott, *Introduction to chemical engineering thermodynamics*. 2005: McGraw-Hill.
42. LeRoy, R.L., C.T. Bowen, and D.J. LeRoy, *The Thermodynamics of Aqueous Water Electrolysis.* Journal of The Electrochemical Society, 1980. **127**(9): p. 1954-1962.
43. Stanley I, S., *Thermodynamics*, in *Encyclopedia of Physical Science and Technology (Third Edition)*, A.M. Editor-in-Chief: Robert, Editor. 2003, Academic Press: New York. p. 639-657.
44. Choi, P., *A simple model for solid polymer electrolyte (SPE) water electrolysis.* Solid State Ionics, 2004. **175**(1-4): p. 535-539.
45. Zeng, K. and D. Zhang, *Recent progress in alkaline water electrolysis for hydrogen production and applications.* Progress in Energy and Combustion Science, 2010. **36**(3): p. 307-326.
46. R.L, L., *Industrial water electrolysis: Present and future.* International Journal of Hydrogen Energy, 1983. **8**(6): p. 401-417.
47. Kerres, J., et al., *Advanced alkaline electrolysis with porous polymeric diaphragms.* Desalination, 1996. **104**(1-2): p. 47-57.
48. LeRoy, R.L. and A.F. Hufnagl, *Progress in industrial demonstration of advanced unipolar electrolysis.* International Journal of Hydrogen Energy, 1983. **8**(8): p. 581-588.
49. Bowen, C.T., et al., *Developments in advanced alkaline water electrolysis.* International Journal of Hydrogen Energy, 1984. **9**(1-2): p. 59-66.
50. O'Brien, J.E., et al., *Parametric study of large-scale production of syngas via high-temperature co-electrolysis.* International Journal of Hydrogen Energy, 2009. **34**(9): p. 4216-4226.
51. Lee, T.S., *Hydrogen Over potential on Pure Metals in Alkaline Solution.* Journal of The Electrochemical Society, 1971. **118**(8): p. 1278-1282.
52. Jones, S.F., G.M. Evans, and K.P. Galvin, *Bubble nucleation from gas cavities — a review.* Advances in Colloid and Interface Science, 1999. **80**(1): p. 27-50.
53. Vogt, H. and R.J. Balzer, *The bubble coverage of gas-evolving electrodes in stagnant electrolytes.* Electrochimica Acta, 2005. **50**(10): p. 2073-2079.
54. Vogt, H., Ö. Aras, and R.J. Balzer, *The limits of the analogy between boiling and gas evolution at electrodes.* International Journal of Heat and Mass Transfer, 2004. **47**(4): p. 787-795.
55. Pollet, B., *Basics of Electrochemistry*. 2009.
56. Pettersson, J., B. Ramsey, and D. Harrison, *A review of the latest developments in electrodes for unitised regenerative polymer electrolyte fuel cells.* Journal of Power Sources, 2006. **157**(1): p. 28-34.

57. Bockris, J.O.M., *Recent Developments in the study of hydrogen overpotential.* 1948: p. 525-577.
58. Siracusano, S., et al., *Optimization of components and assembling in a PEM electrolyzer stack.* International Journal of Hydrogen Energy, 2011. **36**(5): p. 3333-3339.
59. Wang, M., Z. Wang, and Z. Guo, *Water electrolysis enhanced by super gravity field for hydrogen production.* International Journal of Hydrogen Energy, 2010. **35**(8): p. 3198-3205.
60. Santos, D.M.F., et al., *Platinum–rare earth electrodes for hydrogen evolution in alkaline water electrolysis.* International Journal of Hydrogen Energy, 2013. **38**(8): p. 3137-3145.
61. Santos DMF, S.C., Figueiredo JL, *Hydrogen production by alkaline water electrolysis.* Química Nova, 2013. **36** p. 1176-1193.
62. Mauer, A.E., D.W. Kirk, and S.J. Thorpe, *The role of iron in the prevention of nickel electrode deactivation in alkaline electrolysis.* Electrochimica Acta, 2007. **52**(11): p. 3505-3509.
63. Zhou, L. and Y. Cheng, *Catalytic electrolysis of ammonia on platinum in alkaline solution for hydrogen generation.* International Journal of Hydrogen Energy, 2008. **33**(21): p. 5897-5904.
64. Ursua, A., L.M. Gandia, and P. Sanchis, *Hydrogen Production From Water Electrolysis: Current Status and Future Trends.* Proceedings of the IEEE, 2012. **100**(2): p. 410-426.
65. Kothari, R., D. Buddhi, and R.L. Sawhney, *Studies on the effect of temperature of the electrolytes on the rate of production of hydrogen.* International Journal of Hydrogen Energy, 2005. **30**(3): p. 261-263.
66. Miles, M.H., et al., *The oxygen evolution reaction on platinum, iridium, ruthenium and their alloys at 80°C in acid solutions.* Electrochimica Acta, 1978. **23**(6): p. 521-526.
67. Renaud, R. and R.L. LeRoy, *Separator materials for use in alkaline water electrolysers.* International Journal of Hydrogen Energy, 1982. **7**(2): p. 155-166.
68. Grigoriev, S.A., et al., *Optimization of porous current collectors for PEM water electrolysers.* International Journal of Hydrogen Energy, 2009. **34**(11): p. 4968-4973.
69. Wei, G., et al., *The stability of MEA in SPE water electrolysis for hydrogen production.* International Journal of Hydrogen Energy, 2010. **35**(9): p. 3951-3957.
70. Pollet, B.G., *A novel method for preparing PEMFC electrodes by the ultrasonic and sonoelectrochemical techniques.* Electrochemistry Communications, 2009. **11**(7): p. 1445-1448.
71. Carmo, M., et al., *A comprehensive review on PEM water electrolysis.* International Journal of Hydrogen Energy, 2013. **38**(12): p. 4901-4934.
72. Yazici, B., et al., *Investigation of suitable cathodes for the production of hydrogen gas by electrolysis.* International Journal of Hydrogen Energy, 1995. **20**(12): p. 957-965.
73. Grigoriev, S.A., et al., *Platinum and palladium nano-particles supported by graphitic nano-fibers as catalysts for PEM water electrolysis.* International Journal of Hydrogen Energy. **In Press, Corrected Proof**.

74. Balaji, R., et al., *Development and performance evaluation of Proton Exchange Membrane (PEM) based hydrogen generator for portable applications.* International Journal of Hydrogen Energy, 2011. **36**(2): p. 1399-1403.
75. Chae, S.-Y., et al., *Durability study of electrospray deposited Pt film electrode for hydrogen production in PV assisted water electrolysis system.* International Journal of Hydrogen Energy, 2011. **36**(5): p. 3347-3353.
76. Millet, P., et al., *Electrochemical performances of PEM water electrolysis cells and perspectives.* International Journal of Hydrogen Energy, 2010.
77. Lessing, P.A., *Materials for hydrogen generation via water electrolysis.* Journal of Materials Science, 2007. **42**(10): p. 3477-3487.
78. Rasten, E., *Electrocatalysis in water electrolysis with solid polymer electrolyte*1.* Electrochimica Acta, 2003. **48**(25-26): p. 3945-3952.
79. Miles, M.H. and M.A. Thomason, *Periodic Variations of Overvoltages for Water Electrolysis in Acid Solutions from Cyclic Voltammetric Studies.* Journal of The Electrochemical Society, 1976. **123**(10): p. 1459-1461.
80. Matsumoto, Y. and E. Sato, *Electrocatalytic properties of transition metal oxides for oxygen evolution reaction.* Materials Chemistry and Physics, 1986. **14**(5): p. 397-426.
81. Buckley, D.N. and L.D. Burke, *The oxygen electrode. Part 6.-Oxygen evolution and corrosion at iridium anodes.* Journal of the Chemical Society, Faraday Transactions 1: Physical Chemistry in Condensed Phases, 1976. **72**(0): p. 2431-2440.
82. Balej, J., *Electrocatalysts for oxygen evolution in advanced water electrolysis.* International Journal of Hydrogen Energy, 1985. **10**(2): p. 89-99.
83. El-Deab, M.S., et al., *Enhanced water electrolysis: Electrocatalytic generation of oxygen gas at manganese oxide nanorods modified electrodes.* Electrochemistry Communications, 2007. **9**(8): p. 2082-2087.
84. S., G., *Performance of supported catalysts for water electrolysis*, in *Norwegian University of Science and Technology*. 2012.
85. Ma, L., S. Sui, and Y. Zhai, *Investigations on high performance proton exchange membrane water electrolyzer.* International Journal of Hydrogen Energy, 2009. **34**(2): p. 678-684.
86. Su, H., et al., *Performance Investigation of Membrane Electrode Assemblies for Hydrogen Production by Solid Polymer Electrolyte Water Electrolysis.* International Journal of Electrochemical Science, 2012. **7**(5).
87. Marshall, A., et al., *Hydrogen production by advanced proton exchange membrane (PEM) water electrolysers—Reduced energy consumption by improved electrocatalysis.* Energy, 2007. **32**(4): p. 431-436.
88. Song, S., et al., *Electrochemical investigation of electrocatalysts for the oxygen evolution reaction in PEM water electrolyzers.* international journal of hydrogen energy, 2008. **33**(19): p. 4955-4961.
89. Zhang, Y., et al., *Study on a novel manufacturing process of membrane electrode assemblies for solid polymer electrolyte water electrolysis.* Electrochemistry Communications, 2007. **9**(4): p. 667-670.
90. Mayousse, E., et al., *Synthesis and characterization of electrocatalysts for the oxygen evolution in PEM water electrolysis.* International Journal of Hydrogen Energy, 2011. **36**(17): p. 10474-10481.

91. Xu, W. and K. Scott, *The effects of ionomer content on PEM water electrolyser membrane electrode assembly performance.* International Journal of Hydrogen Energy, 2010. **35**(21): p. 12029-12037.
92. Millet, P., et al., *Electrochemical performances of PEM water electrolysis cells and perspectives.* International Journal of Hydrogen Energy, 2011. **36**(6): p. 4134-4142.
93. Goñi-Urtiaga, A., D. Presvytes, and K. Scott, *Solid acids as electrolyte materials for proton exchange membrane (PEM) electrolysis: Review.* International Journal of Hydrogen Energy, 2012. **37**(4): p. 3358-3372.
94. Ito, H., et al., *Properties of Nafion membranes under PEM water electrolysis conditions.* International Journal of Hydrogen Energy, 2011. **36**(17): p. 10527-10540.
95. Mauritz, K.A. and R.B. Moore, *State of understanding of Nafion.* Chemical reviews, 2004. **104**(10): p. 4535-4586.
96. Kreuer, K.-D., *Proton conductivity: materials and applications.* Chemistry of Materials, 1996. **8**(3): p. 610-641.
97. Bose, S., et al., *Polymer membranes for high temperature proton exchange membrane fuel cell: Recent advances and challenges.* Progress in Polymer Science, 2011. **36**(6): p. 813-843.
98. Smitha, B., S. Sridhar, and A.A. Khan, *Solid polymer electrolyte membranes for fuel cell applications—a review.* Journal of Membrane Science, 2005. **259**(1–2): p. 10-26.
99. Peighambardoust, S.J., S. Rowshanzamir, and M. Amjadi, *Review of the proton exchange membranes for fuel cell applications.* International Journal of Hydrogen Energy, 2010. **35**(17): p. 9349-9384.
100. Ivanchev, S.S., *Fluorinated proton-conduction nafion-type membranes, the past and the future.* Russian Journal of Applied Chemistry, 2008. **81**(4): p. 569-584.
101. Wen, S., et al., *Sulfonated poly(ether sulfone) (SPES)/boron phosphate (BPO4) composite membranes for high-temperature proton-exchange membrane fuel cells.* International Journal of Hydrogen Energy, 2009. **34**(21): p. 8982-8991.
102. Eikerling, M. and A.A. Kornyshev, *Proton transfer in a single pore of a polymer electrolyte membrane.* Journal of Electroanalytical Chemistry, 2001. **502**(1-2): p. 1-14.
103. Hauch, A., et al., *Highly efficient high temperature electrolysis.* Journal of Materials Chemistry, 2008. **18**(20): p. 2331-2340.
104. Li, Q., et al., *Approaches and Recent Development of Polymer Electrolyte Membranes for Fuel Cells Operating above 100 °C.* Chemistry of Materials, 2003. **15**(26): p. 4896-4915.
105. Masson, J.P., et al., *Obtention and evaluation of polyethylene-based solid polymer electrolyte membranes for hydrogen production.* International Journal of Hydrogen Energy, 1982. **7**(2): p. 167-171.
106. Wei, G., et al., *SPE water electrolysis with SPEEK/PES blend membrane.* International Journal of Hydrogen Energy, 2010. **35**(15): p. 7778-7783.
107. Jung, H.-Y., et al., *Performance of gold-coated titanium bipolar plates in unitized regenerative fuel cell operation.* Journal of Power Sources, 2009. **194**(2): p. 972-975.

108. Wang, S.-H., J. Peng, and W.-B. Lui, *Surface modification and development of titanium bipolar plates for PEM fuel cells.* Journal of Power Sources, 2006. **160**(1): p. 485-489.
109. Tawfik, H., Y. Hung, and D. Mahajan, *Metal bipolar plates for PEM fuel cell—A review.* Journal of Power Sources, 2007. **163**(2): p. 755-767.
110. Wang, H., M.A. Sweikart, and J.A. Turner, *Stainless steel as bipolar plate material for polymer electrolyte membrane fuel cells.* Journal of Power Sources, 2003. **115**(2): p. 243-251.
111. Ensing, W., *Protons and Sodium Ions Interacting With Nafion Confined Water*, in *FOM Institute AMOLF*. 2012, Utrecht University.
112. Cheng, X., et al., *A review of PEM hydrogen fuel cell contamination: Impacts, mechanisms, and mitigation.* Journal of Power Sources, 2007. **165**(2): p. 739-756.
113. Jie, X., Z.-G. Shao, and B. Yi, *The effect of different valency cations on DMFC performance.* Electrochemistry Communications, 2010. **12**(5): p. 700-702.
114. Zhang, L., et al., *The influence of sodium ion on the solid polymer electrolyte water electrolysis.* International Journal of Hydrogen Energy, 2012. **37**(2): p. 1321-1325.
115. Andolfatto, F., et al., *Solid polymer electrolyte water electrolysis: electrocatalysis and long-term stability.* International Journal of Hydrogen Energy, 1994. **19**(5): p. 421-427.
116. Millet, P., F. Andolfatto, and R. Durand, *Design and performance of a solid polymer electrolyte water electrolyzer.* International Journal of Hydrogen Energy, 1996. **21**(2): p. 87-93.
117. Kelly, M.J., et al., *Contaminant absorption and conductivity in polymer electrolyte membranes.* Journal of Power Sources, 2005. **145**(2): p. 249-252.
118. Hongsirikarn, K., et al., *Effect of cations (Na+, Ca2+, Fe3+) on the conductivity of a Nafion membrane.* Journal of Power Sources, 2010. **195**(21): p. 7213-7220.
119. Okada, T., et al., *The Effect of Impurity Cations on the Transport Characteristics of Perfluorosulfonated Ionomer Membranes.* The Journal of Physical Chemistry B, 1999. **103**(17): p. 3315-3322.
120. Okada, T., et al., *Transport and equilibrium properties of Nafion® membranes with H+ and Na+ ions.* Journal of Electroanalytical Chemistry, 1998. **442**(1–2): p. 137-145.
121. Okada, T., et al., *Ion and water transport characteristics in membranes for polymer electrolyte fuel cells containing H+ and Ca2+ cations.* Journal of the Electrochemical Society, 1997. **144**(8): p. 2744-2750.
122. Millet, P., T. Alleau, and R. Durand, *Characterization of membrane-electrode assemblies for solid polymer electrolyte water electrolysis.* Journal of Applied Electrochemistry, 1993. **23**(4): p. 322-331.
123. Napadensky, E., *Investigation of Proton Conductivity of Cation-Exchanged, Sulfonated Poly(b-Styrene-b-Isobutylene-b-Styrene) Membranes*. 2009, Army Research Laboratory.
124. Izquierdo-Gil, M.A., et al., *Water uptake and salt transport through Nafion cation-exchange membranes with different thicknesses.* Chemical Engineering Science, 2012. **72**(0): p. 1-9.
125. Stenina, I.A., et al., *Ion mobility in Nafion-117 membranes.* Desalination, 2004. **170**(1): p. 49-57.

126. Sandra K. Young, S.F.T., Nora C. Beck Tan, Rick L. Paul, *Determining Extent of Ion-Exchange in Various Counterion Nafion Membranes Using Prompt Gamma Neutron Activation Analysis (PGAA)*. 2002: Army Research Laboratory.
127. Kienitz, B., *The effects of cationic contamination on polymer electrolyte membrane fuel cells*, in *Department of Chemial Engineering*. 2009, Case Western Reserve University.
128. Okada, T., *Effect of ionic contaminants*, in *Handbook of Fuel Cells*. 2010, John Wiley & Sons, Ltd.
129. Okada, T., et al., *Ion and water transport characteristics of Nafion membranes as electrolytes.* Electrochimica Acta, 1998. **43**(24): p. 3741-3747.
130. Okada, T., et al., *Ion and Water Transport Characteristics of Perfluorosulfonated Ionomer Membranes with H+ and Alkali Metal Cations.* The Journal of Physical Chemistry B, 2002. **106**(6): p. 1267-1273.
131. Steck, A. and H.L. Yeager, *Water sorption and cation-exchange selectivity of a perfluorosulfonate ion-exchange polymer.* Analytical Chemistry, 1980. **52**(8): p. 1215-1218.
132. Eisenberg, A., H.L. Yeager, and A.C.S.D.o.P. Chemistry, *Perfluorinated ionomer membranes: developed in advance of the Polymer Division topical workshop on per-fluorinated ionomer membranes, Lake Buena Vista, Florida, February 23-26, 1982*. 1982: American Chemical Society.
133. Lopez, M., B. Kipling, and H.L. Yeager, *Exchange rates and water content of a cation exchange membrane in aprotic solvents.* Analytical Chemistry, 1976. **48**(8): p. 1120-1122.
134. Mikkola, M.S., et al., *The Effect of NaCl in the Cathode Air Stream on PEMFC Performance.* Fuel Cells, 2007. **7**(2): p. 153-158.
135. Wakizoe, M., *NEDO Report, Fy. 1997*. 1998, NEDO.
136. Ohashi, M., C.S. Smith, and J.W. Van Zee, *Effect of Calcium Ion on the Performance of PEMFCs.* ECS Transactions, 2007. **11**(1): p. 877-887.
137. Al-Rousan, A.A., *Reduction of fuel consumption in gasoline engines by introducing HHO gas into intake manifold.* International Journal of Hydrogen Energy, 2010. **35**(23): p. 12930-12935.
138. Musmar, S.e.A. and A.A. Al-Rousan, *Effect of HHO gas on combustion emissions in gasoline engines.* Fuel, 2011. **90**(10): p. 3066-3070.
139. Akansu, S.O., et al., *Internal combustion engines fueled by natural gas—hydrogen mixtures.* International Journal of Hydrogen Energy, 2004. **29**(14): p. 1527-1539.
140. Saravanan, N. and G. Nagarajan, *An experimental investigation of hydrogen-enriched air induction in a diesel engine system.* International Journal of Hydrogen Energy, 2008. **33**(6): p. 1769-1775.
141. Saravanan, N., et al., *An experimental investigation on hydrogen as a dual fuel for diesel engine system with exhaust gas recirculation technique.* Renewable Energy, 2008. **33**(3): p. 422-427.
142. Adnan, R., H.H. Masjuki, and T.M.I. Mahlia. *An experimental investigation of unmodified DI diesel engine with hydrogen addition*. in *Energy and Environment, 2009. ICEE 2009. 3rd International Conference on*. 2009.
143. Saravanan, N. and G. Nagarajan, *An experimental investigation on performance, emissions, and combustion in a manifold injection for different exhaust gas recirculation flowrates in hydrogen-diesel dual-fuel operations.* Proceedings of

the Institution of Mechanical Engineers Part D-Journal of Automobile Engineering, 2008. **222**(D11): p. 2131-2145.

144. Bose, P.K. and D. Maji, *An experimental investigation on engine performance and emissions of a single cylinder diesel engine using hydrogen as inducted fuel and diesel as injected fuel with exhaust gas recirculation.* International Journal of Hydrogen Energy, 2009. **34**(11): p. 4847-4854.
145. Miyamoto, T., et al., *Effect of hydrogen addition to intake gas on combustion and exhaust emission characteristics of a diesel engine.* International Journal of Hydrogen Energy, 2011. **36**(20): p. 13138-13149.
146. Bari, S. and M. Mohammad Esmaeil, *Effect of H2/O2 addition in increasing the thermal efficiency of a diesel engine.* Fuel, 2010. **89**(2): p. 378-383.
147. Schweitzer, J. *Scanning Electron Microscope*. 2006 [cited 2010 10/01/2010]; Available from: http://www.purdue.edu/REM/rs/sem.htm.
148. GlobalSino. *EDX - Energy Dispersive X-Ray Analysis*. 2006 [cited 2013 2nd April 2013]; Available from: http://www.globalsino.com/micro/1/micro9999.html.
149. D, Z. *Introduction to X-ray Photoelectron Spectroscopy and to XPS Applications*. 2007 [cited 2013 28/03/2013]; Available from: http://nanohub.org/resources/2731/download/2007.04.27-zemlyanov.pdf.
150. Montaser, A. and D. Golightly, *Inductively coupled plasmas in analytical atomic spectrometry*. 1987.
151. Technologies, A. *ICP-MS 7500 Series Diagram*. [cited 2014 19/03/2014]; Available from: http://www.chem.agilent.com/cag/feature/10-01/feature.html.
152. Page, A., R. Miller, and D. Keeney, *Total carbon, organic carbon, and organic matter.* Methods of soil analysis. Part, 1982. **2**: p. 539-579.
153. Foundation, G.E.C. *TOC Analysis System Schematic*. [cited 2014 19/03/2014]; Available from: http://nett21.gec.jp/CTT_DATA/WMON/CHAP_4/html/Wmon-089.html.
154. A. Tsolakis, K.D.D., J.M. Herreros, *Evaluation of the effects of a Carbon Clean Direct on-board electrolyser on the performance and emissions of a diesel engine*. 2009, University of Birmingham.
155. Mason, T.J., Lorimer, J. P., Walton, D. J., *Sonoelectrochemistry.* Ultrasonics, 1990. **28**(5): p. 333-337.
156. Madigan, N.A., Hagan, Carolynne R. S., Zhang, Honghua., Coury, Louis A., *Effects of sonication on electrode surfaces and metal particles.* Ultrasonics Sonochemistry, 1996. **3**(3): p. S239-S247.
157. Mason, T.J., *Sonochemistry and sonoprocessing: the link, the trends and (probably) the future.* Ultrasonics Sonochemistry, 2003. **10**(4-5): p. 175-179.
158. Mason, T.J., *Sonochemistry and the environment - Providing a "green" link between chemistry, physics and engineering.* Ultrasonics Sonochemistry, 2007. **14**(4): p. 476-483.
159. Walton, D.J., L.D. Burke, and M.M. Murphy, *Sonoelectrochemistry: Chlorine, hydrogen and oxygen evolution at platinised platinum.* Electrochimica Acta, 1996. **41**(17): p. 2747-2751.
160. R, S., *The hydrogen economy, fuel cells, and electric cars.* Technology in Society, 2003. **25**: p. 455-476.
161. Neburchilov, V., et al., *A review of polymer electrolyte membranes for direct methanol fuel cells.* Journal of Power Sources, 2007. **169**(2): p. 221-238.

162. Yilmaz, A.C., E. Uludamar, and K. Aydin, *Effect of hydroxy (HHO) gas addition on performance and exhaust emissions in compression ignition engines.* International Journal of Hydrogen Energy, 2010. **35**(20): p. 11366-11372.
163. Li, S.-D., C.-C. Wang, and C.-Y. Chen, *Water electrolysis in the presence of an ultrasonic field.* Electrochimica Acta, 2009. **54**(15): p. 3877-3883.
164. Stojić, D.L., et al., *A comparison of alkaline and proton exchange membrane electrolyzers.* Russian Journal of Physical Chemistry A, 2008. **82**(11): p. 1958-1960.
165. Gomes Antunes, J.M., R. Mikalsen, and A.P. Roskilly, *An experimental study of a direct injection compression ignition hydrogen engine.* International Journal of Hydrogen Energy, 2009. **34**(15): p. 6516-6522.
166. Heywood, J.B., *Internal combustion engine fundamentals*. 1988, New York: London: McGraw-Hill.
167. Industries, T. *Properties table of Stainless steel, Metals and other Conductive materials*. [cited 2015 13/02/2015]; Available from: http://www.tibtech.com/conductivity.php.
168. Huang, Y.-X., et al., *A new cathodic electrode deposit with palladium nanoparticles for cost-effective hydrogen production in a microbial electrolysis cell.* International Journal of Hydrogen Energy, 2011. **36**(4): p. 2773-2776.
169. Khanova, L.A. and L.I. Krishtalik, *Kinetics of the hydrogen evolution reaction on gold electrode. A new case of the barrierless discharge.* Journal of Electroanalytical Chemistry, 2011.
170. Dubey, P.K., et al., *Hydrogen generation by water electrolysis using carbon nanotube anode.* International Journal of Hydrogen Energy, 2010. **35**(9): p. 3945-3950.
171. Shi, K., Hu, Kun., Wang, Sheng., Lau, Chung-Yin., Shiu, Kwok-Keung., *Structural studies of electrochemically activated glassy carbon electrode: Effects of chloride anion on the redox responses of copper deposition.* Electrochimica Acta, 2007. **52**(19): p. 5907-5913.
172. Wei, Z.D., et al., *Water electrolysis on carbon electrodes enhanced by surfactant.* Electrochimica Acta, 2007. **52**(9): p. 3323-3329.
173. Ye, F., et al., *Electrocatalytic properties of Ti/Pt-IrO2 anode for oxygen evolution in PEM water electrolysis.* International Journal of Hydrogen Energy, 2010. **35**(15): p. 8049-8055.
174. Singh, D., *Analysis of Urea Electrolysis for Generation of Hydrogen*, in *Russ College of Engineering and Technology*. 2009, Ohio University: Ohio.
175. Laude, T., T. Kobayashi, and Y. Sato, *Electrolysis of LiOH for hydrogen supply.* International Journal of Hydrogen Energy, 2010. **35**(2): p. 585-588.
176. Serebrennikova, I., et al., *Steel corrosion in alkaline batteries.* Electrochimica Acta, 2009. **54**(22): p. 5216-5222.
177. Liu, Z. and G.A. Karim, *Knock characteristics of dual-fuel engines fuelled with hydrogen fuel.* International Journal of Hydrogen Energy, 1995. **20**(11): p. 919-924.
178. Tsolakis, A., et al., *Dual Fuel Diesel Engine Operation Using H2. Effect on Particulate Emissions.* Energy & Fuels, 2005. **19**(2): p. 418-425.
179. Szwaja, S. and K. Grab-Rogalinski, *Hydrogen combustion in a compression ignition diesel engine.* International Journal of Hydrogen Energy, 2009. **34**(10): p. 4413-4421.

180. Verhelst, S. and T. Wallner, *Hydrogen-fueled internal combustion engines.* Progress in Energy and Combustion Science, 2009. **35**(6): p. 490-527.
181. Lata, D.B. and A. Misra, *Theoretical and experimental investigations on the performance of dual fuel diesel engine with hydrogen and LPG as secondary fuels.* International Journal of Hydrogen Energy, 2010. **35**(21): p. 11918-11931.
182. Shrestha S., L.G., Balan G., Souza M., *A before treatment method for reduction of emissions in diesel engines.* SAE Technical Paper No. 2000-01-2791 2000.
183. Kuo, K.K.-y., *Principles of Combuston*. 2 ed. 2005: Wiley-Interscience.
184. Bika A, F.L., Kittleson D *Emissions effects of hydrogen as a supplemental fuel with diesel and biodiesel.* SAE Technical Paper No. 2008-01-0648, 2008.
185. Lilik, G.K., et al., *Hydrogen assisted diesel combustion.* International Journal of Hydrogen Energy, 2010. **35**(9): p. 4382-4398.
186. Shrivastava, M., et al., *Kinetics of Soot Oxidation by NO2.* Environmental Science & Technology, 2010. **44**(12): p. 4796-4801.
187. York APE, A.M., Watling TC, Walker AP, Cox JP, Gast J, *Modelling of the catalyzed continuously regenerating diesel particulate filter (CCR-DPF) system: model development and passive regeneration studies.* SAE Technical Paper No. 2007-01-0043, 2007.
188. Lu, P.W.T. and S. Srinivasan, *Advances in water electrolysis technology with emphasis on use of the solid polymer electrolyte.* Journal of Applied Electrochemistry, 1979. **9**(3): p. 269-283.
189. Nikolic, V.M., et al., *Raising efficiency of hydrogen generation from alkaline water electrolysis - Energy saving.* International Journal of Hydrogen Energy. **In Press, Corrected Proof**.
190. Zhang, H., G. Lin, and J. Chen, *Evaluation and calculation on the efficiency of a water electrolysis system for hydrogen production.* International Journal of Hydrogen Energy, 2010. **35**(20): p. 10851-10858.
191. Mazloomi, S.K. and N. Sulaiman, *Influencing factors of water electrolysis electrical efficiency.* Renewable and Sustainable Energy Reviews, 2012. **16**(6): p. 4257-4263.
192. Bird R, S.W., Lightfoot E, , *Transport Phenomena*. 2nd ed. 2002, New York: John Wiley & Sons.
193. Matsushima, H., Y. Fukunaka, and K. Kuribayashi, *Water electrolysis under microgravity: Part II. Description of gas bubble evolution phenomena.* Electrochimica Acta, 2006. **51**(20): p. 4190-4198.
194. Bocca, C., A. Barbucci, and G. Cerisola, *The influence of surface finishing on the electrocatalytic properties of nickel for the oxygen evolution reaction (OER) in alkaline solution.* International Journal of Hydrogen Energy, 1998. **23**(4): p. 247-252.
195. Abouatallah, R., Kirk, D., Thorpe, S., & Graydon, J., *Reactivation of Nickel Cathodes by Dissolved Vanadium Species During Hydrogen Evolution in Alkaline Mixture.* Electrochimica Acta, 2001. **47**(4): p. 613-621.
196. Marčeta Kaninski, M.P., et al., *Ionic activators in the electrolytic production of hydrogen—cost reduction-analysis of the cathode.* Journal of Power Sources, 2004. **131**(1–2): p. 107-111.
197. Eigeldinger, J. and H. Vogt, *The bubble coverage of gas-evolving electrodes in a flowing electrolyte.* Electrochimica Acta, 2000. **45**(27): p. 4449-4456.

198. Faison JA, P.N., Thornton TJ, , *Method for removing ceramic material from castings using caustic medium with oxygen getter*, U.P. Office, Editor. 1996: US.
199. Martinson, C.A., *Characterisation of a Proton Exchange Membrane Electrolyser Using the Current Interrupt Method*. 2012: North-West University, Potchefstroom Campus.
200. Belvedere, B., et al., *Experimental analysis of a PEM fuel cell performance at variable load with anodic exhaust management optimization.* International Journal of Hydrogen Energy, 2013. **38**(1): p. 385-393.
201. Schalenbach, M., et al., *Pressurized PEM water electrolysis: Efficiency and gas crossover*. International Journal of Hydrogen Energy, 2013. **38**(35): p. 14921-14933.
202. Balat, M., *Potential importance of hydrogen as a future solution to environmental and transportation problems.* International Journal of Hydrogen Energy, 2008. **33**(15): p. 4013-4029.
203. Antonucci V, A.A., Briguglio N, Brunaccini G, Dispenza G, Ferraro M, *Hydrogen Production by PEM Electrolysis for Back-up Power and Electric Vehicle Refill*. 2011.
204. ELGA. *Pure LabWater Guide*. 2013 [cited 2014 27/02/2014]; Available from: http://www.elgalabwater.com/water-quality-en.html.
205. Grigoriev, S.A., et al., *Platinum and palladium nano-particles supported by graphitic nano-fibers as catalysts for PEM water electrolysis.* International Journal of Hydrogen Energy, 2010.
206. Marshall, A.T., et al., *Performance of a PEM water electrolysis cell using IrxRuyTazO2 electrocatalysts for the oxygen evolution electrode.* International Journal of Hydrogen Energy, 2007. **32**(13): p. 2320-2324.
207. Marshall, A., et al., *Hydrogen production by advanced proton exchange membrane (PEM) water electrolysers--Reduced energy consumption by improved electrocatalysis.* Energy, 2007. **32**(4): p. 431-436.
208. Marshall, A., et al., *Performance of a PEM water electrolysis cell using IrxRuyTazO2IrxRuyTazO2 electrocatalysts for the oxygen evolution electrode.* International Journal of Hydrogen Energy, 2007. **32**(13): p. 2320-2324.
209. Green, H. *Hydrogen*.
210. UK, S.E. 2014 [cited 2014 21/07/2014]; Available from: http://www.solar-energy.co.uk/.

Appendices

Appendix: List of Publications

1. Pollet B.G., Symes D., “Chapter 10.2: Sonoelectrochemical Production of Hydrogen” in *Power Ultrasound in Electrochemistry, From Versatile Laboratory Tool to Engineering Solution*, 2012, Wiley, p303-305
2. Symes, D., Al-Duri, B., Dhir, A., Bujalski, W., Green, B., Shields, A., Lees, M., "Design for On-Site Hydrogen Production for Hydrogen Fuel Cell Vehicle Refuelling at University of Birmingham, U.K.", *Energy Procedia*, Vol. 29, 2012, p. 606-615.
3. Symes, D., Al-Duri, B., Dhir, A., Bujalski, W., "Cost-effective design of the alkaline electrolyser for enhanced electrochemical performance and reduced electrode degradation", *International Journal of Low-Carbon Technologies*, 2013, doi: 10.1093/ijlct/ctt034
4. Dhir A., Symes D., Tsolakis A., Dearn K., Herreros J.M., “HHO Fact or Fiction?”, *4th European PEFC and H2 Forum Conference Proceedings*, 2013, Chapter 10, Section A12, p17-27.
5. Symes D., Al-Duri B., Dhir A., “Degradation Characterisation of Nickel Electrodes of an Alkaline Electrolyser”, *4th European PEFC and H2 Forum Conference Proceedings*, 2013, Chapter 6, Section A07, p68-78.
6. Symes D., Taylor-Cox C., Holyfield L., Al-Duri B., Dhir A., “Feasibility of an oxygen-getter with nickel electrodes in alkaline electrolysers”, *Materials for Renewable and Sustainable Energy*, 2014, Volume 27 (3).
7. Symes D., Maillard J.G., Courtney J., Watton J., Meadowcroft A., Chandan A.S., Gurley L., Priestly R., Sedaroglu G., “Development of a hydrogen fuelling infrastructure in the Northeast U.S.A.”, *International Journal of Hydrogen Energy*, 2014, Volume 39 (14) p.7460-7466.